

TECHNISCHE UNIVERSITÄT MÜNCHEN
Lehrstuhl für Statik

**Finite Element Based Simulation, Design and Control
of Piezoelectric and Lightweight Smart Structures**

Michael Fischer

Vollständiger Abdruck der von der Ingenieur fakultät Bau Geo Umwelt
der Technischen Universität München zur Erlangung des akademischen Grades eines

Doktor-Ingenieurs

genehmigten Dissertation.

Vorsitzender:

Univ.-Prof. Dr.-Ing. habil. Fabian Duddeck

Prüfer der Dissertation:

1. Univ.-Prof. Dr.-Ing. Kai-Uwe Bletzinger
2. Univ.-Prof. Dr. rer. nat. Ernst Rank
3. Univ.-Prof. Dr.-Ing. habil. Sven Klinkel,
Rheinisch-Westfälische Technische Hochschule Aachen

Die Dissertation wurde am 27.06.2013 bei der Technischen Universität München
eingereicht und durch die Ingenieur fakultät Bau Geo Umwelt am 01.09.2013 angenom-
men.

Abstract

Smart structures represent a rapidly growing interdisciplinary technology that is adopted in many fields to increase functionality, improve usability or to create even more efficient structures. In the related sensor and actuator technology, piezoelectric materials become more and more prevalent. Numerical simulation methods can be used to facilitate an efficient design and development process of smart structures even before the first prototype is built. In this context, this work presents a finite element based computational framework and related algorithms for the virtual design and simulation of controlled smart lightweight structures.

A novel, geometrically nonlinear piezoelectric composite shell element formulation is presented. The element is completely based on nonlinear, three-dimensional continuum theory and thus allows for the use of arbitrary complete three-dimensional constitutive laws without reduction or manipulation in nonlinear plate and shell analysis. A 8-parameter single-director formulation with Reissner-Mindlin kinematics is developed, which also considers deformations in thickness direction. The element is based on a modified Hu-Washizu functional of the coupled electromechanical problem that eliminates locking phenomena via both the enhanced assumed strain concept (EAS) and the assumed natural strains (ANS) method. Similar to enhanced strains, also enhanced assumed electric field strength terms are introduced to eliminate related parasitic terms and incompatible approximation spaces of the electromechanical problem. A detailed investigation of the diverse locking phenomena is presented, as well as an analysis of the performance of the element enhancement techniques.

Beyond that, the overall design process of smart structures including closed-loop control is focus of this work. Controller design is based on a state space model that is derived from the finite element model and that preserves the geometrically nonlinear equilibrium state and eventual prestress effects of the structure. Discrete time control via an optimal linear-quadratic-Gaussian (LQG) regulator is applied. In the context of control, special focus is put here on prestressed membrane structures and their special issues in the context of controller design.

Several examples demonstrate the performance and accuracy of the presented piezoelectric element formulation and provide comparisons to related element formulations of the literature. Furthermore, the methods and algorithms of all simulation and design steps of a smart structure are illustrated and verified at the example of a smart 4-point tent that adopts closed-loop control for vibration suppression under external loads. Beyond that, the three-dimensional static-aeroelastic simulation and optimization of a solid-state piezo-actuated variable-camber morphing wing for low Reynolds number regimes is presented. Parameter-free structural optimization is used here in order to integrate a flexible, generic and efficient optimization technique in the very early stage of design. The simulation and design results illustrate the workflow and demonstrate a good match to experimental results.

Zusammenfassung

Intelligente Strukturen stellen eine rapide wachsende, interdisziplinäre Technologie dar, die in zahlreichen Anwendungsgebieten eingesetzt wird, um die Funktionalität zu erweitern, die Gebrauchstauglichkeit zu verbessern, oder schlichtweg noch effizientere Strukturen zu entwickeln. In der Sensorik und Aktorik werden dabei zunehmend piezoelektrische Materialien verwendet. Numerische Simulation kann eingesetzt werden, um einen effizienten Entwurfprozess intelligenter Strukturen noch vor der Fertigung des ersten Prototyps zu ermöglichen. In diesem Kontext präsentiert die vorliegende Arbeit ein Rahmenkonzept und zugehörige Methoden und Algorithmen für den virtuellen Entwurf und die Simulation intelligenter Leichtbaustrukturen.

Ein neues, geometrisch nichtlineares Komposit-Schalenelement wird vorgestellt. Das Element basiert auf nichtlinearer, dreidimensionaler (3D) Kontinuumsmechanik und ermöglicht daher die direkte Verwendung von 3D Materialgesetzen ohne notwendige Modifikation für die Platten- oder Schalentheorie. Dazu wird eine 8-Parameter Formulierung mit Einschichttheorie (Singledirektorthorie) und Reissner-Mindlin Kinematik entwickelt, die auch Deformationen in Dickenrichtung berücksichtigt. Das Element basiert auf einem modifizierten Hu-Washizu Funktional des gekoppelten elektromechanischen Problems. Locking-Phänomene werden durch die Enhanced Assumed Strains (EAS) Methode und die Assumed Natural Strains (ANS) Methode beseitigt. Ähnlich zur EAS Methode werden zusätzlich erweiterbare Moden des elektrischen Feldes (EAE Moden) eingeführt, um parasitäre Terme und inkompatible Approximationsräume des elektromechanischen Problems zu beheben.

Zudem wird ein allgemeiner Entwurfsprozess von intelligenten Strukturen inklusive Regelung vorgestellt. Der Reglerentwurf basiert auf einem Zustandsraummodell, das vom Finite Elemente Modell abgeleitet wird und den geometrisch nichtlinearen Gleichgewichtszustand inklusive potentieller Vorspannungseffekte berücksichtigt. Es wird eine zeitdiskrete Regelung mit einem optimalen linear-quadratischen Gauss-Regler (LQG Regler) verwendet. Besonderer Fokus liegt auf dem Reglerentwurf für vorgespannte Membranstrukturen.

Numerische Beispiele demonstrieren die Leistungsfähigkeit und Genauigkeit des vorgestellten piezoelektrischen Elements und zeigen Vergleiche zu Elementformulierungen der Literatur auf. Die Methoden und Algorithmen sämtlicher Simulations- und Entwurfsschritte einer intelligenten Struktur werden am Beispiel eines 4-Punkt-Zeltes demonstriert, das aktive Regelung zur Vibrationskontrolle unter äußeren Lasten verwendet. Außerdem wird die dreidimensionale, statisch-aeroelastische Simulation und Optimierung eines piezoelektrisch aktuierten formadaptiven Flügels mit festen Flugzuständen für die Anwendung im Bereich niedriger Reynoldszahlen vorgestellt. Parameterfreie Strukturoptimierung wird hierbei verwendet, um eine flexible und effiziente Optimierungstechnik bereits in einem frühen Stadium des Entwurfs zu integrieren. Die Ergebnisse illustrieren den Entwurfsprozess und weisen eine gute Übereinstimmung mit den experimentellen Ergebnissen nach.

Acknowledgments

This dissertation was written from 2007 to 2013 during my time as research assistant at the Chair of Structural Analysis (Lehrstuhl für Statik) at the Technische Universität München, Munich, Germany.

I would like to thank sincerely Prof. Dr.-Ing. Kai-Uwe Bletzinger for giving me the possibility to work in his research group. I want to thank him not only for his helpful and inspiring guidance as doctoral supervisor, but also for providing me the academic freedom to develop and realize new ideas and methods. I also want to thank Dr.-Ing. Roland Wüchner for many fruitful discussions.

Furthermore, I would like to address my thanks to the members of my examining jury, Univ.-Prof. Dr. rer. nat. Ernst Rank and Univ.-Prof. Dr.-Ing. Sven Klinkel. Their interest in my work is gratefully appreciated. Also, I want to thank Univ.-Prof. Dr.-Ing. Fabian Duddeck for chairing the jury.

I also want to thank Prof. Dr. Bilgen from the Old Dominion University in Norfolk, USA, for the good cooperation in the Variable-Camber Morphing Wing Project that will be continued.

My position as coordinator of the Bavarian Graduate School of Computational Engineering (BGCE) was funded by the state of Bavaria. This funding for my whole work as research assistant is gratefully acknowledged.

I also want to thank all coworkers at the Chair of Structural Analysis for the friendly cooperation and the pleasant time that I had working with them. I want to especially mention Helmut Masching and Dr. Matthias Firl who inspired my work with numerous discussions.

Finally, I want to thank my family and my dear wife Martina for their continuous patience, their help and their guidance at all times.

Munich, June 2013

Michael Fischer

Contents

1	Introduction	1
1.1	Motivation	1
1.2	Review and Current State of Research	5
1.2.1	Piezoelectricity	5
1.2.2	Finite Element Models of Shells	6
1.2.3	Piezoelectric Shell Element Technology	9
1.2.4	Control	11
1.3	Objectives	12
1.4	Outline of This Thesis	14
2	Fundamentals of Continuum Mechanics and Electrostatics	17
2.1	Namings and Conventions	17
2.2	Differential Geometry	18
2.3	Kinematics	21
2.4	Electrostatics	24
2.5	Stresses and Electric Displacements	26
2.5.1	Stress Measures	26
2.5.2	The Electric Displacement	27
2.6	Conservation Laws	27
2.6.1	Balance of Mass	28
2.6.2	Conservation of Linear Momentum	28
2.6.3	Conservation of Angular Momentum	29
2.6.4	Conservation of Electric Charge	30
2.7	Constitutive Equations	31
2.7.1	Phenomenological Behavior of Piezoelectric Materials	32

2.7.1.1	Crystal Structure	32
2.7.1.2	Direct and Inverse Piezoelectric Effect	34
2.7.2	Continuum Mechanical Description	36
2.7.2.1	Elasticity Tensor	37
2.7.2.2	Piezoelectric Tensor and Permittivity Tensor	39
2.8	Strong Form	40
2.9	Energy Methods and Functionals	42
2.9.1	Principle of Virtual Work	42
2.9.1.1	Derivation by the Minimum Potential Energy Principle	42
2.9.1.2	Derivation from the Method of Weighted Residuals	43
2.9.1.3	Euler Differential Equations	44
2.9.2	Principle of Hu-Washizu	45
2.9.2.1	Derivation from the Minimum Potential Energy Principle	45
2.9.2.2	Euler Differential Equations	49
2.9.3	Modified Principle of Hu-Washizu	50
2.9.3.1	Derivation from the Hu-Washizu Principle	50
2.9.3.2	Derivation as Independent Variational Principle	52
2.9.3.3	Euler Differential Equations	55
2.9.4	Overview	56
3	Fundamentals of the Finite Element Method	59
3.1	Discretization	59
3.2	Convergence	61
3.3	Rank of the System Matrix	62
3.4	The Patch Test	63
3.5	Locking and Incompatible Approximation Spaces	66
3.5.1	Introduction	66
3.5.2	Interpretation of Locking	66
3.5.2.1	Mechanically Motivated Point of View	67
3.5.2.2	Mathematical Point of View	67
3.5.2.3	Numerical Point of View	68
3.5.3	Mechanical Locking Phenomena	69
3.5.3.1	In-Plane Shear Locking	70
3.5.3.2	Transverse Shear Locking	72

3.5.3.3	Trapezoidal Locking	75
3.5.3.4	Curvature Thickness Locking	76
3.5.3.5	Membrane Locking	78
3.5.3.6	Volumetric Locking	78
3.5.4	Electromechanical Locking Phenomena	80
3.5.4.1	Pure Bending	80
3.5.4.2	Shear Loading	81
3.6	Enhanced Element Formulations	82
3.6.1	Reduced Integration	82
3.6.2	ANS Method	83
3.6.3	EAS and EAE Method	86
3.6.3.1	Historical Background of the EAS Method	86
3.6.3.2	Illustration of EAS at a 2D Problem	86
3.6.3.3	Illustration of EAE at a 2D Problem	88
3.6.3.4	Prerequisites for Enhanced Modes	89
4	Theory of the Piezoelectric Composite Shell Element	91
4.1	Geometric Definitions and Kinematic Assumptions	91
4.1.1	Mechanical Part	92
4.1.2	Electrical Part	95
4.1.3	Generalized Representation	96
4.2	Static Variables	96
4.3	Pre-Integration of Material Law	97
4.4	Constitutive Law for Layered Structures	98
4.5	Discretization	101
4.5.1	Approximation of Geometry and Generalized Displacements	101
4.5.2	Approximation of Strains and Electric Field Strength	103
4.5.3	EAS and EAE Method	105
4.5.4	ANS Method	108
4.6	Linearization of Weak Form	109
4.6.1	Restrictions to Pass the Patch Test	112
4.7	Stress and Electric Displacement Recovery	113

5	Closed-Loop Control of Lightweight Structures	115
5.1	Introduction to control theory	115
5.2	Special Characteristics of Membrane Structures	118
5.2.1	Equilibrium Formulation of a Surface Stress Field	118
5.2.2	Inverse Problem Formulation and Regularization	119
5.2.3	Cutting Pattern Generation	122
5.2.4	Challenges for Control in the Context of Membrane Structures . . .	123
5.3	Nonlinear Transient Analysis	123
5.4	Model Order Reduction	124
5.5	State Space Approach	126
5.6	Placement of Actuators and Sensors	127
5.7	Controller Design	129
5.8	Nonlinear Simulation including Control	131
6	Software Implementation	133
6.1	Challenges of Modern Finite Element Software	133
6.2	Problems and Pitfalls of Procedural Programming	133
6.3	Chances Offered by the Object-oriented Programming Paradigm	134
6.4	Object-Oriented Finite Element Programming	135
6.5	Development of Carat++	136
7	Numerical Application Examples	139
7.1	Piezoelectric Patch Tests	140
7.1.1	Model Definition	140
7.1.2	Displacement Patch Test	141
7.1.3	Tension Patch Test	142
7.1.4	Electric Field Patch Test	143
7.1.5	Bending Patch Test	144
7.1.6	Shear Patch Test	146
7.2	Bimorph	149
7.2.1	Sensor Test	149
7.2.2	Actor Test	150
7.2.3	Mesh Distortion Test	150
7.2.4	Geometrically Nonlinear Bimorph Sensor	153

7.3	Scordelis-Lo Roof	155
7.4	Pinched Cylinder	157
7.5	Virtual Design Loop of a Smart Tent	159
7.5.1	Design of the Passive Structure	159
7.5.2	Nonlinear Transient Analysis	161
7.5.3	Model Order Reduction	162
7.5.4	Selection and Placement of Actuators and Sensors	164
7.5.5	Controller Design	165
7.5.6	Nonlinear Simulation including Control	167
7.5.7	Overview of the Design Process	168
7.6	Solid-State Variable-Camber Morphing Wing	170
7.6.1	Static Aeroelastic Model Setup	170
7.6.1.1	Structural Simulation	170
7.6.1.2	Fluid Simulation	172
7.6.1.3	Static-Aeroelastic Coupling	173
7.6.2	Parameter-Free Optimization of the Wing	175
8	Conclusions and Outlook	181
A	Finite Element Shape Functions	191
A.1	Triangular Elements	191
	3-Noded Triangular Element	191
	6-Noded Triangular Element	191
A.2	Quadrilateral Elements	192
	4-Noded Quadrilateral Element	192
	9-Noded Quadrilateral Element	192
B	Nomenclature	193
	Bibliography	199

Chapter 1

Introduction

1.1 Motivation

In the case of thin lightweight structures like tents, stadium roofings, diverse automotive components, aircraft parts or space structures, the objective of the computational design process is usually to minimize the weight of the structure. However, at the same time various constraints stemming from safety, usability or comfort considerations have to be satisfied, like stress, deformation or vibration criteria. In order to increase the static and dynamic performance of structures also in presence of time-varying environmental and operational conditions, the structure can be designed to be *adaptive* or *smart*.

Smart structures, also called *active* or *intelligent structures* can be defined as structural systems with the ability to respond adaptively in a pre-designed manner to changes in environmental conditions using distributed actuators and sensors of high integration level. Sensors and actuators are directed by a controller that allows for the modification of static and dynamic behavior of the system. A detailed discussion of the naming and the terminology can be found e.g. at Clark et al. [CSG98].

An adaptive structure makes use of one or more controllers that analyze the responses obtained from the sensors and use control algorithms in order to produce actuating signals. These signals are subsequently amplified and transferred to the actuators in order to perform a localized action which adapts and adjusts structural characteristics such as its shape, stiffness or damping. A smart structure is able to respond to variable ambient stimuli, regardless if these are internal or external, such as temperature or loads, respectively. In general, control can be applied to structures in order to increase functionality, improve usability or to create even more efficient structures. Intelligent structures represent a rapidly growing interdisciplinary technology embracing the fields of materials, structures, sensor- and actuator systems, information and signal processing, electronics and control.

The application fields range from automotive to aerospace and civil engineering and beyond. Figure 1.1 shows for example the Stuttgart SmartShell which represents an adaptive shell supporting structure out of wood with over 10m span [SmS12]. It is build with a thickness of only 4cm which would be in general too thin to sustain snow and wind loads. In order to reach this high slenderness of the structure, three supports are actively

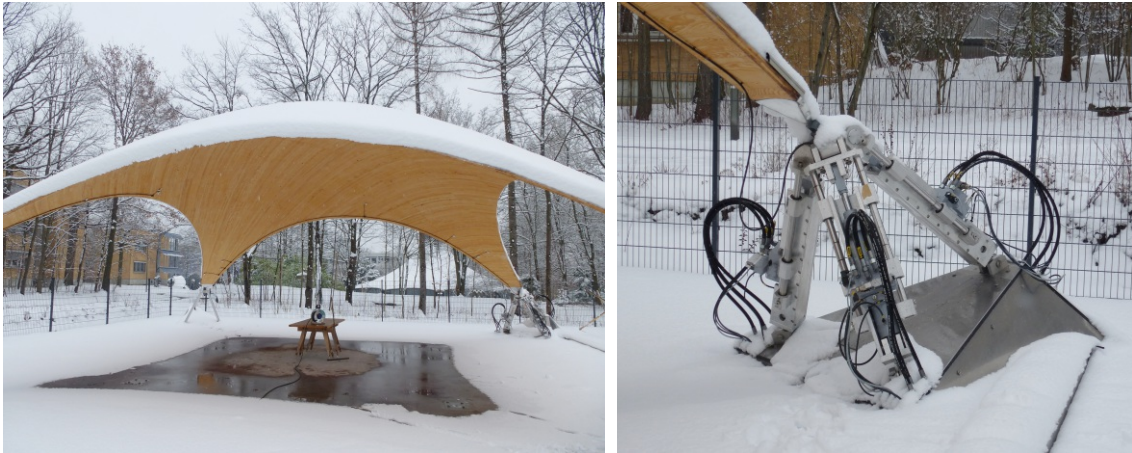


Figure 1.1: The *Stuttgart SmartShell*: actively controlled shell structure under snow load.

controlled in their position in order to allow for a shape adaptation and thus a reduction of stresses and vibrations of the system. In this context, smart technologies open the door to ultra-lightweight design of structures.

Smart structures are also highly interesting in the automotive industry: For example, the missing roof structure of convertibles leads to a lower torsional stiffness of the car structure. Due to the lower stiffness, the car body is more susceptible to vibrations. Active rods based on piezoceramics can be embedded in the frame of convertibles in order to successfully perform vibration reduction [KGF01].

Furthermore, two examples from the field of aeronautics are shown in Figure 1.2: Highly efficient variable-camber morphing wings with smooth and continuous aerodynamic control surfaces can be developed with the help of state-of-the-art piezoelectric actuators (Figure 1.2 a), as discussed in detail in chapter 7.6 of this work. Another example are rotor blades that adopt active control with low profile piezoceramic actuators in the blade skin (Figure 1.2 b). This concept aims at reducing the blade vortex interaction induced vibration by appropriate twisting of the blades in order to improve noise, comfort and flight performance characteristics.

For the design of these smart structures, a wide range of smart materials is used, comprising piezoelectric, electrostrictive and magnetostrictive elements, electrorheological fluids and solids, carbon nanotube actuators, shape memory alloys (SMAs), and many more [SM01, BSW96]. These materials can be used for sensing, actuating or even both as in the case of piezoelectric materials.

Piezoelectricity is a fundamental phenomenon of electromechanical interaction and represents a linear coupling in energy conversion [Ike90]. Piezoelectric materials can generate an electric signal from applied mechanical strain (*direct piezoelectric effect*). In the other way round, piezoelectric materials react on applied electric voltage with mechanical strains (*inverse piezoelectric effect*). That's why piezoelectric materials play a role in both sensor and actor technology. However, piezoelectric materials are of higher interest

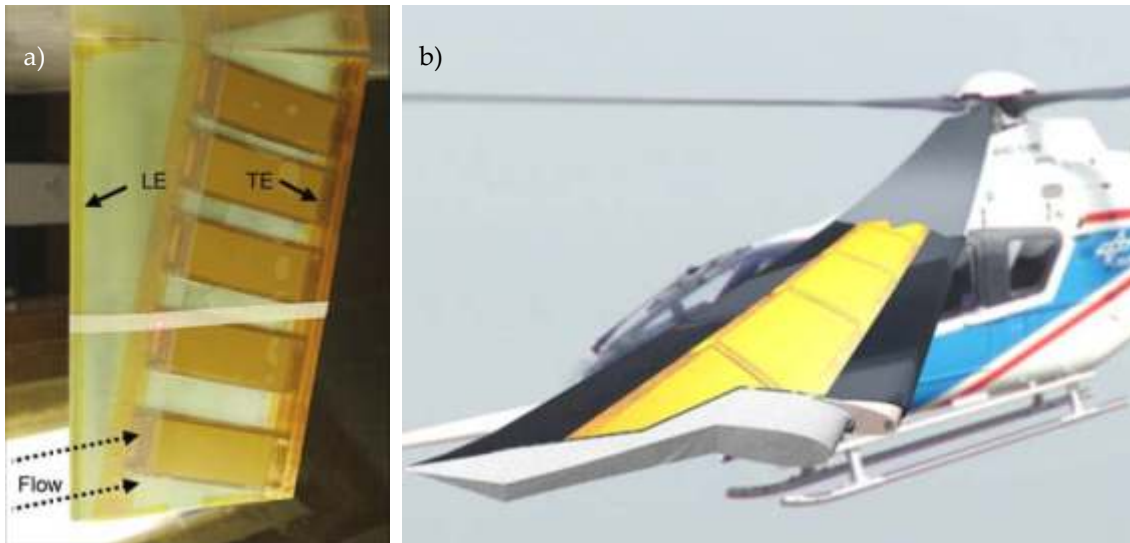


Figure 1.2: Applications of Piezoelectric materials for smart structures: (a) variable-camber morphing wing [BF12] and (b) active rotor blade with low profile piezoceramic actuators in the blade skin [MW05].

in the field of actuation, as there exist several other techniques of comparable quality in the sensor context.

Piezoelectric materials are available as natural materials like quartz as well as in synthetic form e.g. via sintering in the case of piezoelectric ceramics. Due to advancing manufacturing techniques, manifold geometries, layered systems and composites structures with piezoelectric materials are possible. The general advantages of piezoelectric material are short reaction time, high precision, durability and the capability to produce large forces. In static operation states, piezoelectric actuators are comparable with capacitors and consume practically no energy. The typical travel ranges of piezoelectric actors are $10 - 100\mu\text{m}$ and can be considerably increased e.g. via stacked sequences. Bending actuators in general reach a deformation of several millimeters. This can be amplified via tailored embedding into carrier structures using leverage effects.

In general, the application fields of piezoelectric systems can be subdivided into four groups [Sch10]: First of all, energy harvesting systems which transform mechanical energy into electrical energy. An overview of this field can e.g. be found at Erturk and Inman [EI11]. Second, position and shape control where a change in shape is detected, balanced or actively generated. Related application fields range from precise positioning of space antennas up to the control of turbine blades. An related overview of computational aspects of structural shape control is e.g. given by Ziegler [Zie05], while a review of shape control with focus on piezoelectric actuation is presented by Irschik [Irs02]. The third group of application fields is vibration and buckling control, as e.g. in Berger et al. [BGKS00]. And last but not least, the field of health monitoring where piezoelectric elements are used in bridges, buildings and airplanes for an early detection of damages.

Beyond that, the usage of piezoelectricity is part of the daily life today: The direct piezoelectric effect is used in electric cigarette lighters, electronic weighing scales and microphones. Actuation via the inverse piezoelectric effect is used e.g. in diesel injection systems, loudspeakers, and inkjet printers. Furthermore, electronic components combine both effects: An applied voltage leads to a deformation which in turn is detected again. This is the case e.g. in quartz crystal clocks or in the ultrasonic signal processing of parking assist systems.

However, for economical reasons, shorter development cycles and optimal usage of the resources are required. Beyond that, more and more complex and detailed demands have to be considered in modern products. Thus real experiments do not always provide a solution, as they are expensive, time-consuming and often just not practicable. That's why the numerical analysis of single parts or even complete machines or buildings has established itself as efficient tool to predict and design the behavior of systems. Computational simulations are usually the starting point of today's engineering design processes and gain more and more importance. Based on a virtual computer model, the system under consideration can be analyzed, optimized and even redesigned before the first prototype is built. This saves both time and money.

The finite element method has superseded other numerical approximation methods in many applications fields due to its reliability, robustness, efficiency and versatility. Originally developed for structural mechanics applications, the application field of the finite element method today comprises heat conduction, fluid mechanics, electromagnetism, biomechanics or medicine technology. Also in the context of design, analysis and control of flexible mechanical structures, simulations are commonly based on the finite element method. More and more realistic representations of the real systems have to be simulated considering detailed physical and mathematical models that reflect the coupling of the involved fields. That's why the finite element method has to intensify its interdisciplinary character to face the today's requirements.

Smart structures provide unique challenges to the numerical engineer due to their level of complexity: The requirements for the finite element simulation start at the stage of finite element technology: Efficient and accurate finite elements are needed that reflect e.g. the layered structure of piezoelectric composites, the electromechanical coupling of piezoelectric materials, as well as the large deflections that can appear especially in the sensor case. However, not only a model of the structure including the embedded sensors and actuators has to be assessed, but also a suitable control algorithm has to be designed. Thus the finite element method shall provide a comprehensive computational framework for a holistic simulation and design process including the aspects of control. As a consequence, not only the finite element technology is decisive, but also the reach and coverage of design aspects in the computational modeling.

Besides to efficient structures with bending stiffness like shells, also the membrane structures form a group of special importance in efficient lightweight structural design. Prestressed membranes are well suited for lightweight structures due to the extremely low

areal density and the optimal static load carrying behavior. Prominent examples are the well-known minimal surfaces [HT85]. Experimentally, minimal surfaces can be realized by soap films (*soap film analogy*) [BR99]. For the design of highly efficient structures, it is thus reasonable to aim for the combination of the efficiency of (passive) membrane structures with the advantages of active control.

1.2 Review and Current State of Research

1.2.1 Piezoelectricity

In this work, a compact historical review of the developments in piezoelectricity shall be given. A detailed historical review of the early developments in this field can be found e.g. at [Cad64]. A review of the newer developments in piezoelectricity can be found e.g. at [HLW08].

Pierre and Jacques Curie first discovered the piezoelectric effect in 1880 at experiments with tourmaline crystals. They found out that charges are created at specific crystals under mechanical loading and that these charges are directly proportional to the mechanical loading. Lippmann predicted the existence of the inverse effect from thermodynamic considerations. His prediction was verified by the Curies in 1881. In the upcoming years, twenty crystal classes with natural piezoelectric effect have been identified and the macroscopic material constants have been determined. Voigt published an overview of these results with a detailed mathematical description of the known crystals [Voi28]. Starting with the pioneering work of Voigt, the piezoelectric effect became an established branch of crystal physics in the meantime.

The first practical applications go back to 1917, when Rochelle salt was used to generate vibrations for sonars. Further applications have been developed, like accelerometers, ultrasonic devices and microphones. However, the first developments were limited by the rather weak piezoelectric parameters of the naturally available piezoelectric crystals. Starting with the 40ies of the last century, a new class of synthetic materials, called ferroelectrics, have been developed that clearly outperformed the piezoelectric parameters of naturally available materials like quartz or tourmaline crystals. Among others, barium titanate and later zirconate titanate materials with specific properties for particular applications have been produced.

Within the 60ies of the last century, also highly heat-resisting piezoceramic materials have been developed, like lithium niobate with a Curie temperature of 1140° [Sch10]. Besides that, also the development of piezopolymer materials started. A prominent example is polyvinylidene fluoride (PVDF). In contrast to ceramics, where the crystal structure creates the piezoelectric effect, in polymers the intertwined long-chain molecules cause this material behavior by attracting and repelling each other if an electric field is applied. Until today, the development of piezoelectric actuators is continuously advancing. Bending actuators with same orientation of polarization and electric field are the most com-

mon type of actuators. Besides to that, shear actuators with an electric field perpendicular to the polarization gained some importance recently due to the higher efficiency [Ben07]. More and more tailored piezoelectric elements are developed, like the low-profile Macro-Fiber Composite (MFC) actuators. MFC actuators were originally developed at NASA Langley Research Center and offer structural flexibility and high actuation authority [HW03]. The MFC uses rectangular piezoceramic rods sandwiched between layers of adhesive, electrodes and polyimide film. The electrodes are attached to the film in an interdigitated pattern. This assembly enables in-plane poling and in-plane voltage actuation which allows the MFC to utilize the 33-coupling effect, which is higher than the 31-coupling effect used by traditional PZT actuators with through the thickness poling [HKGG93].

New developments also enter the small scales: thin films of crystalline material like aluminum nitride (AlN) are deposited on silicon wafers using semiconductor technologies. Applications include surface acoustic wave sensors (SAWs) that can be used e.g. for touch screens, and radio frequency (RF) filters used in mobile phones. Beyond that, microelectromechanical systems (MEMS) shall be mentioned, where piezoelectric material is used in the context of electronic chips.

The global demand for piezoelectric devices was valued at approximately 14.8 billion US-\$ in 2010. The largest material group for piezoelectric devices are piezocrystal materials, while piezoelectric polymers materials are facing the fastest growth due to low weight and size [Acm11].

1.2.2 Finite Element Models of Shells

From the historical point of view, the first shell models (like many other structural models) have been developed on the basis of engineering evaluation of experiments and heuristic assumptions. Kirchhoff is credited to be the founder of modern plate theory with his publication in 1850 [Kir50], while the first consistent theory of thin shells goes back to August E.H. Love in 1888 [Lov88]. As Love's publication is based on Kirchhoff's work, this shell model became known as the Kirchhoff-Love model. The key assumption is that a mid-surface plane can be used to represent the three-dimensional plate in two-dimensional form. This model has no (independent) rotational degrees of freedom and assumes the cross section to remain straight, unstretched and normal to the mid-surface after deformation. As the strains in thickness direction are assumed to be zero, an appropriate modification of general three-dimensional material laws is required before usage. The related element formulations are commonly called *3-parameter formulations*, because the element deformation can be described with the 3 nodal displacements. In 1960, Koiter presents a concise theory for shells [Koi60]. As his models neglect shear deformations like the Kirchhoff models, the application is here again restricted to thin shells.

However, Reissner introduced already in 1944 shear strains for the calculation of plate deformations [Rei44, Rei45]. He assumed the normal cross section to remain straight, but not necessarily to stay normal to the mid-surface after deformation. The Reissner

plate theory also allows for nonzero normal stresses in thickness direction. Applying the mixed functionals of Hellinger-Reissner, cubic normal stresses in thickness direction can be represented [Hel14, Rei50]. However, the theory still needs a modification of 3D material laws. A plate theory that is based on a pure displacement-formulation and still includes shear deformations has been introduced by Hencky [Hen47] in 1947 and some years later by Mindlin [Min51]. This approach assumes the transversal normal stresses to be zero, which cancels out the normal strain in thickness direction from the equation system. The corresponding concise theory for shells has been presented by Nagdhi in 1972 [Nag72]. Introducing a polynomial description of the displacements in thickness direction, he opened the door for shell models that match the three-dimensional theory with arbitrary exactness. Nevertheless, these shear-deformable shell models are commonly called *shells with Reissner-Mindlin kinematics* due to the origin of the assumption of shear-deformable cross-sections. Following the naming of Bischoff [Bis99], the pure displacement-based shell formulations with shear deformation are called *5-parameter formulation* in the sequel of this work. This name relates to the use of 5 kinematic degrees of freedom (3 displacements and 2 rotational degrees of freedom).

A mathematical basis has been provided later with the method of the *asymptotic analysis*: Here the shell model is compared with the result of the exact three-dimensional equations. A shell model is called asymptotically correct, if the shell model solution converges to the continuum solution in the limit of zero thickness. Possibly the first work of this type has been presented by Goodier in 1938 [Goo38]. Morgenstern presents in 1959 the first mathematical justification of the Kirchhoff theory [Mor59]. Arnold and Falk present in 1996 an investigation of the boundary layers of Reissner-Mindlin plate models with consideration of the transverse shear strain effects [AF96]. The asymptotic analysis of shells started with the work of John in 1965 [Joh65] who investigated error estimates for nonlinear shells. Ciarlet provides with his work in 1996 a general justification of flexural shell equations [CLM96]. Last but not least Lewiński and Telega extended the investigations also to laminate shell structures [LT00].

The fundamental idea of shell models is based on the dimensional reduction of the 3D continuum: Taking advantage of the disparity in length scale, the semi-discretization of the continuum is performed to end up in a two-dimensional problem description. This discretization in thickness direction is completely independent from the (later) discretization within the shell mid-surface. Starting from the mechanical model, two general approaches can be chosen:

- *The Cosserat models* are derived from the weak form of the shell equilibrium differential equation of the Cosserat surface. This method to derive shell models is usually called *direct approach*.
- *Continuum-based shell models* start from the formulation of three-dimensional continua under consideration of shell-specific assumptions.

In principle, both approaches can lead to the same system of differential equations. However, the Cosserat models are based on a two-dimensional shell model which defines

the equilibrium equations directly via stress resultants, without considering the related stresses of a three-dimensional model [CC65, GNW65]. Here, the shell is described as a directed continuum which means that every point is defined via position vector and director vector. These shell models are often called *geometrically exact* since Simo and Fox in 1989 [SFR89a, SFR89b], as the two-dimensional Cosserat surface is exactly described in this formulation. However, this does not imply any approximation quality of the shell deformation or any comparison to continuum-based shell models. A general drawback of the direct method is the difficult application of 3D continuum relations like three-dimensional material laws. Another problem is the modeling of constructional details like stiffeners or connection points [Kos04].

In the case of continuum-based shell models, kinematic resultants and stress resultants are derived from the strains and stresses of the three-dimensional continuum. Doing so, a 2D shell model is derived via appropriate assumptions. This key idea of a dimensional reduction to a 2D surface with appropriate assumptions has been a fundamental basis for the development of both Kirchhoff-Love models [Kir50, Lov88] and Reissner-Mindlin models with shear deformation [Rei44, Min51].

Besides to the two described approaches to derive finite element models, there is a third method: the *degeneration concept* [AIZ68]. Here, the discretization takes place before the dimensional reduction: The continuum is first discretized with three-dimensional solid elements which are then "degenerated" to shell elements. However, apart from the order of dimensional reduction and discretization, strong similarities to continuum-based models can be identified. It can be shown that the methods are even equivalent if the same mechanical assumptions are made [Büc92]. A more detailed investigation and review of the influences of different model assumptions and the related consequences can be found in the literature, e.g. at Bischoff et al. [BWBR04].

Shell models of low order in thickness direction like the 5-parameter formulation still suffer from some severe drawbacks, such as the need for a modification of three-dimensional material laws or the restriction to small strains [Bis99]. Also local effects like geometric discontinuities and delamination effects cannot be investigated. That's why *three-dimensional shell formulations* became more and more vivid in the 1990ies. New elements have been developed which try to combine both the efficiency and ease of evaluation of shell elements on the one hand side and exactness and generality of continuum elements on the other hand side [BR92b, Par95, BGS96].

The convincing property of these elements is the consideration of the complete three-dimensional stress and strain state which requires the thickness change of the shell to be introduced as additional degree of freedom and thus leads to *6-parameter formulations*.

However, the 6-parameter formulation leads to incompatible descriptions of the thickness normal strains and the related energy-conjugate stresses. The resulting stiffening effect in bending situations of curved structures is known as curvature thickness locking (see also section 3.5.3.4). In general, this problem could be solved by using quadratic basis functions for the displacement in thickness direction which would increase the global

degrees of freedom. Büchter, Ramm and Bischoff introduce another approach that adopts an enhanced strain mode as 7th parameter [BR92b, BRR94, Bis99]. This technique allows for a static condensation of the additional degree of freedom on the element level. For these *7-parameter formulations*, the difference between degenerated solid shell elements and "real" shell elements is almost disappearing [BR92c]: The only distinction is the use of real rotational degrees of freedom in the case of shell theory elements while the degeneration concept uses the deformations of the director.

1.2.3 Piezoelectric Shell Element Technology

Since many decades, piezoelectric materials have been indispensable for sensors, actuators, electromechanical resonators, transducers and adaptive structures in general. However, due to the complexity of the piezoelectric governing equations, only a few simple problems such as simply supported beams and plates have been solved analytically [Tie69, RRS93, YBL94]. Since Allik and Hughes [AH70] presented their work on piezoelectric finite element vibration analysis, the finite element method became more and more the dominating practical tool for design and analysis of piezoelectric devices and adaptive structures. There are also simplified models which replace the effect of piezoelectric actors with equivalent forces and moments and which neglect the electromechanical coupling within the constitutive law [Pre02]. However, focus of this work is put on element formulations which consider the full electromechanical coupled problem. Inheriting the approach of Allik and Hughes, a large number of publications until now present finite element formulations which adopt the displacement and the electric potential as the only discretized field variables [SP99].

For the efficient modeling of thin and lightweight structures, piezoelectric shell formulations are of special interest. An overview of different formulations is e.g. given by Saravanos [SH99] and Benjeddou [BLM00]. Similar to the case of pure structural formulations, two main categories of piezoelectric shell finite element models can be identified: On the one hand side, there are solid-shells that model the geometry with upper and lower side of the geometry. Piezoelectric 8-noded solid-shell element formulations are e.g. presented by Sze and Yao [SY00] and Sze et al. [SYY00], Zheng et al. [ZWC04], Tan and Vu-Quok [TVQ05], Klinkel et al. [KGW06] and Klinkel and Wagner [KW06, KW08]. In contrast to that, the second piezoelectric shell element category models the geometry via a reference surface. Such element formulations with focus on 4-noded quadrilaterals can be found e.g. at Lammering [Lam91], Lammering and Mesecke-Rischmann [LMR03], Kögl and Bucalem [KB05] and Legner [Leg11].

All these contributions and in general the majority of publications present quadrilateral elements. In contrast to that, Tzou and Ye also present triangular elements and their performance at piezoelectric bimorphs and semicircular ring shells [TY96]. Also Bernadou and Haenel introduce a triangular piezoelectric element [BH03].

As piezoelectric materials are commonly embedded in layered structures, the first related publications reach back to the 70ies [SC74]. Also the majority of publications of the last two decades consider the application to composites. In this context, solid-shell elements allow for a modeling of each single layer with one separate element. The advantage of this approach is the high approximation level with the option for independent shear deformations of each layer, while the formulation of a tailored laminate theory can be omitted. On the other hand side, the modeling effort and the computational cost are increasing in this case. In contrast to that, shell elements defined on a reference surface must provide a suitable laminate theory to model layered structures. A good overview of different laminate theories for piezoelectric shell elements is delivered by a group of publications of Tzou et al.: For thin shells, piezoelectric elements with *single layer theory* and Kirchhoff-Love hypothesis are introduced [TG89]. The related single layer theory without shear deformation is commonly called *classical laminate theory*. The idea of piezoelectric layered structures is extended in [TZ93] to include shear deformations. In general, related elements with constant shear assumptions over all layers are called *first order shear deformation theory* (FSDT) elements. This approach is further refined e.g. in [TY96] with a theory that assumes layerwise constant shear angles (*multi-layer theory*). A similar approach is adopted by Heyliger et al. for a model with discrete-layer shell theory [HPS96]. An overview of piezoelectric laminate theories can also be found at Saravanos and Heyliger [SH99].

Since the early ages of the finite element method in the 60ies, it has been known from structural applications that finite element formulations based on the principle of virtual work deliver in some cases very inexact results or converge only very slowly. Different element enhancement techniques have been developed to overcome the underlying structural locking effects. Later, these element enhancement techniques also established themselves in the context of electromechanical problems. Several proposed element formulations of the literature reduce the locking effects with biquadratic assumptions for the basis functions [BN01, CYL01]. Selective reduced integration techniques in the context of piezoelectric elements have been applied by Braess and Kaltenbacher to eliminate shear locking [BK08]. Also the assumed natural strains (ANS) method or the mixed interpolated tensorial components (MITC) approach, respectively, have been adopted at piezoelectric elements, such as by Sze and Yao [SY00], Sze et al. [SY00], as well as Kögel and Bucalem [KB05]. Also the enhanced assumed strain (EAS) method according to Simo and Rifai [SR90] has been applied in several piezoelectric elements, such as by Zheng et al. [ZWC04].

However, in the context of electromechanical problems, it is not enough to eliminate "classical" structural locking effects. For a long time, element deficiencies resulting from incompatible approximation spaces of the electromechanical problem have not been investigated. For the first time, De Miranda and Ubertini discuss oscillations of stresses and electric displacements in bending situations in 2003 [MU03, MU04]. These effects actually go back to incompatible approximation spaces of the strains and the electric field.

The critical aspect of the piezoelectric element formulation is here the decision about the used basis functions for the behavior of the electric potential in thickness direction. An overview of different formulations in the literature in this context is given by Kögl and Bucalem [KB05]. Several elements, especially from the earlier developments, assume a linear behavior of the electric potential in thickness direction. However, Wang and Wang showed analytically in 2002 that a linear description of the electric potential in thickness direction is not sufficient for a correct representation of a bending state [WW02]. Legner [Leg11] presents a detailed analysis of incompatible approximation spaces which can be identified to be one basic origin of low element performance besides to "classical" structural locking effects. Legner also introduces the naming *electromechanic weakening*, as the elements tend to larger displacements in contrast to structural locking.

Several *mixed formulations* for electromechanical problems have been presented: Three-field formulations with displacement, electric potential and electric displacement degrees of freedom can be found at Lammering and Mesecke-Rischmann in the context of shallow shells [LMR03], as well as at Sze and Pan [SP99]. A hybrid stress element with the displacements, the electric potential and the stresses as independent fields is introduced by Sze et al. [SYY00]. Furthermore, elements with stresses and electric displacement as additional fields besides to displacements and electric potential are suggested by Sze and Pan [SP99], as well as De Miranda and Ubertini [MU04]. Several authors also suggest complete six-field variational principles derived from the Hu-Washizu functional, e.g. Zheng et al. [ZWC04] and Schulz [Sch10].

The overall majority of the discussed piezoelectric element formulations adopt geometrically linear formulations. Exceptions are the shallow shell element formulations of Wang and Wang [WW02] and Varelis and Saravanos [VS06], the solid shells of Klinkel and Wagner [KW06, KW08], or the formulation of Legner [Leg11].

However, as shown by Tzou and Bao [TB97] and e.g. also Schulz [Sch10], the geometrical nonlinear kinematics can be decisive for the element quality, especially in the case of sensor applications where relatively large deformations may appear. On the other hand side, due to the brittle behavior of piezoelectric material, the consideration of small strains is in most cases reasonable.

1.2.4 Control

The growing interest in the development and application of smart structures requires suitable and reliable simulation tools that contain all main functional parts [Gab02]: The passive structure, the sensors, the actuators and also the control algorithm. In this context, the finite element method provides the necessary basis for a holistic simulation and design concept that also includes the control aspects [GNTK02].

Many publications can be found on the simulation of structural control and controller design in the context of parts with bending stiffness. The first usage of the term *shape control* goes back to Haftka and Adelman who derived finite element formulations for

the shape control of large space structures by applied temperatures [HA85]. Austin et. al. adopt the finite element method for the static shape control of adaptive wings [ARN⁺94]. Zehn and Enzmann present the finite element based controller design and control simulation of an aluminum alloy casting plate [ZE00]. Nestorovic-Trajkov et al. apply finite element based controller design to a funnel-shaped part of a magnetic resonance tomograph [TKG06]. Lefèvre et al. also show extensions of the approach to vibroacoustic effects [LGK03]. A good overview of the finite element based overall design of controlled smart structures is given in [GTK06].

However, also prestressed membranes are interesting candidates for efficient and lightweight smart structures, as they are optimal designs for two reasons: they represent structures of optimal material usage with constant stress state over the thickness and they reflect surfaces of minimal area or minimal weight in the case of uniform prestress. For the design of highly efficient structures, it is thus reasonable to aim for the combination of the efficiency of (passive) membrane structures with the advantages of active control. However, especially slightly prestressed membrane structures exhibit very low mode frequencies and are thus prone to vibration even for small disturbance loads. Furthermore, established control techniques have to be revisited, as the attachment of many sensors, actuators or dampers directly on the membrane would heavily disturb the membrane stress state. Beyond that, membranes represent structures where large deformations, related geometrically nonlinear effects as well as the prestress state are indispensable for a correct representation.

That might have contributed to the fact that only a small number of publications can be found dealing with the control of prestressed membranes in the finite element context. Maji and Starnes present analytical techniques for shape control of deployable membrane structures for space antennas [MS00]. Beyond that, Sakamoto et al. present distributed and localized active vibration control techniques for membrane structures [SPM06]. However, focus is put here on the isolation of membranes from the major disturbance source rather than the control of vibrating membranes. Peng et al. present a scheme for inflatable structure shape control based on genetic algorithms and neural network techniques [PHN06]. They report about the challenges to find good optimal control output due to the strong nonlinear properties of the structures.

1.3 Objectives

One key goal of this work is the development of a flexible, efficient and robust piezoelectric composite shell finite element. A 7-parameter single-director shell formulation with Reissner-Mindlin kinematics [BR92b, BRR94, Bis99] is extended to a composite formulation for the electromechanical problem. Besides to three displacement degrees of freedom and three deformation components of the director, the difference of the electric potential in thickness direction is introduced as nodal degree of freedom. The key aspects of this piezoelectric composite finite element are listed in the sequel:

- An extensible director formulation with director-based degrees of freedom is adopted in order to account at once for rotations as well as thickness deformation.
- The element is completely based on nonlinear, three-dimensional continuum theory. This allows for a concise description of arbitrary complete three-dimensional coupled material equations in the convective coordinate system of the element without reduction or manipulation in nonlinear plate and shell analysis. As a consequence, a complete representation of 3D stress states is possible. Furthermore, complex transformation matrices can be replaced by metric-based transformations.
- A modified Hu-Washizu functional for the electromechanical problem is derived. Introducing an additional orthogonality condition between the enhanced electric field modes and the independent electric displacement field, the general electro-mechanical six-field Hu-Washizu functional can be reduced to a four-field formulation before the discretization takes place. Thus the numerical cost for the discretization, calculation and static condensation of the stress and electric displacement field can be eliminated.
- The enhanced assumed strain (EAS) method is applied to eliminate structural locking effects.
- Similar to enhanced assumed strains, also enhanced assumed electrical (EAE) field modes are introduced to eliminate electromechanical locking phenomena stemming from incompatible approximation spaces.
- Also the Assumed Natural Strains (ANS) method is applied in order to eliminate shear locking in a robust manner also in the context of distorted meshes.
- No restriction to shallow shells is introduced.
- A geometrically nonlinear formulation is adopted to account for large deformations that can appear especially in sensor applications.

A linear coupled material law is assumed. This assumption is reasonable for small electrical and mechanical loading. In order to consider nonlinear piezoelectric material effects, the polarization state of the material must be taken into account. This can be done e.g. by the mathematical Preisach model [Pre35]. For a study of nonlinear material effects and the related numerical simulation in the context of piezoelectric elements, the reader is kindly referred to the literature, such as Schulz [Sch10].

Beyond that, this contribution presents a finite element based computational framework and the related algorithms for the virtual design and nonlinear simulation of controlled smart lightweight structures. Special focus is put here also beyond structures with bending stiffness: Membranes and their special characteristic in the context of control are considered. Form finding is used to determine the optimal structural shape of tensile structures from an inverse formulation of equilibrium. Also the cutting pattern generation

of membranes is integrated in the design process in order to consider fabrication effects already in the earliest possible stage.

Active control is adopted for vibration suppression under external loads like e.g. wind. Controller design is based on a state space model that is derived from the finite element model and that preserves the geometrically nonlinear equilibrium state and the prestress effects of the membrane. Furthermore, discrete time control via an optimal linear-quadratic-Gaussian (LQG) regulator is applied.

The introduced methods and algorithms of all simulation and design steps are benchmarked at two examples with different focus and challenge:

- The simulation and design of an actively controlled smart tent is presented to demonstrate the overall design process of a membrane structure with closed-loop control.
- The design framework is extended to finite element-based structural optimization in the context of static-aeroelastic shape control of a solid-state piezo-actuated variable-camber morphing wing.

Thus in total a computational design framework shall be presented that covers aspects of the sensing and actuation technology, the optimal design of passive parts of smart structures, as well as the controller design.

1.4 Outline of This Thesis

In **chapter 2**, the basic terms and relations of the electromechanical continuum are defined and deduced. As a preparing step for the understanding of the upcoming chapters, the technical notation is introduced and the general behavior of electromechanically coupled structures is illustrated here. Furthermore, an in-depth presentation of variational methods and related functionals is provided in order to provide the basis for the piezoelectric finite element formulation presented later.

Chapter 3 provides selected fundamental aspects of the finite element method as far as needed for the subsequent chapters. One focus is the term of convergence and the resulting requirements for finite element technology. Also the idea of patch tests is presented with its extensions to electromechanical applications. Furthermore, the different locking phenomena are defined, interpreted and illustrated. Besides to the well-known structural locking effects, focus is also on the closely related effects of incompatible approximation spaces of the electric field. In order to provide insight into the locking phenomena, 1D and 2D examples are adopted. Beyond that, the following enhanced finite elements formulations are introduced that face the locking phenomena with different techniques:

- the reduced integration method,
- the assumed natural strain method (ANS),
- the enhanced assumed strain method (EAS) and
- the enhanced assumed electric field strength method (EAE).

The latter method is derived from the EAS method via extension of the modified Hu-Washizu functional to electromechanical problems.

Chapter 4 is dedicated to the theory of the piezoelectric composite shell element formulation. Presenting the assumptions and definitions for geometry, kinematics, electric field, stresses and electric displacements, a geometrically nonlinear finite element formulation based on a modified Hu-Washizu functional is presented. Special focus is put on the discretization aspects, including the adopted element enhancement techniques.

Chapter 5 gives an introduction to the simulation and design of actively controlled elastic structures. As already mentioned, additional focus is put on the special characteristics of prestressed membrane structures and related consequences for the design of sensors, actuators and controller. The state space approach is adopted. The state space model is derived from the finite element model via linearization and modal truncation. A linear-quadratic-Gaussian (LQG) regulator is adopted. The overall design loop is completed with the nonlinear simulation of the structure including control.

Chapter 6 gives a short introduction into the object-oriented software framework *Carat++* that has been developed to realize the overall simulation and design goal.

Chapter 7 provides numerical examples for the validation of the presented algorithms and formulations. In the first part of this chapter, the presented piezoelectric composite shell formulation is tested at several benchmark examples. In this context, the applied element enhancement techniques to avoid locking are discussed in detail concerning efficiency and robustness. Furthermore, in a separate example the overall virtual design process of a actively controlled smart structure is shown at the example of a tent structure. The final example demonstrates the static-aeroelastic simulation and the design of a shape adaptive solid-state piezo-actuated variable-camber morphing wing, including aeroelastic coupling and FE-based structural optimization.

Last but not least, **chapter 8** provides a short conclusion and summary of the key aspects of this work. Additionally, a short outlook is given.

Chapter 2

Fundamentals of Continuum Mechanics and Electrostatics

In this chapter, the basic terms and relations of continuum mechanics and electrostatics are defined and deduced. Analyzing the electromechanical continuum, the technical notation is introduced and the general behavior of electromechanically coupled structures is illustrated. Thus this part forms a notational and phenomenological basis for further considerations in the upcoming chapters of this work.

For a deeper study of this field, the reader is kindly referred to the literature. Further information related to structural continuum mechanics can be found e.g. at Müller [Mül06], Truesdell and Noll [TN60], Malvern [Mal69], Marsden and Hughes [MH83], Mang and Hofstetter [MH00], Eringen [Eri62] as well as Parisch [Par03]. Beyond that, the reader can find an in-depth presentation of the concise theory of electromechanics e.g. at Crowley [Cro86], Maugin [Mau88] and Yang [Yan05].

2.1 Namings and Conventions

Throughout this work, both index notation and absolute notation is used for vectors and tensors. It has been tried to comply with the standard conventions in modern publications of the addressed fields of research.

In general, operators are printed as standard characters, scalars as italics, vectors are printed with small bold face letters, whereas tensors of second or higher order are printed with capital bold-printed letters. Quantities that are needed in both reference and current configuration are identified with uppercase and lowercase letters, respectively (see chapter 2.2). Some distinct exceptions from these conventions are made where needed to avoid name collisions: E.g. the electric field strength is named $\vec{\mathbf{E}}$ in order to prevent ambiguity errors with the Green-Lagrange strain tensor \mathbf{E} and the unit vectors \mathbf{e}_i .

Some further points that might need clarification shall be listed below. Let \mathbf{a} and \mathbf{b} be vectors, then:

$$\mathbf{a}^T \mathbf{b} = a_i b^i = a^i b_i \quad (2.1)$$

represents the inner product. Subscripts indicate covariant components, superscripts mark contravariant components.

Furthermore, letters used as superscripts denote explicit dependencies from another variable [Fel89], like e.g. \mathbf{E}^u describing the strain tensor resulting via kinematic equations from the displacement field \mathbf{u} .

The scalar product of second-order tensors is denoted like the following:

$$\mathbf{A} : \mathbf{B} := A^{ij} g_i \otimes g_j : B_{kl} g^k \otimes g^l = A^{ij} B_{ij} \quad (2.2)$$

The dyadic product (or tensor product) of two vectors $\mathbf{a}, \mathbf{b} \in \mathbb{R}^3$ is implicitly defined with:

$$(\mathbf{a} \otimes \mathbf{b}) \cdot \mathbf{c} = \mathbf{a} (\mathbf{b} \cdot \mathbf{c}) \quad \forall \mathbf{c} \in \mathbb{R}^3 \quad (2.3)$$

When using index notation, indices in small Greek letters take the values $\{1,2\}$, indices in small Latin letters take the values $\{1,2,3\}$. The Einstein summation convention:

$$a_i b^i := \sum_3^{i=1} a_i b^i \quad (2.4)$$

holds for both Latin and Greek indices if appearing twice in a product. An overview of all defined terms is provided in a nomenclature in Table B.1 in appendix B.

2.2 Differential Geometry

A body is defined as a bounded set of material points Ω . The surface or boundary of the body, respectively, is labeled with Γ . A body has at any time t a specific configuration in the three-dimensional physical space, also called Euclidean space \mathbb{E}^3 .

To describe the geometrical position of a body and its movement in space, two general approaches can be distinguished:

- The Euler approach observes fixed points in space and the changes of their properties.
- The Lagrangian approach investigates the movement of single points in space. That's why it is commonly called material point of view.

In this work, the Lagrangian description is used. It can be extended from points to bodies: The Lagrangian approach observes the movement and the deformation of a body in the three-dimensional Euclidean space.

In order to determine the body and each of its points, a point of origin \mathbf{O} has to be defined in \mathbb{E}^3 . An immovable Cartesian coordinate system is introduced which is defined

by the ortho-normalized base vectors $\mathbf{e}_i = \mathbf{e}^i$. This coordinate system allows for easy identification of arbitrary points in space via the position vector \mathbf{X} :

$$\mathbf{X} = X^i \mathbf{e}_i = X^1 \mathbf{e}_1 + X^2 \mathbf{e}_2 + X^3 \mathbf{e}_3 \quad (2.5)$$

Especially for the description of thin free-form geometries, it is advantageous to use curvilinear convective coordinate systems that can be regarded as permanently connected to the (shell) body.

Thus curvilinear convective coordinate systems are introduced using the covariant basis \mathbf{G}_i and the contravariant basis \mathbf{G}^i . With the corresponding contravariant coordinates θ^i and the covariant coordinates θ_i , the position vector can be expressed as:

$$\mathbf{X} = \theta^i \mathbf{G}_i = \theta_i \mathbf{G}^i \quad (2.6)$$

Describing the geometry of a structure, a distinction has to be made between reference ("material") configuration and actual configuration.

Choosing an arbitrary reference time $t = t_0$, the mapping of the body at this time is called reference configuration. The actual configuration depicts the position at a point of time $t > t_0$ after a deformation or movement of the observed body (Figure 2.1). The convention is used that capital letters describe the reference configuration and small letters stand for the actual configuration (see also chapter 2.1).

For every point of the body, the reference configuration can thus be described by the position vector $\mathbf{X}(\theta^1, \theta^2, \theta^3)$ and the actual configuration can be depicted by $\mathbf{x}(\theta^1, \theta^2, \theta^3)$. Consequently, the overall body is clearly defined in both configurations via a field of position vectors. Furthermore, the location-dependent covariant base vectors for the curvilinear

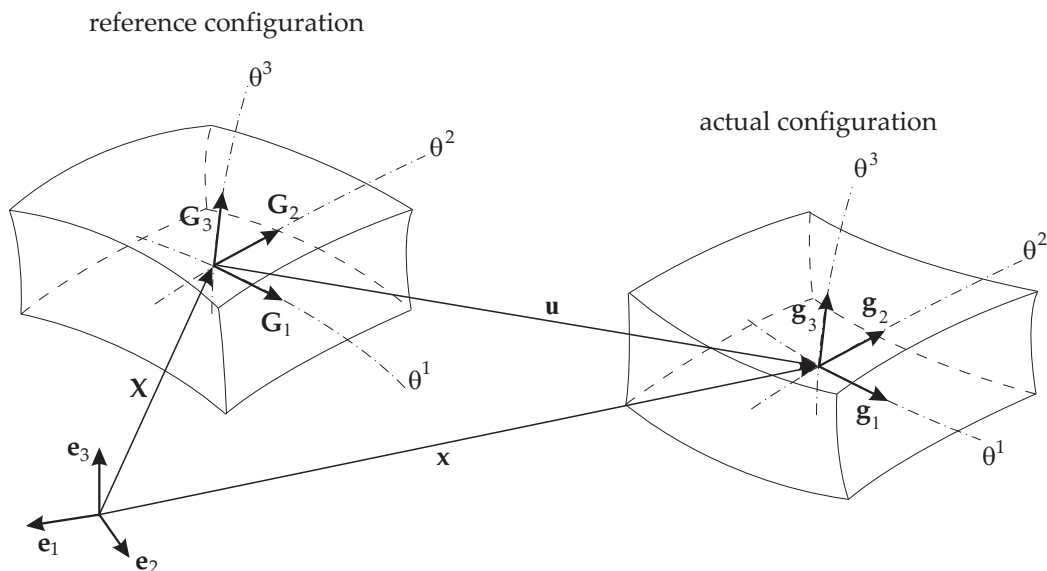


Figure 2.1: Reference and actual configuration of a differential body element.

coordinate system can be derived from the position vectors as follows for both configurations:

$$\mathbf{G}_i = \frac{\partial \mathbf{X}}{\partial \theta^i} = \mathbf{X}_{,i} \quad , \quad \mathbf{g}_i = \frac{\partial \mathbf{x}}{\partial \theta^i} = \mathbf{x}_{,i} \quad (2.7)$$

The convention that $(\cdot)_{,i} = \frac{\partial(\cdot)}{\partial \theta^i}$ stands for the partial derivative with respect to contravariant convective coordinates will be used further on in this work. Following equ. (2.7), the contravariant base vectors can be derived:

$$\mathbf{G}^i = \frac{\partial \theta^i}{\partial \mathbf{X}} \quad , \quad \mathbf{g}^i = \frac{\partial \theta^i}{\partial \mathbf{x}} \quad (2.8)$$

The duality property:

$$\mathbf{G}_i \cdot \mathbf{G}^j = \mathbf{G}_i^j = \delta_i^j = \begin{cases} 0 & i \neq j \\ 1 & i = j \end{cases} \quad (2.9)$$

of covariant and contravariant base vectors will be used later in the context of energy expressions. The metric tensor (also called identity tensor) with its covariant and contravariant representation is defined as follows:

$$\mathbf{G} = G_{ij} \mathbf{G}^i \otimes \mathbf{G}^j = G^{ij} \mathbf{G}_i \otimes \mathbf{G}_j \quad (2.10)$$

The metric coefficients are computed by the scalar product of the corresponding base vectors:

$$G_{ij} = \mathbf{G}_i \cdot \mathbf{G}_j \quad , \quad G^{ij} = \mathbf{G}^i \cdot \mathbf{G}^j \quad (2.11)$$

Equ. (2.11) is commonly called the *first fundamental form (of surfaces)*. It enables the calculation of curvature and metric properties of a surface, such as lengths of curves on the surface, angles between such curves, or surface areas. The contravariant metric coefficients G^{ij} can also be obtained by the inverse of the covariant metric coefficient matrix:

$$[G^{ij}] = [G_{ij}]^{-1} \quad (2.12)$$

As a consequence, the metric provides a reversible and definite arithmetic operation in order to transform the co- and contravariant base vectors into each other:

$$\mathbf{G}^i = G^{ij} \mathbf{G}_j \quad , \quad \mathbf{G}_i = G_{ij} \mathbf{G}^j \quad (2.13)$$

Extending the idea of equ. (2.13), the continuum mechanical description allows for a clear transformation of tensors of arbitrary order between different bases. This will be used in the element formulation in chapter 4 for tensors of second to fourth order to account for a description of geometry, kinematics and piezoelectric material law in best-suited coordinate systems.

Let $\mathbf{a}_i \otimes \mathbf{a}_j$ and $\mathbf{b}_i \otimes \mathbf{b}_j$ describe two (arbitrary) bases with their related contravariant counterparts $\mathbf{a}^i \otimes \mathbf{a}^j$ and $\mathbf{b}^i \otimes \mathbf{b}^j$. A second-order tensor \mathbf{C} can be expressed using these bases as:

$$\mathbf{C} = a^{ij} \mathbf{a}_i \otimes \mathbf{a}_j = a_{ij} \mathbf{a}^i \otimes \mathbf{a}^j = b^{ij} \mathbf{b}_i \otimes \mathbf{b}_j = b_{ij} \mathbf{b}^i \otimes \mathbf{b}^j \quad (2.14)$$

Now it shall be assumed that the coefficients of tensor \mathbf{C} shall be transformed from the basis $\mathbf{a}^i \otimes \mathbf{a}^j$ to the basis $\mathbf{b}^i \otimes \mathbf{b}^j$:

$$a_{ij}\mathbf{a}^i \otimes \mathbf{a}^j = b_{ij}\mathbf{b}^i \otimes \mathbf{b}^j \quad (2.15)$$

The transformation of the tensor coefficients can be easily performed by taking advantage of the duality property of equ. (2.9). Thus multiplying the covariant base vectors \mathbf{b}_k and \mathbf{b}_l from two sides to equ. (2.15) leads to:

$$\begin{aligned} a_{ij}\mathbf{b}_k(\mathbf{a}^i \otimes \mathbf{a}^j)\mathbf{b}_l &= b_{ij}\mathbf{b}_k(\mathbf{b}^i \otimes \mathbf{b}^j)\mathbf{b}_l \\ a_{ij}(\mathbf{b}_k \cdot \mathbf{a}^i)(\mathbf{a}^j \cdot \mathbf{b}_l) &= b_{ij}(\mathbf{b}_k \cdot \mathbf{b}^i)(\mathbf{b}^j \cdot \mathbf{b}_l) \\ &= b_{ij}\delta_k^i\delta_l^j \\ &= b_{kl} \end{aligned} \quad (2.16)$$

This approach is applicable to any pair of covariant or contravariant bases. Thus for a general transformation of a second order tensor the following transformations can be stated:

$$b_{kl} = a_{ij}(\mathbf{b}_k \cdot \mathbf{a}^i)(\mathbf{a}^j \cdot \mathbf{b}_l) \quad (2.17)$$

$$b^{kl} = a_{ij}(\mathbf{b}^k \cdot \mathbf{a}^i)(\mathbf{a}^j \cdot \mathbf{b}^l) \quad (2.18)$$

$$b_{kl} = a^{ij}(\mathbf{b}_k \cdot \mathbf{a}_i)(\mathbf{a}_j \cdot \mathbf{b}_l) \quad (2.19)$$

$$b^{kl} = a^{ij}(\mathbf{b}^k \cdot \mathbf{a}_i)(\mathbf{a}_j \cdot \mathbf{b}^l) \quad (2.20)$$

Beyond that, this transformation approach is extendable to tensors of order n . Instead of 2 pairs of co- and contravariant base vectors of initial and destination coordinate system as shown in equ. (2.17) - (2.20), the transformation is extended to n pairs, respectively.

Furthermore, the curvature properties of a surface are described by the curvature tensor coefficients $B_{\alpha\beta}$ which is defined as follows:

$$B_{\alpha\beta} = -\mathbf{G}_\alpha \cdot \mathbf{G}_{3,\beta} = -\mathbf{G}_\beta \cdot \mathbf{G}_{3,\alpha} = \mathbf{G}_{\alpha,\beta} \cdot \mathbf{G}_3 \quad (2.21)$$

The curvature description according to equ. (2.21) is called the *second fundamental form of surfaces*.

Summing up, geometry and movement of a body are thus clearly defined via position vectors and the metric. As a consequence, all subsequent quantities, like strain measures or geometric mappings, can be derived from that.

2.3 Kinematics

Kinematics is the branch of classical mechanics that describes the motion of points and bodies in space in dependence of time, but without consideration of the causes of motion [Whi04]. Thus it provides a relationship between the geometric quantities under consideration. The kinematics is usually described with the measures of distance (change of

position vector), velocity and acceleration. In the present context of structural continuum mechanics, the kinematics describes the relationship between the displacements and the strains in the body Ω , and the displacements and their prescribed values at the boundary denoted with Γ .

The movement of a material point P of the body Ω can be described with the displacement vector \mathbf{u} which is defined as difference of the position vectors of actual and reference configuration:

$$\mathbf{u} = \mathbf{x} - \mathbf{X} \quad (2.22)$$

Furthermore, the mapping of a differential line element in the reference configuration $d\mathbf{X}$ into a differential line element in the deformed configuration $d\mathbf{x}$ is depicted by the deformation gradient \mathbf{F} [Hol04]:

$$d\mathbf{x} = \mathbf{F} \cdot d\mathbf{X} \quad (2.23)$$

It describes the deformation in a infinitesimal area around a particle, whereas its component values are finite. \mathbf{F} is a tensor of second order which is in general not symmetric: $\mathbf{F} \neq \mathbf{F}^T$. It provides an unambiguous relation between deformed and undeformed geometry. From the continuum mechanical point of view, the deformation gradient and its variations due to inverting and transposing are defined as follows:

$$\mathbf{F} = \mathbf{g}_i \otimes \mathbf{G}^i \quad (2.24)$$

$$\mathbf{F}^T = \mathbf{G}^i \otimes \mathbf{g}_i \quad (2.25)$$

$$\mathbf{F}^{-1} = \mathbf{G}_i \otimes \mathbf{g}^i \quad (2.26)$$

$$\mathbf{F}^{-T} = \mathbf{g}^i \otimes \mathbf{G}_i \quad (2.27)$$

The components of \mathbf{F} can be determined via:

$$\mathbf{F} = \text{grad } \mathbf{x} = \frac{d\mathbf{x}}{d\mathbf{X}} = \begin{bmatrix} \frac{dx}{dX} & \frac{dx}{dY} & \frac{dx}{dZ} \\ \frac{dy}{dX} & \frac{dy}{dY} & \frac{dy}{dZ} \\ \frac{dz}{dX} & \frac{dz}{dY} & \frac{dz}{dZ} \end{bmatrix} \quad (2.28)$$

With the help of the deformation gradient, it is possible to transform the undeformed basis \mathbf{G}_i into the deformed basis \mathbf{g}_i and vice versa [MH83]. The deformed bases are obtained via forward transformation (*push forward*):

$$\mathbf{g}_i = \frac{d\mathbf{x}}{d\mathbf{X}} \cdot \frac{\partial \mathbf{X}}{\partial \theta^i} = \mathbf{F} \cdot \mathbf{G}_i \quad (2.29)$$

$$\mathbf{g}^i = \mathbf{F}^{-T} \cdot \mathbf{G}^i \quad (2.30)$$

and the undeformed bases are obtained via backward transformation (*pull back*):

$$\mathbf{G}_i = \mathbf{F}^{-1} \cdot \mathbf{g}_i \quad (2.31)$$

$$\mathbf{G}^i = \mathbf{F}^T \cdot \mathbf{g}^i \quad (2.32)$$

Let the determinant of the deformation gradient be labeled with J . Then J indicates the ratio of deformed differential volume element dV to the corresponding undeformed differential volume element dV_0 :

$$J := \det(\mathbf{F}) = \frac{dV}{dV_0} \quad (2.33)$$

To enable the transformations in both directions according to equ. (2.29) - (2.32), the mapping must be bijective. Thus the existence of \mathbf{F}^{-1} must be guaranteed. Beyond that, the mapping that is described via \mathbf{F} must be continuous. This is a necessary condition to exclude cases of self-intersections and negative volumes. Thus all in all, the positive definiteness of \mathbf{F} must be given:

$$J > 0 \quad (2.34)$$

With the deformation gradient and its determinant, it is now possible to describe the transformation of a differential surface element between deformed and undeformed configuration:

$$\mathbf{n} da = \det(\mathbf{F}) \mathbf{F}^{-T} \mathbf{N} dA = J \mathbf{F}^{-T} \mathbf{N} dA \quad (2.35)$$

The term da stands for the differential surface element and \mathbf{n} defines the unit surface normal in the actual configuration. dA and \mathbf{N} represent the corresponding terms of the reference configuration. Furthermore, it holds for the volume elements dV and dv of reference and actual configuration:

$$dv = \det(\mathbf{F}) dV \quad (2.36)$$

However, as the deformation described by the deformation gradient \mathbf{F} also contains rigid body motions, it cannot be directly used as a measure for strains. While a variety of different strain measures exist, this work focuses on the Green-Lagrange strain tensor \mathbf{E} :

$$\mathbf{E} = \frac{1}{2} (\mathbf{F}^T \mathbf{F} - \mathbf{I}) = E_{ij} \mathbf{G}^i \otimes \mathbf{G}^j \quad (2.37)$$

The Green-Lagrange strains \mathbf{E} represent a nonlinear relation between deformations and strains (see equ. (2.37)) and are an appropriate measure for strains under large deformations. \mathbf{E} is a symmetric tensor and relates the strain measure to the reference configuration. Furthermore, inserting equ. (2.24) and (2.25) into equ. (2.37) yields [Hol04]:

$$\begin{aligned} \mathbf{E} &= \frac{1}{2} (\mathbf{F}^T \mathbf{F} - \mathbf{I}) \\ &= \frac{1}{2} \left((\mathbf{G}^i \otimes \mathbf{g}_i) (\mathbf{g}_j \otimes \mathbf{G}^j) - G_{ij} \mathbf{G}^i \otimes \mathbf{G}^j \right) \\ &= \frac{1}{2} (g_{ij} - G_{ij}) \mathbf{G}^i \otimes \mathbf{G}^j \end{aligned} \quad (2.38)$$

Thus referring to the contravariant basis the coefficients of the Green-Lagrange strain tensor can be calculated from the covariant base vectors of both configurations [Mül06]:

$$E_{ij} = \frac{1}{2} (\mathbf{g}_i \cdot \mathbf{g}_j - \mathbf{G}_i \cdot \mathbf{G}_j) = \frac{1}{2} (g_{ij} - G_{ij}) \quad (2.39)$$

The Green-Lagrange strain tensor can also be described in dependence of the displacement field \mathbf{u} and the basis of the reference geometry \mathbf{G}_i :

$$E_{ij} = \frac{1}{2} (\mathbf{G}_i \cdot \mathbf{u}_{,j} + \mathbf{G}_j \cdot \mathbf{u}_{,i} + \mathbf{u}_{,i} \cdot \mathbf{u}_{,j}) \quad (2.40)$$

This allows for an easy identification of the linear and nonlinear part of the strain measure. In addition to the kinematic field equation according to equ. (2.38), the displacement boundary conditions $\hat{\mathbf{u}}$ have to be considered that have to be fulfilled at the Dirichlet boundary:

$$\mathbf{u} = \hat{\mathbf{u}} \quad \text{on } \Gamma_u \quad (2.41)$$

The Dirichlet boundary condition is commonly called *essential boundary condition*.

2.4 Electrostatics

In combination with (structural) continuum mechanics, the theory of electrostatics provides the theoretical basis for the mathematical description of the investigated electromechanical problems of this work. While this chapter focuses on definitions and aspects relevant for the presented piezoelectric element formulation, the reader can find detailed information about the general field of electrostatics and electrodynamics for example at [Gri99], [Jac99], [BD97], [Jon02] and [Gre02].

Let the position of a stationary point charge of quantity Q_i be given by the location vector \mathbf{X}_i . Furthermore, $\vec{\mathbf{F}}_c$ is the electrically induced force that acts between two point charges of quantity Q_a and Q_b in the direction of their connection line. Then the Coulomb's law states:

$$\|\vec{\mathbf{F}}_c\| = \frac{Q_a Q_b}{4\pi\epsilon_0 \|\mathbf{X}_a - \mathbf{X}_b\|^2} \quad (2.42)$$

$\vec{\mathbf{F}}_c$ is called Coulomb force. The constant ϵ_0 is commonly called the *vacuum permittivity*, *permittivity of free space* or *dielectric constant*. It holds: $\epsilon_0 = 8.854 \cdot 10^{-12} \frac{\text{C}^2}{\text{Jm}}$. If more than two point charges exist in the considered space, the resulting force of each point charge can be determined applying the superposition principle. Equation (2.42) forms the basis of the field of electrostatics. It is the electrostatic analogon to Newton's (inverse-square) law of universal gravitation.

The electrical field strength is defined at a position \mathbf{X} via the fraction of resulting force over the quantity of the point charge:

$$\vec{\mathbf{E}}(\mathbf{X}) := \frac{\vec{\mathbf{F}}_c}{Q} \quad (2.43)$$

The work that is needed to move a body with a specific charge from position \mathbf{X}_0 to \mathbf{X}_1 is path-independent. Choosing \mathbf{X}_0 as reference position, the electric potential can be defined as:

$$\varphi = \int_{\mathbf{X}_1}^{\mathbf{X}_0} \vec{\mathbf{E}} d\mathbf{X} \quad (2.44)$$

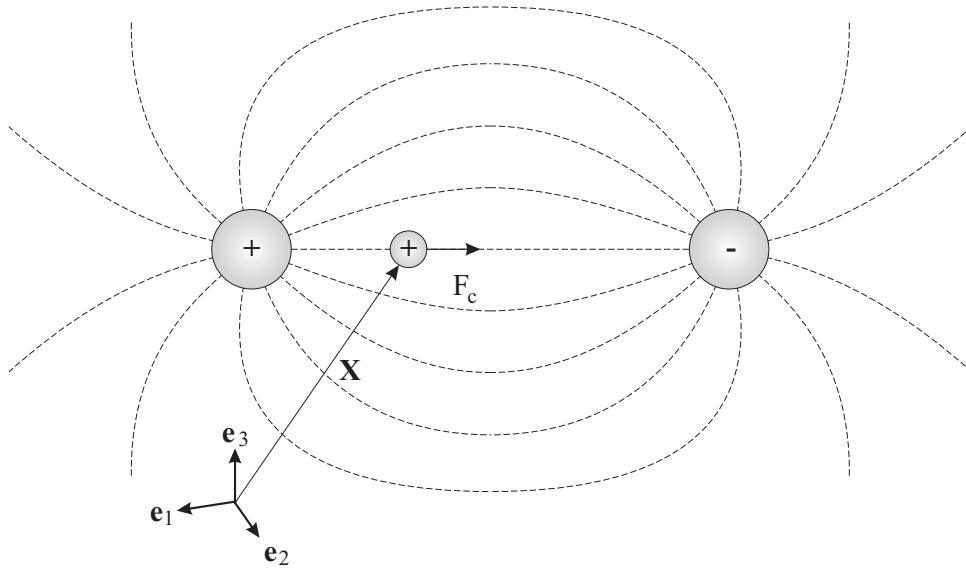


Figure 2.2: Charged particle in an electrical field of two point charges.

Vice versa, the electrical field can be described as gradient of the scalar field of the electric potential $\varphi(\mathbf{X})$:

$$\vec{\mathbf{E}} = -\text{grad } \varphi \quad (2.45)$$

Assuming a space with stationary point charges, the electric field strength is a rotation-free force field:

$$\text{rot } \vec{\mathbf{E}} = 0 \quad (2.46)$$

From a physical point of view, there exists only an electric potential in the actual configuration which reads as follows:

$$\varphi_t = \int_{x_1}^{x_0} \vec{\mathbf{e}} \, d\mathbf{x} = \int_{x_1}^{x_0} \vec{\mathbf{E}} \mathbf{F}^{-1} \, d\mathbf{x} \quad (2.47)$$

Besides to the field equation according to equ. (2.45), also the boundary of the field φ has to be defined. For boundaries Γ_φ of ideally conductive material it can be stated:

$$\varphi = \hat{\varphi} = \text{const. on } \Gamma_\varphi \quad (2.48)$$

This forms the essential boundary condition for the electric potential field.

2.5 Stresses and Electric Displacements

2.5.1 Stress Measures

First of all, the *Cauchy stress* vector \mathbf{t} shall be introduced. It describes the physically acting stresses in the actual configuration:

$$\mathbf{t} = \lim_{\Delta a \rightarrow 0} \frac{\Delta \mathbf{p}}{\Delta a} = \frac{d\mathbf{p}}{da} \quad (2.49)$$

Here $\Delta \mathbf{p}$ denotes the force acting on a infinitesimal, deformed piece of area Δa . Introducing the unit normal vector \mathbf{n} of the piece of area da , the Cauchy stress vector \mathbf{t} can be computed from the symmetric Cauchy stress tensor σ :

$$\mathbf{t} = \sigma \mathbf{n} \quad (2.50)$$

This relation is also known as *Cauchy theorem*. Furthermore, σ is defined in the covariant basis of the actual configuration according to:

$$\sigma = \sigma^T = \sigma^{ij} \mathbf{g}_i \otimes \mathbf{g}_j \quad (2.51)$$

In contrast to that, the *Second Piola-Kirchhoff (PK2) stresses* are defined with respect to the reference configuration. Furthermore, the PK2 stresses are the energetically conjugate stress measure to the Green-Lagrange strains introduced in chapter 2.3. The Cauchy stress tensor and the PK2 stress tensor can be transformed into each other with the help of the deformation gradient \mathbf{F} :

$$\mathbf{S} = \det(\mathbf{F}) \mathbf{F}^{-1} \cdot \sigma \cdot \mathbf{F}^{-T} \quad (2.52)$$

Due to the symmetry of the Cauchy stresses (see also chapter 2.6.3) and the symmetry conserving mapping according to equ. (2.52), it can be deduced that also the PK2 stresses have symmetry properties:

$$\mathbf{S} = \mathbf{S}^T \quad (2.53)$$

For the components of the PK2 stresses it holds:

$$\mathbf{S} = S^{ij} \mathbf{G}_i \otimes \mathbf{G}_j \quad (2.54)$$

As the PK2 stress tensor describes stresses relative to the reference configuration, its components do not allow for an intuitive physical interpretation. Another commonly used stress measure is the first Piola-Kirchhoff stress tensor \mathbf{P} which is sometimes also called *tensor of nominal stresses*:

$$\mathbf{P} = \mathbf{P}^{ij} \mathbf{g}_i \otimes \mathbf{G}_j \quad (2.55)$$

It relates the force in the actual configuration to an oriented area dA in the reference configuration. It can be defined with:

$$\mathbf{P} := \det[\mathbf{F}] \sigma \mathbf{F}^{-T} \quad (2.56)$$

However, in contrast to σ , it is in general not symmetric. Using the inverse of the deformation gradient \mathbf{F}^{-1} , the 2nd Piola-Kirchhoff stress tensor \mathbf{S} can be derived from the 1st Piola-Kirchhoff stress tensor \mathbf{P} :

$$\mathbf{S} = \mathbf{F}^{-1}\mathbf{P} \quad (2.57)$$

2.5.2 The Electric Displacement

First of all, the term *voltage* has to be introduced. It can be defined as difference $\Delta\varphi$ of the electric potential of two points:

$$U = \Delta\varphi = \varphi_1 - \varphi_2 = \int_{\mathbf{x}_1}^{\mathbf{x}_0} \vec{\mathbf{E}} d\mathbf{X} - \int_{\mathbf{x}_2}^{\mathbf{x}_0} \vec{\mathbf{E}} d\mathbf{X} \quad (2.58)$$

In a dielectric material the presence of an electric field $\vec{\mathbf{E}}$ causes the bound charges in the material (atomic nuclei and their electrons) to slightly separate. This induces a local electric dipole moment. The electric displacement $\vec{\mathbf{D}}$ is defined as:

$$\vec{\mathbf{D}} = \epsilon_0 \vec{\mathbf{E}} + \vec{\mathbf{P}} \quad (2.59)$$

where ϵ_0 is the vacuum permittivity introduced in chapter 2.4, and $\vec{\mathbf{P}}$ is the (macroscopic) density of the permanent and induced electric dipole moments in the material, called *polarization density*. The electric flux Ψ is defined with:

$$\Psi = \int_{\Gamma} \vec{\mathbf{D}} \cdot \mathbf{N} dA \quad (2.60)$$

Thus only the part of the electric displacement field that is perpendicular to the surface contributes to the electric flux.

The set of geometrical points with a voltage of zero to each other forms a *equipotential surface*. The electric displacement field $\vec{\mathbf{D}}$ is perpendicular to the equipotential surfaces. Finally, the electric flux through a closed surface is equal to the charge enclosed by this surface:

$$\Psi = \oint_{\Gamma} \vec{\mathbf{D}} \cdot \mathbf{N} dA = \int_{\Omega} \rho_0^{el} dV = Q \quad (2.61)$$

where ρ_0^{el} is the electric charge density (see also chapter 2.6.4)

2.6 Conservation Laws

Within this chapter, a short introduction to the conservation laws in the context of deformable dielectric structures shall be given. Conservation laws, also called integral equations of balance, are a fundamental basis for the mathematical description of physical processes. The conservation laws of mass, linear momentum, angular momentum and electric charge are presented.

The general structure of a balance law for a physical field measure $Z(x, t)$ in spatial representation is [TN60]:

$$\frac{d}{dt} \int_{\Omega} Z \, dv = \int_{\Omega} (\Xi_f + \Xi_p) \, dv + \int_{\Gamma} \Lambda \, da \quad (2.62)$$

with Ξ_f being the volumetric flow (inflow and outflow), Ξ_p being the volumetric production, and Λ being the surface flow (inflow and outflow).

2.6.1 Balance of Mass

Let the material body Ω be a closed system. Then the overall mass does not change during the deformation process.

Let furthermore $\rho_0 = \rho_0(\mathbf{X})$ be the density in the reference configuration Ω_0 and $\rho = \rho(\mathbf{X}, t)$ the density in the actual configuration Ω . Then it can be stated:

$$m = \int_{\Omega_0} \rho_0 dV = \int_{\Omega} \rho dv = \int_{\Omega} dm \quad (2.63)$$

As there is neither a flux nor a production of mass in the context of the body under consideration, all terms of the right hand side in equ. (2.62) vanish. Thus using $Z = \rho$, equ. (2.62) leads to:

$$\frac{d}{dt} \int_{\Omega} \rho \, dv = \frac{d}{dt} m = 0 \quad (2.64)$$

Balance laws hold for any subdomain $\Omega_s \subset \Omega$ and consequently for any point x of the body. This is expressed via the local form of the conservation law which can be derived from the related integral form. Accordingly, using:

$$\frac{d}{dt} (\det \mathbf{F}) = \operatorname{div} \dot{\mathbf{x}} \det \mathbf{F} \quad (2.65)$$

the local representation of the balance of mass can be obtained from equ. (2.36) and (2.64):

$$\dot{\rho} + \rho \operatorname{div} [\dot{\mathbf{x}}] = 0 \quad (2.66)$$

This equation is known as *continuity equation* according to Euler and d'Alembert.

2.6.2 Conservation of Linear Momentum

Let the material body Ω be in a closed system which means that it does not exchange any matter with the outside and it is not acted on by outside forces. Then the total momentum is constant. This fact is implied by Newton's second law of motion. It says that the change of momentum with time is equal to the resultant of all forces that act on the body Ω .

Starting again from equ. (2.62), it is now assumed that $Z = \rho \dot{\mathbf{x}}$. With the gravitational force per unit volume $\rho \mathbf{b}$ and the electromagnetically induced volume forces $\vec{\mathbf{f}}^{el}$, we can

formulate $\Xi_f = \rho \mathbf{b} + \vec{\mathbf{f}}^{el}$. Furthermore it can be assumed that $\Xi_p = 0$. Considering the surface traction $\hat{\mathbf{t}}$, it can be stated $\Lambda = \hat{\mathbf{t}}$. Thus it finally follows from equ. (2.62):

$$\frac{d}{dt} \int_{\Omega} \rho \dot{\mathbf{x}} dv = \int_{\Omega} (\rho \mathbf{b} + \vec{\mathbf{f}}^{el}) dv + \int_{\Gamma} \hat{\mathbf{t}} da \quad (2.67)$$

Furthermore, using equ. (2.36) one can derive a relation between the densities of reference and actual configuration:

$$\rho_0(\mathbf{X}) = \det(\mathbf{F}) \rho(\mathbf{x}, t) \quad (2.68)$$

Using equ. (2.68) and transforming the surface integral into a volume integral with the help of the divergence theorem, the local representation of the conservation law of linear momentum in the actual configuration can now be derived from equ. (2.67):

$$\rho \ddot{\mathbf{x}} = \rho \mathbf{b} + \vec{\mathbf{f}}^{el} + \text{div} \sigma \quad (2.69)$$

It has been shown that the effect of the electromagnetically induced volume forces is negligible for the technical application of piezoelectric elements [Mau88], [Kam01]. Consequently, a pure mechanical type of conservation law is obtained:

$$\rho \ddot{\mathbf{x}} = \rho \mathbf{b} + \text{div} \sigma \quad (2.70)$$

This reduction to a pure mechanical conservation law is a common approach in the context of piezoelectric finite element development [KW08, Sch10, Leg11].

Neglecting the acceleration term, also the static equilibrium conditions can be derived from the conservation law of linear momentum.

$$\text{div}(\sigma) + \rho \mathbf{b} = 0 \quad (2.71)$$

$$\sigma \mathbf{n} = \hat{\mathbf{t}} \quad (2.72)$$

Here, equ. (2.71) is the static field equation and equ. (2.72) is the static boundary condition. The term $\hat{\mathbf{t}}$ represents the boundary surface traction.

Rewritten in reference configuration and in dependence of the Second Piola-Kirchhoff stresses one obtains:

$$\text{div}(\mathbf{FS}) + \rho_0 \mathbf{b}_0 = 0 \quad (2.73)$$

$$\mathbf{FSN} = \hat{\mathbf{t}}_0 \quad (2.74)$$

2.6.3 Conservation of Angular Momentum

The law of conservation of angular momentum states that no change of angular momentum can occur in a closed system if no external torque acts on the system. Consequently, the angular momentum before an event involving only internal torques or no torques is equal to the angular momentum after the event.

The angular momentum \mathbf{L} with respect to a given center of rotation \mathbf{x}_0 is defined with:

$$\mathbf{L} = \int_{\Omega} (\mathbf{x} - \mathbf{x}_0) \times \rho \dot{\mathbf{x}} dv \quad (2.75)$$

Furthermore, we can state:

$$\Xi_f = \vec{\mathbf{m}}^{el} + (\mathbf{x} - \mathbf{x}_0) \times (\rho \mathbf{b} + \vec{\mathbf{f}}^{el}) \quad (2.76)$$

where $\vec{\mathbf{m}}^{el}$ is the electrically induced moment per unit volume. With $\Xi_p = 0$, $\Lambda = (\mathbf{x} - \mathbf{x}_0) \times \hat{\mathbf{t}}$ and the lever arm $\bar{\mathbf{x}} := \mathbf{x} - \mathbf{x}_0$ it can be obtained from equ. (2.62):

$$\frac{d}{dt} \int_{\Omega} \bar{\mathbf{x}} \times \rho \dot{\mathbf{x}} dv = \int_{\Omega} [\vec{\mathbf{m}}^{el} + \bar{\mathbf{x}} \times (\rho \mathbf{b} + \vec{\mathbf{f}}^{el})] dv + \int_{\Gamma} \bar{\mathbf{x}} \times \hat{\mathbf{t}} da \quad (2.77)$$

Following the explanations in chapter 2.6.2, both $\vec{\mathbf{f}}^{el}$ and $\vec{\mathbf{m}}^{el}$ can be neglected for the focus of this work. Similarly to the conservation law of linear momentum, a pure mechanical representation can be obtained:

$$\frac{d}{dt} \int_{\Omega} \bar{\mathbf{x}} \times \rho \dot{\mathbf{x}} dv = \int_{\Omega} \bar{\mathbf{x}} \times \rho \mathbf{b} dv + \int_{\Gamma} \bar{\mathbf{x}} \times \hat{\mathbf{t}} da \quad (2.78)$$

A transformation into the local form of the conservation law of angular momentum can be performed using the local form of conservation of mass according to equ. (2.66). This leads to the known symmetry of the Cauchy stresses [Bal10]:

$$\sigma_{ij} = \sigma_{ji} \quad (2.79)$$

2.6.4 Conservation of Electric Charge

Let the material body Ω be again a closed system. Electric charges can be created and eliminated, however, this happens in a balanced manner in the closed system. Thus the overall electric charge does not change.

Let ρ_0^{el} be the electric charge density in the reference configuration. Then the electric charge q can be defined as follows:

$$q = \int_{\Omega} \rho_0^{el} dV \quad (2.80)$$

The electric charge can only change if an electric current $I \neq 0$ exists. The electric current I can be described with the electric current density \mathbf{j}_0^{el} in the reference configuration:

$$I = \int_{\Omega} \text{div } \mathbf{j}_0^{el} dV \quad (2.81)$$

Again, starting from equ. (2.62), a conservation law can be obtained. The local form is

$$\dot{\rho}_0^{el} + \text{div } \mathbf{j}_0^{el} = 0 \quad (2.82)$$

This equation corresponds to the local conservation law of mass according to equ. (2.66). Furthermore, it can be identified that the conservation law of electric charge is not affected by mechanical measures.

The conservation of electric charge can also be derived from the Maxwell's equations that describe the physical behavior in electromagnetic fields. The Maxwell equations form the basis of classical electrodynamics and define relations between the magnetic field $\vec{\mathbf{H}}$, the magnetic flux density $\vec{\mathbf{B}}$, the electric field $\vec{\mathbf{E}}$, the electric displacement $\vec{\mathbf{D}}$, the electric current density \mathbf{j}_0^{el} and the electric charge density ρ_0^{el} :

$$\operatorname{rot} \vec{\mathbf{H}} = \mathbf{j}_0^{el} + \frac{\partial \vec{\mathbf{D}}}{\partial t} \quad (\text{Ampere's circuital law}) \quad (2.83)$$

$$\operatorname{div} \vec{\mathbf{B}} = 0 \quad (\text{Gauss's law for magnetism}) \quad (2.84)$$

$$\operatorname{rot} \vec{\mathbf{E}} = -\frac{\partial \vec{\mathbf{B}}}{\partial t} \quad (\text{Maxwell - Faraday equation}) \quad (2.85)$$

$$\operatorname{div} \vec{\mathbf{D}} = \rho_0^{el} \quad (\text{Gauss's law}) \quad (2.86)$$

Assuming a quasi-static problem, the electric and magnetic field equations are decoupled [Jac99]. Furthermore, as the piezoelectric materials are in general not magnetizable and of low conductivity, the magnetic components can be neglected and the magnetic flux density can be set to $\vec{\mathbf{B}} = 0$. Thus equ. (2.85) leads again to the relation of equ. (2.46). Transforming equ. (2.86) into integral form leads to

$$\int_{\Gamma} \vec{\mathbf{D}} \cdot \mathbf{N} dA = \int_{\Omega} \rho_0^{el} dV \quad (2.87)$$

which says that the electric flux through the surface of a body is equal to the overall charge of the body. Furthermore, the natural boundary condition for the electric displacement boundary $\Gamma_{\vec{\mathbf{D}}}$ can be derived from equ. (2.87):

$$\vec{\mathbf{D}} \cdot \mathbf{N} = -\hat{q}_0 \quad \text{on } \Gamma_{\vec{\mathbf{D}}} \quad (2.88)$$

with \hat{q}_0 being the electric surface charge on the boundary. There are different conventions with respect to the sign of \hat{q}_0 in the literature (see e.g. [KW06, MR04, Sch10]). The minus-sign is chosen here which also reflects the result of a consistent derivation in chapter 2.9.2.1.

2.7 Constitutive Equations

The constitutive equation (often called material law) defines the relation between static and kinematic field quantities of a structure. In the context of deformable dielectric materials this means the coupled relation between strains and electric fields on the one hand side and stresses and electric displacements on the other hand side.

For further details about the theory of constitutive equations beyond the explanations

in the sequel, the reader is referred to the literature: Concise theory of material laws in the context of structural continuum mechanics can be found e.g. at Simo and Hughes [SH98], Mang and Hofstetter [MH00], Malvern [Mal69], as well as Stein and Barthold [SB93]. Further literature about electromechanics, piezoelectricity and the derivation of the material law from thermodynamic potentials can be found e.g. at Crowley [Cro86], Maugin [Mau88], Ikeda [Ike90] and Yang [Yan05].

2.7.1 Phenomenological Behavior of Piezoelectric Materials

Before a continuum mechanical description of the constitutive equations is started in the sequel, a short introduction into the phenomenological behavior of piezoelectric materials shall be given. The word piezoelectricity means "electricity resulting from pressure". It is derived from the ancient Greek word $\piίεζειν$ (piezein), which means to squeeze or press, and $ήλεκτρον$ (electron), which stands for amber, an ancient source of electric charge.

2.7.1.1 Crystal Structure

The piezoelectric effect is based on the occurrence of electric dipole moments in solids. The latter property is commonly induced by crystal lattices with asymmetries. This is e.g. the case for ceramics with perovskite structure (Figure 2.3), like lead titanate ($PbTiO_3$), barium titanate ($BaTiO_3$) and lead zirconate titanate ($Pb(Zr_xTi_{1-x})O_3$, $0 \leq x \leq 1$). Further perovskite materials can be found e.g. at Jaffe [Jaf71].

Depending on the temperature, the unit cell turns into different geometries. Above the Curie temperature, the unit cell is in the cubic phase where the structure is symmetric and no piezoelectric behavior is present (also called *paraelectric phase*). Lowering the temperature below Curie temperature, the charge concentrations can move such that electric dipole moments arise.

Dependent from the size of charge concentration movement and the size of electric dipole moment generation, also the shape of the unit cell changes. Barium titanate is often used in the literature as demonstration example in this context [Jaf71, Sch10]: Gradually reducing the temperature, the unit cell turns first from a cubic system to a tetragonal system via stretching in the direction of one axis. With further decreasing temperature, the rectangular orientation of the unit cell is more and more lost and the shape turns into an orthorhombic system and finally a rhombohedral system where the latter has the highest unit cell polarization (Figure 2.4).

The polarization in these phases happens without applying an external electric field or pressure, and is known as *spontaneous polarization* if it is a permanent electric dipole moment. When spontaneous polarization occurs, dipoles near each other tend to be aligned in regions, the so-called *Weiss domains*. However, as the different domains have random

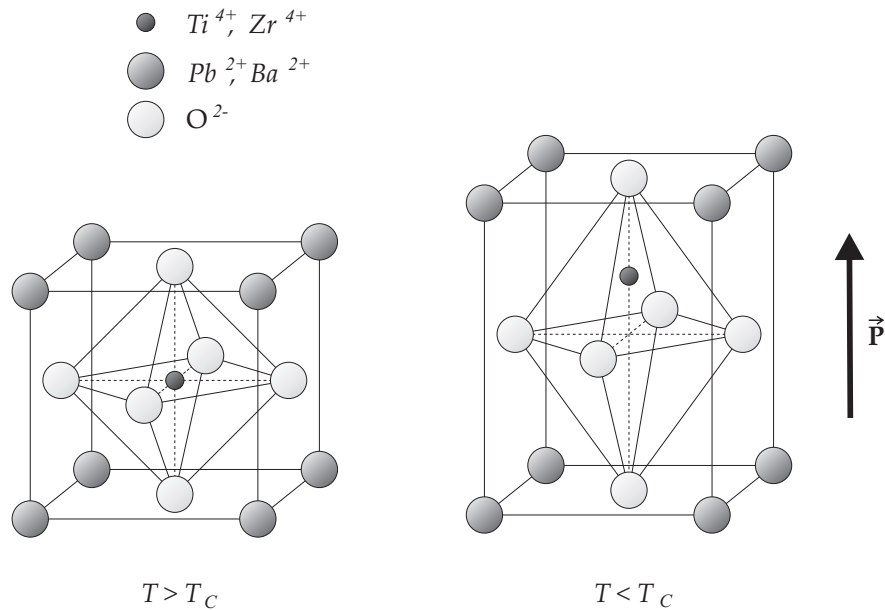


Figure 2.3: Crystal structure of perovskite: Unit cell in cubic phase ($T > T_C$) and tetragonal phase ($T < T_C$).

polarization orientation, there is no polarization existing from the macroscopic point of view.

Nevertheless, for several piezoelectric materials the domains can be aligned using the process of *poling* where a strong electric field \vec{E} is applied across the material, usually at elevated temperatures. An increase of the temperature beyond the Curie temperature would lead to a loss of any piezoelectric behavior again. Materials that show a remanent or non-remnant change of the polarization under an applied electrical field are called *dielectrics*. Dielectrics are electrical insulators: When a dielectric is placed in an electric field, electric charges do not flow through the material, but only slightly shift from their average equilibrium positions causing dielectric polarization. Piezoelectric materials are the sub-group of the dielectrics that exhibit the piezoelectric effect.

Some materials, called *pyroelectric*, exhibit electric dipole moments even in the absence of an external electric field. In pyroelectric materials, a temporary voltage is generated when the material is heated or cooled. *Ferroelectric* crystals are pyroelectric crystals in which the direction of the spontaneous polarization can be switched to another remanent orientation by an external electric field. All ferroelectric materials are piezoelectric materials, but not the other way round. There are also piezoelectric materials that have a macroscopic polarization just due to their atomic lattice structure. The polarization can either be of permanent type or be generated via mechanical pressure.

An overview of this classification is given in Figure 2.5 which can also be found e.g. at [Kao04, Kli06].

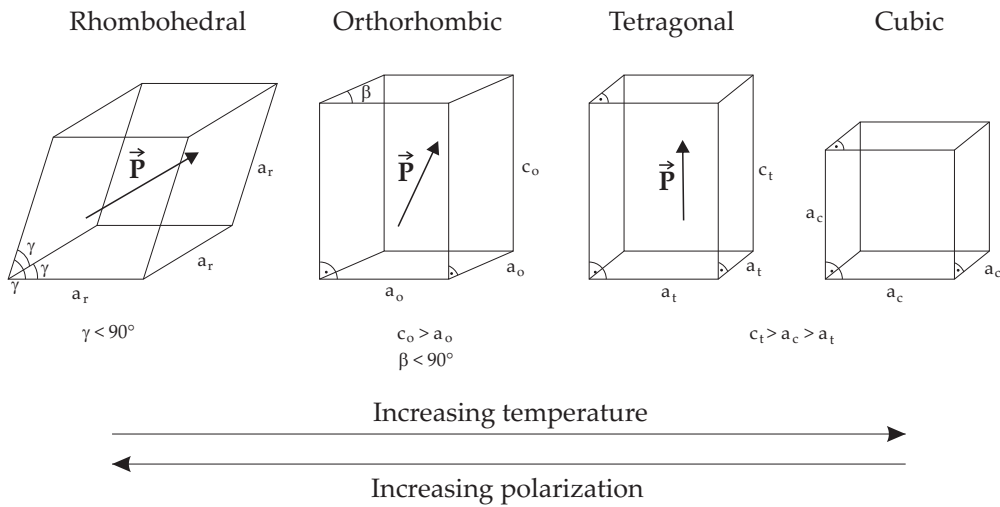


Figure 2.4: Phases of barium titanate (see also e.g. at [KLBC93]).

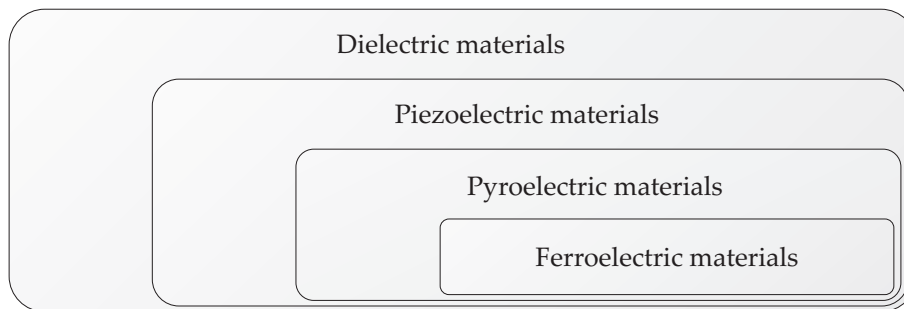


Figure 2.5: Classification of dielectric materials.

2.7.1.2 Direct and Inverse Piezoelectric Effect

As stated above, piezoelectric materials are a class of materials which can be polarized not only by an electric field, but also by application of a mechanical stress.

In piezoelectric materials, mechanical stresses due to external forces induce displacements in the positive and negative lattice elements which leads to a change of the macroscopic polarization \vec{P} . The resulting formation of an electric field \vec{E} puts an electric potential on insulated electrodes on the surface of the probe which can be used as output signal for sensors. This effect is called *direct piezoelectric effect* and sometimes also referred to as the generator effect in the literature.

Dependent from the mechanical loading with respect to the polarization direction, three different types can be identified according to the electric output signal that can be measured (Figure 2.6):

- The *longitudinal effect* where normal stresses are applied parallel to the polarization. The size of the charge depends here only on the applied force. The only way to

increase the charge (and thus the sensor sensitivity) is to connect several plates mechanically in series and electrically in parallel.

- The shear effect which can be subdivided into two subgroups [Sch10]: The *longitudinal shear effect* where shear is applied with a shear plane normal that is parallel to the polarization. and the *transverse shear effect* where shear is applied with a shear plane normal that is perpendicular to the polarization. The shear effect is just as the longitudinal effect independent from size and shape of the piezoelectric element.
- The *transversal effect* where normal stresses are applied in a transverse direction to the polarization. The transversal effect has the unique property that the generated charge is dependent on the aspect ratio of the probe. That's why pressure sensors are commonly based on the transversal effect.

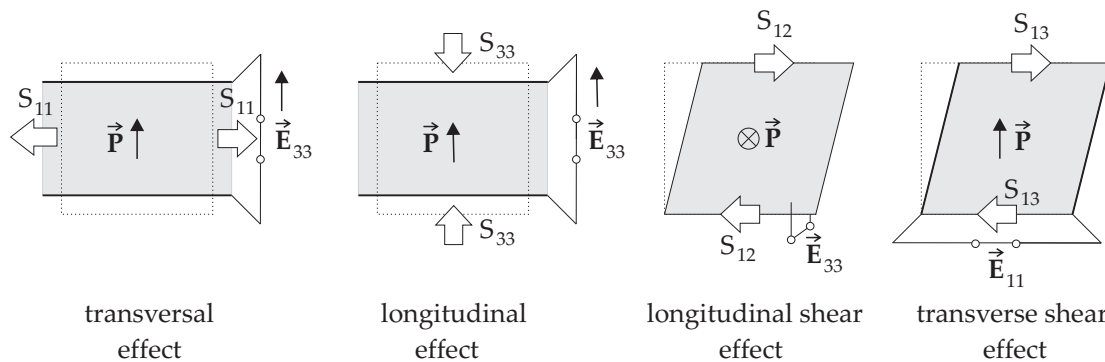


Figure 2.6: Types of direct piezoelectric effects dependent from mechanical loading with respect to polarization direction.

Conversely, the application of an electric voltage to an piezoelectric body also leads to a shift of the centers of positive and negative charge which results in a deformation of the probe (*inverse piezoelectric effect*). The amount and type of deformation is a function of the polarity, the voltage applied and the direction of the polarization vector. Dependent from the orientation of the applied electrical field with respect to the polarization, one can identify the following types of inverse piezoelectric effects:

- Extension: an electrical field in the direction of the polarization leads to an extension of the probe in this direction with an contraction in the transversal directions.
- Compression: if the electrical field is oriented in opposite direction, the probe performs a contraction in this direction with an extension in the transversal directions.
- Shear: an electric field perpendicular to the polarization results into a shear deformation of the probe.

If free deformation is constrained in the body, mechanical stresses are generated. The inverse piezoelectric effect is frequently also called the *motor effect*. The inverse piezoelectric effect can be used for various actuator types.

Applying an external voltage, all piezoelectric effects (longitudinal, transversal and shear) can be used to control deformations. Limitations concerning obtainable deformations can be exceeded with stacked sequences, additional lever arms via substrate materials or special constructions like the bimorph beam (see simulation example in chapter 7.2).

If an electric field is applied to an probe, the resulting strains consist in general of an elastic strain part and a remanent strain part. The remanent strain part is related to a permanent change of the polarization and remains after deactivation of the electric field. In this work it is assumed that the applied electric field is small enough such that the remanent strain part can be neglected.

2.7.2 Continuum Mechanical Description

In pure mechanical applications, it is a well-known approach to derive the stresses from the strain energy density $W^{mech}(\mathbf{E})$:

$$\mathbf{S}^{mech} = \frac{\partial W^{mech}(\mathbf{E})}{\partial \mathbf{E}} \quad (2.89)$$

Similarly, the stresses and electric displacements can be derived from a thermodynamic energy function in an electromechanical generalization of this approach [Ike90]. To describe the energy density function in the context of piezoelectricity, different combinations of independent field variables are possible [Tie69].

In this work, the *electric enthalpy density* W_H is chosen, in which the Green-Lagrange strain tensor \mathbf{E} and the electric field $\vec{\mathbf{E}}$ are the independent variables:

$$W_H = W_H(\mathbf{E}, \vec{\mathbf{E}}) \quad (2.90)$$

Using the second law of thermodynamics and assuming a reversible process [Kli06], one can derive:

$$\mathbf{S} = \frac{\partial W_H(\mathbf{E}, \vec{\mathbf{E}})}{\partial \mathbf{E}} \quad (2.91)$$

$$-\vec{\mathbf{D}} = \frac{\partial W_H(\mathbf{E}, \vec{\mathbf{E}})}{\partial \vec{\mathbf{E}}} \quad (2.92)$$

Thus the energy conjugate quantities to \mathbf{E} and $\vec{\mathbf{E}}$, namely the second Piola-Kirchhoff (PK2) stress tensor \mathbf{S} and the vector of the electric displacements $\vec{\mathbf{D}}$ are obtained.

The material tensor of fourth order is denoted by \mathbf{C} . It provides a relation between stress and strain and represents a fourth order tensor:

$$\mathbf{C} = C^{ijkl} \mathbf{G}_i \otimes \mathbf{G}_j \otimes \mathbf{G}_k \otimes \mathbf{G}_l \quad (2.93)$$

Furthermore, if a potential exist, it holds:

$$\mathbf{C}^{ijkl} := \frac{\partial^2 W_H(\mathbf{E}, \vec{\mathbf{E}})}{\partial E_{ij} \partial E_{kl}} \quad (2.94)$$

Accordingly, one can derive the 3rd order *piezoelectric coupling tensor*:

$$\mathfrak{e}^{ijk} := -\frac{\partial^2 W_H(\mathbf{E}, \vec{\mathbf{E}})}{\partial E_{ij} \partial \vec{E}_k} \quad (2.95)$$

and the second order *permittivity tensor*:

$$\epsilon^{ij} := -\frac{\partial^2 W_H(\mathbf{E}, \vec{\mathbf{E}})}{\partial \vec{E}_i \partial \vec{E}_j} \quad (2.96)$$

Now the material tensors of equ. (2.94), equ. (2.95) and equ. (2.96) shall be discussed a bit more in detail. Linear constitutive equations are assumed. In the context of piezoelectricity, this means that a linear mapping between strain tensor and electric field on the one hand side and stress tensor and electric displacement on the other hand side is assumed. Using index notation, the material law can be stated as follows:

$$S^{ij} = C^{ijkl} E_{kl} - \mathfrak{e}^{mij} \vec{E}_m \quad (2.97)$$

$$\vec{D}^i = \mathfrak{e}^{ijk} E_{jk} + \epsilon^{il} \vec{E}_l \quad (2.98)$$

The electric displacement describes the charge per unit area and can thus be regarded as electrical counterpart of the mechanical stresses. It should be mentioned that also other formulation variants of the constitutive equations can be found in the literature depending on the choice of the dependent variable fields at the right side of equ. (2.97) and (2.98) (see e.g. [Ike90], [HLW08]): e.g. also the polarization $\vec{\mathbf{P}}$ can be used as electrical variable field. However, these formulation variants can be transformed into each other via tensor operations.

In contrast to the common approach of enhanced piezoelectric element formulations of the actual literature, no matrix representation of the material law in Voigt notation is needed. In contrast, a pure continuum-mechanical description in convective coordinates is adopted. Thus for base transformations, no tailored energy-conserving transformation rules are needed that consider the author-dependent ordering of the entries in the strain vector, stress vector, etc. This also enhances the clarity of the related implementation. However, besides to the continuum mechanical description a Voigt notation is introduced in the sequel where it seemed appropriate to highlight single aspects.

2.7.2.1 Elasticity Tensor

The described linear mapping of the material law in equ. (2.97) and (2.98) implies an elasticity tensor \mathbf{C} with only constant entries. In general, \mathbf{C} would exhibit $3^4 = 81$ entries.

Due to the symmetry of the Green-Lagrange strains and the PK2 stresses as discussed in chapter 2.3 and 2.5.1, one can deduce:

$$C^{ijkl} = C^{jikl} \quad (2.99)$$

$$C^{ijkl} = C^{ijlk} \quad (2.100)$$

Furthermore, one can state according to the Young's theorem:

$$C^{ijkl} = C^{klij} \quad (2.101)$$

if the order of the partial derivatives in equ. (2.94) is freely selectable. This is true as an elastic potential exists and thus the work of the stresses is path-independent.

In total this means that in general 21 independent constants are needed in the elasticity tensor. Dependent on further symmetry conditions and assumptions due to the chosen material law, this number of constants can further be reduced.

In the case of linear elastic isotropic material, two independent material parameters are sufficient to describe the elasticity tensor. In mathematical literature, the Lamé constants λ and μ are commonly used in this context. In engineering literature, the more intuitively accessible parameters Young's modulus E and Poisson's ratio ν are predominantly used. A transformation between these parameter pairs can be done with:

$$\lambda = \frac{E\nu}{(1+\nu)(1-2\nu)}, \quad \mu = \frac{E}{2(1+\nu)} \quad (2.102)$$

Using the Lamé constants, the components of the material tensor are:

$$C^{ijkl} = \lambda G^{ij}G^{kl} + \mu(G^{ik}G^{jl} + G^{il}G^{kj}) \quad (2.103)$$

In the case of orthotropic material behavior of a three-dimensional structure, there exist three symmetry planes of elastic material behavior that are perpendicular to each other. The number of independent material constants reduces to nine. Here it is advantageous to introduce a orthonormal basis $\{\mathbf{G}_1^*, \mathbf{G}_2^*, \mathbf{G}_3^*\}$ that reflects the symmetry planes of the orthotropic material:

$$\mathbf{C} = C^*{}^{ijkl} \mathbf{G}_i^* \otimes \mathbf{G}_j^* \otimes \mathbf{G}_k^* \otimes \mathbf{G}_l^* \quad (2.104)$$

Then a decoupling of shear terms and normal strain terms is possible. To describe the orthotropic material, the following definitions are made in the orthonormal basis $\{\mathbf{G}_1^*, \mathbf{G}_2^*, \mathbf{G}_3^*\}$:

- E_1, E_2 and E_3 represent the Young's moduli in the three coordinate directions.
- $\nu_{ij} = \frac{E_{jj}}{E_{ii}}$ is the Poisson's ratio for strains in j -direction due to stress in i -direction.
- G_{12}, G_{13} and G_{23} are the shear moduli of the 1-2-plane, 1-3-plane and 2-3-plane.

Now the non-zero entries of the elasticity tensor can be defined as:

$$\begin{aligned} C^{*1111} &= \frac{1 - \nu_{23}\nu_{32}}{\Delta_E} E_1 ; C^{*2222} = \frac{1 - \nu_{13}\nu_{31}}{\Delta_E} E_2 ; C^{*3333} = \frac{1 - \nu_{12}\nu_{21}}{\Delta_E} E_3 \\ C^{*1122} &= \frac{\nu_{12} + \nu_{13}\nu_{32}}{\Delta_E} E_2 ; C^{*1133} = \frac{\nu_{13} + \nu_{12}\nu_{23}}{\Delta_E} E_3 ; C^{*2233} = \frac{\nu_{23} + \nu_{21}\nu_{13}}{\Delta_E} E_3 \\ C^{*1212} &= G_{12} ; C^{*1313} = G_{13} ; C^{*2323} = G_{23} \end{aligned} \quad (2.105)$$

with

$$\Delta_E = 1 - \nu_{12}\nu_{21} - \nu_{13}\nu_{31} - \nu_{23}\nu_{32} - 2\nu_{31}\nu_{12}\nu_{23} \quad (2.106)$$

2.7.2.2 Piezoelectric Tensor and Permittivity Tensor

The second-order tensor of dielectric constants contains 6 independent coefficients which represent the permittivity of the dielectric material. It describes the behavior of electric charge if it is subjected to electrical voltage. The entries of the permittivity tensor are usually described with:

$$\epsilon^{ij} = \epsilon_0 \epsilon_r^{ij} \quad (2.107)$$

where ϵ_0 is the vacuum permittivity as introduced in chapter 2.4, and ϵ_r is the relative permittivity of the material.

Similar to the description of the orthotropic elastic material description above, it is advantageous to describe the piezoelectric material behavior in an orthonormal basis $\{\mathbf{G}_1^*, \mathbf{G}_2^*, \mathbf{G}_3^*\}$ that reflects the polarization orientation of the piezoelectric material. Then the permittivity tensor only contains nonzero entries at the diagonal entries:

$$\epsilon^{ij} = 0 \quad \forall \quad \{(i, j) | i \neq j\} \quad (2.108)$$

However, piezoelectric material commonly exhibits an isotropic behavior in the transversal direction to the polarization. This reduces the independent coefficients of ϵ^{ij} to two. In the literature, the permittivity coefficient in transversal direction is usually identified with ϵ^{11} and the permittivity coefficient in the polarization direction is commonly denoted with ϵ^{33} .

The third-order tensor of the piezoelectric constants e^{ijk} represents the coupling between the mechanical and electrical fields. Consequently, the absolute value of the piezoelectric constants represent the level of interaction between electrical and mechanical response of the structure. In the general case, e^{ijk} would contain 18 independent coefficients.

Again assuming a polarization only in \mathbf{G}_3^* direction, the following nonzero entries appear in the piezoelectric tensor:

- e^{311} and e^{322} represent the transversal effect: A deformation is generated perpendicular to the applied electric field.
- e^{333} represents the longitudinal effect: If an electric field in the polarization direction is applied, the structure shows a deformation in this polarization direction.

- e^{113} , e^{131} , e^{223} and e^{232} represent the shear effect: Electric fields perpendicular to the polarization direction cause shear deformations in the structure.

Furthermore, for the most piezoelectric materials isotropic behavior in the transversal directions to the polarization can be assumed. It holds: $e^{311} = e^{322}$ and $e^{113} = e^{131} = e^{223} = e^{232}$. Thus the number reduces to three independent parameters which reflect the basic actor types of the longitudinal effect, transversal effect and shear effect. In the literature, the Voigt matrix notation is very common to describe piezoelectric finite elements. Table 2.1 gives an overview of related tensor and Voigt notations.

type of piezoelectric effect	piezoelectric tensor entry	Voigt notation naming
transversal effect	$e^{311} = e^{322}$	$e^{31} = e^{32}$
longitudinal effect	e^{333}	e^{33}
shear effect	$e^{113} = e^{131} = e^{223} = e^{232}$	e^{15}

Table 2.1: Relation between piezoelectric tensor entries and common naming in literature with Voigt notation.

As these namings stemming from Voigt notation are quite established, they will be used in chapter 7 to refer to the single piezoelectric constants of the numerical examples.

2.8 Strong Form

In the past chapters, the field equations (2.37), (2.45), (2.73), (2.86), (2.97), (2.97), as well as the essential and natural boundary conditions according to equ. (2.41), (2.48), (2.74) and (2.88) have been derived. Together this equations form the strong form of the electromechanical boundary value problem as summarized in Table 2.2. Strong form means in this context that the problem is defined by a system of ordinary and partial differential equations, supplemented by suitable boundary conditions.

	Mechanical	Electrical
Kinematic field equations:	$\mathbf{E} = \frac{1}{2} (\mathbf{F}^T \mathbf{F} - \mathbf{I}) \quad \text{in } \Omega$	$\vec{\mathbf{E}} = -\text{grad } \varphi \quad \text{in } \Omega$
Conservation laws:	$\text{div}(\mathbf{FS}) + \rho_0 (\mathbf{b}_0 - \ddot{\mathbf{x}}) = 0 \quad \text{in } \Omega$	$\text{div } \vec{\mathbf{D}} - \rho_0^{\text{el}} = 0 \quad \text{in } \Omega$
Constitutive equations:	$S^{ij} = C^{ijkl} E_{kl} - e^{mij} \vec{E}_m \quad \text{in } \Omega$ $\vec{D}^i = e^{ijk} E_{jk} + \epsilon^{il} \vec{E}_l \quad \text{in } \Omega$	
Essential b/c:	$\mathbf{u} = \hat{\mathbf{u}} \quad \text{on } \Gamma_{\mathbf{u}}$	$\varphi = \hat{\varphi} \quad \text{on } \Gamma_{\varphi}$
Natural b/c:	$\mathbf{FSN} = \hat{\mathbf{t}}_0 \quad \text{on } \Gamma_{\mathbf{S}}$	$\vec{\mathbf{D}} \cdot \mathbf{N} = -\hat{q}_0 \quad \text{on } \Gamma_{\vec{\mathbf{D}}}$

Table 2.2: Strong form of the coupled electromechanical problem.

For the definitions of the four boundary types it holds:

$$\Gamma_{\mathbf{u}} \cup \Gamma_{\mathbf{S}} = \Gamma, \quad \Gamma_{\mathbf{u}} \cap \Gamma_{\mathbf{S}} = \emptyset \quad (2.109)$$

$$\Gamma_{\varphi} \cup \Gamma_{\vec{\mathbf{D}}} = \Gamma, \quad \Gamma_{\varphi} \cap \Gamma_{\vec{\mathbf{D}}} = \emptyset \quad (2.110)$$

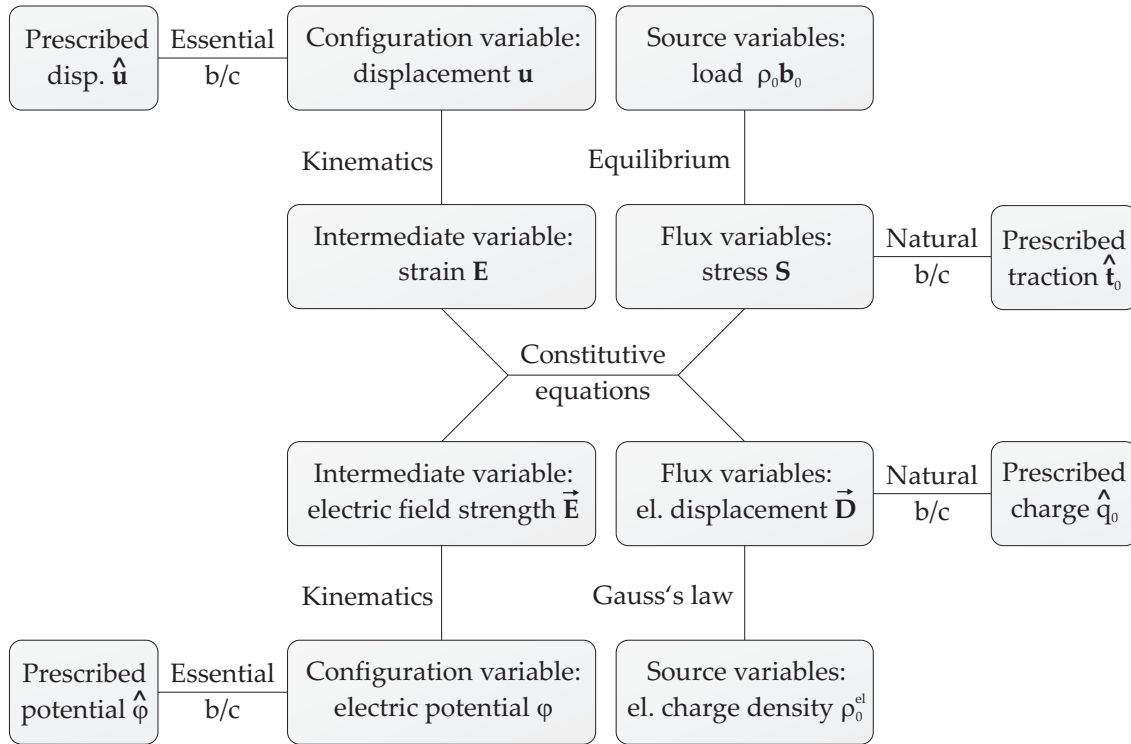


Figure 2.7: Tonti diagram of the coupled electromechanical problem.

The Tonti diagram (Figure 2.7) is a suitable method for a systematic presentation of the relations between the six fields \mathbf{u} , φ , \mathbf{E} , $\vec{\mathbf{E}}$, \mathbf{S} and $\vec{\mathbf{D}}$. The diagram shows the dependencies of the fields due to kinematic, constitutive and balance equations. Furthermore, it provides the generic namings of the fields: The displacement field and the potential field represent the *configuration variables* or *primary variables*, the strain and the electric field strength are the *intermediate variables* and finally the stress and the electric displacement are called the *flux variables* [Ton72, Ton03, Fel06].

As an analytical solution of the strong form is in general not available, integral formulations are often used to generate approximation methods. These integral formulations do not fulfill the differential equation at each single point, but in the sense of an integral mean value. As a consequence, these formulations are commonly called *weak form*. The weak form is the basis for the formulation of finite elements and can be derived via functional analysis from the strong form (see chapter 2.9). A common approach is to derive the weak form via multiplication of the strong form with a test function and subsequent

integration over the domain Ω . Another alternative to derive the weak form is the principle of the minimum of the potential energy. These techniques are used in chapter 2.9 to derive suitable weak formulations of the electromechanic problem.

Finally, it shall be mentioned that strong and weak form are equivalent formulations as long as identical solution spaces are assumed and no discretization is performed yet.

2.9 Energy Methods and Functionals

For the mathematical analysis of piezoelectric structures, a coupled system of partial differential equations has to be solved. As the direct solution of the strong form of the problem is in general not possible, variational formulations are adopted: Weak formulations are generated to enable the use of numerical solution methods like the finite element method.

An overview of variational formulations can be found e.g. at Stein [Ste64], Oden and Reddy [OR76], as well as Felippa [Fel94]. Variational formulations with focus on electromechanical problems can be found e.g. at Sze and Pan [SP99], Lammering and Mesecke-Rischmann [LMR03], as well as Klinkel [KW08].

2.9.1 Principle of Virtual Work

The principle of virtual work is the variational basis for classical displacement-based finite element formulations in structural mechanics. The principle of virtual work states that an arbitrary, geometrically compatible, infinitesimal displacement $\delta \mathbf{u}$ (so-called virtual displacement) does not cause any work for a mechanical system in equilibrium state. This allows for an intuitive mechanical interpretation: the virtual work of the inner forces must be negative equal to the virtual work of the outer forces. The principle of virtual work is equivalent to the postulation of equilibrium.

In the context of electromechanical problems, there are also virtual potentials $\delta \varphi$ besides to virtual displacements $\delta \mathbf{u}$. Furthermore, besides to equilibrium, also the electrical conservation law according to equ. (2.86) is considered. Apart from that, the general idea of the principle of virtual work stays the same.

2.9.1.1 Derivation by the Minimum Potential Energy Principle

The principle of virtual work can be derived with the principle of minimum potential energy, where the term energy refers here to the electromechanical problem. Hereby, the stationary value of the underlying potential is calculated:

$$\begin{aligned} \Pi(\mathbf{u}, \varphi) &= \Pi^{int} + \Pi_V^{ext} + \Pi_A^{ext} \\ &= \int_{\Omega} W_H dV - \int_{\Omega} W_V^{ext} dV - \int_{\Gamma_S} W_{\Gamma_S}^{ext} dA - \int_{\Gamma_D} W_{\Gamma_D}^{ext} dA \rightarrow stat. \end{aligned} \quad (2.111)$$

which summarizes all internal and external work contributions of both volume and boundary of the body. The constitutive equations are already implicitly included via the definition of the electric enthalpy density (see chapter 2.7.2). Using

$$\mathbf{E} = \frac{1}{2} (\mathbf{F}^T \cdot \mathbf{F} - \mathbf{I}) = \mathbf{E}^u \quad (2.112)$$

$$\vec{\mathbf{E}} = -\text{grad } \varphi = \vec{\mathbf{E}}^\varphi \quad (2.113)$$

$$\mathbf{u} = \hat{\mathbf{u}} \quad \text{on } \Gamma_u \quad (2.114)$$

$$\varphi = \hat{\varphi} \quad \text{on } \Gamma_\varphi \quad (2.115)$$

in the potential formulation of equ. (2.111) and assuming a quasi-static problem leads to:

$$\begin{aligned} \Pi(\mathbf{u}, \varphi) = & \int_{\Omega} \left[W_H(\mathbf{E}^u, \vec{\mathbf{E}}^\varphi) dV - \rho_0 \mathbf{b}_0 \cdot \mathbf{u} + \rho_0^{el} \cdot \varphi \right] dV \\ & - \int_{\Gamma_S} \hat{\mathbf{t}}_0 \cdot \mathbf{u} dA + \int_{\Gamma_{\bar{b}}} \hat{q}_0 \cdot \varphi dA \end{aligned} \quad (2.116)$$

In this context, the upper indices \mathbf{u} and φ are not meant to be an exponent. These indices should demonstrate the direct dependency of the strain tensor and the electric field strength from the displacement field and the potential field, respectively. Setting the first variation of equ. (2.116) to zero finally results in the principle of virtual work:

$$\begin{aligned} \delta\Pi(\mathbf{u}, \varphi) = & \int_{\Omega} \left[\frac{\partial W_H}{\partial \mathbf{E}^u} : \delta \mathbf{E}^u + \frac{\partial W_H}{\partial \vec{\mathbf{E}}^\varphi} \cdot \delta \vec{\mathbf{E}}^\varphi - \rho_0 \mathbf{b}_0 \cdot \delta \mathbf{u} + \rho_0^{el} \cdot \delta \varphi \right] dV \\ & - \int_{\Gamma_S} \hat{\mathbf{t}}_0 \cdot \delta \mathbf{u} dA + \int_{\Gamma_{\bar{b}}} \hat{q}_0 \cdot \delta \varphi dA = 0 \end{aligned} \quad (2.117)$$

with

$$\delta \mathbf{E}^u = \delta \mathbf{F}^T \cdot \mathbf{F} = \mathbf{F}^T \cdot \delta \mathbf{F} = \mathbf{F}^T \cdot \text{grad } \delta \mathbf{u} \quad (2.118)$$

$$\delta \vec{\mathbf{E}}^\varphi = -\text{grad } \delta \varphi \quad (2.119)$$

2.9.1.2 Derivation from the Method of Weighted Residuals

The principle of virtual work can also be derived from the conservation laws via the method of weighted residuals. The method of weighted residuals does not require the existence of a potential and is e.g. also valid for inelastic constitutive laws. The kinematic equations and the constitutive equations are fulfilled in their strong form.

The conservation laws of equ. (2.73) and (2.86) and the Neumann boundary conditions of equ. (2.74) and (2.88) are multiplied with arbitrary scalar test functions $\delta \mathbf{u}$ and $\delta \varphi$ and integrated over the domain Ω and the boundaries Γ_S and $\Gamma_{\bar{b}}$, respectively. This results in:

$$\begin{aligned} & \int_{\Omega} (\text{div}(\mathbf{FS}) + \rho_0 \mathbf{b}_0) \cdot \delta \mathbf{u} d\Omega + \int_{\Omega} (\text{div}(-\vec{\mathbf{D}}) + \rho_0^{el}) \cdot \delta \varphi d\Omega \\ & + \int_{\Gamma_S} (\hat{\mathbf{t}}_0 - \mathbf{t}) \cdot \delta \mathbf{u} dA + \int_{\Gamma_{\bar{b}}} (\hat{q}_0 - q) \cdot \delta \varphi dA = 0 \end{aligned} \quad (2.120)$$

where \mathbf{t} stands for the surface stress vector with $\mathbf{t} = \mathbf{F} \cdot \mathbf{S} \cdot \mathbf{N}$ and q represents the electric surface charge with $q = -\vec{\mathbf{D}} \cdot \mathbf{N}$.

Again it is assumed here that the strain tensor and the electric field strength is derived from the kinematic field equations. Reformulation and partial integration leads again to the weak form according to equ. (2.117).

2.9.1.3 Euler Differential Equations

Now the Euler differential equations should be derived. To do so, the first two terms of equ. (2.117) are reformulated:

$$\begin{aligned} \frac{\partial W_H}{\partial \mathbf{E}^{\mathbf{u}}} : \delta \mathbf{E}^{\mathbf{u}} &= \frac{\partial W_H}{\partial \mathbf{E}^{\mathbf{u}}} : \mathbf{F}^T \cdot \text{grad } \delta \mathbf{u} \\ &= \mathbf{F} \cdot \frac{\partial W_H}{\partial \mathbf{E}^{\mathbf{u}}} : \text{grad } \delta \mathbf{u} = \mathbf{F} \cdot \mathbf{S}^{\mathbf{u}} : \text{grad } \delta \mathbf{u} \end{aligned} \quad (2.121)$$

$$\frac{\partial W_H}{\partial \vec{\mathbf{E}}^{\varphi}} \cdot \delta \vec{\mathbf{E}}^{\varphi} = -\vec{\mathbf{D}}^{\varphi} \cdot (-\text{grad } \delta \varphi) \quad (2.122)$$

Inserting equ. (2.121) and (2.122) into the principle of virtual work of equ. (2.117) yields:

$$\begin{aligned} \delta \Pi(\mathbf{u}, \varphi) &= \int_{\Omega} \left[\mathbf{F} \cdot \mathbf{S}^{\mathbf{u}} : \text{grad } \delta \mathbf{u} + \vec{\mathbf{D}}^{\varphi} \cdot \text{grad } \delta \varphi - \rho_0 \mathbf{b}_0 \cdot \delta \mathbf{u} + \rho_0^{el} \cdot \delta \varphi \right] dV \\ &\quad - \int_{\Gamma_S} \hat{\mathbf{t}}_0 \cdot \delta \mathbf{u} dA + \int_{\Gamma_B} \hat{q}_0 \cdot \delta \varphi dA = 0 \end{aligned} \quad (2.123)$$

Using the product rule and the divergence theorem reveals:

$$\int_{\Omega} \text{grad } \delta \mathbf{u} : \mathbf{F} \cdot \mathbf{S}^{\mathbf{u}} dV = \int_{\Gamma_S} \mathbf{F} \cdot \mathbf{S}^{\mathbf{u}} \cdot \mathbf{N} \cdot \delta \mathbf{u} dA - \int_{\Omega} \delta \mathbf{u} \cdot \text{div} (\mathbf{F} \cdot \mathbf{S}^{\mathbf{u}}) dV \quad (2.124)$$

$$\int_{\Omega} \text{grad } \delta \varphi \cdot \vec{\mathbf{D}}^{\varphi} dV = \int_{\Gamma_B} \vec{\mathbf{D}}^{\varphi} \cdot \mathbf{N} \cdot \delta \varphi dA - \int_{\Omega} \delta \varphi \cdot \text{div} \vec{\mathbf{D}}^{\varphi} dV \quad (2.125)$$

Now equ. (2.124) and (2.125) can be inserted in equ. (2.123) to obtain the following modified representation:

$$\begin{aligned} \delta \Pi(\mathbf{u}) &= \int_{\Omega} \delta \mathbf{u} \cdot (-\text{div} (\mathbf{F} \cdot \mathbf{S}^{\mathbf{u}}) - \rho_0 \mathbf{b}_0) dV - \int_{\Gamma_S} \delta \mathbf{u} \cdot (\hat{\mathbf{t}}_0 - \mathbf{t}^{\mathbf{u}}) dA \\ &\quad + \int_{\Omega} \delta \varphi \cdot (-\text{div} \vec{\mathbf{D}}^{\varphi} + \rho_0^{el}) dV + \int_{\Gamma_B} \delta \varphi (\hat{q}_0 - q^{\varphi}) dA = 0 \end{aligned} \quad (2.126)$$

where $\mathbf{t}^{\mathbf{u}}$ stands for the surface stress vector with $\mathbf{t}^{\mathbf{u}} = \mathbf{F} \cdot \mathbf{S}^{\mathbf{u}} \cdot \mathbf{N}$ and q^{φ} represents the electric surface charge q^{φ} with $q^{\varphi} = -\vec{\mathbf{D}}^{\varphi} \cdot \mathbf{N}$. Based on the fundamental lemma in the calculus of variations, we can derive the Euler equations of the principle of virtual work:

$$\operatorname{div}(\mathbf{F} \cdot \mathbf{S}^u) + \rho_0 \mathbf{b}_0 = 0 \quad \text{in } \Omega \quad (\text{equilibrium condition}) \quad (2.127)$$

$$\operatorname{div} \vec{\mathbf{D}}^\varphi - \rho_0^{el} = 0 \quad \text{in } \Omega \quad (\text{Gauss's law}) \quad (2.128)$$

$$\mathbf{t}^u = \hat{\mathbf{t}}_0 \quad \text{on } \Gamma_{\mathbf{S}} \quad (\text{Natural boundary condition}) \quad (2.129)$$

$$q^\varphi = \hat{q}_0 \quad \text{on } \Gamma_{\vec{\mathbf{D}}} \quad (\text{Natural boundary condition}) \quad (2.130)$$

The principle of virtual work is the variational basis for all so-called *irreducible* finite element formulations which means that the number of independent field variables cannot be further reduced [ZTZ05]. All Euler equations are only dependent from the fields \mathbf{u} and φ . These fields are the only ones that have to be discretized and are subjected to special continuity requirements to guarantee stability and convergence (see chapter 3.2). Constitutive equations, kinematics and kinematic boundary conditions are fulfilled in an exact manner (strong formulation), the conservation law and the natural boundary conditions are only satisfied in the integral sense (weak formulation).

However, numerous enhanced element formulations introduce further independent fields, like strain, stress, electric field strength or electric displacement. Thus the principle of virtual work is not suitable anymore for the derivation of these elements and new variational principles have to be adopted. To this goal, the Hu-Washizu principle is introduced in the next chapter.

2.9.2 Principle of Hu-Washizu

Following the principle of Hu-Washizu [Hu55, Whi04], three independent fields are defined in the case of a pure mechanical problem: The displacements \mathbf{u} , the strains \mathbf{E} and the stresses \mathbf{S} . Accordingly, in the case of an electromechanical problem the electric potential φ , the electric field $\vec{\mathbf{E}}$ and the electric displacement field $\vec{\mathbf{D}}$ are defined as additional independent fields. Consequently, the principle of Hu-Washizu represents the most general form of multi-field functionals.

The principle guarantees highest possible flexibility for the formulation of finite elements, as also the approximation of the six wanted fields can be defined independently. Beyond that, the variable fields \mathbf{u} and φ do not need to fulfill the kinematic boundary conditions in a strict sense and thus can be chosen from a larger space.

2.9.2.1 Derivation from the Minimum Potential Energy Principle

Similar to the principle of virtual displacements, the Hu-Washizu functional can be derived starting from the formulation of the energy potential. However, the kinematic equations are not introduced into the functional via insertion (*elimination method*), but

via Lagrangian Multipliers (*multiplier method*). Assuming a quasi-static problem, one can state:

$$\begin{aligned}
\Pi_{HW}(\mathbf{u}, \varphi, \mathbf{E}, \vec{\mathbf{E}}, \lambda_1, \lambda_2, \boldsymbol{\mu}_1, \boldsymbol{\mu}_2) &= \int_{\Omega} \left[W_H(\mathbf{E}, \vec{\mathbf{E}}) + \lambda_1 : (\mathbf{E}^u - \mathbf{E}) + \lambda_2 \cdot (\vec{\mathbf{E}}^\varphi - \vec{\mathbf{E}}) \right] dV \\
&- \int_{\Omega} \rho_0 \mathbf{b}_0 \cdot \mathbf{u} dV - \int_{\Gamma_S} \hat{\mathbf{t}}_0 \cdot \mathbf{u} dA \\
&+ \int_{\Omega} \rho_0^{el} \cdot \varphi dV + \int_{\Gamma_{\vec{\mathbf{D}}}} \hat{\mathbf{q}}_0 \cdot \varphi dA \\
&+ \int_{\Gamma_u} \boldsymbol{\mu}_1 \cdot (\hat{\mathbf{u}} - \mathbf{u}) dA \\
&+ \int_{\Gamma_\varphi} \boldsymbol{\mu}_2 \cdot (\hat{\varphi} - \varphi) dA \rightarrow stat. \tag{2.131}
\end{aligned}$$

It is a common approach in the literature to directly assign the physical measures of the stresses and electric displacements to the Lagrangian parameters. In contrast to this approach, in this work the stresses and the electric displacements are not directly inserted as additional independent fields from the start. Instead, sharing and extending the argumentation of Bischoff [Bis99], it must be considered that the fields \mathbf{S} and $\vec{\mathbf{D}}$ are already defined via the energy function in equ. (2.91) and equ. (2.92). Thus introducing the fields \mathbf{S} and $\vec{\mathbf{D}}$ as independent variables would be wrong from a formal point of view. However, as it is shown in the sequel, a natural identification of the Lagrangian parameters is possible with the straight-forward derivation of the Euler equations. So no a priori assumptions about the Lagrangian parameters is needed.

Performing the variation of equ. (2.131) leads to

$$\begin{aligned}
\delta\Pi_{HW} &= \int_{\Omega} \left[\frac{\partial W_H}{\partial \mathbf{E}} : \delta\mathbf{E} + \frac{\partial W_H}{\partial \vec{\mathbf{E}}} \cdot \delta\vec{\mathbf{E}} + \delta\lambda_1 : (\mathbf{E}^u - \mathbf{E}) + \delta\lambda_2 \cdot (\vec{\mathbf{E}}^\varphi - \vec{\mathbf{E}}) \right] dV \\
&+ \int_{\Omega} [\lambda_1 : \delta\mathbf{E}^u - \lambda_1 : \delta\mathbf{E}] dV + \int_{\Omega} [\lambda_2 \cdot \delta\vec{\mathbf{E}}^\varphi - \lambda_2 \cdot \delta\vec{\mathbf{E}}] dV \\
&- \int_{\Omega} \rho_0 \mathbf{b}_0 \cdot \delta\mathbf{u} dV - \int_{\Gamma_S} \hat{\mathbf{t}}_0 \cdot \delta\mathbf{u} dA + \int_{\Omega} \rho_0^{el} \cdot \delta\varphi dV + \int_{\Gamma_{\vec{\mathbf{D}}}} \hat{\mathbf{q}}_0 \cdot \delta\varphi dA \\
&+ \int_{\Gamma_u} \delta\boldsymbol{\mu}_1 \cdot (\hat{\mathbf{u}} - \mathbf{u}) dA + \int_{\Gamma_\varphi} \delta\boldsymbol{\mu}_2 \cdot (\hat{\varphi} - \varphi) dA = 0 \tag{2.132}
\end{aligned}$$

According to equ. (2.118) and (2.119), we can insert $\delta\mathbf{E}^u = \mathbf{F}^T \cdot \text{grad } \delta\mathbf{u}$ and $\delta\mathbf{E}^\varphi = -\text{grad } \delta\varphi$ into equ. (2.132). Furthermore, we can deduce by using the product rule and the divergence theorem:

$$\int_{\Omega} \text{grad } \delta\mathbf{u} : \mathbf{F} \cdot \lambda_1 dV = \int_{\Gamma_S} \mathbf{F} \cdot \lambda_1 \cdot \mathbf{N} \cdot \delta\mathbf{u} dA - \int_{\Omega} \delta\mathbf{u} \cdot \text{div} (\mathbf{F} \cdot \lambda_1) dV \tag{2.133}$$

as well as:

$$\int_{\Omega} \lambda_2 \cdot \text{grad } \delta\varphi dV = \int_{\Gamma_{\vec{\mathbf{D}}}} \lambda_2 \cdot \mathbf{N} \delta\varphi dA - \int_{\Omega} \text{div } \lambda_2 \delta\varphi dV \tag{2.134}$$

Thus using equ. (2.133) and equ. (2.134) within the first variation according to equ. (2.132) leads to:

$$\begin{aligned}
\delta\Pi_{HW} &= \int_{\Omega} \left[\frac{\partial W_H}{\partial \mathbf{E}} : \delta \mathbf{E} + \frac{\partial W_H}{\partial \vec{\mathbf{E}}} \cdot \delta \vec{\mathbf{E}} + \delta \lambda_1 : (\mathbf{E}^u - \mathbf{E}) + \delta \lambda_2 \cdot (\vec{\mathbf{E}}^\varphi - \vec{\mathbf{E}}) \right] dV \\
&- \int_{\Omega} \left[\delta \mathbf{u} \cdot \operatorname{div} (\mathbf{F} \cdot \lambda_1) - \operatorname{div} \lambda_2 \delta \varphi + \lambda_1 : \delta \mathbf{E} + \lambda_2 \cdot \delta \vec{\mathbf{E}} \right] dV \\
&- \int_{\Omega} \rho_0 \mathbf{b}_0 \cdot \delta \mathbf{u} dV + \int_{\Omega} \rho_0^{el} \cdot \delta \varphi dV \\
&- \int_{\Gamma_S} (\hat{\mathbf{t}}_0 - \mathbf{F} \cdot \lambda_1 \cdot \mathbf{N}) \cdot \delta \mathbf{u} dA + \int_{\Gamma_{\bar{\mathbf{D}}}} (\hat{q}_0 - \lambda_2 \cdot \mathbf{N}) \cdot \delta \varphi dA \\
&+ \int_{\Gamma_u} \delta \boldsymbol{\mu}_1 \cdot (\hat{\mathbf{u}} - \mathbf{u}) dA + \int_{\Gamma_\varphi} \delta \boldsymbol{\mu}_2 \cdot (\hat{\varphi} - \varphi) dA = 0
\end{aligned} \tag{2.135}$$

Unlike to the derivation of the method of virtual displacements, here it is not searched for minimum points but for stationary points. This also affects the convergence properties of the derived finite element formulations: While displacement-based elements are guaranteed to converge strictly starting from lower values, this is not necessarily the case anymore for finite elements based on the Hu-Washizu functional [BRB99].

Based on the fundamental lemma in calculus of variations, it can be derived:

$$\operatorname{div}(\mathbf{F} \cdot \lambda_1) + \rho_0 \mathbf{b}_0 = 0, \quad \mathbf{E}^u - \mathbf{E} = 0, \quad \frac{\partial W_H}{\partial \mathbf{E}} - \lambda_1 = 0 \quad \text{in } \Omega \tag{2.136}$$

$$\operatorname{div}(\lambda_2) + \rho_0^{el} = 0, \quad \vec{\mathbf{E}}^\varphi - \vec{\mathbf{E}} = 0, \quad \frac{\partial W_H}{\partial \vec{\mathbf{E}}} - \lambda_2 = 0 \quad \text{in } \Omega \tag{2.137}$$

$$\hat{\mathbf{t}}_0 - \mathbf{F} \cdot \lambda_1 \cdot \mathbf{N} = 0 \quad \text{on } \Gamma_S, \quad \hat{\mathbf{u}} - \mathbf{u} = 0 \quad \text{on } \Gamma_u \tag{2.138}$$

$$\hat{q}_0 - \lambda_2 \cdot \mathbf{N} = 0 \quad \text{on } \Gamma_{\bar{\mathbf{D}}}, \quad \hat{\varphi} - \varphi = 0 \quad \text{on } \Gamma_\varphi \tag{2.139}$$

Thus in total ten Euler equations are obtained. First of all, it can be seen that the Lagrange parameters $\boldsymbol{\mu}_1$ and $\boldsymbol{\mu}_2$ dropped out in the derivation of the Euler equations. They serve as test functions for the kinematic field equations. Considering the units of $\boldsymbol{\mu}_1$ and $\boldsymbol{\mu}_2$, the following choice of the test functions can be made: The dependent stress resultant vector \mathbf{t}^S is assigned to $\boldsymbol{\mu}_1$, and $\boldsymbol{\mu}_2$ is replaced by the dependent charge $q^{\bar{\mathbf{D}}}$ resulting from the electric displacement. Furthermore, inserting equ. (2.91) in the last part of equ. (2.136), one obtains:

$$\mathbf{S} = \lambda_1 \tag{2.140}$$

which means that the stresses are equal to the Lagrangian parameter λ_1 in a weak sense, but not pointwisely. Similarly, inserting equ. (2.92) in the last part of equ. (2.137) leads to:

$$-\bar{\mathbf{D}} = \lambda_2 \tag{2.141}$$

These results for the Lagrange parameters can be inserted into equ. (2.131):

$$\begin{aligned}
\Pi_{HW}(\mathbf{u}, \varphi, \mathbf{E}, \vec{\mathbf{E}}, \mathbf{S}, \vec{\mathbf{D}}) &= \int_{\Omega} \left[W_H(\mathbf{E}, \vec{\mathbf{E}}) + \mathbf{S} : (\mathbf{E}^u - \mathbf{E}) - \vec{\mathbf{D}} \cdot (\vec{\mathbf{E}}^\varphi - \vec{\mathbf{E}}) \right] dV \\
&- \int_{\Omega} \rho_0 \mathbf{b}_0 \cdot \mathbf{u} dV - \int_{\Gamma_s} \hat{\mathbf{t}}_0 \cdot \mathbf{u} dA + \int_{\Omega} \rho_0^{el} \cdot \varphi dV + \int_{\Gamma_{\vec{\mathbf{D}}}} \hat{q}_0 \cdot \varphi dA \\
&+ \int_{\Gamma_u} \mathbf{t}^S \cdot (\hat{\mathbf{u}} - \mathbf{u}) dA + \int_{\Gamma_\varphi} q^{\vec{\mathbf{D}}} \cdot (\hat{\varphi} - \varphi) dA \rightarrow stat. \quad (2.142)
\end{aligned}$$

which is the standard variational functional of Hu-Washizu type known from the literature. However, it should be pointed out, that both \mathbf{S} and $\vec{\mathbf{D}}$ are now redefined and the constitutive equations are only fulfilled in a weak sense. The related first variation of equ. (2.142) is finally:

$$\begin{aligned}
\delta\Pi_{HW} &= \int_{\Omega} \left[\frac{\partial W_H}{\partial \mathbf{E}} : \delta\mathbf{E} + \frac{\partial W_H}{\partial \vec{\mathbf{E}}} \cdot \delta\vec{\mathbf{E}} + \delta\mathbf{S} : (\mathbf{E}^u - \mathbf{E}) - \delta\vec{\mathbf{D}} \cdot (\vec{\mathbf{E}}^\varphi - \vec{\mathbf{E}}) \right] dV \\
&+ \int_{\Omega} [\mathbf{S} : \delta\mathbf{E}^u - \mathbf{S} : \delta\mathbf{E}] dV + \int_{\Omega} [-\vec{\mathbf{D}} \cdot \delta\vec{\mathbf{E}}^\varphi + \vec{\mathbf{D}} \cdot \delta\vec{\mathbf{E}}] dV \\
&- \int_{\Omega} \rho_0 \mathbf{b}_0 \cdot \delta\mathbf{u} dV - \int_{\Gamma_s} \hat{\mathbf{t}}_0 \cdot \delta\mathbf{u} dA + \int_{\Omega} \rho_0^{el} \cdot \delta\varphi dV + \int_{\Gamma_{\vec{\mathbf{D}}}} \hat{q}_0 \cdot \delta\varphi dA \\
&+ \int_{\Gamma_u} \delta\mathbf{t}^S \cdot (\hat{\mathbf{u}} - \mathbf{u}) dA + \int_{\Gamma_\varphi} \delta q^{\vec{\mathbf{D}}} \cdot (\hat{\varphi} - \varphi) dA = 0 \quad (2.143)
\end{aligned}$$

which is equivalent to

$$\begin{aligned}
\delta\Pi_{HW} &= \int_{\Omega} \left[\frac{\partial W_H}{\partial \mathbf{E}} : \delta\mathbf{E} + \frac{\partial W_H}{\partial \vec{\mathbf{E}}} \cdot \delta\vec{\mathbf{E}} + \delta\mathbf{S} : (\mathbf{E}^u - \mathbf{E}) - \delta\vec{\mathbf{D}} \cdot (\vec{\mathbf{E}}^\varphi - \vec{\mathbf{E}}) \right] dV \\
&- \int_{\Omega} [\delta\mathbf{u} \cdot \text{div}(\mathbf{F} \cdot \mathbf{S}) - \text{div} \vec{\mathbf{D}} \delta\varphi + \mathbf{S} : \delta\mathbf{E} - \vec{\mathbf{D}} \cdot \delta\vec{\mathbf{E}} + \rho_0 \mathbf{b}_0 \cdot \delta\mathbf{u} - \rho_0^{el} \cdot \delta\varphi] dV \\
&- \int_{\Gamma_s} (\hat{\mathbf{t}}_0 - \mathbf{t}^S) \cdot \delta\mathbf{u} dA + \int_{\Gamma_{\vec{\mathbf{D}}}} (\hat{q}_0 + \vec{\mathbf{D}} \cdot \mathbf{N}) \cdot \delta\varphi dA \\
&+ \int_{\Gamma_u} \delta\mathbf{t}^S \cdot (\hat{\mathbf{u}} - \mathbf{u}) dA + \int_{\Gamma_\varphi} \delta q^{\vec{\mathbf{D}}} \cdot (\hat{\varphi} - \varphi) dA = 0 \quad (2.144)
\end{aligned}$$

2.9.2.2 Euler Differential Equations

Using the fundamental lemma of calculus of variations, the Euler equations can be derived from equ. (2.143). The obtained field equations are:

$$\operatorname{div}(\mathbf{F} \cdot \mathbf{S}) + \rho_0 \mathbf{b}_0 = 0 \quad \text{in } \Omega \quad (\text{Equilibrium condition}) \quad (2.145)$$

$$\operatorname{div} \vec{\mathbf{D}} - \rho_0^{el} = 0 \quad \text{in } \Omega \quad (\text{Gauss's law}) \quad (2.146)$$

$$\mathbf{E}^u - \mathbf{E} = 0 \quad \text{in } \Omega \quad (\text{kinematic equation}) \quad (2.147)$$

$$\vec{\mathbf{E}}^\varphi - \vec{\mathbf{E}} = 0 \quad \text{in } \Omega \quad (\text{kinematic equation}) \quad (2.148)$$

$$\frac{\partial W_H}{\partial \mathbf{E}} - \mathbf{S} = 0 \quad \text{in } \Omega \quad (\text{constitutive law}) \quad (2.149)$$

$$\frac{\partial W_H}{\partial \vec{\mathbf{E}}} + \vec{\mathbf{D}} = 0 \quad \text{in } \Omega \quad (\text{constitutive law}) \quad (2.150)$$

while the boundary conditions are obtained as:

$$\hat{\mathbf{t}}_0 - \mathbf{F} \cdot \mathbf{S} \cdot \mathbf{N} = 0 \quad \text{on } \Gamma_{\mathbf{S}} \quad (\text{Mechanical natural b/c}) \quad (2.151)$$

$$\hat{q}_0 + \vec{\mathbf{D}} \cdot \mathbf{N} = 0 \quad \text{on } \Gamma_{\vec{\mathbf{D}}} \quad (\text{Electrical natural b/c}) \quad (2.152)$$

$$\hat{\mathbf{u}} - \mathbf{u} = 0 \quad \text{on } \Gamma_{\mathbf{u}} \quad (\text{Mechanical essential b/c}) \quad (2.153)$$

$$\hat{\varphi} - \varphi = 0 \quad \text{on } \Gamma_{\varphi} \quad (\text{Electrical essential b/c}) \quad (2.154)$$

The fields of \mathbf{u} and φ have to be chosen from the Sobolev space $H^1(\Omega)$ in order to provide second power integrable derivatives and continuity at the boundaries. However, \mathbf{E} , $\vec{\mathbf{E}}$, \mathbf{S} and $\vec{\mathbf{D}}$ can be chosen from the Lebesgue space L^2 as the square of the function itself must be integrable while no continuity is required between the subdomains of elements. This means that the related unknowns can be determined and eliminated on the element level via static condensation.

All governing equations are covered in equ. (2.142) and (2.143) in a weak sense, no additional constraint equations are needed. Consequently, all six fields have to be discretized if finite element formulations are derived from this functional. This approach has been adopted e.g. by Sze and Pan [SP99] and Klinkel and Wagner [KW06]. However, this results in a large discretization effort and consequently a large numerical effort.

On the other hand side, satisfying single fields as constraint equations in a strong sense, the number of independent fields can be reduced. Sze and Pan presented in this context degenerated functionals with (\mathbf{u}, φ) , $(\vec{\mathbf{D}}, \mathbf{u}, \varphi)$, $(\mathbf{S}, \mathbf{u}, \varphi)$ and $(\mathbf{S}, \vec{\mathbf{D}}, \mathbf{u}, \varphi)$ as independent fields. However, this approach introduces again locking phenomena (chapter 3.5) and thus can severely reduce the element quality, most visible in the irreducible (\mathbf{u}, φ) -functional.

Thus it would be preferable to derive a functional that covers the advantages of both worlds: The inclusion of the full capacities of the Hu-Washizu functional to eliminate element deficiencies like locking, but also the reduction of the discretized fields to minimize numerical cost. An approach of this type based on the Hu-Washizu functional is presented in the next chapter.

2.9.3 Modified Principle of Hu-Washizu

An interesting alternative of an enhanced finite element formulation has been initially introduced by Simo and Rifai [SR90] in the context of pure mechanical problems with the *Enhanced Assumed Strain (EAS) Method*. The basic idea of the EAS method is the extension of the displacement-dependent strains by so-called *Enhanced Strains* $\tilde{\mathbf{E}}$. These additional assumed strains are introduced in order to eliminate parasitic strains that cause the locking phenomena which decrease the element quality (see chapter 3.5).

Similar to enhanced strains, also enhanced electric field strength terms can be introduced to eliminate related parasitic terms of the electromechanical problem. This approach that applies the idea of the EAS method to the electrical fields of the coupled problem is called *Enhanced Assumed Electrics (EAE) Method* in this work.

2.9.3.1 Derivation from the Hu-Washizu Principle

Starting point of the variational derivation is the principle of Hu-Washizu according to chapter 2.9.2. For the sake of clarity, at first only the internal potential part of equ. (2.143) is investigated:

$$\begin{aligned} \delta\Pi_{HW}^{int} &= \int_{\Omega} \left[\frac{\partial W_H}{\partial \mathbf{E}} : \delta \mathbf{E} + \frac{\partial W_H}{\partial \tilde{\mathbf{E}}} \cdot \delta \tilde{\mathbf{E}} + \delta \mathbf{S} : (\mathbf{E}^u - \mathbf{E}) - \delta \tilde{\mathbf{D}} \cdot (\tilde{\mathbf{E}}^\varphi - \tilde{\mathbf{E}}) \right] dV \\ &+ \int_{\Omega} [\mathbf{S} : \delta \mathbf{E}^u - \mathbf{S} : \delta \mathbf{E}] dV + \int_{\Omega} [-\tilde{\mathbf{D}} \cdot \delta \tilde{\mathbf{E}}^\varphi + \tilde{\mathbf{D}} \cdot \delta \tilde{\mathbf{E}}] dV \end{aligned} \quad (2.155)$$

The enhanced strains are now introduced via re-parameterization of the strain field \mathbf{E} :

$$\mathbf{E} = \frac{1}{2}(\mathbf{F}^T \cdot \mathbf{F} - \mathbf{I}) + \tilde{\mathbf{E}} = \mathbf{E}^u + \tilde{\mathbf{E}} \quad (2.156)$$

Accordingly, also the electric field strength is re-parameterized:

$$\tilde{\mathbf{E}} = -\text{grad } \varphi + \tilde{\tilde{\mathbf{E}}} = \tilde{\mathbf{E}}^\varphi + \tilde{\tilde{\mathbf{E}}} \quad (2.157)$$

Consequently, the original independent fields \mathbf{E} and $\tilde{\mathbf{E}}$ are eliminated. Inserting equ. (2.156) and (2.157) into the functional of equ. (2.155) leads to:

$$\begin{aligned} \delta\Pi_{MHW}^{int}(\mathbf{u}, \varphi, \tilde{\mathbf{E}}, \tilde{\tilde{\mathbf{E}}}, \mathbf{S}, \mathbf{D}) &= \int_{\Omega} \left[\frac{\partial W_H}{\partial \mathbf{E}^u} : \delta \mathbf{E}^u + \frac{\partial W_H}{\partial \tilde{\mathbf{E}}} : \delta \tilde{\mathbf{E}} \right] dV \\ &+ \int_{\Omega} \left[\frac{\partial W_H}{\partial \tilde{\mathbf{E}}^\varphi} \cdot \delta \tilde{\mathbf{E}}^\varphi + \frac{\partial W_H}{\partial \tilde{\tilde{\mathbf{E}}}} \cdot \delta \tilde{\tilde{\mathbf{E}}} \right] dV \\ &+ \int_{\Omega} \left[\delta \mathbf{S} : (-\tilde{\mathbf{E}}) - \delta \tilde{\mathbf{D}} \cdot (-\tilde{\tilde{\mathbf{E}}}) \right] dV \\ &+ \int_{\Omega} [\mathbf{S} : \delta \mathbf{E}^u - \mathbf{S} : \delta (\mathbf{E}^u + \tilde{\mathbf{E}})] dV \\ &+ \int_{\Omega} [-\tilde{\mathbf{D}} \cdot \delta \tilde{\mathbf{E}}^\varphi + \tilde{\mathbf{D}} \cdot \delta (\tilde{\mathbf{E}}^\varphi + \tilde{\tilde{\mathbf{E}}})] dV \end{aligned} \quad (2.158)$$

This equation can be simplified to:

$$\begin{aligned} \delta\Pi_{MHW}^{int}(\mathbf{u}, \varphi, \tilde{\mathbf{E}}, \tilde{\tilde{\mathbf{E}}}, \mathbf{S}, \mathbf{D}) &= \int_{\Omega} \left[\frac{\partial W_H}{\partial \mathbf{E}^u} : \delta \mathbf{E}^u + \frac{\partial W_H}{\partial \tilde{\mathbf{E}}} : \delta \tilde{\mathbf{E}} \right] dV \\ &+ \int_{\Omega} \left[\frac{\partial W_H}{\partial \tilde{\mathbf{E}}^\varphi} \cdot \delta \tilde{\mathbf{E}}^\varphi + \frac{\partial W_H}{\partial \tilde{\tilde{\mathbf{E}}}} \cdot \delta \tilde{\tilde{\mathbf{E}}} \right] dV \\ &- \int_{\Omega} \left[\delta \mathbf{S} : \tilde{\mathbf{E}} - \delta \tilde{\mathbf{D}} \cdot \tilde{\tilde{\mathbf{E}}} + \mathbf{S} : \delta \tilde{\mathbf{E}} - \tilde{\mathbf{D}} \cdot \delta \tilde{\tilde{\mathbf{E}}} \right] dV \quad (2.159) \end{aligned}$$

The enhanced strains $\tilde{\mathbf{E}}$ and the enhanced electric field strength $\tilde{\tilde{\mathbf{E}}}$ are chosen in a way such that they fulfill the orthogonality condition:

$$\int_{\Omega} \mathbf{S} : \tilde{\mathbf{E}} d\Omega = 0 \quad (2.160)$$

$$\int_{\Omega} \tilde{\mathbf{D}} \cdot \tilde{\tilde{\mathbf{E}}} d\Omega = 0 \quad (2.161)$$

The condition of equ. (2.160) makes sure that the existing stresses do not introduce additional work contributions in combination with the additional enhanced strains. Thus it can be avoided that $\tilde{\mathbf{E}}$ introduces new parasitic strains which would lead to additional energy terms and related stiffening effects of the structure. Similarly, equ. (2.161) formulates the electrical counterpart of equ. (2.160). The enhanced electrical field has to be chosen such that no additional energy terms are generated in combination with the existing electric displacement field.

Furthermore, taking advantage of equations (2.160) and (2.161) in equ. (2.159) leads to:

$$\begin{aligned} \delta\Pi_{MHW}^{int}(\mathbf{u}, \varphi, \tilde{\mathbf{E}}, \tilde{\tilde{\mathbf{E}}}) &= \int_{\Omega} \left[\frac{\partial W_H}{\partial \mathbf{E}^u} : \delta \mathbf{E}^u + \frac{\partial W_H}{\partial \tilde{\mathbf{E}}} : \delta \tilde{\mathbf{E}} \right] dV \\ &+ \int_{\Omega} \left[\frac{\partial W_H}{\partial \tilde{\mathbf{E}}^\varphi} \cdot \delta \tilde{\mathbf{E}}^\varphi + \frac{\partial W_H}{\partial \tilde{\tilde{\mathbf{E}}}} \cdot \delta \tilde{\tilde{\mathbf{E}}} \right] dV \quad (2.162) \end{aligned}$$

Recalling equ. (2.91) and (2.92), this can be reformulated such that:

$$\begin{aligned} \delta\Pi_{MHW}^{int}(\mathbf{u}, \varphi, \tilde{\mathbf{E}}, \tilde{\tilde{\mathbf{E}}}) &= \int_{\Omega} \left[\mathbf{S}^{\mathbf{E}^u} : \delta \mathbf{E}^u + \mathbf{S}^{\tilde{\mathbf{E}}} : \delta \tilde{\mathbf{E}} \right] dV \\ &- \int_{\Omega} \left[\tilde{\mathbf{D}}^{\tilde{\mathbf{E}}^\varphi} : \delta \tilde{\mathbf{E}}^\varphi + \mathbf{D}^{\tilde{\tilde{\mathbf{E}}}} : \delta \tilde{\tilde{\mathbf{E}}} \right] dV \quad (2.163) \end{aligned}$$

Summing up, it is obtained for the overall variation of the potential:

$$\begin{aligned} \delta\Pi_{MHW}(\mathbf{u}, \varphi, \tilde{\mathbf{E}}, \tilde{\tilde{\mathbf{E}}}) &= \int_{\Omega} \left[\mathbf{S}^{\mathbf{E}^u} : \delta \mathbf{E}^u + \mathbf{S}^{\tilde{\mathbf{E}}} : \delta \tilde{\mathbf{E}} - \mathbf{D}^{\tilde{\mathbf{E}}^\varphi} : \delta \tilde{\mathbf{E}}^\varphi - \mathbf{D}^{\tilde{\tilde{\mathbf{E}}}} : \delta \tilde{\tilde{\mathbf{E}}} \right] dV \\ &- \int_{\Omega} \rho_0 \mathbf{b}_0 \cdot \delta \mathbf{u} dV - \int_{\Gamma_s} \hat{\mathbf{t}}_0 \cdot \delta \mathbf{u} dA + \int_{\Omega} \rho_0^{el} \cdot \delta \varphi dV + \int_{\Gamma_b} \hat{q}_0 \cdot \delta \varphi dA \\ &+ \int_{\Gamma_u} \delta \mathbf{t}^{\mathbf{S}} \cdot (\hat{\mathbf{u}} - \mathbf{u}) dA + \int_{\Gamma_\varphi} \delta q^{\tilde{\mathbf{D}}} \cdot (\hat{\varphi} - \varphi) dA = 0 \quad (2.164) \end{aligned}$$

It can be observed that the orthogonality conditions of equ. (2.160) and (2.161) have completely eliminated the stress \mathbf{S} and the electric displacement $\vec{\mathbf{D}}$ as independent variable fields in equ. (2.164).

The functional is only dependent from the four fields \mathbf{u} , φ , $\tilde{\mathbf{E}}$ and $\tilde{\tilde{\mathbf{E}}}$. It is also worthwhile to mention that the originally introduced stresses \mathbf{S} and electric displacements $\vec{\mathbf{D}}$ represent in fact independent fields. They are *not* coupled with the strains \mathbf{E} and the electric field strength $\vec{\mathbf{E}}$ via the constitutive equations. The coupling effect of the material law has only been used in the context of the dependent stresses $\mathbf{S}^{\tilde{\mathbf{E}}}$ and $\mathbf{S}^{\tilde{\tilde{\mathbf{E}}}}$ and the dependent electric displacements $\vec{\mathbf{D}}^{\tilde{\mathbf{E}}}$ and $\vec{\mathbf{D}}^{\tilde{\tilde{\mathbf{E}}}}$. This fact will be of importance later in the context of stress and electric displacement recovery in the post-processing of a finite element formulation (see chapter 4.5.3).

2.9.3.2 Derivation as Independent Variational Principle

Besides to the derivation from the Hu-Washizu functional, the modified Hu-Washizu functional can also be considered as independent principle. This idea has already been presented by Bischoff in the context of structural problems [Bis99]. This approach is applicable as well in the context of electromechanical problems. Starting point is the following potential formulation:

$$\begin{aligned} \Pi(\mathbf{u}, \varphi, \mathbf{E}, \vec{\mathbf{E}}) &= \int_{\Omega} \left[W_H(\mathbf{E}, \vec{\mathbf{E}}) dV - \rho_0 \mathbf{b}_0 \cdot \mathbf{u} + \rho_0^{el} \cdot \varphi \right] dV \\ &\quad - \int_{\Gamma_S} \hat{\mathbf{t}}_0 \cdot \mathbf{u} dA + \int_{\Gamma_{\vec{\mathbf{D}}}} \hat{q}_0 \cdot \varphi dA \rightarrow stat. \end{aligned} \quad (2.165)$$

The re-parameterization according to equ. (2.156) and (2.157) can also be stated as:

$$\tilde{\mathbf{E}} := \mathbf{E} - \mathbf{E}^u \quad (2.166)$$

$$\tilde{\tilde{\mathbf{E}}} := \vec{\mathbf{E}} - \vec{\mathbf{E}}^\varphi \quad (2.167)$$

Thus the fields $\tilde{\mathbf{E}}$ and $\tilde{\tilde{\mathbf{E}}}$ actually represent the residua of the two kinematic equations. Similar to the derivation of the principle of Hu-Washizu in chapter 2.9.2.1, the kinematic equations are not introduced into the functional via insertion, but via Lagrangian Multipliers:

$$\begin{aligned} \Pi_{HW}^{mod}(\mathbf{u}, \varphi, \tilde{\mathbf{E}}, \tilde{\tilde{\mathbf{E}}}, \lambda_1, \lambda_2, \mu_1, \mu_2) &= \int_{\Omega} \left[W_H(\mathbf{u}, \varphi, \tilde{\mathbf{E}}, \tilde{\tilde{\mathbf{E}}}) - \lambda_1 : \tilde{\mathbf{E}} - \lambda_2 \cdot \tilde{\tilde{\mathbf{E}}} \right] dV \\ &\quad - \int_{\Omega} \rho_0 \mathbf{b}_0 \cdot \mathbf{u} dV - \int_{\Gamma_S} \hat{\mathbf{t}}_0 \cdot \mathbf{u} dA \\ &\quad + \int_{\Omega} \rho_0^{el} \cdot \varphi dV + \int_{\Gamma_{\vec{\mathbf{D}}}} \hat{q}_0 \cdot \varphi dA \\ &\quad + \int_{\Gamma_u} \mu_1 \cdot (\hat{\mathbf{u}} - \mathbf{u}) dA \\ &\quad + \int_{\Gamma_\varphi} \mu_2 \cdot (\hat{\varphi} - \varphi) dA \rightarrow stat. \end{aligned} \quad (2.168)$$

For comparison reasons, the signs of the terms at λ_1 and λ_2 are chosen to be minus here in order to coincide with the kinematic definitions of the derivation of the Hu-Washizu functional in equ. (2.132) of chapter 2.9.2.1. Performing the first variation of equ. (2.168) leads to:

$$\begin{aligned}
\delta\Pi_{HW}^{mod} &= \int_{\Omega} \left[\frac{\partial W_H}{\partial \mathbf{E}^u} : \delta \mathbf{E}^u + \frac{\partial W_H}{\partial \vec{\mathbf{E}}^\varphi} \cdot \delta \vec{\mathbf{E}}^\varphi + \frac{\partial W_H}{\partial \vec{\mathbf{E}}} : \delta \vec{\mathbf{E}} + \frac{\partial W_H}{\partial \tilde{\vec{\mathbf{E}}}} \cdot \delta \tilde{\vec{\mathbf{E}}} \right] dV \\
&- \int_{\Omega} \left[\delta \lambda_1 : \vec{\mathbf{E}} + \lambda_1 : \delta \vec{\mathbf{E}} + \delta \lambda_2 \cdot \tilde{\vec{\mathbf{E}}} + \lambda_2 \cdot \delta \tilde{\vec{\mathbf{E}}} \right] dV \\
&- \int_{\Omega} \rho_0 \mathbf{b}_0 \cdot \delta \mathbf{u} dV - \int_{\Gamma_s} \hat{\mathbf{t}}_0 \cdot \delta \mathbf{u} dA + \int_{\Omega} \rho_0^{el} \cdot \delta \varphi dV + \int_{\Gamma_B} \hat{q}_0 \cdot \delta \varphi dA \\
&+ \int_{\Gamma_u} \delta \boldsymbol{\mu}_1 \cdot (\hat{\mathbf{u}} - \mathbf{u}) dA + \int_{\Gamma_\varphi} \delta \boldsymbol{\mu}_2 \cdot (\hat{\varphi} - \varphi) dA = 0
\end{aligned} \tag{2.169}$$

Using the product rule and the divergence theorem one can state:

$$\begin{aligned}
\int_{\Omega} \frac{\partial W_H}{\partial \mathbf{E}^u} : \delta \mathbf{E}^u &= \int_{\Gamma_s} \mathbf{F} \cdot \frac{\partial W_H}{\partial \mathbf{E}^u} \cdot \mathbf{N} \cdot \delta \mathbf{u} dA - \int_{\Omega} \delta \mathbf{u} \cdot \operatorname{div} \left(\mathbf{F} \cdot \frac{\partial W_H}{\partial \mathbf{E}^u} \right) dV \\
&= \int_{\Gamma_s} \mathbf{t}^u \cdot \delta \mathbf{u} dA - \int_{\Omega} \delta \mathbf{u} \cdot \operatorname{div} (\mathbf{F} \cdot \mathbf{S}^u) dV
\end{aligned} \tag{2.170}$$

$$\begin{aligned}
\int_{\Omega} \frac{\partial W_H}{\partial \vec{\mathbf{E}}^\varphi} \cdot \delta \vec{\mathbf{E}}^\varphi &= - \int_{\Gamma_B} \frac{\partial W_H}{\partial \vec{\mathbf{E}}^\varphi} \cdot \mathbf{N} \cdot \delta \varphi dA + \int_{\Omega} \delta \varphi \cdot \operatorname{div} \left(\frac{\partial W_H}{\partial \vec{\mathbf{E}}^\varphi} \right) dV \\
&= - \int_{\Gamma_B} q^\varphi \cdot \delta \varphi dA + \int_{\Omega} \delta \varphi \cdot \operatorname{div} (-\vec{\mathbf{D}}) dV
\end{aligned} \tag{2.171}$$

Thus using equ. (2.170) and (2.171) in equ. (2.169) leads to:

$$\begin{aligned}
\delta\Pi_{HW}^{mod} &= \int_{\Omega} \left[\frac{\partial W_H}{\partial \vec{\mathbf{E}}} : \delta \vec{\mathbf{E}} + \frac{\partial W_H}{\partial \tilde{\vec{\mathbf{E}}}} \cdot \delta \tilde{\vec{\mathbf{E}}} \right] dV \\
&- \int_{\Omega} \left[\delta \mathbf{u} \cdot \operatorname{div} (\mathbf{F} \cdot \mathbf{S}^u) + \delta \varphi \cdot \operatorname{div} \vec{\mathbf{D}} \right] dV \\
&- \int_{\Omega} \left[\delta \lambda_1 : \vec{\mathbf{E}} + \lambda_1 : \delta \vec{\mathbf{E}} + \delta \lambda_2 \cdot \tilde{\vec{\mathbf{E}}} + \lambda_2 \cdot \delta \tilde{\vec{\mathbf{E}}} \right] dV \\
&- \int_{\Omega} \rho_0 \mathbf{b}_0 \cdot \delta \mathbf{u} dV + \int_{\Omega} \rho_0^{el} \cdot \delta \varphi dV \\
&- \int_{\Gamma_s} (\hat{\mathbf{t}}_0 - \mathbf{t}^u) \cdot \delta \mathbf{u} dA + \int_{\Gamma_B} (\hat{q}_0 - q^\varphi) \cdot \delta \varphi dA \\
&+ \int_{\Gamma_u} \delta \boldsymbol{\mu}_1 \cdot (\hat{\mathbf{u}} - \mathbf{u}) dA + \int_{\Gamma_\varphi} \delta \boldsymbol{\mu}_2 \cdot (\hat{\varphi} - \varphi) dA = 0
\end{aligned} \tag{2.172}$$

Based on the fundamental lemma in calculus of variations, it can be derived:

$$\operatorname{div} (\mathbf{F} \cdot \mathbf{S}^u) + \rho_0 \mathbf{b}_0 = 0, \quad \operatorname{div} (\vec{\mathbf{D}}^\varphi) - \rho_0^{el} = 0 \quad \text{in } \Omega \tag{2.173}$$

$$\vec{\mathbf{E}} = 0, \quad \tilde{\vec{\mathbf{E}}} = 0 \quad \text{in } \Omega \tag{2.174}$$

$$\frac{\partial W_H(\mathbf{u}, \varphi, \tilde{\mathbf{E}}, \tilde{\tilde{\mathbf{E}}})}{\partial \tilde{\mathbf{E}}} = \lambda_1, \quad \frac{\partial W_H(\mathbf{u}, \varphi, \tilde{\mathbf{E}}, \tilde{\tilde{\mathbf{E}}})}{\partial \tilde{\tilde{\mathbf{E}}}} = \lambda_2 \quad \text{in } \Omega \quad (2.175)$$

$$\hat{\mathbf{t}}_0 - \mathbf{t}^u = 0 \quad \text{on } \Gamma_S, \quad \hat{q}_0 - q^\varphi = 0 \quad \text{on } \Gamma_{\tilde{\mathbf{D}}} \quad (2.176)$$

$$\hat{\mathbf{u}} - \mathbf{u} = 0 \quad \text{on } \Gamma_u, \quad \hat{\varphi} - \varphi = 0 \quad \text{on } \Gamma_\varphi \quad (2.177)$$

At this stage, in total ten Euler equations are obtained. Analogously to the approach in chapter 2.9.2.1, the Lagrange parameters can be identified now.

It can be observed that the Lagrange parameters μ_1 and μ_2 are serving again as test functions for the kinematic field equations and drop out in the derivation of the Euler equations. Just like in chapter 2.9.2.1, μ_1 is assigned to be the stress resultant vector \mathbf{t}^S , and μ_2 is replaced by the dependent charge $q^{\tilde{\mathbf{D}}}$ resulting from the electric displacement.

Considering the units in the Euler equations, λ_1 can be identified with the stress tensor:

$$\mathbf{S} := \lambda_1 \quad (2.178)$$

However, as the stress tensor is already defined via the constitutive law, this has to be considered as a redefinition of the stresses. The constitutive law is fulfilled by \mathbf{S} now only in a weak sense any more. Similarly, it can be deduced:

$$-\tilde{\mathbf{D}} = \lambda_2 \quad (2.179)$$

which accordingly leads to a weak formulation in the second part of the constitutive law. Summing up, the derivation as an independent variational principle leads to a concise identification of the Lagrangian parameters. Inserting the Lagrangian parameters according to equ. (2.178) and (2.179) into the functional according to equ. (2.169), we end up again in the same result as in the direct derivation approach from the Hu-Washizu principle in equ. (2.159) in chapter 2.9.3.1.

The use of the orthogonality conditions according to equ. (2.160) and (2.161) has been intentionally postponed in the derivation of this chapter in order to maintain all equations needed to determine the Lagrangian parameters. Using the orthogonality conditions with the knowledge about the Lagrangian parameters leads again to equ. (2.164) or the equivalent representation:

$$\begin{aligned} \delta \Pi_{HW}^{int}(\mathbf{u}, \varphi, \tilde{\mathbf{E}}, \tilde{\tilde{\mathbf{E}}}) &= \int_{\Omega} \left[\frac{\partial W_H}{\partial \tilde{\mathbf{E}}} : \delta \tilde{\mathbf{E}} + \frac{\partial W_H}{\partial \tilde{\tilde{\mathbf{E}}}} : \delta \tilde{\tilde{\mathbf{E}}} \right] dV \\ &\quad - \int_{\Omega} \left[\delta \mathbf{u} \cdot \text{div}(\mathbf{F} \cdot \mathbf{S}^u) + \delta \varphi \cdot \text{div} \tilde{\mathbf{D}}^\varphi \right] dV \\ &\quad - \int_{\Omega} \rho_0 \mathbf{b}_0 \cdot \delta \mathbf{u} dV + \int_{\Omega} \rho_0^{el} \cdot \delta \varphi dV \\ &\quad - \int_{\Gamma_S} (\hat{\mathbf{t}}_0 - \mathbf{t}^u) \cdot \delta \mathbf{u} dA + \int_{\Gamma_{\tilde{\mathbf{D}}}} (\hat{q}_0 - q^\varphi) \cdot \delta \varphi dA \\ &\quad + \int_{\Gamma_u} \delta \mathbf{t}^S \cdot (\hat{\mathbf{u}} - \mathbf{u}) dA + \int_{\Gamma_\varphi} \delta q^{\tilde{\mathbf{D}}} \cdot (\hat{\varphi} - \varphi) dA = 0 \end{aligned} \quad (2.180)$$

2.9.3.3 Euler Differential Equations

Similar to the approach in chapter 2.9.2, now the Euler differential equations can be derived. Using the fundamental lemma of calculus of variations, the Euler equations can be derived from equ. (2.164). The obtained field equations are:

$$\operatorname{div}(\mathbf{F} \cdot \mathbf{S}^u) + \rho_0 \mathbf{b}_0 = 0 \quad \text{in } \Omega \quad (2.181)$$

$$\operatorname{div} \vec{\mathbf{D}}^\varphi - \rho_0^{el} = 0 \quad \text{in } \Omega \quad (2.182)$$

$$\frac{\partial W_H}{\partial \vec{\mathbf{E}}} = \mathbf{S}^{\vec{\mathbf{E}}} = 0 \quad \text{in } \Omega \quad (2.183)$$

$$\frac{\partial W_H}{\partial \vec{\tilde{\mathbf{E}}}} = \vec{\mathbf{D}}^{\vec{\tilde{\mathbf{E}}}} = 0 \quad \text{in } \Omega \quad (2.184)$$

The equations (2.181) and (2.182) contain in a mixed form the constitutive laws and conservation laws. Equation (2.183) contains the consequence of the orthogonality condition of equ. (2.160): The stress \mathbf{S} and the enhanced strains $\vec{\mathbf{E}}$ must not contain any energy conjugated contributions. Thus any stress $\mathbf{S}^{\vec{\mathbf{E}}}$ resulting from enhanced strains must vanish. For the same reasons the enhanced electric displacements $\vec{\mathbf{D}}^{\vec{\tilde{\mathbf{E}}}}$ must vanish according to equ. (2.184). Besides to that, the kinematic equations have been defined a priori via equ. (2.166) and (2.167):

$$\vec{\mathbf{E}} = 0 \quad \text{in } \Omega \quad (\text{kinematic equation}) \quad (2.185)$$

$$\vec{\tilde{\mathbf{E}}} = 0 \quad \text{in } \Omega \quad (\text{kinematic equation}) \quad (2.186)$$

These equations might be surprising at the first glance as they postulate the vanishing of the enhanced fields. The reason is that so far no discretization has been performed yet. For the continuous problem, it makes indeed sense to require all strains and electric field strengths to be of compatible type with respect to displacements and electric potential. Only at the case of the discretized problem the enhanced strains $\vec{\mathbf{E}}$ and the enhanced electric field strength $\vec{\tilde{\mathbf{E}}}$ is indeed introduced in order to enrich the element formulation and eliminate the locking phenomena (chapter 3.5).

Last but not least, the boundary conditions are obtained from equ. (2.164) as:

$$\hat{\mathbf{t}}_0 - \mathbf{t}^u = 0 \quad \text{on } \Gamma_S \quad (\text{Mechanical natural b/c}) \quad (2.187)$$

$$\hat{q}_0 - q^\varphi = 0 \quad \text{on } \Gamma_D \quad (\text{Electrical natural b/c}) \quad (2.188)$$

$$\hat{\mathbf{u}} - \mathbf{u} = 0 \quad \text{on } \Gamma_u \quad (\text{Mechanical essential b/c}) \quad (2.189)$$

$$\hat{\varphi} - \varphi = 0 \quad \text{on } \Gamma_\varphi \quad (\text{Electrical essential b/c}) \quad (2.190)$$

which coincide with the results of the original Hu-Washizu principle in chapter 2.9.2. Summing up, the modified Hu-Washizu functional allows for the elimination of the stress tensor as well as the electric displacement vector. This is also favorable in the context of finite element development, as less fields have to be discretized and thus the computational efficiency is increased.

2.9.4 Overview

In the previous sections, the principle of virtual work (chapter 2.9.1), the Hu-Washizu functional (chapter 2.9.2) and the modified Hu-Washizu principle (chapter 2.9.3) have been presented as possible variational formulations to derive finite element formulations. In general, many more functionals can be derived dependent from the type and number of the independent field variables. These functionals represent all combinations of strong and weak fulfillment of the field equations and the boundary conditions. For example, also the principle of Hellinger-Reissner [Hel14, Rei50] is used for the design of enhanced elements. Besides to contributions with pure mechanical focus [PC82, PS84], also some Hellinger-Reissner-based elements for electromechanical problems have been presented [ZZF03, SYY04].

Table 2.3 provides an overview of the variational formulations. From the principle of virtual work up to the Hu-Washizu functional the number of independent variable fields is increasing which leads to growing flexibility of the possible element formulations, as the approximation of the independent fields can be done independently from each other in the discretization process.

Variational principle:	Variables:	Euler equations: (weak formulation)	Constraint equations: (fulfilled pointwisely)
Virtual Work	\mathbf{u}, φ	- equilibrium - static b/c	- kinematic field equ. - constitutive equ. - kinematic b/c
Hellinger-Reissner	$\mathbf{u}, \varphi, \mathbf{S}, \vec{\mathbf{D}}$	- equilibrium - kinematic field equ. - static b/c - kinematic b/c	- constitutive equ.
Hu-Washizu	$\mathbf{u}, \varphi, \mathbf{S}, \vec{\mathbf{D}}, \mathbf{E}, \vec{\mathbf{E}}$	- equilibrium - kinematic field equ. - constitutive equ. - static b/c - kinematic b/c	

Table 2.3: Variational principles and their strongly and weakly formulated contributions.

In general it can be stated that *mixed formulations* with an extended number of independent fields are computationally more expensive than so-called *single-field formulations* based on the principle of virtual work. In this context, so-called *hybrid-mixed formulations* are advantageous. Starting from a multi-field functional, additional degrees of freedom are already eliminated on the element level via static condensation. With this approach, the global number of degrees of freedom can be reduced to the number of a corresponding single-field formulation. Thus the computational overhead compared to single-field

formulations can be reduced to the construction of the additional element matrices and the static condensation. Several common methods for enhanced elements like the EAS method and EAE method (chapter 4.5.3) are based on these hybrid-mixed formulations.

Chapter 3

Fundamentals of the Finite Element Method

The basis for the derivation of finite elements is given by the functionals as introduced in chapter 2.9. This chapter is meant to provide selected aspects that are relevant in the focus of this work. Thus it is by no means a general introduction into the finite element method. Detailed information to the fundamentals of the finite element method can be found e.g. at Zienkiewicz and Taylor [ZTZ05, ZT05], Hughes [Hug00] and Bathe [Bat02].

3.1 Discretization

From the mathematical point of view, the finite element method is a numerical approximation method for the solution of partial differential equations of elliptic type. For mechanical problems of arbitrary geometry and arbitrary natural and essential boundary conditions, a continuous and exact solution of the underlying differential equations is in general not available.

Consequently numerical solution schemes are adopted that discretize the problem formulation. Discretization means the transformation of the continuous mathematical model into a discrete problem with a finite number of unknowns (degrees of freedom). Focus of this work is the spatial discretization which is performed for both electrical and mechanical fields with the finite element method. Other common spatial discretization schemes are the boundary element method (BEM), the finite difference method (FDM), the finite volume method (FVM), spectral methods and meshfree methods.

In the context of the finite element method, spatial discretization means the decomposition of the domain Ω into subdomains Ω^e , the *elements*. In this context, not only the geometry, but also the displacement field and the electric potential field of these subdomains are approximated. This is done via the calculation of the respective values at discrete nodal points while the values in between are obtained by interpolation via shape functions N^k .

The specific finite element formulation has fundamental influence on the quality of the finite element calculation results. The essential requirements for a finite element are [Kos04]:

- Reliability (robustness, stability).
- Efficiency (high exactness at low computational effort).
- Flexibility (large application field).

These are competing requirements that have to be met at the same time and in a satisfying manner.

The calculation of arbitrary structures rises the question for suitable finite elements. The abundance of existing finite element formulations can be assigned to two general families of elements: *continuum elements* and *structural elements* (see also chapter 1.2.2). Continuum elements open the larger application field due to their universality. They are the best choice for massive models or models without clear geometric structure. They result from subdivision of the 1d-, 2d- or 3d-continuum. A disadvantage is the rather difficult interpretation of results, as no structural orientation (like thickness direction) and no engineering-relevant measures like stress resultants are shipped with the element formulation. Structural elements resemble fabricated structural components like bars, trusses, beams, plates and shells. The basic difference to continuum elements are additional assumptions with respect to deformation and stress states. In other words: Structural elements can be derived from continuum elements by additional kinematic and stress-related restrictions. The development of structural elements is driven by the idea to condense the complex three-dimensional description to the essential components of structural response, like stretching, bending, shear, and so on. The use of structural elements has two essential advantages:

- The number of degrees of freedom and thus the computational effort is considerably reduced compared to continuum elements.
- The results allow for a direct interpretation of the results. The mechanical insight and the consideration of possible boundary conditions is considerably facilitated.

Focus of this work is put on the development of a new enhanced shell element. The development of shell elements goes - just like in the case of any other structural element development - through the stages of mechanical model, mathematical model and finally numerical model. The final shell element is influenced by the decisions at the setup of the original mechanical model as well as all assumptions that are taken during these stages of the model. In this context, one has to distinguish between assumptions of the shell model on the one hand side and assumptions and decisions of the discretization on the other hand side. The first group relates to assumptions for the derivation of the governing equations of the continuum shell theory. The second group relates to possible errors that are introduced due to the discretization of the finite element. However, the latter errors due to discretization can be eliminated via mesh refinement, while the assumptions and possible restrictions of the shell model remain.

3.2 Convergence

First of all, of course, the assumed mathematical model should capture the physics in a reasonable manner. Considering that as a precondition, the fundamental idea for the application of the finite element method is the requirement of convergence: The finite element solution shall approach the analytical solution of the mathematical model if the FE mesh is refined and thus the element size approaches zero.

In order to perform a detailed description of the requirements of convergence, the *variational index* has to be defined first. Let $\Pi(\mathbf{u}_{tot})$ be the energy functional that the considered finite element discretization is based on. Let also \mathbf{u}_{tot} be the vector of all primary variables with m as the highest (spatial) derivative order of \mathbf{u}_{tot} that appears in the energy functional Π . Then m is called variational index.

The requirements for convergence of displacement-based elements can be broken down to the following requests for the element formulation and in particular the chosen shape functions [Fel04, Fis07]:

- *Completeness*: The set of shape functions must be able to exactly represent all polynomial terms up to order m , where m is the variational index of the problem. The set of shape functions is then called m -complete.
- *Compatibility*: The shape functions must guarantee continuity of the primary variables between the elements. As a consequence, material gaps and interpenetrations can be excluded for the deformed state.
- *Correct Rank*: The stiffness matrix must provide the correct rank which means that it must not possess any zero-energy mode other than rigid body modes. In other words: No unphysical zero energy modes may exist.
- *Positive Jacobian Determinant*: Characterizing the local metrics of the natural element coordinate system, the Jacobian determinant represents a measure for element distortion and thus for mesh quality. The requirement of a positive Jacobian in every point of the element excludes excessive element distortion which would result in self penetration of the geometry.

If the requirements for completeness and compatibility are satisfied, the so-called *consistency* condition between discrete and mathematical model is given (see also Figure 3.1). Besides to that, the correct rank of the stiffness matrix and a positive Jacobian determinant contribute to the property of *stability* of the finite element model. In particular, stability with respect to external loads is required. This means that small variations in the external loads are only allowed to result in finite variations in the primary variables (i.e. displacements or electric voltages in the context of this work). The request of stability addresses e.g. unphysical zero-energy modes that must be avoided.

According to the theorem of Lax-Wendroff, which originally addresses the method of

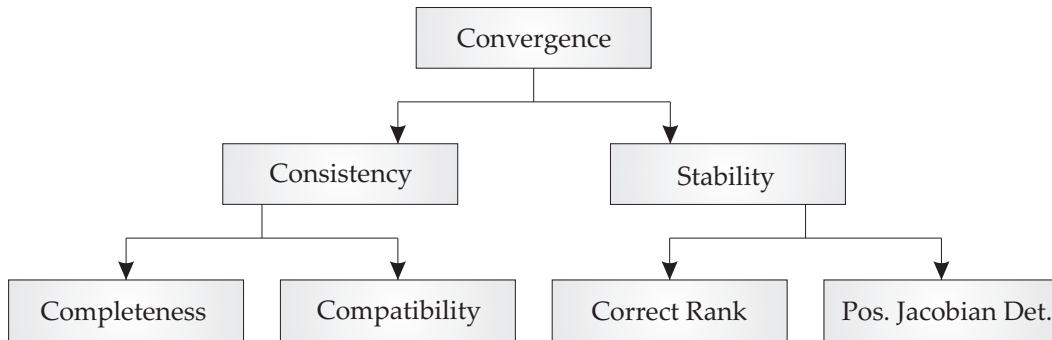


Figure 3.1: Convergence requirements for finite element shape functions.

finite differences for fluid mechanics [LW60], completeness and stability result in the wanted property of convergence.

However, completeness is the only necessary condition for convergence. The compatibility is actually not a necessary condition for convergence in any case. An exception is e.g. provided with the method of incompatible modes [WTDG73]. And there are also numerically unstable elements used in special situations, e.g. for the modeling of local singularities [Fel04]. Nevertheless, the list of requirements according to table 3.1 provides a sufficient condition for convergence and thus a good guideline for finite element design.

3.3 Rank of the System Matrix

As discussed in the chapter before, the correct rank of the system matrix is a fundamental prerequisite for the stability of the element formulation. The correct rank of the element system matrix \mathbf{K}_e is denoted with rank_c and can be determined with:

$$\text{rank}_c(\mathbf{K}_e) = n_{DOF} - n_{RBM} \quad (3.1)$$

where n_{DOF} is the number of element degrees of freedom and n_{RBM} is the number of rigid body modes. If an element delivers a system matrix of correct rank, then the rigid body modes represent the only zero energy modes. In the case of a statically determinate support condition, no inner kinematics are arising. In order to guaranty the stability of the overall element grouping, each element should show the correct rank of the element system matrix. As a consequence, also the assembled global system matrix is of correct rank.

In the case of a too low rank, singular equation systems can arise. In the contrary, if the correct rank is exceeded, rigid body motions cannot be represented without energy contributions which severely compromises convergence.

However, there are cases where elements of too low rank form a global system matrix of correct rank: *Non-communicable zero energy modes* are indeed zero energy modes of the

single element, but they are stabilized due to neighboring elements in a suitable element grouping (see Figure 3.2).

In contrast to that, communicable zero energy modes also arise in element groupings. As a consequence, the well-known *hourglass modes* can arise in the deformation. Other common namings in the literature are *keystoning*, *kinematic modes* oder *mesh instability*. Communicable zero energy modes in general prevent a successful finite element calculation, as the system is either not solvable due to singularities, or the system solution is dominated by the wrong zero energy mode contributions in the solution field.

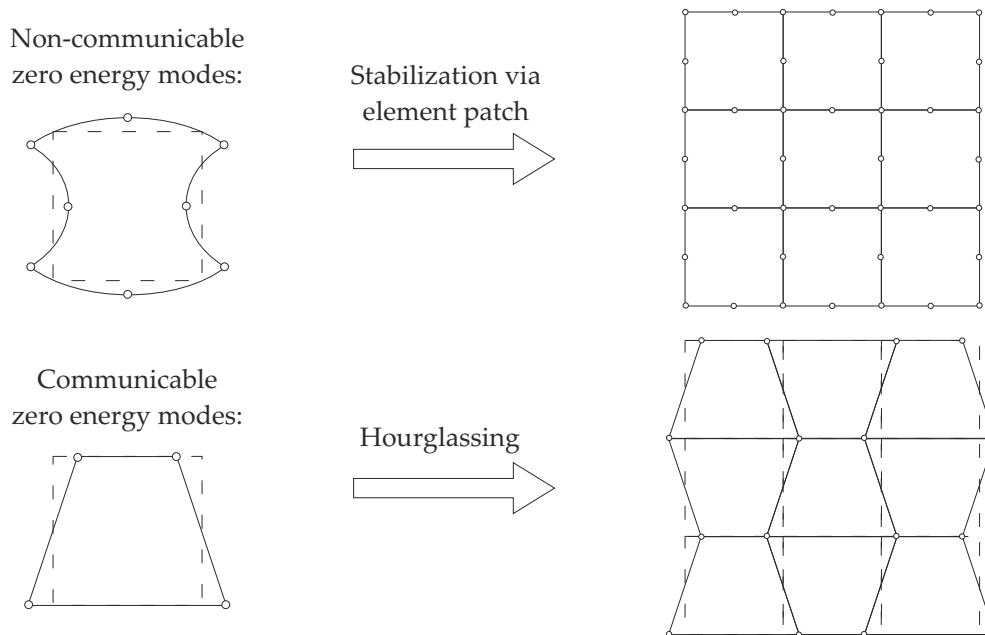


Figure 3.2: Types of zero energy modes (ZEM).

For proper element definitions based on the functionals described in chapter 2.9 with complete numerical integration, no unwanted zero energy modes are to be expected. However, enhanced element formulations based on reduced integration (see chapter 3.6.1) can lead to losses in the system matrix rank and thus to element stability problems.

3.4 The Patch Test

The patch test in its original form has been introduced by Irons in 1966 [Iro66b]. From then on, a large number of variants have been evolved and it became a key tool to test advanced finite element formulations [ZTZ05]. Also specialized patch tests for piezoelectric elements have been proposed [KW06], [Leg11]. The patch test has been introduced as a mean to easily verify the convergence of a finite element formulation to the correct result. It examines at an patch of (arbitrary) distorted elements if a constant distribution of the state fields can be correctly reproduced. The element passes the standard patch test if the

finite element solution is the same as the exact solution. The underlying idea of the patch test is that elements that can exactly reproduce constant states and rigid body movements should be able to reproduce any kind of state if the mesh is fine enough. Additionally, it also allows for an analytical investigation besides to the numerical verification.

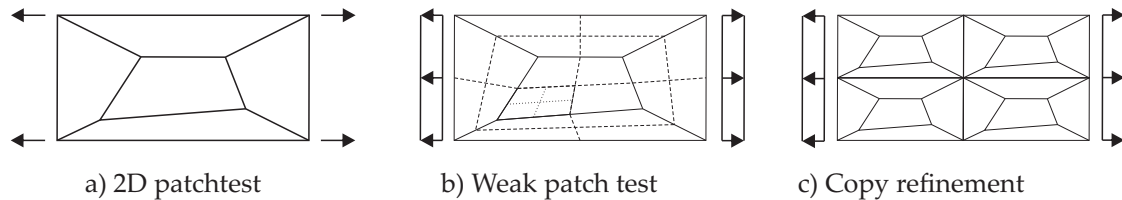


Figure 3.3: Patch test meshes.

For completeness it should be mentioned that there are also one-element patch tests which adopt additional assumptions in order to reduce the original patch test to one element. Bergan and Hanssen developed the so called *Individual Element Test (IET)* which can be carried out directly on the stiffness relations of one element [BH76]. The very intuitive physical idea behind this test is that the boundary forces of neighboring elements must cancel out each other in a uniform stress state. The passing of the IET is a sufficient condition for passing the standard patchtest. Beside to that, Taylor et al. [TZSC86] present the *Single Element Test (SET)* to track possible zero energy modes that might be hidden when several elements are assembled.

The *weak patch test* checks if the element can pass the standard patch test at least for increasing mesh refinement. Here the mesh of the standard patch test is refined by recursively cutting between the midpoints of the element edges such that each element results in four new elements (Figure 3.3 b). This results into elements that turn into a parallelogram shape for increasing refinement [Kos04]. This patch test is e.g. also passed by the non-conforming elements introduced by Wilson [WTDG73]. However, if the mesh refinement is performed by copying of the original mesh as shown in Figure 3.3 c, the patch test is not passed by elements that don't pass the standard patch test.

Focus of this work is put on *multielement tests* (Figure 3.4), where a set of at least two elements (patch) are examined such that also possible incompatibility effects at the common edge or surface between the elements can be investigated. In general, the patch can also contain elements of different type to test element mixability (*heterogeneous patch test*). In contrast to that, *homogeneous patch tests* only use elements of same formulation type as well as same material properties. The homogeneous multielement patch test can be further subdivided into subgroups: At the *displacement patch test*, Dirichlet boundary conditions are applied to the patch and it is investigated if constant strain and rigid body modes are reproduced correctly. In the context of piezoelectric elements, additionally the correct representation of a constant electric field state can be examined (see also chapter 7.1.4). At the *force patch test*, Neumann boundary conditions are applied to verify if the patch can exactly reproduce constant stress and electric displacement states. However, a minimum number of Dirichlet boundary conditions has to be applied in order to elimi-

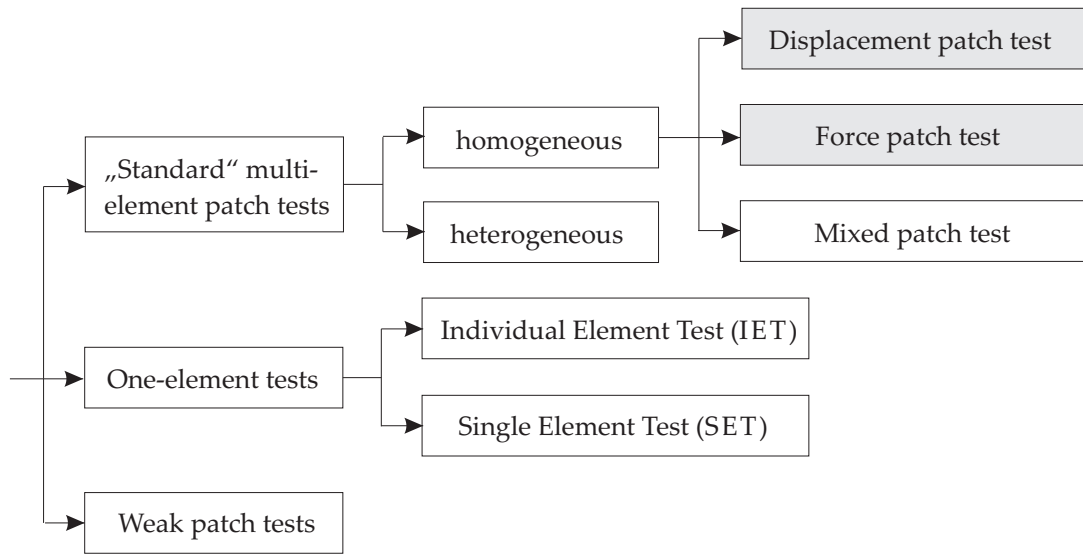


Figure 3.4: Overview of the patch test variants (gray: applied variants to test the presented element).

nate rigid body motions. Besides to that, there are also *mixed patch tests* that combine both force and displacement boundary conditions (beyond rigid body mode preventions).

The basic idea behind the patch test is that "a good element must solve simple problems exactly whether individually, or as component of arbitrary patches" [Fel06]. And if the element can reproduce constant states and rigid body motions correctly, it should be able to approximate any solution state if the mesh is fine enough. Nevertheless, it has been shown that the passing of the patch test is neither a necessary nor a sufficient condition for convergence [Bis99, Kos04]. Instead, it is dependent from the specific patch test and the specific element formulation with its underlying theory. For several beam, plate and shell element formulations a failing in the patch test can be permissible without losing convergence. However, these elements must provide stiffness relations that are dependent from the element slenderness to maintain convergence to the correct solution. This necessitates suitable methods like stabilization techniques (see e.g. [LSV93]). For all cases where the thickness is just a scaling parameter for the stiffness, the patch test must be passed and thus represents a necessary condition for convergence. And there are elements like the purely displacement-based 8-noded hexahedron that passes the tension patch test but severely suffers from diverse locking phenomena [Fis07] such that the low convergence rate prevents from a practical use with reasonable numerical effort.

Summing up, a passing of the patch test can be considered as a fundamental quality attribute and shall be targeted in finite element design. However, a combination of several patch test types is reasonable, and it should be supplemented with further element benchmark examples in order to guarantee not only convergence but also a reasonable convergence rate.

3.5 Locking and Incompatible Approximation Spaces

3.5.1 Introduction

Already in the 60ies of the last century, it has been discovered that irreducible finite element formulations deliver in some cases very inexact results or converge only very slowly to the correct result. B. Fraeijs de Veubeke discovered this already in 1965 at 3-noded triangular elements and 4-noded quadrilateral elements [dV65].

First suggestions for the element enhancement were driven by the idea of the increase of the order of the basis functions [Iro66a]. This turned out to be a reasonable means against locking in many cases, however the actual reasons for the locking effects remained unexplored. In 1973, for the first time a solution strategy for elements with low order of basis functions has been presented by Doherty, Wilson and Taylor. Their approach, the *method of the incompatible modes* [WTDG73], has initially been discussed in a very controversial manner. However, it formed the basis of the later EAS method.

The term *locking* goes back to the association that the element *locks* itself against displacements. The term established itself only in the mid-seventies to describe the phenomenon that leads to a strong underestimation of the displacements or strong overestimation of the structural stiffness at the finite element calculation. In 1985, the publication of suitable test examples by MacNeal und Harder [MH85] as well as by Belytschko et al. [BSL⁺85] established a cornerstone of the further finite element development: This allowed for a posteriori checks of finite elements with respect to their liability to the different locking phenomena.

Nevertheless, the focus stayed on the avoidance of locking and the definition of new element formulations, while the theoretical foundations and reasons of locking still stayed unexplored. Only in 1992, Babuska und Suri published a comprehensive analysis and systematic characterization of the locking effects [BS92]. Babuska und Suri [BS92] identified the dependency of the solution from a *critical parameter* as fundamental property of every locking phenomenon: For a fixed mesh density the locking-induced error increases steadily if the critical parameter approaches its critical value $\lambda \rightarrow \lambda_{crit}$. Thus locking can also be defined as reduced convergence rate in dependence of a critical parameter.

For reasons of clearness, this chapter makes recourse to 1D- and 2D-examples to provide a deeper insight into the causes of locking and highlight solution strategies to eliminate related element deficiencies. Furthermore, linearized strain and stress measures are assumed throughout this section. However, the gained insight is clearly utilizable in the context of the advanced composite shell element presented in chapter 4.

3.5.2 Interpretation of Locking

Different point of views contribute to a comprehensive interpretation of locking. Three different views are presented in the sequel to provide the basis for an investigation of both mechanical and electromechanical locking effects in chapter 3.5.3 and 3.5.4. For further

details to the three presented point of views of locking the reader is kindly referred to Bischoff and Koschnick [Bis05, Kos04].

3.5.2.1 Mechanically Motivated Point of View

The most intuitive way to interpret locking is the mechanically motivated point of view: The locking effect is explained with the unwanted existence of parasitic stresses. Parasitic means here that these contributions do not exist in the analytical solution but only in the discrete solution. The resulting parasitic contributions to the overall internal energy lead to additional, artificial stiffness. As a consequence, also the primary variables are affected after the solution of the underlying equation system.

With increasing rate of parasitic stiffness, the overall mechanical behavior is dominated by the locking effect and the results are useless.

The drawback of the mechanically motivated point of view is the rather arbitrary and unreliable identification of parasitic strains or stresses. Linear triangular elements for example are free of parasitic stresses but exhibit severe stiffening defects [Fis07].

However, the interpretation of the stiffening effects as the existence of parasitic stresses also led to the development of a lot of enhanced element formulation techniques, e.g. the method of reduced integration (chapter 3.6.1), the assumed natural strain method (chapter 3.6.2) or the enhanced assumed strain method (chapter 3.6.3).

3.5.2.2 Mathematical Point of View

From a mathematical point of view, the ill-conditioning of the system of partial differential equations is analyzed. Thus the analysis of locking effects is based on the convergence properties of the underlying functional. The term *locking* is rarely used in mathematically oriented literature. An important contribution has been made by Babuska und Suri with their comprehensive analysis characterization of the locking effects [BS92].

In the mathematical context, the Céa's lemma can be used for error estimation and convergence evaluation [Bra97]. The Céa's lemma provides an upper bound for the error of elements of irreducible form. However, as it assumes structured meshes, it does not account for mesh distortion effects. Thus the element-dependent sensitivity to mesh distortions must be investigated separately.

Again the critical parameter λ_{crit} can be identified as measure that triggers the convergence behavior: With $\lambda \rightarrow \lambda_{crit}$, the ratio between the stiffness terms in the discretized equation system strongly increases. This leads to a dominant behavior of the parasitic terms (see also section 3.5.2.1).

Furthermore, it is important to verify if the variational formulation of the element under consideration has an *unique* solution. A common approach in the context of irreducible element formulations is here the inf-sup condition (see e.g. Braess [Bra97] or Bischoff [Bis99]). Combining the verification of the continuity condition and the verification of

the inf-sup condition which proves the V-ellipticity of the functional, the existence of a unique solution can be proven.

In the context of multi-field functionals, the inf-sup condition is not enough. Instead, the *Babuska-Brezzi condition* has to be examined which goes back to the work of Babuska and Azis [BA72] as well as Brezzi [Bre74]. A short and clear introduction to the Babuska-Brezzi condition can be found at Braess [Bra97] and Bischoff [Bis99].

All in all, the mathematical point of view focuses on the proof of stability and convergence of the element formulation. However, the mechanical background of the problem is not under investigation.

3.5.2.3 Numerical Point of View

Last but not least, the third point of view to interpret locking effects is the numerical one suggested by Hughes [Hug00]. To do so, a *constraint ratio* is defined:

$$r = \frac{n_{eq}}{n_c} = \frac{n_{nodes} \cdot n_{dof}}{n_c} \quad (3.2)$$

where n_{eq} describes the overall number of degrees of freedom that contribute to the constraint equations under consideration. Furthermore, n_c denotes the number of system constraints, like the Bernoulli- or Kirchhoff-condition for beams and plates (in the context of transverse shear locking) or the incompressibility condition of solid elements (in the context of volumetric locking).

However, the definition of r according to equ. (3.2) introduces a discretization dependency. Thus an infinitely large, structured mesh is assumed to derive conclusions for a single element. Under these conditions, the ratio of node number to element number is determined for different element types. Examples of 2d-elements are given in table 3.1.

Linear triangular elements:	$n_{nodes}^3 = \frac{1}{2}$
Bilinear quadrilateral elements:	$n_{nodes}^4 = 1$
Quadratic triangular elements:	$n_{nodes}^6 = 2$
Bi-quadratic quadrilateral elements:	$n_{nodes}^9 = 4$

Table 3.1: Ratio of node number to element number [Kos04].

In the case of numerical integration, the number of constraint equations is determined by the number of Gaussian points as the constraint equations are only to be fulfilled there. A violation of a constraint equation at any other position would not be recognized. Thus the constraint ratio can be determined with:

$$r = \frac{n_{eq}}{n_c} = \frac{n_{nodes}^i \cdot n_{elem} \cdot n_{dof}}{n_G \cdot n_{c,elem} \cdot n_{dof}} = \frac{n_{nodes}^i \cdot n_{elem}}{n_G \cdot n_{c,elem}} \quad (3.3)$$

where n_G is the number of Gaussian points per element, $n_{c,elem}$ denotes the number of constraint equations per element and n_{elem} represents the element number. Summing up, the constraint ratio according to equ. (3.3) is only dependent on the element shape, the number of element degrees of freedom, the number of elements and the number of Gauss points. Thus for a system with given geometry and given element type, there is only the number of Gaussian points n_G in order to manipulate the constraint ratio r .

The numerical point of view is a heuristic approach which is not so much a precise method to analyze arbitrary finite elements as an easy and efficient tool to investigate the disposition of the element to locking. Comparing the calculated constraint ratio r with the optimal constraint ratio r_k obtained from the continuous problem, three cases can be distinguished:

- $r < r_k$: Disposition to locking.
- $r = r_k$: Optimal case: neither disposition to locking, nor to zero energy kinematics.
- $r > r_k$: Possible disposition to zero energy modes.

Thus elements with a disposition to locking (and thus too small constraint ratio r) can be improved by reducing the number of Gaussian points. This corresponds to the effects of the *method of reduced integration* as introduced in chapter 3.6.1

It should be pointed out that this numerical point of view is intended to give a fast and easy estimation of the disposition to locking, without mathematical rigor. Furthermore, the method is not for all elements as reliable as for incompressible solid elements which the method was initially introduced for [Hug00]. Beyond that, the sensitivity of elements to mesh distortion is not covered.

3.5.3 Mechanical Locking Phenomena

The following chapter is meant to provide a review and summary of the reasons that lead to the stiffening effects of the structural locking phenomena. This insight is the prerequisite to develop and evaluate suitable element enhancement techniques. Further insight to this topic is given e.g. at [Kos04, Bis99, Fis07]. Focus is put here on pure mechanical types of locking. However, it must be pointed out that these element deficiencies are in the same way crucial as well for coupled electromechanical problems (see examples in chapter 7). Locking effects that directly stem from the electrical fields will be covered separately in chapter 3.5.4.

Using the critical parameter λ_{crit} , a classification of the stiffening effects in geometrical and material locking effects is possible (see Table 3.2). Thus the classification is done here based on the system constraint which is responsible for the stiffening effect (see also numerical point of view in chapter 3.5.2.3).

	Locking types	Critical parameter
Geometric locking effects	(Inplane) shear locking:	Element aspect ratio
	Transverse shear locking:	Slenderness
	Membrane locking:	Slenderness
	Trapezoidal locking:	Element aspect ratio
	Curvature thickness locking:	Slenderness
Material locking effects	Volumetric locking:	Bulk modulus (Poisson's ratio)

Table 3.2: Overview: Mechanical locking phenomena and related critical parameters.

3.5.3.1 In-Plane Shear Locking

In-plane shear locking can arise at solid elements, shell elements and plates in membrane action. The name goes back to parasitic strain that is responsible for this locking effect: the arising (in-plane) shear in a bending situation. In-plane shear locking is especially significant if elements of low order are subjected to pure bending deformations.

Insight to this locking phenomenon shall be given at the example of a linear elastic 2D-problem modeled with solid elements (see e.g. also [Kos04]). Table 3.3 shows the correct results for strains and stresses of the continuous problem of inextensional bending.

For reasons of clarity, the global and the natural coordinate system are set to have the same origin and orientation. The vertical displacements u_3 are obtained to have a quadratic behavior in ξ while the horizontal displacements u_1 are linearly dependent in both ξ und ζ . As a consequence, normal strains E_{11} with a linear dependence in ζ are obtained, while E_{33} und E_{13} disappear. Following the assumption of a linear elastic material law, a normal stress S^{11} with linear dependence from ζ is obtained, while S^{33} and S^{13} cancel out.

However, it can be identified by an investigation of the deformation modes that this bending state cannot be represented adequately by an element formulation with bilinear basis functions. All presentable deformation states of the bilinear element can be derived from a linear combination of the deformation modes shown in tab. 3.4. This can be reformulated with:

$$\begin{aligned} u_1 &= c_1 + c_2 \cdot \xi + c_3 \cdot \zeta + c_4 \cdot \xi\zeta \\ u_3 &= c_5 + c_6 \cdot \zeta + c_7 \cdot \xi + c_8 \cdot \xi\zeta \end{aligned} \quad (3.4)$$

In table 3.4, the modes 1 and 5 represent the rigid body modes, modes 2 and 6 reflect normal strains, and modes 3 and 7 show states of constant shear. Thus only the modes 4 and 8 are remaining to represent the bending state according to tab. 3.3. However, both modes 4 and 8 represent a coupled state of linear shear and linear normal strain.

Thus in order to represent a strain state E_{11} that is linearly dependent from ζ , only deformation mode 4 can be activated. While the normal strains E_{11} and E_{33} and thus also the

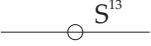
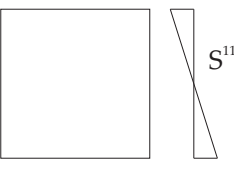
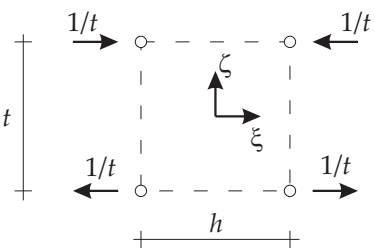
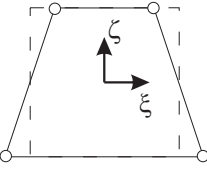
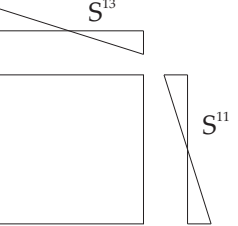
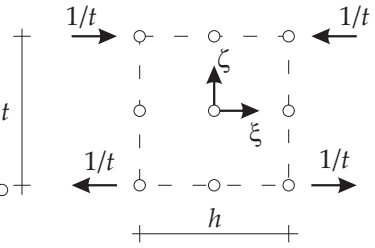
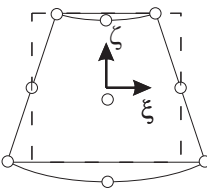
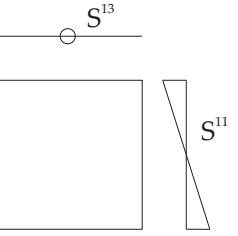
<p>Correct state according to linear bending theory:</p>	$u_1 \sim \zeta \zeta$ $u_3 \sim -\frac{1}{2} \zeta^2$	$S^{11} \sim \frac{E}{1-\nu^2} \zeta$ $S^{33} = 0$ $S^{13} = 0$  
<p>Solution of a bilinear element:</p>	$u_1 \sim \zeta \zeta$ $u_3 = 0$	$S^{11} \sim \frac{E}{1-\nu^2} \zeta$ $S^{33} = 0$ $S^{13} \sim \frac{E}{2(1+\nu)} \zeta$   
<p>Solution of a biquadratic element:</p>	$u_1 \sim \zeta \zeta$ $u_3 \sim -\frac{1}{2} \zeta^2$	$S^{11} \sim \frac{E}{1-\nu^2} \zeta$ $S^{33} = 0$ $S^{13} = 0$   

Table 3.3: Deformation and stress state in case of pure bending.

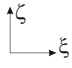
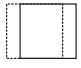
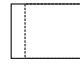
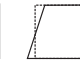
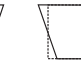



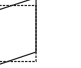
Deformation mode	1	2	3	4	5	6	7	8
								
	c_1	c_2	c_3	c_4	c_5	c_6	c_7	c_8
u_1	1	ζ	ζ	$\zeta\zeta$	-	-	-	-
u_3	-	-	-	-	1	ζ	ζ	$\zeta\zeta$
$E_{11} = u_{1,1}$	0	c_2	0	$c_4 \cdot \zeta$	0	0	0	0
$E_{33} = u_{3,3}$	0	0	0	0	0	c_6	0	$c_8 \cdot \zeta$
$E_{13} = \frac{1}{2}(u_{1,3} + u_{3,1})$	0	0	c_3	$c_4 \cdot \zeta$	0	0	c_7	$c_8 \cdot \zeta$

Table 3.4: Overview of the 8 deformation modes of the linear 2D quadrilateral element.

normal stresses S^{11} and S^{33} can be represented correctly, the shear strain and stresses do not cancel out as required (see table 3.3). In general, as soon as pure bending has to be described, the arising of parasitic shear stresses is inevitable.

In order to further investigate the influence of the parasitic shear stresses, the inner potential of this 2D example is formulated [Kos04]:

$$\Pi_{bilin}^{int} = \frac{1}{2} \int_{\frac{t}{2}}^{-\frac{t}{2}} \int_{\frac{h}{2}}^{-\frac{h}{2}} (S^{11}E_{11} + S^{13}E_{13}) dx dz = \frac{Et^3h}{24(1-\nu^2)} \left(\underbrace{1}_{\text{bending part}} + \underbrace{\left(\frac{h}{t}\right)^2 \cdot \frac{1-\nu}{2}}_{\text{parasitic shear part}} \right) \quad (3.5)$$

where a plane stress situation and a thickness of 1.0 is assumed for simplicity. The contribution of the parasitic shear part within the inner potential of equ. (3.5) is proportional to the square of the aspect ratio $\left(\frac{h}{t}\right)^2$. This explains the weak performance of related elements for high aspect ratios $\frac{h}{t}$ and approves the aspect ratio to be the critical parameter according to tab. 3.2. In contrast to the bilinear element, the biquadratic element is able to correctly represent the pure bending state according to Table 3.3.

3.5.3.2 Transverse Shear Locking

The name of transverse shear locking goes back to parasitic strain that is responsible for this locking effect: the arising (in-plane) shear in a bending situation. Transverse shear locking is known for oscillations of the transverse shear on the element level. Thus a reasonable stress analysis is in general not possible due to the zig-zag shape of the transverse shear stresses.

Transverse shear locking only appears at structural elements that consider transverse shear strains. Thus this locking effect is restricted to Timoshenko beams, as well as Reissner-Mindlin plates and shells with related kinematics. The critical parameter is the element slenderness. Due to the early development of structural elements like beams, plates and shells, this locking effect is already known for a long time. However, the intensive scientific treatment of this locking phenomenon originates from the devastating effects of transverse shear locking on the finite element results [Bis05]. For thin shells with formulations based on irreducible forms, it is practically impossible to gain satisfying finite element results with a reasonable amount of effort.

The background of transverse shear locking shall be demonstrated at the 2D-example of a two-noded Timoshenko beam element [Bis99, Kos04].

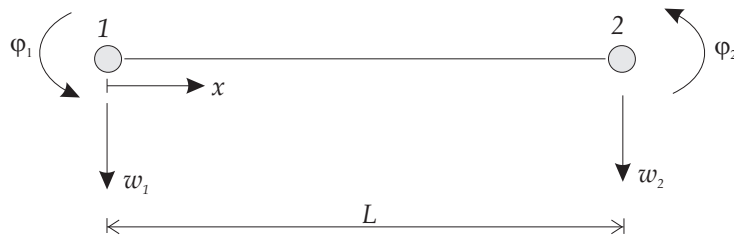


Figure 3.5: 2-noded Timoshenko beam element with its degrees of freedom.

The transverse shear strain γ is defined to be positive in counterclockwise direction, while $w' = \partial w / \partial x$ is oriented in clockwise direction. Figure 3.6 shows the kinematics for an infinitesimal beam element in the deformed case of shear and bending.

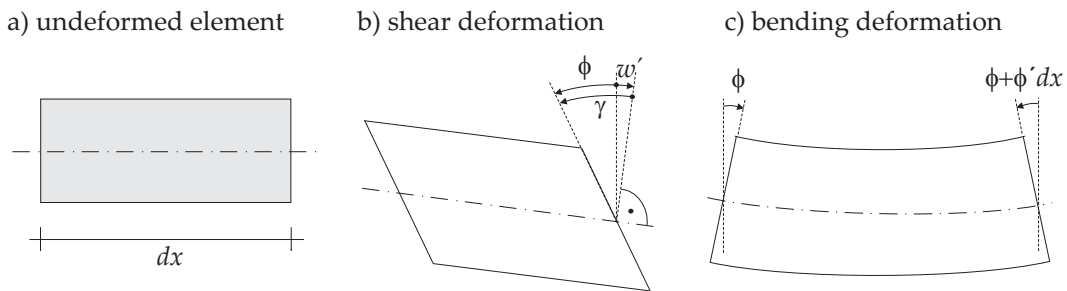


Figure 3.6: Kinematics of an infinitesimal part of a Timoshenko beam.

Thus the kinematic field equation for shear deformation can be defined with:

$$\gamma = \frac{\partial w}{\partial x} + \phi = w' + \phi \quad (3.6)$$

Separated linear assumptions are made for the behavior of displacement w and rotation ϕ of the Timoshenko beam:

$$w^h(x) = \sum_{i=1}^2 N^i(x) \cdot w_i = \left(1 - \frac{x}{L}\right) w_1 + \frac{x}{L} w_2 \quad (3.7)$$

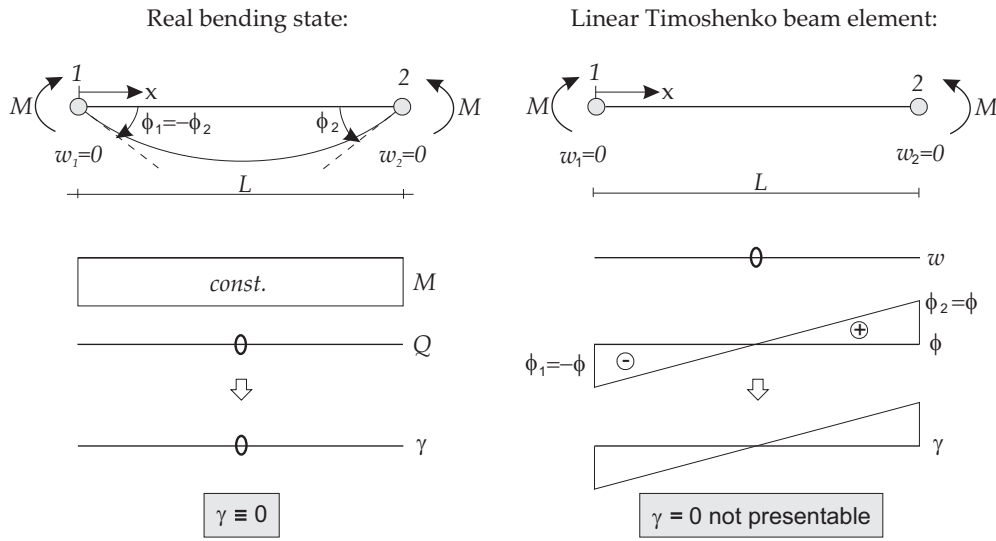


Figure 3.7: Timoshenko beam element: Parasitic shear strain in pure bending state.

$$\varphi^h(x) = \sum_{i=1}^2 N^i(x) \cdot \varphi_i = \left(1 - \frac{x}{L}\right) \varphi_1 + \frac{x}{L} \varphi_2 \quad (3.8)$$

where the index h reflects the discretization. Thus the discretized form of the transverse shear results in:

$$\begin{aligned} \gamma^h(x) &= \frac{\partial w^h}{\partial x} + \varphi^h = \sum_{i=1}^2 \left(N_{,x}^i \cdot w_i + N^i \cdot \varphi_i \right) \\ &= \frac{1}{L} (w_2 - w_1) + \varphi_1 + \frac{x}{L} (\varphi_2 - \varphi_1) \end{aligned} \quad (3.9)$$

With the investigation of a pure bending state, the deficiencies of a two-noded Timoshenko beam element can be revealed. A linear shear distribution is obtained from equ. (3.9) if the kinematic boundary conditions $w_1 = w_2 = 0$ and $\varphi = \varphi_2 = -\varphi_1 \neq 0$ are inserted.

$$\gamma^h(x) = \varphi \cdot \left(\frac{2x}{L} - 1 \right) \neq 0 \quad (3.10)$$

Thus the shear strains do not vanish according to equ. (3.10) as they should according to the analytical result. Figure 3.7 brings the finite element model of the linear Timoshenko beam face to face with the correct analytical state.

The origin of these parasitic shear strains lies in the deficient balancing of the basis formulations for displacements and rotations. The usage of separated basis functions for the displacements and the rotations results in linear behavior of the rotations and a constant behavior of the displacements (Figure 3.7). Thus the linear contribution of the shear strains cannot be balanced and the constraint equation $\gamma = 0$ cannot be fulfilled along the overall element.

Similar to the investigations of the in-plane shear locking at an bilinear 2d-element in chapter 3.5.3.1, now the contribution of parasitic strains to the overall strain energy shall be examined [Kos04]:

$$\Pi^{bending} = \frac{Et^3}{24} \int_x \kappa^2 dx = \frac{Et^3}{24} \int_0^L (\varphi_{,x})^2 dx = \frac{Et^3}{6L} \phi^2 \quad (3.11)$$

$$\Pi^{shear} = \frac{Et}{1-\nu} \int_x \gamma^2 dx = \alpha_s \frac{Et}{1-\nu} \int_0^L (\varphi - w_{,x})^2 dx = \alpha_s \frac{EtL}{3(1-\nu)} \phi^2 \quad (3.12)$$

with the shear correction factor $\alpha_s = 5/6$. Thus the ratio of shear to bending energy results in:

$$\Pi^{shear} / \Pi^{bending} = \frac{2\alpha_s}{(1-\nu)} \cdot \left(\frac{L}{t}\right)^2 \quad (3.13)$$

The proportion factor $\left(\frac{L}{t}\right)^2$ means that the influence of shear energy increases for beams with increasing slenderness. However this contradicts the behavior of real structures where the shear part also vanishes if the thickness approaches zero. Thus this shear energy can be identified to be parasitic, and the critical parameter is obviously the slenderness, i.e. the ratio of length to thickness. Furthermore, equ. (3.13) shows that increasing mesh refinement let the result again tend to the correct solution as the slenderness $\frac{L}{t}$ is decreased again in this case. However, in many cases the needed amount of mesh refinement precludes satisfying finite element results with an reasonable amount of effort, and deficiencies like the parasitic zig-zag shape of the shear stress cannot be eliminated with mesh refinement.

3.5.3.3 Trapezoidal Locking

Trapezoidal locking can only show up at curved systems with bending action. It primarily arises at solid elements. However, this locking effect can also arise in the context of shell structures that exhibit in-plane curvature. The trapezoidal shape is a natural consequence of the discretization of a curved structure and not the accidental effect of an arbitrary mesh distortion (see Figure 3.8).

In order to guarantee that only locking phenomena and no mesh distortion effects are observed, curved structures with regular meshing should be chosen. A four-noded trapezoidal plate element according to Figure 3.9 under bending deformation is chosen for the investigations. The strains in the local coordinate system of the element are defined with:

$$E_{11}^{bilin} = \frac{ht}{2} \zeta (\alpha \zeta - 1) \quad (3.14)$$

$$E_{33}^{bilin} = \frac{\alpha ht}{2} (\zeta^2 - 1) \quad (3.15)$$

$$E_{13}^{bilin} = \frac{ht}{2} \xi (2\alpha \zeta - 1) \quad (3.16)$$

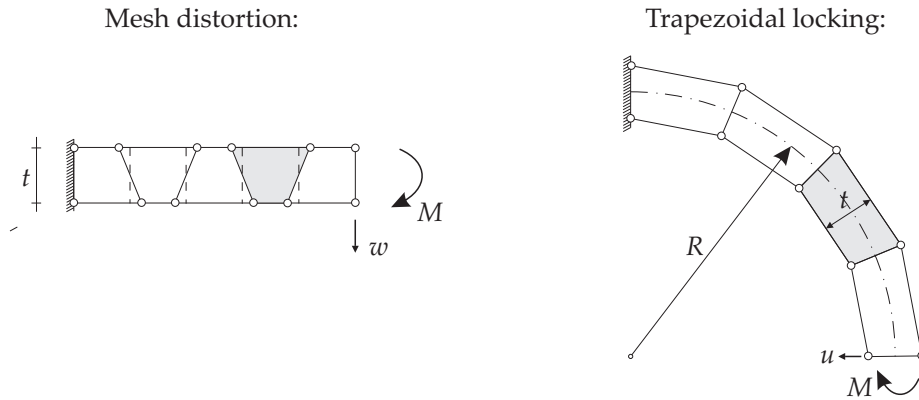


Figure 3.8: Distinction of trapezoidal mesh distortion and trapezoidal locking

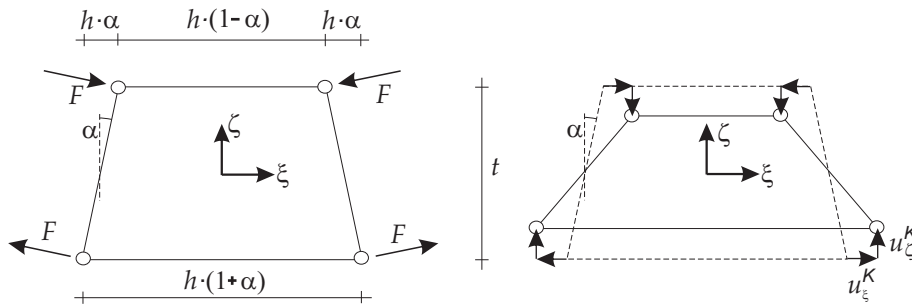


Figure 3.9: Trapezoidal bilinear element subjected to bending.

The correct strain components for pure bending are:

$$E_{11} \sim \zeta \tag{3.17}$$

$$E_{22} = 0 \tag{3.18}$$

$$E_{12} = 0 \tag{3.19}$$

It can be identified that all three strain components differ from the correct values if $\alpha \neq 0$. The error grows with increasing α which is a measure for the curvature of the structure. Analogously to the in-plane shear locking of the bilinear solid element shown above in this chapter, the parasitic shear strains E_{13}^{bilin} are linear with respect to ζ . The parasitic normal strains E_{33}^{bilin} have a quadratic shape and vanish along the element edges with $\zeta = \pm 1$. This defect is unique for trapezoidal locking and thus a useful measure to identify this locking phenomenon.

3.5.3.4 Curvature Thickness Locking

Curvature thickness locking is commonly categorized as an special case of trapezoidal locking. In 1994, this locking phenomenon has been described for the first time by Ramm, Bischoff and Braun [RBB94]. As the presented piezoelectric shell element in chapter 4

belongs to this category, this locking effect is also described in this work.

Like identified above in the context of trapezoidal locking, the parasitic stresses are again normal stresses in thickness direction. Similar to the distinction of in-plane shear locking and transverse shear locking, a distinction between trapezoidal locking and curvature thickness locking can be made by the element plane that reveals the parasitic strains. This locking phenomenon only appears at shell elements that are deformable in thickness direction and that use difference vectors of averaged directors as degrees of freedom. The phenomenon of curvature thickness locking shall be investigated at a linear beam element subjected to bending.

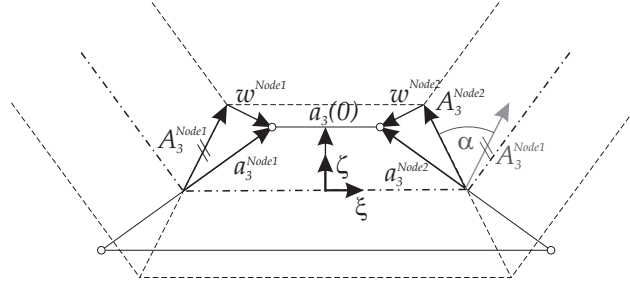


Figure 3.10: Curvature thickness locking: Parasitic normal strains.

The director $\mathbf{A}_3^{Node i}$ represents the normal to the discretized shell mid-surface at node i . It is determined by averaging the normals of the neighboring elements at this node i . Accordingly, $\mathbf{a}_3^{Node i}$ represents the discretized director at node i in the deformed configuration. The director along a linear beam element can be determined with:

$$\mathbf{A}_3^h = \frac{1}{2} (1 - \zeta) \mathbf{A}_3^{Node 1} + \frac{1}{2} (1 + \zeta) \mathbf{A}_3^{Node 2} \quad (3.20)$$

In the same way, the deformation vector of the director from reference configuration to actual configuration can be interpolated with:

$$\mathbf{w}^h = \frac{1}{2} (1 - \zeta) \mathbf{w}^{Node 1} + \frac{1}{2} (1 + \zeta) \mathbf{w}^{Node 2} \quad (3.21)$$

In the case of pure bending, the director is expected to have no change in length and it holds: $\mathbf{A}_3 \cdot \mathbf{w} = 0$. Assuming a symmetric bending deformation with $|\mathbf{w}| = |\mathbf{w}^{Node 1}| = |\mathbf{w}^{Node 2}|$, it holds due to simple trigonometric relations [Kos04]:

$$\mathbf{A}_3^{Node 1} \cdot \mathbf{w}^{Node 2} = \mathbf{A}_3^{Node 2} \cdot \mathbf{w}^{Node 1} = \frac{t}{2} \sin(\alpha) |\mathbf{w}| \quad (3.22)$$

Using the relations of equ. (3.20) - (3.22), the parasitic normal strains can be derived:

$$\mathbf{E}_{33}^h = \mathbf{A}_3^h \cdot \mathbf{w}^h = \frac{1}{4} (1 - \zeta^2) t \sin(\alpha) |\mathbf{w}| \quad (3.23)$$

This relation reveals that curvature thickness locking is indeed only existing in the context of curved structures. In the case of zero curvature ($\alpha = 0$), the parasitic normal

strains according to equ. (3.23) are vanishing. Furthermore, a mesh refinement leads to reduction of the angle α between neighboring directors and thus leads to a reduction of the parasitic strains. The critical parameter of curvature thickness locking is the slenderness of the element.

All these aspects of curvature thickness locking shown at the example of a linear beam element hold analogously in the case of the presented piezoelectric shell element of chapter 4, as it also adopts extensible and averaged directors. Consequently, a suitable element enhancement by the EAS method will be applied to eliminate this locking phenomenon.

3.5.3.5 Membrane Locking

Membrane locking only shows up in the case of curved structures, just like trapezoidal locking. It can arise at beam, shell and solid elements. Membrane locking is the stiffening effect of parasitic membrane stresses in the case of inextensional bending. Similarly to transverse shear locking, the parasitic strains exhibit an oscillating behavior and the slenderness can be identified as the critical parameter. In general, the severity of the detrimental effects of membrane locking can be comparable to the malicious effects of shear locking. In the context of membrane locking, it is not of importance if the element is based on shear-deformable kinematics or not, as the decisive normal strains are not dependent from these assumptions.

In contrast to trapezoidal locking, membrane locking only arises if the element itself is curved, and not only the structure. As a consequence, linear triangular elements are free of membrane locking, while elements of quadratic or higher basis functions usually show strong membrane locking effects [Kos04].

The mathematical view of membrane locking shows striking parallels to transverse shear locking. Instead of transverse shear stiffness, now the membrane stiffness is the critical part. Furthermore, small errors in the kinematic representation of the deformation are enlarged due to the ill-conditioning of the problem. This effect increases with the growing critical parameter slenderness.

A prominent demonstration example of membrane locking is the weakly curved beam (Marguerre beam, see e.g. [Kos04, Bis05]) which is discretized with a three-noded beam element with quadratic basis functions.

However, it should be mentioned that the piezoelectric shell elements of chapter 4 with linear basis functions are only weakly affected by membrane locking.

3.5.3.6 Volumetric Locking

In contrast to all other presented locking effects, volumetric locking is not a kinematic or geometric effect, but depends on a material parameter: the Poisson's ratio ν . That's why this phenomenon is also commonly called *Poisson locking* in the literature. In general, volumetric locking is based on the existence of parasitic volumetric strains at deviatoric

deformation modes [AR93]. For $\nu = 0$, volumetric locking is precluded. With growing Poisson's ratio, the problem is more and more ill-conditioned from a mathematical point of view. With $\nu \rightarrow 0,5$ and thus for a compression modulus going to infinity, the material tends to be incompressible. The related critical constraint is

$$\operatorname{div}(\mathbf{u}) = u_{i,i} = u_{1,1} + u_{2,2} + u_{3,3} = 0 \quad (3.24)$$

For demonstration purposes, a plane strain state is assumed with the related material law

$$\begin{bmatrix} S^{11} \\ S^{33} \\ S^{13} \end{bmatrix} = \frac{E}{(1+\nu)(1-2\nu)} \begin{bmatrix} 1-\nu & \nu & 0 \\ \nu & 1-\nu & 0 \\ 0 & 0 & \frac{1-2\nu}{2} \end{bmatrix} \begin{bmatrix} E_{11} \\ E_{33} \\ E_{13} \end{bmatrix} \quad (3.25)$$

and with $E_{22} = u_{2,2} = 0$, which reduces equ. (3.24) to:

$$\operatorname{div}(\mathbf{u}) = u_{1,1} + u_{3,3} = 0 \quad (3.26)$$

This condition is e.g. fulfilled by the following deformation state [Kos04]:

$$\begin{aligned} u_1 &\sim \zeta\zeta & E_{11} &= \zeta & S^{11} &= \frac{E(1-\nu)\zeta}{(1+\nu)(1-2\nu)} - \frac{E\nu\zeta}{(1+\nu)(1-2\nu)(1-\nu)} = \frac{E}{1-\nu^2}\zeta \\ u_3 &\sim -\frac{1}{2}\zeta^2 - \frac{\nu}{2(1-\nu)}\zeta^2 & E_{33} &= -\frac{\nu}{1-\nu}\zeta & S^{33} &= 0 \\ & & E_{13} &= 0 & S^{13} &= 0 \end{aligned} \quad (3.27)$$

However, if this strain state is approximated with plate elements with bilinear basis functions, this results in:

$$\begin{aligned} u_1^{bilin} &\sim \zeta\zeta & E_{11}^{bilin} &= \zeta & S^{11\ bilin} &= \frac{E(1-\nu)}{(1+\nu)(1-2\nu)}\zeta \\ u_3^{bilin} &= \text{const.} & E_{33}^{bilin} &= 0 & S^{33\ bilin} &= \frac{E\nu}{(1+\nu)(1-2\nu)}\zeta \\ & & E_{13}^{bilin} &= \zeta & S^{13\ bilin} &= \frac{E}{2(1+\nu)}\zeta \end{aligned} \quad (3.28)$$

This example confirms the increase of parasitic stresses with growing critical parameter: In the limit $\nu \rightarrow 0,5$, both $S^{11\ bilin}$ and $S^{33\ bilin}$ are going to infinity. Figure 3.11 illustrates the origin of volumetric locking: In the real bending state, the material fibers of the upper cross sectional area are getting thinner due to Poisson effects, while the fibers of the lower area are expanding under pressure. This leads to a displacement of the centerline of the cross section for $\nu \neq 0$. However, this effect cannot be represented by a bilinear plate element, as the basis function prescribes a linear interpolation between the corner nodes. Thus if the four nodes do not move vertically, each point within the element is as well fixed in vertical direction. In other words: The origin of volumetric locking is based in the missing feature to represent linear strains in thickness (here: ζ -) direction.

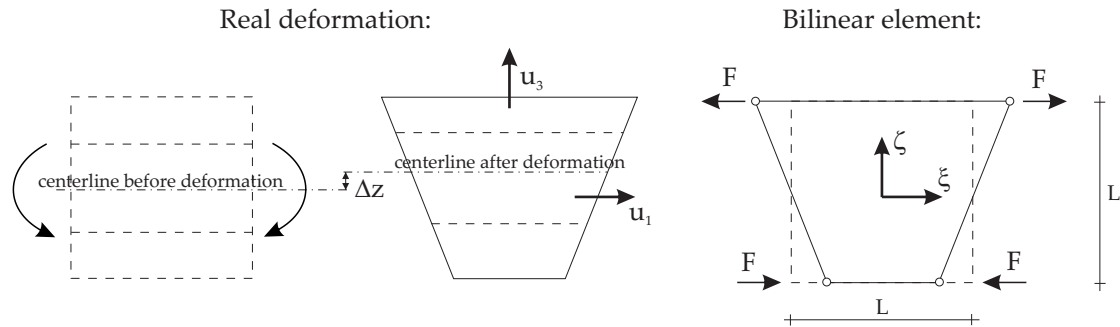


Figure 3.11: Volumetric locking of the bilinear plate element.

3.5.4 Electromechanical Locking Phenomena

Besides to the "classical" mechanical locking phenomena described in chapter 3.5.3, piezoelectric elements can suffer from further locking effects that are directly related to the electric field discretization. This shall be demonstrated at 2D examples of piezoelectric material with polarization \vec{P}_3 which is assumed to be the thickness direction.

A linear ansatz of the electric potential field in thickness direction is assumed. The electric field is derived as described in chapter 2.4. Thus \vec{E}_1 is capable to represent linear behavior, while \vec{E}_3 is only of constant type.

3.5.4.1 Pure Bending

Already in the case of transverse shear locking, it has been shown that deficient balancing of the basis formulations for the primary variables can be the origin of locking. In the case of transverse shear locking, the balancing between the separate basis functions for displacement and rotation has been identified to be crucial. In the case of electromechanical locking, the deficient balancing of the basis functions of the displacement field and the electric potential field is the origin of the locking phenomenon.

For demonstration purposes, the case of pure bending of the 2D electromechanical problem is investigated (compare also Legner [Leg11]). The analytic solution according to linear bending theory leads to a strain component E_{11} that is linear along the thickness direction. Similarly, also the electric field \vec{E}_3 shows a linear behavior over the thickness in the analytic solution (Figure 3.12).

However, in the case of the element formulation with linear ansatz of the electric potential field in thickness direction, the electric field \vec{E}_3 can only be represented by a constant behavior over the thickness. Beyond that, the linear strain E_{11} is linked in one deformation mode to the constant \vec{E}_3 in the same manner as it is linked to the linear shear strain E_{31} (compare Table 3.4 of structural in-plane shear locking and Figure 3.12). Thus summing up, this element suffers from both in-plane shear locking and electromechanical locking if subjected to bending.

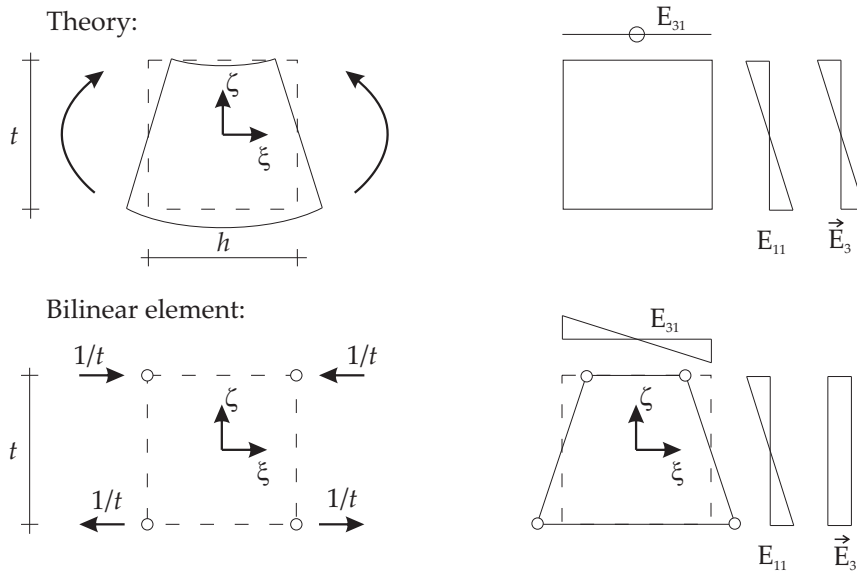


Figure 3.12: Pure bending state of a piezoelectric material.

3.5.4.2 Shear Loading

As a second test case, a clamped piezoelectric beam subjected to a single load shall be investigated. Again all strain and electric field strength components of the pure bending case are activated as in the example before. Beyond that, the analytic solution shows a shear strain E_{13} and an electric field strength \vec{E}_1 that both have a quadratic behavior along the thickness direction.

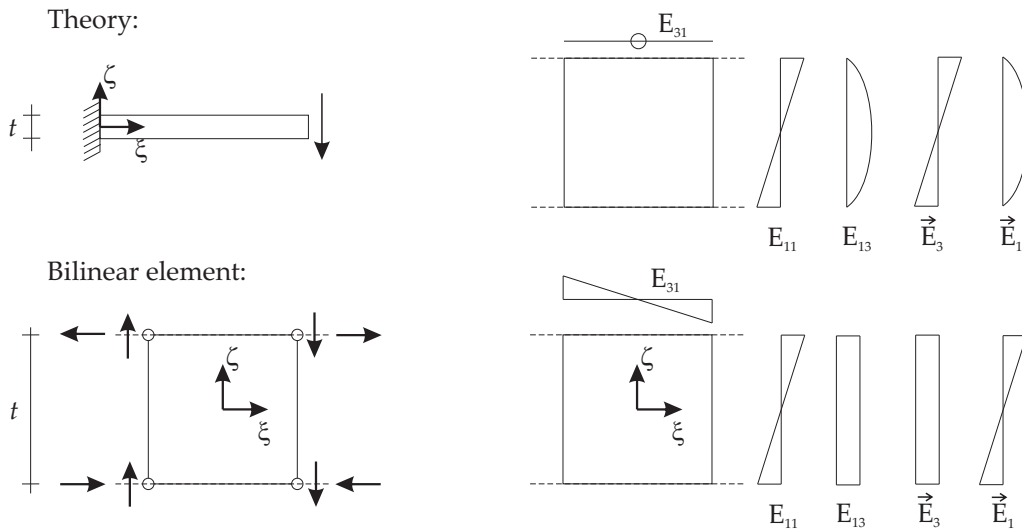


Figure 3.13: Shear loading on a piezoelectric beam.

The numerical result of the chosen linear element shows again the parasitic linear shear strain E_{13} as well as the defective constant electric field strength \vec{E}_3 due to the bending mode. The shear strain E_{13} can only be approximated by a constant shear mode. However, this is in general sufficient, as a shear correction factor can be integrated to eliminate this induced error.

However, the quadratic shape of the electric field strength \vec{E}_1 can by no means be represented with the chosen linear interpolation of the electric potential. All in all, the parasitic electric field contributions can severely deteriorate the potential field approximation and thus lead to wrong representation of sensor signals - even if the shear locking effects can be eliminated.

3.6 Enhanced Element Formulations

Due to the serious influence of locking, an independent research branch of finite element technology has established itself within the past 50 years which is dedicated to the development of locking-free elements. As a consequence of intensive research in this field, numerous element enhancement techniques have been developed.

The principles of some established element enhancement techniques shall be presented in this chapter. For reasons of clearness, this chapter makes again recourse to 1D- and 2D-examples and assumes linearized strain and stress measures to provide a deeper insight. Details of the enhanced element formulation techniques related to the presented piezoelectric shell element are postponed to chapter 4.

3.6.1 Reduced Integration

The uniform reduced integration (URI) goes back to a publication of 1969 by Doherty, Wilson and Taylor about 2D solid elements [DWT69]. It represents from the historical point of view the first method in order to avoid locking phenomena.

The basic idea is the choice of a reduced integration order compared to the correct one that would actually be necessary for a correct integration. The uniform reduced integration is a easy and effective method to eliminate locking phenomena. On top of that, computational time can be saved. In seldom cases, even the equivalence of reduced integration and mixed formulations can be shown [MH78].

Critical drawback of this method is the possible existence of zero energy modes (see chapter 3.3). For example the 8-noded hexahedron that is integrated with 1 Gaussian integration point instead of the actually needed 2x2x2 Gaussian points leads to 12 unwanted zero energy modes which create hourglass deformation modes [Fis07]. The correct result is completely hidden by dominating zero energy modes. In general, the method of uniform reduced integration is useless as long as zero energy modes enter the result.

However, already in the origins of the method, the improved approach of the *selective reduced integration* (SRI) has been applied. It is based on the principle idea to split the strain

energy into mechanically motivated parts and to integrate the related contributions to the stiffness matrix with different integration rules. Just like in the previous chapter, the 4-noded quadrilateral solid element can be used as example: The parasitic shear stresses of in-plane shear locking with linear behavior (compare Table 3.3 in chapter 3.5.3.1) can easily be eliminated by integration of the shear stiffness contribution by 1 Gauss point. This means that a suitable reduced integration can efficiently blank out the parasitic terms. The normal stresses can be integrated with 2x2 Gaussian points without any changes. As a consequence, the selective reduced integration often generates a good compromise between efficiency and stability. However, the SRI elements - although to a smaller degree - still suffer from the same deficiencies as URI elements.

Also the numerical point of view of locking (chapter 3.5.2.3) provides a useful interpretation of the reduced integration approach: The number of Gaussian points is a suitable parameter to manipulate the constraint ratio according to equ. (3.2) and consequently the disposition to locking. In order to increase the constraint ratio r in the case of locking, the number of Gaussian points in the denominator of r just has to be reduced. In the same manner, $r > r_k$ represents in the case of a too small number of Gaussian points the risk of zero energy modes.

The uniform reduced integration as well as the selective reduced integration have been widely used as well in the context of shell elements. Also transverse shear locking of plates can be tackled by selective reduced integration if shear and bending contributions are separated. However, the resulting element stiffness can lose the correct rank and then stability is not guaranteed anymore [Kos04].

However, reduced integration gets more complicated in the 3D case. Instead of one shear strain term in the 2D case, three shear terms E_{12} , E_{13} and E_{23} have to be integrated in a reduced manner along the coordinate axes of the linear parasitic strains. Also the separation of the reduced integrated contributions gets more difficult. On top of that, SRI and URI elements are usually highly prone to element distortion such that the element result quality considerably decreases in these cases.

3.6.2 ANS Method

The investigation of the parasitic strains as origin of locking has been the starting point of the method of assumed natural strains (ANS). The basic idea of the ANS method is the suitable modification of the strain field such that the parasitic terms are eliminated [HT81, BD85]. In today's element formulations, the ANS method has established itself especially in order to avoid transverse shear locking. Also the presented piezoelectric element formulation in chapter 4 adopts the ANS approach in this context.

A prominent example for the illustration of the ANS method is the 4-noded bilinear Reissner-Mindlin plate element (Figure 3.14). Here the displacements w_i and the rotations ϕ_i are interpolated linearly and independent from each other (compare also the Timoshenko beam in section 3.5.3.2). For illustration purposes, the case of uniaxial, pure

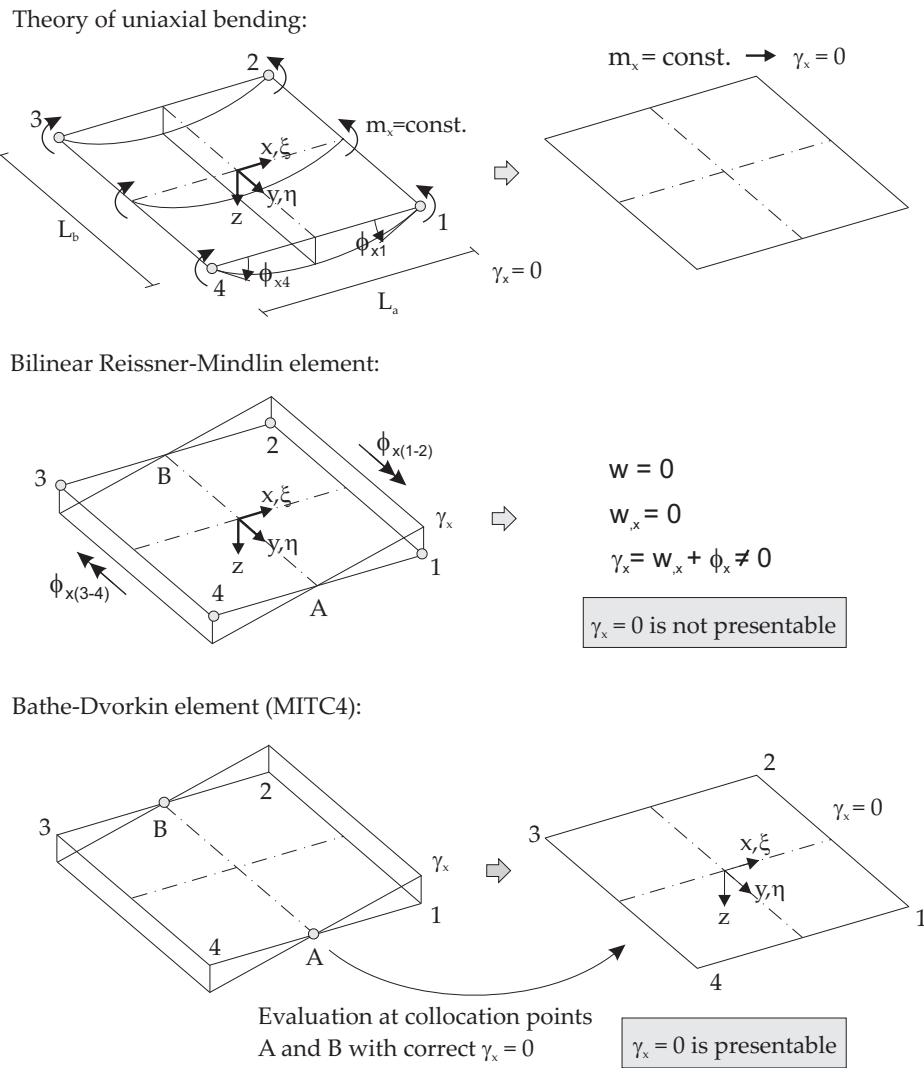


Figure 3.14: ANS method: Illustration at the example of the MITC4 element.

bending with $m_x = \text{const.}$ shall be examined [Kos04, Fis07]. Similar to the defect of a linear interpolated Timoshenko beam element, the shear strains γ_x do not vanish but show a linear behavior. Thus parasitic shear strains arise and form the origin of strong transverse shear locking effects as described in chapter 3.5.3.2.

The ANS method evaluates the strains of the displacement-based element at discrete points that provide correct strains results without parasitic effects. These points are called *sampling points* or *collocation points* and are denoted by *A, B, C, D* in Figure 3.14 and Figure 3.15. Using the strain values at the collocation points, modified strain fields can be defined with the help of appropriate basis functions (Figure 3.15).

Depending on the order of the element basis functions and the specific strain contributions to be modified, different collocation points have to be determined. The determination of the collocation points is done a priori using appropriate test cases. For example

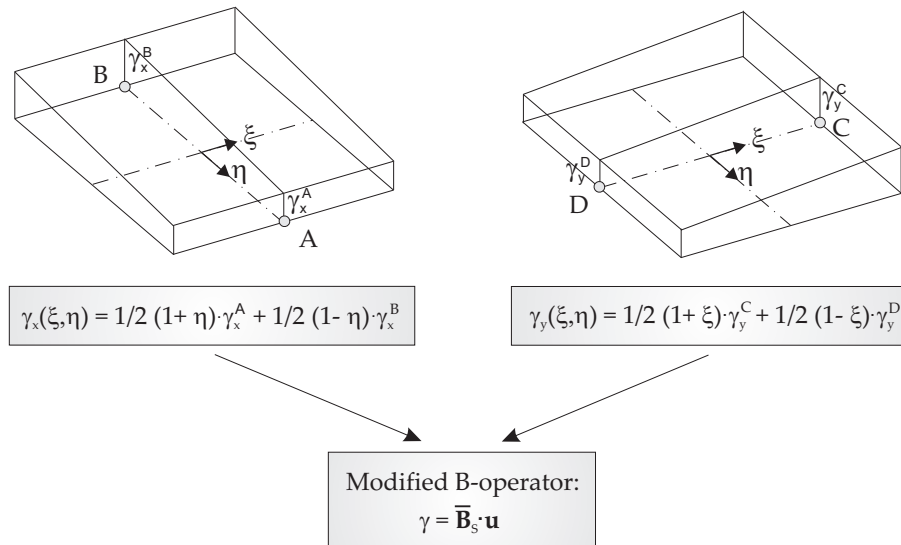


Figure 3.15: ANS method: Modified shear strain interpolation of the MITC4 element.

in the case of the bilinear Reissner-Mindlin plate element, the zero-crossing points of the original, displacement-based strains of the load case of pure uniaxial bending are used. The modified strains can be described in terms of the original nodal deformation vector \mathbf{u} of the element. Thus no additional degrees of freedom have to be defined. The modification of the strain field leads finally to a modified B-operator which maps the element deformation vector to the strain field. At the example of the MITC4 element, the discretized transverse shear strain γ is defined as follows:

$$\gamma = \bar{\mathbf{B}}_S \mathbf{u} \quad (3.29)$$

Thus the stiffness matrix of the ANS element results in [Kos04]:

$$\mathbf{K} = \underbrace{\int_{-1}^1 \int_{-1}^1 \mathbf{B}_B^T \mathbf{C}_B \mathbf{B}_B \det(\mathbf{J}) d\xi d\eta}_{\text{unchanged bending part}} + \underbrace{\int_{-1}^1 \int_{-1}^1 \bar{\mathbf{B}}_S^T \mathbf{C}_S \bar{\mathbf{B}}_S \det(\mathbf{J}) d\xi d\eta}_{\text{modified shear part}} \quad (3.30)$$

Due to the modification of the B-operator, the ANS method belongs to the *B-bar methods*. Furthermore, the ANS method can be consistently derived from a mixed functional [SH86].

In principle, the ANS method would be applicable to any kind of parasitic strain as long as enough collocation points can be identified. The criteria for the choice of the collocation points stay the same as in the case of transverse shear locking. Thus the ANS method can in general eliminate curvature thickness locking, as the related parasitic normal strains vanish at element edges. Also the membrane locking of 9-noded elements has been successfully eliminated by the ANS method [Bis99]. However, independent

modifications, test cases, collocation points and interpolation functions would be necessary for all the different geometrical locking effects. Furthermore, the ANS method is not well-suited for the elimination of volumetric locking [Kos04].

3.6.3 EAS and EAE Method

3.6.3.1 Historical Background of the EAS Method

The method of the enhanced assumed strains (EAS) goes back to a new formulation for elements of low order of basis functions published by Doherty, Wilson and Taylor in 1973 [WTDG73]. The so-called "Q6" element has been presented, a bilinear isoparametric 2D solid element (compare also Table 3.3 in chapter 3.5.3.1) that has been enhanced by two quadratic displacement modes. The added displacement modes are not part of the linear interpolation of the displacement field, as they would in general violate the compatibility between the elements.

In general, the basic idea is to add additional displacement modes such that the corresponding strain modes eliminate parasitic strains and enlarge the space of correctly representable strain modes of the original element formulation.

Due to this incompatibility and the initially missing mathematical foundation, the method was subject of controversial discussions in the seventies of the last century, despite of the successful application to solid elements as well as thick shell elements [WTDG73]. The criticism of Strang became famous with his statement "*Two wrongs make a right in California*" [SF73]. As the initial Q6 element did not pass the patch test, Taylor et al. presented 1976 the improved version called "QM6" [TBW76]. This element is able to pass the patch test, however it exhibits higher sensitivity to mesh distortions. This approach of Taylor, Wilson et al. became famous as the *method of incompatible modes* and became the basis for the development of the EAS method. Later, in 1990, the variational basis of the EAS method was presented by Simo and Rifai using the modified principle of Hu-Washizu ("*Two rights do make a right, even in California*" [SR90]). The EAS method comprises the method of incompatible modes as special case and represents a widely used technique in today's elements to eliminate locking effects.

3.6.3.2 Illustration of EAS at a 2D Problem

Recalling the variation of the modified Hu-Washizu functional with its extension for electromechanical problems according to equ. (2.164):

$$\delta \Pi_{MHW}(\mathbf{u}, \varphi, \tilde{\mathbf{E}}, \tilde{\tilde{\mathbf{E}}}) = \int_{\Omega} \left[\mathbf{S}^{\mathbf{E}^u} : \delta \mathbf{E}^u + \mathbf{S}^{\tilde{\mathbf{E}}} : \delta \tilde{\mathbf{E}} - \bar{\mathbf{D}}^{\tilde{\mathbf{E}}^\varphi} : \delta \tilde{\mathbf{E}}^\varphi - \bar{\mathbf{D}}^{\tilde{\tilde{\mathbf{E}}}} : \delta \tilde{\tilde{\mathbf{E}}} \right] dV - \delta \Pi_{MHW}^{ext} \quad (3.31)$$

additional *enhanced strains* are introduced besides to the displacement-compatible strains of standard elements of irreducible form. These additional strain terms are introduced in order to balance the unwanted parasitic strains that cause the locking phenomena (see

also section 3.5). This a fundamental difference of the EAS method to the B-bar methods which try to reach locking-free elements via the elimination of the parasitic strains. In contrast to the method of incompatible modes, no displacement modes have to be designed which would lead again to derived strain modes. In the contrary, the enhanced strain modes are defined directly.

For reasons of clarity, the principle of the EAS method is illustrated at the example of the 2D 4-noded linear plane stress solid element [SR90, Kos04, Fis07]. In order to merge EAS and EAE in one example, the ξ - ζ -plane is used. Table 3.5 shows again the 8 compatible displacement modes that have been introduced in the context of in-plane shear locking in section 3.5.


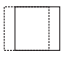
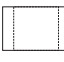
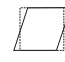
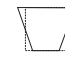

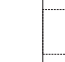

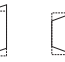
	Deformation modes								EAS modes			
	1	2	3	4	5	6	7	8	1	2	3	4
												
	c_1	c_2	c_3	c_4	c_5	c_6	c_7	c_8	α_1	α_2	α_3	α_4
u_1	1	ξ	ζ	$\xi\zeta$	-	-	-	-	$\frac{\xi^2-1}{2}$	-	-	$\frac{\zeta^2-1}{2}$
u_3	-	-	-	-	1	ζ	ξ	$\xi\zeta$	-	$\frac{\zeta^2-1}{2}$	$\frac{\xi^2-1}{2}$	-
E_{11}	0	1	0	ζ	0	0	0	0	ξ	0	0	0
E_{33}	0	0	0	0	0	1	0	ξ	0	ζ	0	0
E_{13}	0	0	1	ξ	0	0	1	ζ	0	0	ξ	ζ

Table 3.5: Linear 2D quadrilateral element: compatible deformation modes and EAS modes.

Four additional strains modes are added to the element formulation. These enhanced assumed strains can be collected in a matrix $\bar{\mathbf{M}}_4$:

$$\bar{\mathbf{M}}_4 = \begin{bmatrix} \xi & 0 & 0 & 0 \\ 0 & \zeta & 0 & 0 \\ 0 & 0 & \xi & \zeta \end{bmatrix} \quad (3.32)$$

In total, this results in a (in ξ and ζ) linear description of all strain components. Furthermore, Table 3.5 also shows the corresponding displacement modes that belong to the enhanced strain modes which reveals the equivalence to the QM6 element of Taylor et al. based on the method of incompatible modes. In general, for each incompatible mode a corresponding enhanced strain mode can be formulated. However, not all enhanced strain modes are representable by incompatible displacement modes.

The choice of the specific EAS modes 3 and 4 can be explained at the resulting term for the discretized shear strains:

$$E_{13} = c_3 + c_7 + (\alpha_3 + c_4) \xi + (\alpha_4 + c_8) \zeta \quad (3.33)$$

Thus in case of a bending deformation according to deformation mode 4, for example, it holds: $c_4 \neq 0$. The related parasitic shear strains can be eliminated if the EAS coefficients are chosen appropriately with $\alpha_3 = -c_4$. In the same way, α_4 can balance parasitic shear strains stemming from c_8 . As a consequence, bending deformations can be in general represented without any parasitic shear strains in this case. The finite element is shear-locking free for uniaxial bending.

The enhanced strains related to α_1 and α_2 are needed for the elimination of volumetric locking (see also section 3.5.3.6). These linear enhanced strains are needed to fulfill the incompressibility condition in the case of (in-plane) bending according to deformation modes 4 and 8 (Table 3.5). This can be verified looking at the corresponding stresses of a bending deformation mode assuming a linear elastic material:

$$\begin{bmatrix} S^{11} \\ S^{33} \\ S^{13} \end{bmatrix} = \frac{E}{(1+\nu)(1-2\nu)} \begin{bmatrix} 1-\nu & \nu & 0 \\ \nu & 1-\nu & 0 \\ 0 & 0 & \frac{1-2\nu}{2} \end{bmatrix} \begin{bmatrix} c_4 \cdot \zeta \\ 0 \\ c_4 \cdot \xi \end{bmatrix} = \begin{bmatrix} \frac{E(1-\nu)}{(1+\nu)(1-2\nu)} \cdot c_4 \cdot \zeta \\ \frac{\nu E}{(1+\nu)(1-2\nu)} \cdot c_4 \cdot \zeta \\ \frac{E}{2(1+\nu)} \cdot c_4 \cdot \xi \end{bmatrix} \quad (3.34)$$

Here the shear strains are visible again that can be balanced via EAS mode α_3 . The origin of volumetric locking is based on the stresses S^{33} which show the coupling of the normal strains via the Poisson's ratio ν . However, the EAS parameter α_2 can be chosen such that a stress state with zero normal stresses in ζ -direction is representable. Thus the EAS modes of matrix \bar{M}_4 are sufficient to generate a bilinear element that is completely free of volumetric locking [AR93].

In the case of distorted meshes and multi-dimensional bending states, additional enhanced strain modes can further improve the element result quality. Using \bar{M}_7 for example, a complete bilinear strain state can be represented:

$$\bar{M}_7 = \begin{bmatrix} \xi & 0 & 0 & 0 & \xi\xi & 0 & 0 \\ 0 & \zeta & 0 & 0 & 0 & \xi\zeta & 0 \\ 0 & 0 & \xi & \zeta & 0 & 0 & \xi\zeta \end{bmatrix} \quad (3.35)$$

With these 7 enhanced strain modes, the element provides in total 15 modes, consisting of 3 rigid body modes and 12 deformation modes. For this bilinear 2D element, \bar{M}_7 provides the optimum number of enhanced strains [AR93]. Further enhanced strain modes would lead to the same stiffness matrix in this example.

3.6.3.3 Illustration of EAE at a 2D Problem

Similar to enhanced strains, also enhanced assumed electric field strength terms can be introduced in order to eliminate related parasitic terms and incompatible approximation spaces of the electromechanical problem (EAE Method).

Recalling the case of structural electromechanical locking according to Figure 3.13 in chapter 3.5.4, a linear electric field representation in thickness direction is missing in order to eliminate electromechanical locking in a pure bending state. This can be established by

a suitable $\vec{\tilde{E}}_3$ -enhancement. Furthermore, a constant representation of the normal strains in longitudinal direction can be constructed by the EAE method in order to eliminate parasitic fields that appear in the context of shear loading. Of course, a constant mode $\vec{\tilde{E}}_1$ does not match the analytical result of a quadratic behavior. However, this is not necessarily needed, as a correct result of the primary variables can also be generated adopting a correction factor comparable with the commonly used shear correction factor. Thus summing up, all parasitic field effects and incompatible approximation spaces can be balanced, as illustrated in Figure 3.16.

An detailed analysis of the single enhanced electric field modes will be provided in chapter 4.5.3 in the context of the discretization of the piezoelectric shell element formulation.

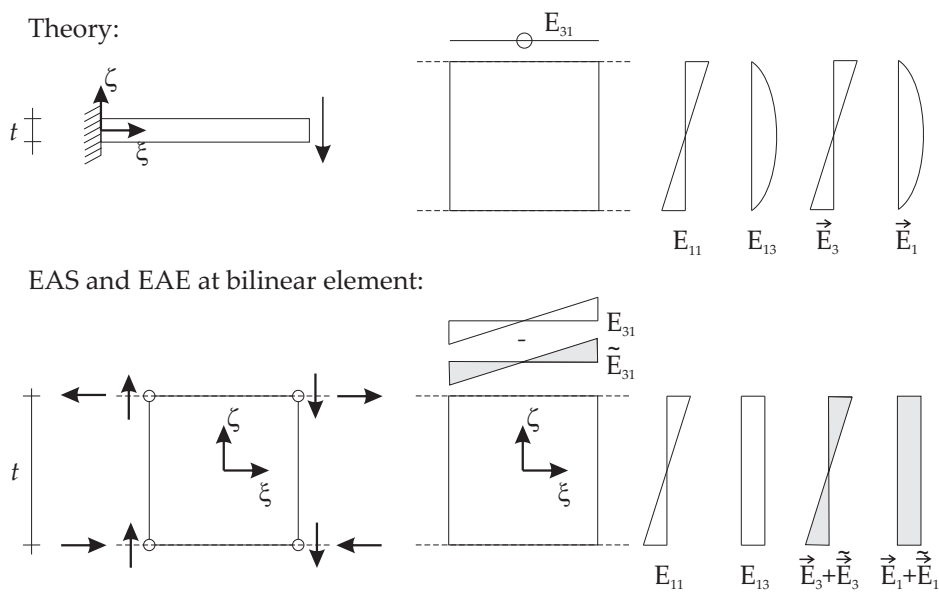


Figure 3.16: EAS and EAE principle at the example of a bilinear 2D element.

3.6.3.4 Prerequisites for Enhanced Modes

The side constraints for the determination of shape functions for enhanced assumed strain modes and enhanced assumed electric field strength modes result from the requirements for stability and consistency (see also section 3.2):

1. The enhanced modes are allowed to be C^{-1} -continuous.
2. The enhanced modes must be linear independent from the compatible modes.
3. The enhanced modes must be linear independent from all other enhanced modes.
4. The orthogonality conditions of equ. (2.160) and (2.161) must be fulfilled.

Requirement 1 can be illustrated at the example of in plane shear locking: the parasitic shear strains exhibit a zig-zag behavior which of course can only be balanced with enhanced strains of same type.

Requirement 2 is needed to exclude zero energy modes and thus to guarantee stability. This can be illustrated at the following example:

$$\overline{\mathbf{M}}_5^{ZEM} = \begin{bmatrix} \zeta & 0 & 0 & 0 & \zeta \\ 0 & \zeta & 0 & 0 & 0 \\ 0 & 0 & \zeta & \zeta & 0 \end{bmatrix} \quad (3.36)$$

The matrix $\overline{\mathbf{M}}_5^{ZEM}$ introduces a zero energy mode that is hidden behind a linear combination of three modes:

$$\begin{bmatrix} E_{11} \\ E_{33} \\ E_{13} \end{bmatrix} = c_4 \begin{bmatrix} \zeta \\ 0 \\ \zeta \end{bmatrix} + \alpha_3 \begin{bmatrix} 0 \\ 0 \\ \zeta \end{bmatrix} + \alpha_5 \begin{bmatrix} \zeta \\ 0 \\ 0 \end{bmatrix} = \begin{bmatrix} 0 \\ 0 \\ 0 \end{bmatrix} \quad \text{with } c_4 = -\alpha_3 = -\alpha_5 \quad (3.37)$$

Requirement 3 results from the necessity to invert the matrix of enhanced modes for the static condensation of the additional parameters on the element level.

Requirement 4 is a fundamental assumption of the variational derivation of the underlying electromechanical functional. The assumptions are prerequisite for the successful elimination of the stress field and the electric displacement field from the Hu-Washizu functional.

The in-depth derivation of the discretized formulation of the EAS method and the EAE method is discussed later in section 4.5.3

Chapter 4

Theory of the Piezoelectric Composite Shell Element

4.1 Geometric Definitions and Kinematic Assumptions

In order to efficiently describe the shell element, the element mid-surface is explicitly defined. The position vector to the point on the mid-surface in the reference configuration and actual configuration shall be denoted with \mathbf{R} and \mathbf{r} , respectively.

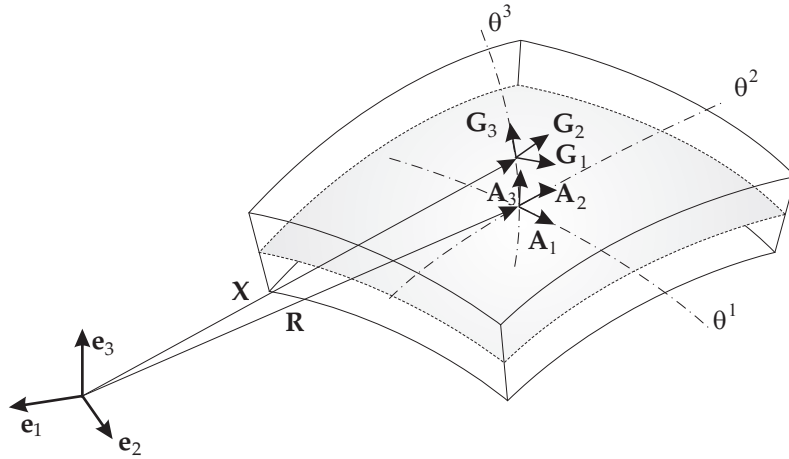


Figure 4.1: Definition of shell geometry with bases of mid-surface and shell body.

Following the definition according to equ. (2.7), the covariant base vectors at the shell mid-surface are defined using the derivatives of the position vector with respect to local coordinates:

$$\mathbf{A}_\alpha = \mathbf{R}_{,\alpha}, \quad \mathbf{a}_\alpha = \mathbf{r}_{,\alpha} \quad (4.1)$$

The director \mathbf{A}_3 is not derived from the position vector, but is established being perpendicular to \mathbf{A}_1 and \mathbf{A}_2 . The length of \mathbf{A}_3 is defined to be the half of the element thickness:

$$\mathbf{A}_3 = \frac{h}{2} \frac{\mathbf{A}_1 \times \mathbf{A}_2}{|\mathbf{A}_1 \times \mathbf{A}_2|} \quad (4.2)$$

Having introduced this covariant basis on the shell mid-surface in the reference configuration, we can now describe the position vector \mathbf{X} of any point of the shell body by the shell mid-surface and the director \mathbf{A}_3 [Büc92, Bis99]:

$$\mathbf{X} = \mathbf{R} + \theta^3 \mathbf{A}_3 \quad \text{with } -1 < \theta^3 < +1 \quad (4.3)$$

For the actual configuration we can formulate accordingly:

$$\mathbf{x} = \mathbf{r} + \theta^3 \mathbf{a}_3 \quad (4.4)$$

4.1.1 Mechanical Part

With equ. (4.3) and (4.4), a complete description of the geometry in reference and actual configuration is given. As shown in chapter 2.3, this is sufficient to describe all (mechanical) kinematic variables. Using the location vector of a point of the mid-surface in the actual configuration:

$$\mathbf{r} = \mathbf{R} + \mathbf{v} \quad (4.5)$$

together with the relation of the director in the actual configuration:

$$\mathbf{a}_3 = \mathbf{A}_3 + \mathbf{w} \quad (4.6)$$

one obtains the general description of the displacements of a point of the shell body:

$$\begin{aligned} \mathbf{u} &= \mathbf{x} - \mathbf{X} = \mathbf{R} + \mathbf{v} + \theta^3 (\mathbf{A}_3 + \mathbf{w}) - (\mathbf{R} + \theta^3 \mathbf{A}_3) \\ &= \mathbf{v} + \theta^3 \mathbf{w} \end{aligned} \quad (4.7)$$

Thus the assumptions of the shell model so far lead to 6 independent nodal degrees of freedom: 3 displacement components v_1, v_2 and v_3 of the mid-surface, and three components w_1, w_2 and w_3 of the difference vector between the directors in actual and reference configuration (Figure 4.2).

However, as a resulting 6-parameter shell with these degrees of freedom would suffer from Poisson-thickness locking, a linear normal enhanced strain mode in thickness direction is added according to Bischoff [Bis99]:

$$E_{33} = E_{33}^u + \tilde{E}_{33} \quad (4.8)$$

The mathematical justification for adding additional strain modes is based on the Hu-Washizu functional that is used to derive this enhanced element.

As shown in chapter 2.3, a pure continuum mechanical description of strains in 3-dimensional space requires 6 components to completely describe the deformation state of a material point: the three normal strain components E_{11}, E_{22}, E_{33} and the three shear strain components E_{12}, E_{13} and E_{23} .

However, in order to separate the thickness direction in the shell element formulation, the 3-dimensional continuum view must be transferred to a 2-dimensional shell element

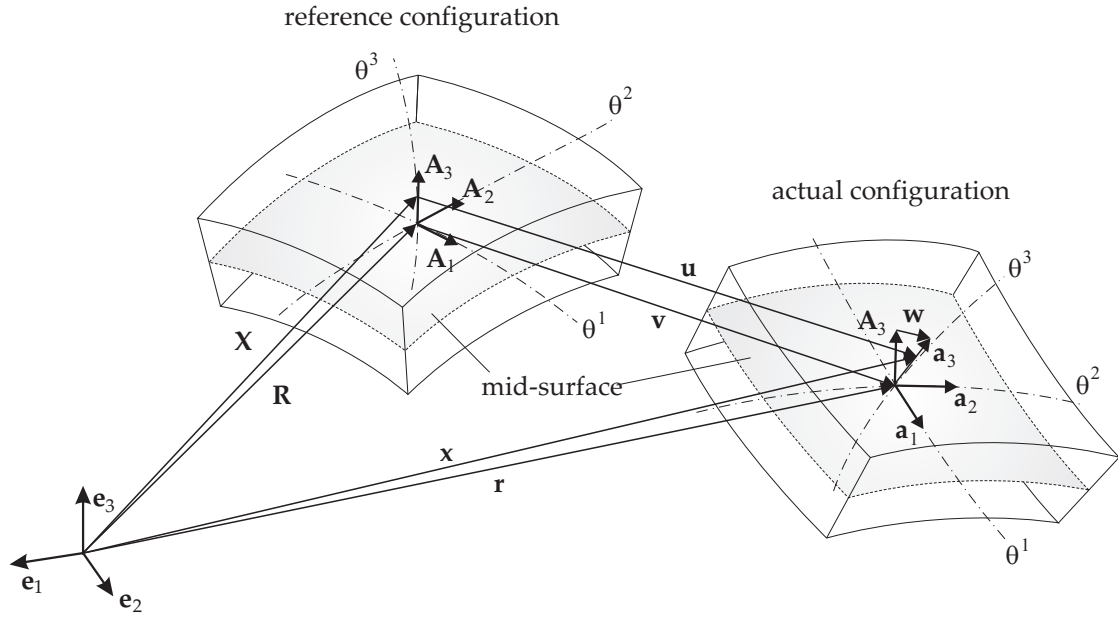


Figure 4.2: Definition of shell deformation.

point of view where the thickness dimension is separated. To this goal, strain and curvature measures must be defined that represent energetically conjugate quantities to the stress resultants. For conventional 5-parameter shells this means introducing membrane strains, curvature and shear strains. For the piezoelectric formulation, electric field components are added that are constant and linear over the thickness. Beyond that, enhanced strain and enhanced electric field terms have to be added to the group of kinematic variables as shown in the sequel.

Starting point for the derivation is the convective coordinate system with its covariant base vectors according to equ. (2.7). Taking advantage of the geometric and kinematic assumptions made in section 4.1, the base vectors of a point of the shell body can be defined in dependence of the shell mid-surface:

$$\mathbf{G}_\alpha = \mathbf{X}_{,\alpha} = \mathbf{R}_{,\alpha} + \theta^3 \mathbf{A}_{3,\alpha} \quad (4.9)$$

$$\mathbf{g}_\alpha = \mathbf{x}_{,\alpha} = \mathbf{r}_{,\alpha} + \theta^3 \mathbf{a}_{3,\alpha} \quad (4.10)$$

Using the covariant base vectors according to equ. (4.1), one obtains:

$$\mathbf{G}_\alpha = \mathbf{A}_\alpha + \theta^3 \mathbf{A}_{3,\alpha} \quad (4.11)$$

$$\mathbf{g}_\alpha = \mathbf{a}_\alpha + \theta^3 \mathbf{a}_{3,\alpha} \quad (4.12)$$

The director vector of a shell volume position is equal to the director of the related shell mid-surface position:

$$\mathbf{G}_3 = \mathbf{A}_3 \quad (4.13)$$

$$\mathbf{g}_3 = \mathbf{a}_3 \quad (4.14)$$

In three-dimensional continuum theory, the Green-Lagrange strain tensor is dependent on its position in three-dimensional space. In the convective coordinate system of the shell, this means a dependence from all three coordinates θ^i . While θ^1 and θ^2 are incorporated via the base vectors and the mid-surface definition, the dependence from θ^3 has to be separately considered due to the semi-discretization in thickness direction. Owing to the kinematic assumption in chapter 4.1, the function space in thickness direction of the components of \mathbf{E} are restricted to polynomials up to second order in θ^3 .

Thus the components of the Green-Lagrange strain tensor can be decomposed into contributions that are constant, linear and quadratic in θ^3 .

$$E_{ij} = E_{ij}^u + \tilde{E}_{ij} = \alpha_{ij} + \theta^3 \beta_{ij} + (\theta^3)^2 \gamma_{ij} \quad (4.15)$$

The components of \mathbf{E}^u can be derived via setting equ. (2.39) equal to the ansatz according to equ. (4.15):

$$E_{ij}^u = \frac{1}{2} (\mathbf{g}_i \cdot \mathbf{g}_j - \mathbf{G}_i \cdot \mathbf{G}_j) = \alpha_{ij}^u + \theta^3 \beta_{ij}^u + (\theta^3)^2 \gamma_{ij}^u \quad (4.16)$$

Via inserting equ. (4.11) - (4.14) one obtains:

$$\alpha_{\alpha\beta}^u = \frac{1}{2} (\mathbf{a}_\alpha \cdot \mathbf{a}_\beta - \mathbf{A}_\alpha \cdot \mathbf{A}_\beta), \quad (4.17)$$

$$\alpha_{\alpha 3}^u = \frac{1}{2} (\mathbf{a}_\alpha \cdot \mathbf{a}_3 - \mathbf{A}_\alpha \cdot \mathbf{A}_3), \quad (4.18)$$

$$\alpha_{33}^u = \frac{1}{2} (\mathbf{a}_3 \cdot \mathbf{a}_3 - \mathbf{A}_3 \cdot \mathbf{A}_3), \quad (4.19)$$

$$\beta_{\alpha\beta}^u = \frac{1}{2} (\mathbf{a}_\alpha \cdot \mathbf{a}_{3,\beta} + \mathbf{a}_\beta \cdot \mathbf{a}_{3,\alpha} - \mathbf{A}_\alpha \cdot \mathbf{A}_{3,\beta} - \mathbf{A}_\beta \cdot \mathbf{A}_{3,\alpha}), \quad (4.20)$$

$$\beta_{\alpha 3}^u = \frac{1}{2} (\mathbf{a}_{3,\alpha} \cdot \mathbf{a}_3 - \mathbf{A}_{3,\alpha} \cdot \mathbf{A}_3), \quad (4.21)$$

$$\beta_{33}^u = 0, \quad (4.22)$$

$$\gamma_{\alpha\beta}^u = \frac{1}{2} (\mathbf{a}_{3,\alpha} \cdot \mathbf{a}_{3,\beta} - \mathbf{A}_{3,\alpha} \cdot \mathbf{A}_{3,\beta}), \quad (4.23)$$

$$\gamma_{\alpha 3}^u = 0, \quad (4.24)$$

$$\gamma_{33}^u = 0. \quad (4.25)$$

In the following, the behavior of the strains in thickness direction are assumed to be linear. Thus the quadratic terms γ_{ij} in equ. (4.16) cancel out. Related errors are restricted to cases of strong bending deformations of relatively thick or strongly curved shells and to cases of strong gradients of strains in thickness direction [Büc92, BRR94, Bis99].

Following the definition of equ. (4.8), the additional strain tensor components \tilde{E}_{ij} are zero except for the contribution of linear normal strains in thickness direction. Thus the components E_{ij} finally result in:

$$E_{ij} = E_{ij}^u \quad \forall (i, j) \neq (3, 3), \quad (4.26)$$

$$E_{33} = E_{33}^u + \tilde{E}_{33} = \alpha_{33}^u + \theta^3 \tilde{\beta} \quad (4.27)$$

It should be mentioned that this special treatment of \vec{E}_{33} is based on the idea to provide this additional strain component as 7th parameter in the element formulation. Thus equ. (4.27) and (4.27) refer to the "basic" 7-parameter formulation. The definition of further enhanced strain modes according to the modified Hu-Washizu functional is explained later in chapter 4.5.3. Thus this separate treatment of \vec{E}_{33} here is by no means a restriction of the enhanced assumed strain (EAS) method.

4.1.2 Electrical Part

Similar to the approach in equ. (4.15) for the Green-Lagrange strain, the electrical field can be assumed to be subdivided into contributions that are constant and linear in θ^3 :

$$\vec{E}_i = \vec{E}_i^\varphi + \vec{\tilde{E}}_i = \vec{\alpha}_i + \theta^3 \vec{\beta}_i \quad (4.28)$$

Starting from equ. (2.45), the Green-Lagrange electrical field strength can be defined in the convective coordinate system of the shell with:

$$\vec{E}^\varphi = \begin{bmatrix} \vec{E}_1^\varphi \\ \vec{E}_2^\varphi \\ \vec{E}_3^\varphi \end{bmatrix} = -\frac{\partial \varphi}{\partial \theta^i} \mathbf{G}^i \quad (4.29)$$

A polarization of the piezoelectric material in thickness direction is assumed. Furthermore, the electrodes are assumed to be positioned at the upper and lower surface of the shell. Thus the potential in thickness direction is of major importance. Furthermore, it is a common approach to ground one electrode while the other electrode is loaded with an electric potential. Thus it is sufficient to consider the potential difference $\Delta\varphi$ in the thickness direction instead of single potentials at the lower and the upper surface. As a consequence, the electric field strength results in

$$\vec{E}_1^\varphi = -\frac{\partial \Delta\varphi}{\partial \theta^1} \mathbf{G}^1, \quad \vec{E}_2^\varphi = -\frac{\partial \Delta\varphi}{\partial \theta^2} \mathbf{G}^2 \quad (4.30)$$

$$\vec{E}_3^\varphi = -\frac{1}{2} \Delta\varphi \mathbf{G}^3 \quad (4.31)$$

Thus one obtains:

$$\vec{\alpha}_1^\varphi = -\frac{\partial \Delta\varphi}{\partial \theta^1} \quad (4.32)$$

$$\vec{\alpha}_2^\varphi = -\frac{\partial \Delta\varphi}{\partial \theta^2} \quad (4.33)$$

$$\vec{\alpha}_3^\varphi = -\frac{1}{2} \Delta\varphi \quad (4.34)$$

$$\vec{\beta}_1^\varphi = 0 \quad (4.35)$$

$$\vec{\beta}_2^\varphi = 0 \quad (4.36)$$

$$\vec{\beta}_3^\varphi = 0 \quad (4.37)$$

4.1.3 Generalized Representation

Combining the mechanical and electrical contributions of the kinematics, a generalized representation can be defined. This also facilitates a unified approach for electrical and mechanical fields in discretization and implementation. The vector of the degrees of freedom of node i can be stated as:

$$\bar{\mathbf{d}}^i = \left[v_1^i \ v_2^i \ v_3^i \ w_1^i \ w_2^i \ w_3^i \ \Delta\varphi^i \right]^T \quad (4.38)$$

In the same manner, a generalized vector of shell strains $\bar{\mathbf{E}}$ can be defined using equ. (4.15) and equ. (4.28):

$$\bar{\mathbf{E}} = \left[\alpha_{11} \ \alpha_{12} \ \alpha_{13} \ \alpha_{22} \ \alpha_{23} \ \alpha_{33} \ \beta_{11} \ \beta_{12} \ \beta_{13} \ \beta_{22} \ \beta_{23} \ \beta_{33} \ \vec{\alpha}_1 \ \vec{\alpha}_2 \ \vec{\alpha}_3 \ \vec{\beta}_1 \ \vec{\beta}_2 \ \vec{\beta}_3 \right]^T \quad (4.39)$$

where the first six entries describe the membrane and shear strains, and the second six entries describe the bending strains. Furthermore, the last six entries represent the electric field components that are constant or linear in θ^3 . Thus in total a vector of 18 entries has been defined to describe the generalized strains (including the electric field strength terms). Evaluating the actual contributions to the entries of equ. (4.39) from the kinematics, the vector:

$$\bar{\mathbf{E}}^{u\varphi} = \left[\alpha_{11}^u \ \alpha_{12}^u \ \alpha_{13}^u \ \alpha_{22}^u \ \alpha_{23}^u \ \alpha_{33}^u \ \beta_{11}^u \ \beta_{12}^u \ \beta_{13}^u \ \beta_{22}^u \ \beta_{23}^u \ \beta_{33}^u \ 0 \ \vec{\alpha}_1^\varphi \ \vec{\alpha}_2^\varphi \ \vec{\alpha}_3^\varphi \ 0 \ 0 \ 0 \right]^T \quad (4.40)$$

is obtained.

4.2 Static Variables

The shell element formulation is driven by the idea to transform the shell volume integration into an integration over the shell mid-surface. To this goal, the generalized shell strain vector has been defined in section 4.1.3. The next step in this context is the definition of resulting static variables. To this goal, the shell shifter tensor \mathbf{Z} is defined:

$$\mathbf{Z} = \mathbf{G}_i \otimes \mathbf{A}^i \quad (4.41)$$

which provides a relation between the differential volume element dV and the differential surface element dA . With $\bar{\mu} = |\mathbf{Z}|$ it holds:

$$dV = \bar{\mu} \, d\theta^3 \, dA \quad (4.42)$$

Using the description of differential volume and surface with covariant base vectors:

$$dV = (\mathbf{G}_1 \times \mathbf{G}_2) \cdot \mathbf{G}_3 \, d\theta^3 \, d\theta^2 \, d\theta^1 \quad (4.43)$$

$$dA = |\mathbf{A}_1 \times \mathbf{A}_2| \, d\theta^2 \, d\theta^1 \quad (4.44)$$

and inserting equ. (4.43) and (4.44) in the relation of equ. (4.42), a calculation rule for $\bar{\mu}$ is obtained:

$$\bar{\mu} = \frac{(\mathbf{G}_1 \times \mathbf{G}_2) \cdot \mathbf{G}_3}{|\mathbf{A}_1 \times \mathbf{A}_2|} \quad (4.45)$$

Now the resulting static variables can be determined via integration in thickness direction:

$$n^{ij} = \int_{-1}^1 S^{ij} \bar{\mu} d\theta^3 \quad (4.46)$$

$$m^{ij} = \int_{-1}^1 S^{ij} \theta^3 \bar{\mu} d\theta^3 \quad (4.47)$$

where $n^{\alpha\beta}$ represent the membrane forces, $n^{\alpha 3}$ denote the shear forces and $m^{\alpha\beta}$ are the bending moments. Accordingly, also electric displacement resultants can be defined:

$$\vec{d}_0^i = \int_{-1}^1 \bar{D}^i \bar{\mu} d\theta^3 \quad (4.48)$$

$$\vec{d}_1^i = \int_{-1}^1 \bar{D}^i \theta^3 \bar{\mu} d\theta^3 \quad (4.49)$$

Collecting the contributions of equ. (4.46) - (4.49) in a vector representation, a generalized vector of resulting static variables is defined as:

$$\begin{aligned} \bar{\mathbf{S}} &= \left[n^{ij} \quad m^{ij} \quad \vec{d}_0^i \quad \vec{d}_1^i \right]^T \\ &= \left[n^{11} \quad n^{12} \quad n^{13} \quad n^{22} \quad n^{23} \quad n^{33} \quad m^{11} \quad m^{12} \quad m^{13} \quad m^{22} \quad m^{23} \quad m^{33} \quad -\vec{d}_0^1 \quad -\vec{d}_0^2 \quad -\vec{d}_0^3 \quad -\vec{d}_1^1 \quad -\vec{d}_1^2 \quad -\vec{d}_1^3 \right]^T \end{aligned} \quad (4.50)$$

Again a vector of 18 entries is obtained which corresponds to the generalized vector of shell strains $\bar{\mathbf{E}}$ in equ. (4.39).

4.3 Pre-Integration of Material Law

In section 2.7.2, constitutive relations of a piezoelectric continuum have been derived. Now constitutive relations for the shell-related measures of generalized stresses and strains are developed. To this goal, a pre-integration in thickness direction is performed considering the single contributions of the coupled material law:

$$D_{C,M}^{ijkl} = \int_{-1}^1 C^{ijkl} (\theta^3)^M \bar{\mu} d\theta^3, \quad \text{with } M \in \{0,1,2\} \quad (4.51)$$

$$D_{e,M}^{ijk} = \int_{-1}^1 e^{ijk} (\theta^3)^M \bar{\mu} d\theta^3, \quad \text{with } M \in \{0,1,2\} \quad (4.52)$$

$$D_{\epsilon,M}^{il} = \int_{-1}^1 \epsilon^{ijk} (\theta^3)^M \bar{\mu} d\theta^3, \quad \text{with } M \in \{0,1,2\} \quad (4.53)$$

Using the definitions of equ. (4.51) - (4.53), it holds:

$$\begin{bmatrix} n^{ij} \\ m^{ij} \\ \vec{d}_0^i \\ \vec{d}_1^i \end{bmatrix} = \begin{bmatrix} D_{C,0}^{ijkl} & D_{C,1}^{ijkl} & D_{e,0}^{ijk} & D_{e,1}^{ijk} \\ D_{C,1}^{ijkl} & D_{C,2}^{ijkl} & D_{e,1}^{ijk} & D_{e,2}^{ijk} \\ D_{e,0}^{ikl} & D_{e,1}^{ikl} & D_{e,0}^{ik} & D_{e,1}^{ik} \\ D_{e,1}^{ikl} & D_{e,2}^{ikl} & D_{e,1}^{ik} & D_{e,2}^{ik} \end{bmatrix} \begin{bmatrix} \alpha_{kl} \\ \beta_{kl} \\ \vec{\alpha}_k \\ \vec{\beta}_k \end{bmatrix} \quad (4.54)$$

The electric enthalpy density according to equ. (2.90):

$$W_H^{3D} = \frac{1}{2} S^{ij} E_{ij} - \frac{1}{2} \vec{D}^i \vec{E}^i \quad (4.55)$$

can thus be defined as well as term that is pre-integrated in thickness direction:

$$\begin{aligned} W_H^{2D} = \frac{1}{2} \vec{S} \cdot \vec{E} = \frac{1}{2} & (\alpha_{ij} D_{C,0}^{ijkl} \alpha_{kl} + 2\alpha_{ij} D_{C,1}^{ijkl} \beta_{kl} + 2\alpha_{ij} D_{e,0}^{ijk} \vec{\alpha}_k + 2\alpha_{ij} D_{e,1}^{ijk} \vec{\beta}_k \\ & + \beta_{ij} D_{C,2}^{ijkl} \beta_{kl} + 2\beta_{ij} D_{e,1}^{ijk} \vec{\alpha}_k + 2\beta_{ij} D_{e,2}^{ijk} \vec{\beta}_k \\ & + \vec{\alpha}_i D_{e,0}^{ik} \vec{\alpha}_k + 2\vec{\alpha}_i D_{e,1}^{ik} \vec{\beta}_k + \vec{\beta}_i D_{e,2}^{ik} \vec{\beta}_k) \end{aligned} \quad (4.56)$$

As a consequence, the related potential of the electric enthalpy can thus be defined not only via volume integration, but also via integration of the mid-surface:

$$\Pi_{MHW}^{int} = \int_{\Omega} W_H^{3D} dV = \int_A W_H^{2D} dA \quad (4.57)$$

and so the circle is complete for a thorough representation of the finite element formulation on the mid-surface. For this pre-integration approach in thickness direction, no specific assumptions have been made with respect to the material law. Thus the approach is in general also applicable to nonlinear material laws that cannot be represented in the form of equ. (4.54).

4.4 Constitutive Law for Layered Structures

Piezoelectric material is commonly embedded in layered structures in order to actively control or to monitor the overall system. These compounds of mechanical and piezoelectrical layers are called *piezoelectric laminates*. Accordingly, the usage of fiber reinforced materials in combination with piezoelectric materials forms the category of *piezoelectric composites*.

In order to describe the mathematical model of these structures, different laminate theories and numerical models have been developed [SH99]. The basic differences of the models are mainly related to different assumptions for the electromechanical behavior in thickness direction. There are also models that restrict the formulation to one piezoelectric layer or include only actuation.

In this work, a single director theory is applied to derive the piezoelectric composite element [Bra95]. A straight, extensible director is assumed. The application of the single director theory is reasonable for moderate thickness and stiffness relations of the single layers to each other.

Recalling equ. (2.104), the material tensor of a single layer L is described in the layer coordinate systems that reflects symmetry planes and orientations of the respective material law. Also the piezoelectric coupling tensor and the permittivity tensor can be described in such a layer-specific suitable coordinate system.

$$\mathbf{C}_L = C_L^{*ijkl} \mathbf{G}_i^* \otimes \mathbf{G}_j^* \otimes \mathbf{G}_k^* \otimes \mathbf{G}_l^* \quad (4.58)$$

$$\mathbf{e} = e^{*ijk} \mathbf{G}_i^* \otimes \mathbf{G}_j^* \otimes \mathbf{G}_k^* \quad (4.59)$$

$$\boldsymbol{\epsilon} = \epsilon^{*ij} \mathbf{G}_i^* \otimes \mathbf{G}_j^* \quad (4.60)$$

The explicit form of the components of C_L^{*ijkl} in the case of isotropic and orthotropic material have been presented in section 2.7.2.

Following the general approach of tensor transformation shown in equ. (2.14) - (2.16), the material tensors can be transformed into the overall laminate coordinate system:

$$\mathbf{C}_L = C_L^{ijkl} \mathbf{G}_i \otimes \mathbf{G}_j \otimes \mathbf{G}_k \otimes \mathbf{G}_l \quad (4.61)$$

$$\mathbf{e} = e^{ijk} \mathbf{G}_i \otimes \mathbf{G}_j \otimes \mathbf{G}_k \quad (4.62)$$

$$\boldsymbol{\epsilon} = \epsilon^{ij} \mathbf{G}_i \otimes \mathbf{G}_j \quad (4.63)$$

In total, the material tensor can be described dependent on the thickness coordinate [Bra95]:

$$\mathbf{C}(\theta^3) = \begin{cases} \mathbf{C}_{NL} & \tilde{\theta}_{NL}^3 < \theta^3 < \tilde{\theta}_{NL+1}^3 = +1 \\ \mathbf{C}_{NL-1} & \tilde{\theta}_{NL-1}^3 < \theta^3 < \tilde{\theta}_{NL}^3 \\ \vdots & \vdots \\ \mathbf{C}_2 & \tilde{\theta}_2^3 < \theta^3 < \tilde{\theta}_3^3 \\ \mathbf{C}_1 & -1 = \tilde{\theta}_1^3 < \theta^3 < \tilde{\theta}_2^3 \end{cases} \quad (4.64)$$

where the coordinate $\tilde{\theta}_i^3$ describes the distance of the overall composite mid-surface to the interface between the layers $i - 1$ and i (Figure 4.3). The index NL stands for the number of layers of the composite. The coordinates $\tilde{\theta}_i^3$ can be derived from the thicknesses of the single layers:

$$\tilde{\theta}_i^3 = -1 + \frac{2}{h} \sum_{j=1}^{i-1} h_j \quad \text{for } i = 2, \dots, NL \quad (4.65)$$

For the numerical integration in thickness direction, the integral has to be divided into separate integrals of the single layers. A coordinate transformation from the thickness

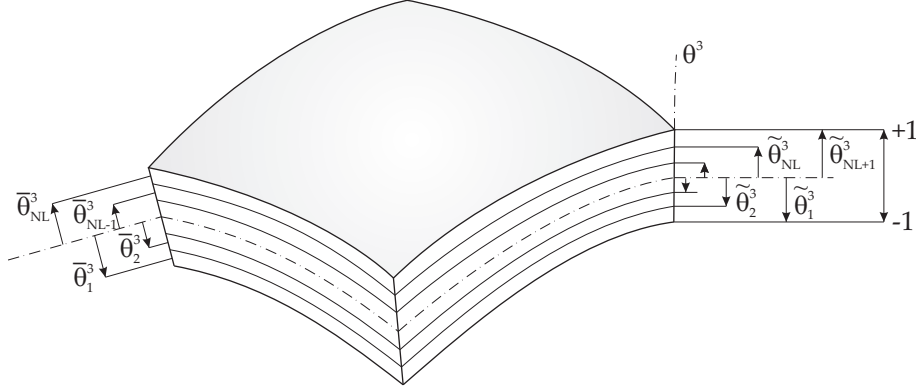


Figure 4.3: Piezoelectric Composite: Definition of layer interfaces and layer mid-surfaces.

coordinate of layer L to the laminate thickness coordinate (Figure 4.4) allows for an application of the standard Gaussian integration rules [PN79]:

$$\theta^3 = -1 + \frac{1}{h} \left[-h_L (1 - \theta_L^3) + 2 \sum_{i=1}^L h_i \right] \quad (4.66)$$

$$d\theta^3 = \frac{h_L}{h} d\theta_L^3 \quad (4.67)$$

Using this transformation, each single layer L can be integrated on $\theta_L^3 \in [-1, +1]$. Thus the equations (4.51) - (4.53) can be rewritten in the context of layered piezoelectric structures as:

$$D_{C,M}^{ijkl} = \sum_{L=1}^{NL} \frac{h_L}{h^{M+1}} \int_{-1}^1 \left[-h - h_L (1 - \theta_L^3) + 2 \sum_{i=1}^L h_i \right]^M \cdot C_L^{ijkl} \bar{\mu}_{\theta_L} d\theta_L^3, \quad \text{with } M \in \{0,1,2\} \quad (4.68)$$

$$D_{e,M}^{ijk} = \sum_{L=1}^{NL} \frac{h_L}{h^{M+1}} \int_{-1}^1 \left[-h - h_L (1 - \theta_L^3) + 2 \sum_{i=1}^L h_i \right]^M \cdot e^{ijk} \bar{\mu}_{\theta_L} d\theta_L^3, \quad \text{with } M \in \{0,1,2\} \quad (4.69)$$

$$D_{\epsilon,M}^{il} = \sum_{L=1}^{NL} \frac{h_L}{h^{M+1}} \int_{-1}^1 \left[-h - h_L (1 - \theta_L^3) + 2 \sum_{i=1}^L h_i \right]^M \cdot \epsilon^{ijk} \bar{\mu}_{\theta_L} d\theta_L^3, \quad \text{with } M \in \{0,1,2\} \quad (4.70)$$

where $\bar{\mu}_{\theta_L}$ represents the shell shifter that adopts as well the transformed dependency from the thickness coordinate θ^3 .

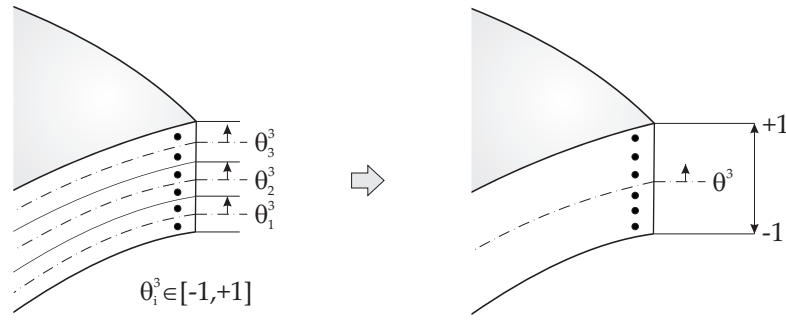


Figure 4.4: Piezoelectric Composite: Transformation of layer thickness coordinates into laminate coordinate system (number of Gaussian points depicted with dots).

4.5 Discretization

In the preceding sections, the finite element formulation has been investigated in a general continuum mechanical description. The semi-discretization in thickness direction has been performed in order to apply a pre-integration of the material law in thickness direction. Now the discretization of the shell mid-surface shall be done. The piezoelectric finite elements of this work belong to the class of Lagrange elements. An explicit definition of shape functions and related node numbering can be found in appendix A. It should be pointed out that so far no assumptions about the discretization of the element mid-surface have been made. Thus all derivations so far apply for any element discretization. However, special focus is put on the 4-noded quadrilateral element in the sequel for the specification and explanation of EAS modes and EAE modes.

4.5.1 Approximation of Geometry and Generalized Displacements

In the sequel, a general discretization formulation for an element with n nodes is pursued. Adopting the shape functions $N_I = N_I(\xi, \eta)$, the position vector R and the director A_3 are discretized as follows:

$$\mathbf{R}_h = N_I \mathbf{R}^I \quad (4.71)$$

$$\mathbf{A}_{3h} = N_I \mathbf{A}_3^I \quad (4.72)$$

where the shape functions N_I have to fulfill the geometric constraint:

$$\sum_{I=1}^n N_I = 1 \quad (4.73)$$

In the case of Lagrange shape functions, the fulfillment of equ. (4.73) is a fundamental condition to guarantee completeness (see chapter 3.2). The index h stands for the characteristic element size at the discretization and indicates the finite element approximation.

At finite element nodes that belong to several elements, an averaged director is constructed. This averaging is by no means a simplification or approximation [Bis99], but follows from the degeneration concept (see also chapter 1.2.2) and reflects the effects of the discretization of curved structures.

The base vectors \mathbf{A}_1 and \mathbf{A}_2 are the derivatives of the position vector \mathbf{R} with respect to the convective coordinates according to equ. (4.1). Thus it holds:

$$\mathbf{A}_{\alpha_h} = N_{I,\alpha} \mathbf{R}^I \quad (4.74)$$

with

$$N_{I,1} = \frac{\partial N_I}{\partial \xi}, \quad N_{I,2} = \frac{\partial N_I}{\partial \eta} \quad (4.75)$$

Finite element formulations are called *isoparametric*¹ if the same set of shape functions is used for the interpolation of the element geometry as well as the primary variables [ZTZ05]. In this work, only isoparametric element formulations are developed. Thus the primary variables are interpolated within the element with:

$$\mathbf{v}_h = N_I \mathbf{v}^I \quad (4.76)$$

$$\mathbf{w}_h = N_I \mathbf{w}^I \quad (4.77)$$

$$\Delta \varphi_h = N_I \Delta \varphi^I \quad (4.78)$$

From equ. (4.76) and (4.77) it follows for the discretized displacement vector:

$$\mathbf{u}_h = \begin{bmatrix} v_{1_h} \\ v_{2_h} \\ v_{3_h} \end{bmatrix} + \theta^3 \begin{bmatrix} w_{1_h} \\ w_{2_h} \\ w_{3_h} \end{bmatrix} \quad (4.79)$$

Furthermore, the discretized version of the generalized vector of primary variables can be defined as follows:

$$\bar{\mathbf{u}}_h = \begin{bmatrix} u_h \\ \Delta \varphi_h \end{bmatrix} = \bar{\mathbf{N}} \cdot \bar{\mathbf{d}} \quad (4.80)$$

with

$$\bar{\mathbf{N}} = \begin{bmatrix} N_1 & 0 & 0 & \zeta N_1 & 0 & 0 & 0 & \dots & N_n & 0 & 0 & \zeta N_n & 0 & 0 & 0 \\ 0 & N_1 & 0 & 0 & \zeta N_1 & 0 & 0 & \dots & 0 & N_n & 0 & 0 & \zeta N_n & 0 & 0 \\ 0 & 0 & N_1 & 0 & 0 & \zeta N_1 & 0 & \dots & 0 & 0 & N_n & 0 & 0 & \zeta N_n & 0 \\ 0 & 0 & 0 & 0 & 0 & 0 & N_1 & \dots & 0 & 0 & 0 & 0 & 0 & 0 & N_n \end{bmatrix} \quad (4.81)$$

and

$$\bar{\mathbf{d}}^T = \left[v_1^1 \ v_2^1 \ v_3^1 \ w_1^1 \ w_2^1 \ w_3^1 \ \Delta \varphi^1 \mid \dots \mid v_1^n \ v_2^n \ v_3^n \ w_1^n \ w_2^n \ w_3^n \ \Delta \varphi^n \right] \quad (4.82)$$

¹From ancient Greek: *ισο* = equal

Thus the vector $\bar{\mathbf{d}}$ comprises all displacement and potential difference degrees of freedom of the finite element. Furthermore, the discretized directors of the actual configuration can be defined using equ. (4.76) and (4.77):

$$\mathbf{a}_{\alpha_h} = N_{I,\alpha} \mathbf{r}^I = N_{I,\alpha} \mathbf{R}^I + N_{I,\alpha} \mathbf{v}^I \quad (4.83)$$

$$\mathbf{a}_{3_h} = N_I \mathbf{a}_3^I + N_I \mathbf{w}^I \quad (4.84)$$

Beyond that, also the variation of the covariant base vectors in both configurations is needed:

$$\delta \mathbf{A}_\alpha = \delta \mathbf{A}_3 = 0 \quad \rightarrow \quad \delta \mathbf{A}_{\alpha_h} = \delta \mathbf{A}_{3_h} = 0 \quad (4.85)$$

$$\delta \mathbf{a}_\alpha = \delta \mathbf{v}_{,\alpha} \quad \rightarrow \quad \delta \mathbf{a}_{\alpha_h} = N_{I,\alpha} \delta \mathbf{v}^I \quad (4.86)$$

$$\delta \mathbf{a}_3 = \delta \mathbf{w} \quad \rightarrow \quad \delta \mathbf{a}_{3_h} = N_I \delta \mathbf{w}^I \quad (4.87)$$

4.5.2 Approximation of Strains and Electric Field Strength

The discretized electric field strength is directly obtained from equ. (4.30):

$$\vec{E}_{\alpha_h}^\varphi = -N_{I,\alpha} \Delta \varphi^I \quad (4.88)$$

The component in thickness direction is obtained with

$$\vec{E}_{3_h}^\varphi = -\frac{1}{2} N_I \Delta \varphi^I \quad (4.89)$$

The discretized strain tensor is derived from equ. (4.16) with the related components of equ. (4.17) - (4.22). Inserting the discretized base vectors according to equ. (4.72), (4.74), (4.83) and (4.84) leads to the discretized representation. In accordance to equ. (4.40), a generalized discretized strain vector can be generated:

$$\mathbf{E}_h^{\mathbf{u}\varphi} = \left[\alpha_{11_h}^u \alpha_{12_h}^u \alpha_{13_h}^u \alpha_{22_h}^u \alpha_{23_h}^u \alpha_{33_h}^u \beta_{11_h}^u \beta_{12_h}^u \beta_{13_h}^u \beta_{22_h}^u \beta_{23_h}^u \ 0 \ \vec{\alpha}_{1_h}^\varphi \ \vec{\alpha}_{2_h}^\varphi \ \vec{\alpha}_{3_h}^\varphi \ 0 \ 0 \ 0 \right] \quad (4.90)$$

Furthermore, for the discretization of the modified Hu-Washizu functional according to equ. (3.31), a representation of the variation of strain tensor and electric field strength is needed. In this context, it holds:

$$\delta \mathbf{E}_h^{\mathbf{u}} = \frac{\partial \mathbf{E}_h^{\mathbf{u}}}{\partial \bar{\mathbf{d}}} \delta \bar{\mathbf{d}} = \mathbf{E}_{h,d}^{\mathbf{u}} \delta \bar{\mathbf{d}} \quad (4.91)$$

$$\delta \vec{E}_h^\varphi = \frac{\partial \vec{E}_h^\varphi}{\partial \bar{\mathbf{d}}} \delta \bar{\mathbf{d}} = \vec{E}_{h,d}^\varphi \delta \bar{\mathbf{d}} \quad (4.92)$$

Thus the single strain tensor components can be derived:

$$\delta\alpha_{\alpha\beta}^u = \frac{1}{2} (\delta\mathbf{a}_\alpha \cdot \mathbf{a}_\beta + \mathbf{a}_\alpha \cdot \delta\mathbf{a}_\beta) \quad (4.93)$$

$$\delta\alpha_{\alpha 3}^u = \frac{1}{2} (\delta\mathbf{a}_\alpha \cdot \mathbf{a}_3 + \mathbf{a}_\alpha \cdot \delta\mathbf{a}_3) \quad (4.94)$$

$$\delta\alpha_{33}^u = \delta\mathbf{a}_3 \cdot \mathbf{a}_3 \quad (4.95)$$

$$\delta\beta_{\alpha\beta}^u = \frac{1}{2} (\delta\mathbf{a}_\alpha \cdot \mathbf{a}_{3,\beta} + \mathbf{a}_\alpha \cdot \delta\mathbf{a}_{3,\beta} + \delta\mathbf{a}_\beta \cdot \mathbf{a}_{3,\alpha} + \mathbf{a}_\beta \cdot \delta\mathbf{a}_{3,\alpha}) \quad (4.96)$$

$$\delta\beta_{\alpha 3}^u = \frac{1}{2} (\delta\mathbf{a}_{3,\alpha} \cdot \mathbf{a}_3 + \mathbf{a}_{3,\alpha} \cdot \delta\mathbf{a}_3) \quad (4.97)$$

$$\delta\bar{\alpha}_\alpha^\varphi = -\delta\Delta\varphi_{,\alpha} \quad (4.98)$$

$$\delta\bar{\alpha}_3^\varphi = -\frac{1}{2}\delta\Delta\varphi \quad (4.99)$$

This leads in discretized form to:

$$\delta\alpha_{\alpha\beta}^u = \frac{1}{2} (\mathbf{a}_\beta N_{I,\alpha} + \mathbf{a}_\alpha N_{I,\beta}) \delta\mathbf{v}^I = \boldsymbol{\alpha}_{\alpha\beta}^{u'} \cdot \delta\bar{\mathbf{d}} \quad (4.100)$$

$$\delta\alpha_{\alpha 3}^u = \frac{1}{2} (\mathbf{a}_3 N_{I,\alpha} \delta\mathbf{v}^I + \mathbf{a}_\alpha N_I \delta\mathbf{w}^I) = \boldsymbol{\alpha}_{\alpha 3}^{u'} \cdot \delta\bar{\mathbf{d}} \quad (4.101)$$

$$\delta\alpha_{33}^u = \mathbf{a}_3 N_I \delta\mathbf{w}^I = \boldsymbol{\alpha}_{33}^{u'} \cdot \delta\bar{\mathbf{d}} \quad (4.102)$$

$$\delta\beta_{\alpha\beta}^u = \frac{1}{2} (\mathbf{a}_{3,\alpha} N_{I,\beta} + \mathbf{a}_{3,\beta} N_{I,\alpha}) \delta\mathbf{v}^I + \frac{1}{2} (\mathbf{a}_\alpha N_{I,\beta} + \mathbf{a}_\beta N_{I,\alpha}) \delta\mathbf{w}^I = \boldsymbol{\beta}_{\alpha\beta}^{u'} \cdot \delta\bar{\mathbf{d}} \quad (4.103)$$

$$\delta\beta_{\alpha 3}^u = \frac{1}{2} (\mathbf{a}_{3,\alpha} N_I + \mathbf{a}_3 N_{I,\alpha}) \delta\mathbf{w}^I = \boldsymbol{\beta}_{\alpha 3}^{u'} \cdot \delta\bar{\mathbf{d}} \quad (4.104)$$

$$\delta\bar{\alpha}_\alpha^\varphi = N_{I,\alpha} \delta\Delta\varphi^I = \bar{\boldsymbol{\alpha}}_{\alpha h}^{\varphi'} \cdot \delta\bar{\mathbf{d}} \quad (4.105)$$

$$\delta\bar{\alpha}_3^\varphi = \frac{1}{2} N_I \delta\Delta\varphi^I = \bar{\boldsymbol{\alpha}}_{3h}^{\varphi'} \cdot \delta\bar{\mathbf{d}} \quad (4.106)$$

Also the variation components can be collected in a generalized vector form:

$$\bar{\mathbf{E}}_{h,d}^{u\varphi} = \left[\boldsymbol{\alpha}_{11h}^{u'} \ \boldsymbol{\alpha}_{12h}^{u'} \ \boldsymbol{\alpha}_{13h}^{u'} \ \boldsymbol{\alpha}_{22h}^{u'} \ \boldsymbol{\alpha}_{23h}^{u'} \ \boldsymbol{\alpha}_{33h}^{u'} \ \boldsymbol{\beta}_{11h}^{u'} \ \boldsymbol{\beta}_{12h}^{u'} \ \boldsymbol{\beta}_{13h}^{u'} \ \boldsymbol{\beta}_{22h}^{u'} \ \boldsymbol{\beta}_{23h}^{u'} \ 0 \ \bar{\boldsymbol{\alpha}}_{1h}^{\varphi'} \ \bar{\boldsymbol{\alpha}}_{2h}^{\varphi'} \ \bar{\boldsymbol{\alpha}}_{3h}^{\varphi'} \ 0 \ 0 \ 0 \right]^T \quad (4.107)$$

Beyond that, also the second Gateaux derivatives of the terms in equ. (4.93) - (4.99) will be needed later in the context of the linearization of the functional:

$$D\delta\alpha_{\alpha\beta}^u = \frac{1}{2} (\delta\mathbf{a}_\alpha \cdot D\mathbf{a}_\beta + D\mathbf{a}_\alpha \cdot \delta\mathbf{a}_\beta) \quad (4.108)$$

$$D\delta\alpha_{\alpha 3}^u = \frac{1}{2} (\delta\mathbf{a}_\alpha \cdot D\mathbf{a}_3 + D\mathbf{a}_\alpha \cdot \delta\mathbf{a}_3) \quad (4.109)$$

$$D\delta\alpha_{33}^u = \delta\mathbf{a}_3 \cdot D\mathbf{a}_3 \quad (4.110)$$

$$D\delta\beta_{\alpha\beta}^u = \frac{1}{2} (\delta\mathbf{a}_\alpha \cdot D\mathbf{a}_{3,\beta} + D\mathbf{a}_\alpha \cdot \delta\mathbf{a}_{3,\beta} + \delta\mathbf{a}_\beta \cdot D\mathbf{a}_{3,\alpha} + D\mathbf{a}_\beta \cdot \delta\mathbf{a}_{3,\alpha}) \quad (4.111)$$

$$D\delta\beta_{\alpha 3}^u = \frac{1}{2} (\delta\mathbf{a}_{3,\alpha} \cdot D\mathbf{a}_3 + D\mathbf{a}_{3,\alpha} \cdot \delta\mathbf{a}_3) \quad (4.112)$$

$$D\delta\bar{\alpha}_\alpha^\varphi = 0 \quad (4.113)$$

$$D\delta\bar{\alpha}_3^\varphi = 0 \quad (4.114)$$

A discretization leads to:

$$\bar{\mathbf{E}}_{h,dd}^{\mathbf{u}\varphi} = \left[\alpha_{11h}^{u'''} \alpha_{12h}^{u'''} \alpha_{13h}^{u'''} \alpha_{22h}^{u'''} \alpha_{23h}^{u'''} \alpha_{33h}^{u'''} \beta_{11h}^{u'''} \beta_{12h}^{u'''} \beta_{13h}^{u'''} \beta_{22h}^{u'''} \beta_{23h}^{u'''} 0 \bar{\alpha}_{1h}^{\varphi''} \bar{\alpha}_{2h}^{\varphi''} \bar{\alpha}_{3h}^{\varphi''} 0 0 0 \right]^T \quad (4.115)$$

with:

$$D\delta\alpha_{\alpha\beta}^u = \frac{1}{2}\Delta\mathbf{v}^K (N_{K,\beta}N_{I,\alpha} + N_{K,\alpha}N_{I,\beta}) \delta\mathbf{v}^I = \Delta\bar{\mathbf{d}}^T \alpha_{\alpha\beta}^{u'''} \delta\bar{\mathbf{d}} \quad (4.116)$$

$$D\delta\alpha_{\alpha 3}^u = \frac{1}{2} \left(\Delta\mathbf{w}^K N_K N_{I,\alpha} \delta\mathbf{v}^I + \Delta\mathbf{v}^K N_{K,\alpha} N_I \delta\mathbf{w}^I \right) = \Delta\bar{\mathbf{d}}^T \alpha_{\alpha 3}^{u'''} \delta\bar{\mathbf{d}} \quad (4.117)$$

$$D\delta\alpha_{33}^u = \Delta\mathbf{w}^K N_K N_I \delta\mathbf{w}^I = \Delta\bar{\mathbf{d}}^T \alpha_{33}^{u'''} \delta\bar{\mathbf{d}} \quad (4.118)$$

$$\begin{aligned} D\delta\beta_{\alpha\beta}^u &= \frac{1}{2}\Delta\mathbf{w}^K (N_{K,\alpha}N_{I,\beta} + N_{K,\beta}N_{I,\alpha}) \delta\mathbf{v}^I + \frac{1}{2}\Delta\mathbf{v}^K (N_{K,\alpha}N_{I,\beta} + N_{K,\beta}N_{I,\alpha}) \delta\mathbf{w}^I \\ &= \Delta\bar{\mathbf{d}}^T \beta_{\alpha\beta}^{u'''} \delta\bar{\mathbf{d}} \end{aligned} \quad (4.119)$$

$$D\delta\beta_{\alpha 3}^u = \frac{1}{2}\Delta\mathbf{w}^K (N_{K,\alpha}N_I + N_K N_{I,\alpha}) \delta\mathbf{w}^I = \Delta\bar{\mathbf{d}}^T \beta_{\alpha 3}^{u'''} \delta\bar{\mathbf{d}} \quad (4.120)$$

$$D\delta\bar{\alpha}_{\alpha}^{\varphi} = \bar{\alpha}_{\alpha h}^{\varphi''} = 0 \quad (4.121)$$

$$D\delta\bar{\alpha}_{3}^{\varphi} = \bar{\alpha}_{3h}^{\varphi''} = 0 \quad (4.122)$$

4.5.3 EAS and EAE Method

Besides to the displacement field and the electric potential field, also the enhanced modes have to be discretized. However, as the contravariant base vectors are dependent from the finite element mesh as well as from position within the element, it is not recommendable to directly discretize

$$\tilde{\mathbf{E}} = \tilde{E}_{ij} \mathbf{G}^i \otimes \mathbf{G}^j \quad (4.123)$$

$$\tilde{\mathbf{E}} = \tilde{E}_i \mathbf{G}^i \quad (4.124)$$

The reason is that the orthogonality conditions according to equ. (2.160) and (2.161) can be hardly fulfilled within convective coordinate systems which are by nature position-dependent. Thus the enhanced modes shall be defined with respect to a basis that does not interfere with the wanted behavior of the discretization. Consequently, the enhanced modes are defined in the basis of the contravariant vectors \mathbf{A}_0^i on the element center on the element mid-surface. This approach reflects the suggestion of Simo und Rifai in 1990 to define the enhanced strains in a suitable local coordinate system in order to pass the patch test for arbitrary geometries (see also chapter 4.6.1 for a separate discussion of this issue). The final enhanced modes are then obtained via tensor transformation as shown in equ. (2.17) postulating

$$\tilde{E}_{ij} \mathbf{G}^i \otimes \mathbf{G}^j = \tilde{E}_{ij}^0 \mathbf{A}_0^i \otimes \mathbf{A}_0^j \quad (4.125)$$

$$\tilde{E}_i \mathbf{G}^i = \tilde{E}_i^0 \mathbf{A}_0^i \quad (4.126)$$

The enhanced modes in the sequel are all defined in this fixed coordinate system in the center of the element mid-surface. Similarly to the approach of the preceding sections, the enhanced strains and enhanced electrical field strength terms are collected in one generalized vector.

$$\bar{\mathbf{E}}_h = \tilde{\mathbf{M}}\boldsymbol{\alpha} + \bar{\mathbf{M}}\bar{\boldsymbol{\alpha}} = \bar{\mathbf{M}}\bar{\boldsymbol{\alpha}} \quad (4.127)$$

where $\bar{\mathbf{M}}$ represents the matrix of enhanced modes and the vector $\bar{\boldsymbol{\alpha}}$ contains the related degrees of freedom. Assuming a 4-noded quadrilateral element, the following enhanced modes are reasonable:

$$\tilde{\mathbf{M}} = \begin{bmatrix} \zeta & 0 & 0 & 0 & 0 & 0 & 0 & 0 & 0 & 0 & 0 & 0 & 0 & 0 & 0 & 0 & 0 & 0 & 0 & 0 \\ 0 & 0 & \zeta & \eta & 0 & 0 & 0 & 0 & 0 & 0 & 0 & 0 & 0 & 0 & 0 & 0 & 0 & 0 & 0 & 0 \\ 0 & 0 & 0 & 0 & 0 & 0 & 0 & 0 & 0 & 0 & 0 & 0 & \zeta & \zeta\eta & 0 & 0 & 0 & 0 & 0 & 0 \\ 0 & \eta & 0 & 0 & 0 & 0 & 0 & 0 & 0 & 0 & 0 & 0 & 0 & 0 & 0 & 0 & 0 & 0 & 0 & 0 \\ 0 & 0 & 0 & 0 & 0 & 0 & 0 & 0 & 0 & 0 & 0 & 0 & 0 & 0 & \eta & \zeta\eta & 0 & 0 & 0 & 0 \\ 0 & 0 & 0 & 0 & 0 & 0 & 0 & 0 & 0 & 0 & 0 & 0 & 0 & 0 & 0 & 0 & 0 & 0 & 0 & 0 \\ 0 & 0 & 0 & 0 & \zeta & 0 & 0 & 0 & 0 & 0 & 0 & 0 & 0 & 0 & 0 & 0 & 0 & 0 & 0 & 0 \\ 0 & 0 & 0 & 0 & 0 & 0 & \zeta & \eta & 0 & 0 & 0 & 0 & 0 & 0 & 0 & 0 & 0 & 0 & 0 & 0 \\ 0 & 0 & 0 & 0 & 0 & 0 & 0 & 0 & 0 & 0 & 0 & 0 & 0 & 0 & 0 & 0 & 0 & \zeta & \zeta\eta & 0 & 0 \\ 0 & 0 & 0 & 0 & 0 & \eta & 0 & 0 & 0 & 0 & 0 & 0 & 0 & 0 & 0 & 0 & 0 & 0 & 0 & 0 & 0 \\ 0 & 0 & 0 & 0 & 0 & 0 & 0 & 0 & 0 & 0 & 0 & 0 & 0 & 0 & 0 & 0 & 0 & 0 & 0 & \eta & \zeta\eta \\ 0 & 0 & 0 & 0 & 0 & 0 & 0 & 0 & 0 & 0 & 1 & \zeta & \eta & \zeta\eta & 0 & 0 & 0 & 0 & 0 & 0 & 0 \\ 0 & 0 \\ 0 & 0 \\ 0 & 0 \\ 0 & 0 \\ 0 & 0 \\ 0 & 0 \\ 0 & 0 \end{bmatrix}$$

membrane stresses
bending stresses
thickness stresses
const. shear stresses
lin. shear stresses

(4.128)

In general, the enhanced assumed strain modes allow for a stepwise supplementation of the existing displacement-based strains according to equ. (4.107). Thus incompatible approximation spaces can be adjusted and parasitic strains can be eliminated with suitable enhanced modes.

Columns 1 - 4 in equ. (4.128) add the missing terms to provide membrane stresses that are linear in both ζ and η . As a next step, also the mixed terms for a complete bilinear representation in ζ and η could be added.

Columns 5 - 8 in equ. (4.128) add missing modes of the bending strains. Just as in the case of the membrane modes, as well here the mixed terms $\zeta\eta$ could additionally be added to generate a complete bilinear representation.

The linear thickness deformation has been introduced in the 9th column of matrix $\tilde{\mathbf{M}}$. Thus the existence of this enhanced mode decides about the existence of the 7th parameter of the element formulation. If no enhanced thickness strains are added here, the

element represents only a 6-parameter formulation (compare section 1.2.2). Modes 10-12 complete the linear thickness deformations to be bilinear in ζ and η .

The columns 13 - 16 in equ. (4.128) provide the needed enhanced modes of (in thickness direction) constant shear to eliminate shear locking. The modes 13 and 15 can be compared with the enhanced modes of column 3 and 4 of the 2D illustration example in equ. (3.32) in chapter 3.6.3. In both cases, enhanced shear modes are offered in order to allow for a "decoupling" of bending modes from related parasitic strains.

Finally, columns 17 - 20 offer (in thickness direction) linear enhanced shear modes that are in total bilinear ζ and η .

The second part of matrix $\vec{\mathbf{M}}$ according to equ. (4.127) offers in a similar manner enhanced modes for the electric field strength:

$$\vec{\mathbf{M}} = \begin{array}{c} \left[\begin{array}{cccc|cccc} 0 & 0 & 0 & 0 & 0 & 0 & 0 & 0 \\ 0 & 0 & 0 & 0 & 0 & 0 & 0 & 0 \\ 0 & 0 & 0 & 0 & 0 & 0 & 0 & 0 \\ 0 & 0 & 0 & 0 & 0 & 0 & 0 & 0 \\ 0 & 0 & 0 & 0 & 0 & 0 & 0 & 0 \\ 0 & 0 & 0 & 0 & 0 & 0 & 0 & 0 \\ 0 & 0 & 0 & 0 & 0 & 0 & 0 & 0 \\ 0 & 0 & 0 & 0 & 0 & 0 & 0 & 0 \\ 0 & 0 & 0 & 0 & 0 & 0 & 0 & 0 \\ 0 & 0 & 0 & 0 & 0 & 0 & 0 & 0 \\ 0 & 0 & 0 & 0 & 0 & 0 & 0 & 0 \\ 0 & 0 & 0 & 0 & 0 & 0 & 0 & 0 \\ 0 & 0 & 0 & 0 & 0 & 0 & 0 & 0 \\ 0 & 0 & 0 & 0 & 0 & 0 & 0 & 0 \\ 0 & 0 & 0 & 0 & 0 & 0 & 0 & 0 \\ 0 & 0 & 0 & 0 & 0 & 0 & 0 & 0 \\ 0 & 0 & 0 & 0 & 0 & 0 & 0 & 0 \\ 1 & 0 & \zeta & 0 & 0 & 0 & 0 & 0 \\ 0 & 1 & 0 & \eta & 0 & 0 & 0 & 0 \\ 0 & 0 & 0 & 0 & 0 & 0 & 0 & 0 \\ 0 & 0 & 0 & 0 & 0 & 0 & 0 & 0 \\ 0 & 0 & 0 & 0 & 0 & 0 & 0 & 0 \\ 0 & 0 & 0 & 0 & 0 & 0 & 0 & 0 \\ 0 & 0 & 0 & 0 & 1 & \zeta & \eta & \zeta\eta \end{array} \right] \end{array} \quad (4.129)$$

const. \vec{E}_a

lin. el. field \vec{E}_3

The already existing electric field modes for \vec{E}_1 and \vec{E}_2 according to equ. (4.105) only offer a coupled combination of constant and linear electric field components. This causes electromechanical locking under shear loading as presented in Figure 3.13 in chapter 3.5.4.2. For this reason, columns 1 and 2 of matrix $\vec{\mathbf{M}}$ in equ. (4.129) offer independent modes of constant electric field components \vec{E}_1 and \vec{E}_2 . This allows for a constant or linear behavior of \vec{E}_1 and \vec{E}_2 without parasitic electric field contributions (see also the shear patch test example in chapter 7.1.6). For distorted meshes, columns 3 and 4 in equ. (4.129) provide missing modes that are linear in ζ and η .

Intentionally, no enhanced modes for the constant electric field \vec{E}_3 are added. This is due to the fact that this field is already completely described by the original element formu-

lation. Eventually offered enhanced modes of this type would violate the prerequisite of linear independence from the compatible modes and thus lead to singularities in the element formulation (compare chapter 3.6.3.4). For similar reasons, Legner introduces constant enhanced modes only in the context of \vec{E}_1 and \vec{E}_2 [Leg11].

Furthermore, columns 5 - 8 in equ. (4.129) provide a complete representation of the in thickness linear behaving electric field component \vec{E}_3 which is completely missing in the electric field modes derived from the kinematic relations. These modes are needed to correctly represent the case of pure bending as described in chapter 3.5.4.1.

Additionally, further electric field modes could be added just as described in the context of enhanced strains. However, it will be shown in the examples in chapter 7 that the enhanced electric field modes as presented in equ. (4.129) can already efficiently eliminate the discussed locking effects. For the variation of the strain tensor, it holds:

$$\delta \tilde{\mathbf{E}}_h = \frac{\partial \tilde{\mathbf{E}}_h}{\partial \tilde{\mathbf{a}}} \delta \tilde{\mathbf{a}} = \tilde{\mathbf{E}}_{h,\tilde{\mathbf{a}}} \delta \tilde{\mathbf{a}} \quad (4.130)$$

In the case of the standard Hu-Washizu functional the stresses as well as the electric displacement would have to be discretized. This would also require to consider additional conditions concerning number and construction of the related basis functions in order to guarantee numerical element stability [BF91]. As the presented modified Hu-Washizu functional has been adopted, the stresses as well as the electric displacement are not needed to be discretized.

4.5.4 ANS Method

For the elimination of transverse shear locking, the ANS method is applied as efficient alternative to the EAS method. As the element is defined via the natural coordinate system of the element, an easy identification of the transverse shear terms is possible.

The collocation points can be determined via the investigation of the parasitic strains in suitable test cases. For the 4-noded element, the collocation points can be identified in accordance with the MITC4 element presented in chapter 3.6.2 with:

$$\begin{aligned} (\xi_A, \eta_A) &= (0,1), \quad (\xi_B, \eta_B) = (0, -1) \quad \text{for } \alpha_{13_h}^u \\ (\xi_C, \eta_C) &= (1,0), \quad (\xi_D, \eta_D) = (-1,0) \quad \text{for } \alpha_{23_h}^u \end{aligned} \quad (4.131)$$

For the collocation points of other discretizations like the 9-noded quadrilateral element, the reader is referred to the literature [BR92b, Bis99]. Now the discrete transverse shear strains at the collocation points K can be evaluated:

$$\alpha_{13_h}^{uK} = \mathbf{B}_S^{\xi}(\xi_K, \eta_K) \cdot \mathbf{d} \quad (4.132)$$

$$\alpha_{23_h}^{uK} = \mathbf{B}_S^{\eta}(\xi_K, \eta_K) \cdot \mathbf{d} \quad (4.133)$$

where the index S of the B-operator indicates shear just as in equ. (3.29) at the introduction of the ANS method. The discretized strain values are then determined via the ANS shape functions:

$$\alpha_{13_h}^u = \sum_{K=1}^{n_K} \bar{N}_K^{\zeta} \alpha_{13_h}^{uK} \quad (4.134)$$

$$\alpha_{23_h}^u = \sum_{K=1}^{n_K} \bar{N}_K^{\eta} \alpha_{23_h}^{uK} \quad (4.135)$$

with n_K being the number of collocation points. In the case of the 4-noded quadrilateral, equ. (4.134) and (4.135) can be specified to:

$$\alpha_{13_h}^u = \frac{1}{2} (1 + \eta) \alpha_{13_h}^{uA} + \frac{1}{2} (1 - \eta) \alpha_{13_h}^{uB} \quad (4.136)$$

$$\alpha_{23_h}^u = \frac{1}{2} (1 + \zeta) \alpha_{23_h}^{uC} + \frac{1}{2} (1 - \zeta) \alpha_{23_h}^{uD} \quad (4.137)$$

Thus in total the ANS-modified transverse shear strains are obtained to be:

$$\alpha_{13_h}^u = \sum_{K=1}^{n_K} \left[\bar{N}_K^{\zeta} \mathbf{B}_S^{\zeta}(\zeta_K, \eta_K) \right] \cdot \mathbf{d} = \bar{\mathbf{B}}_S^{\zeta} \cdot \mathbf{d} \quad (4.138)$$

$$\alpha_{23_h}^u = \sum_{K=1}^{n_K} \left[\bar{N}_K^{\eta} \mathbf{B}_S^{\eta}(\zeta_K, \eta_K) \right] \cdot \mathbf{d} = \bar{\mathbf{B}}_S^{\eta} \cdot \mathbf{d} \quad (4.139)$$

In equ. (4.107), the initial transverse shear terms are replaced by the ANS-modified terms. As a consequence, also the Gateaux derivatives according to equ. (4.109) are affected by the ANS improvements. As the next chapter will reveal, this means that the ANS method provides modifications for both the elastic stiffness matrix and the geometric stiffness matrix.

4.6 Linearization of Weak Form

Recalling equ. (3.31), the discretized version of the modified Hu-Washizu functional related to one element can be described with:

$$\begin{aligned} \delta \Pi_{MHW}^e(\mathbf{u}, \varphi, \tilde{\mathbf{E}}, \tilde{\tilde{\mathbf{E}}}) &\approx \delta \Pi_{MHW_h}(\bar{\mathbf{d}}, \bar{\alpha}) \\ &= \int_{\Omega} \left[\delta \mathbf{E}_h^u : \mathbf{S}_h^E + \delta \tilde{\mathbf{E}}_h : \mathbf{S}_h^{\tilde{\mathbf{E}}} - \delta \tilde{\mathbf{E}}_h^{\varphi} : \tilde{\mathbf{D}}_h^{\tilde{\mathbf{E}}\varphi} - \delta \tilde{\tilde{\mathbf{E}}}_h : \tilde{\mathbf{D}}_h^{\tilde{\tilde{\mathbf{E}}}} \right] dV - \delta \Pi_{MHW}^{ext} \\ &= \int_{A_e} \left[\delta \tilde{\mathbf{E}}_h^{u\varphi} \cdot \tilde{\mathbf{S}}_h^{E^{u\varphi}} + \delta \tilde{\tilde{\mathbf{E}}}_h \cdot \tilde{\mathbf{S}}_h^{\tilde{\mathbf{E}}} \right] dA - \delta \Pi_{MHW}^{ext} \\ &= \delta \bar{\mathbf{d}} \int_{A_e} \tilde{\mathbf{E}}_{h,d}^{u\varphi} \cdot \tilde{\mathbf{S}}_h^{E^{u\varphi}} dA + \delta \bar{\alpha} \int_{A_e} \tilde{\tilde{\mathbf{E}}}_{h,\alpha} \cdot \tilde{\mathbf{S}}_h^{\tilde{\mathbf{E}}} dA - \delta \Pi_{MHW}^{ext h} \\ &= 0 \end{aligned} \quad (4.140)$$

with

$$\delta\Pi_{MHW}^{ext} = \bar{\mathbf{P}} \cdot \delta\bar{\mathbf{d}} \quad (4.141)$$

where $\bar{\mathbf{P}}$ represents the generalized load vector that is assumed to be independent from the displacement field. Furthermore, equ. (4.140) takes advantage of the generalized vector representations introduced in the last sections.

For the solution of the nonlinear equation system, iterative predictor-corrector methods like the Newton-Raphson approach are recommendable. The reader is referred to the literature for the various incremental solution schemes (e.g. [Arg65, Cri81, Ram81]). For the iterative solution process, a linearized form of the varied potential in equ. (4.140) is needed:

$$\delta\Pi_{MHW}^e(\bar{\mathbf{d}}, \bar{\boldsymbol{\alpha}}) = \text{LIN } \delta\Pi_{MHW}^e(\bar{\mathbf{d}}^i, \bar{\boldsymbol{\alpha}}^i) + R(\bar{\mathbf{d}}^i, \bar{\boldsymbol{\alpha}}^i) \quad (4.142)$$

where

$$\begin{aligned} \text{LIN } \delta\Pi_{MHW}^e(\bar{\mathbf{d}}^i, \bar{\boldsymbol{\alpha}}^i) &= \delta\Pi_{MHW}^e(\bar{\mathbf{d}}^i, \bar{\boldsymbol{\alpha}}^i) \\ &+ \left. \frac{\partial\delta\Pi_{MHW}^e(\bar{\mathbf{d}}, \bar{\boldsymbol{\alpha}})}{\partial\bar{\mathbf{d}}}\right|_{\bar{\mathbf{d}}=\bar{\mathbf{d}}^i} \Delta\bar{\mathbf{d}} + \left. \frac{\partial\delta\Pi_{MHW}^e(\bar{\mathbf{d}}, \bar{\boldsymbol{\alpha}})}{\partial\bar{\boldsymbol{\alpha}}}\right|_{\bar{\boldsymbol{\alpha}}=\bar{\boldsymbol{\alpha}}^i} \Delta\bar{\boldsymbol{\alpha}} \end{aligned} \quad (4.143)$$

The Gateaux derivatives needed in equ. (4.143) can be determined as follows:

$$\frac{\partial\delta\Pi_{MHW}^e(\bar{\mathbf{d}}, \bar{\boldsymbol{\alpha}})}{\partial\bar{\mathbf{d}}} = \delta\bar{\mathbf{d}} \int_{A_e} \bar{\mathbf{E}}_{h,dd}^{u\varphi} \cdot \bar{\mathbf{S}}_h^{E^{u\varphi}} + \bar{\mathbf{E}}_{h,d}^{u\varphi} \cdot \bar{\mathbf{S}}_{h,d}^{E^{u\varphi}} dA + \delta\bar{\boldsymbol{\alpha}} \int_{A_e} \bar{\mathbf{E}}_{h,\alpha} \cdot \bar{\mathbf{S}}_{h,d}^{\bar{E}} dA \quad (4.144)$$

$$\frac{\partial\delta\Pi_{MHW}^e(\bar{\mathbf{d}}, \bar{\boldsymbol{\alpha}})}{\partial\bar{\boldsymbol{\alpha}}} = \delta\bar{\mathbf{d}} \int_{A_e} \bar{\mathbf{E}}_{h,d}^{u\varphi} \cdot \bar{\mathbf{S}}_{h,\alpha}^{E^{u\varphi}} dA + \delta\bar{\boldsymbol{\alpha}} \int_{A_e} \bar{\mathbf{E}}_{h,\alpha} \cdot \bar{\mathbf{S}}_{h,\alpha}^{\bar{E}} dA \quad (4.145)$$

Thus using equ. (4.144) and (4.145) in equ. (4.143) leads to the linearized incremental element equation system:

$$\begin{aligned} &\delta\bar{\mathbf{d}} \int_{A_e} \bar{\mathbf{E}}_{h,d}^{u\varphi} \cdot \bar{\mathbf{S}}_h^{E^{u\varphi}} dA + \delta\bar{\boldsymbol{\alpha}} \int_{A_e} \bar{\mathbf{E}}_{h,\alpha} \cdot \bar{\mathbf{S}}_h^{\bar{E}} dA - \delta\bar{\mathbf{d}} \cdot \mathbf{P} \\ &+ \delta\bar{\mathbf{d}} \int_{A_e} \left[\bar{\mathbf{E}}_{h,dd}^{u\varphi} \cdot \bar{\mathbf{S}}_h^{E^{u\varphi}} + \bar{\mathbf{E}}_{h,d}^{u\varphi} \cdot \bar{\mathbf{S}}_{h,d}^{E^{u\varphi}} \right] dA \Delta\bar{\mathbf{d}} + \delta\bar{\boldsymbol{\alpha}} \int_{A_e} \bar{\mathbf{E}}_{h,\alpha} \cdot \bar{\mathbf{S}}_{h,d}^{\bar{E}} dA \Delta\bar{\boldsymbol{\alpha}} \\ &+ \delta\bar{\mathbf{d}} \int_{A_e} \bar{\mathbf{E}}_{h,d}^{u\varphi} \cdot \bar{\mathbf{S}}_{h,\alpha}^{E^{u\varphi}} dA \Delta\bar{\boldsymbol{\alpha}} + \delta\bar{\boldsymbol{\alpha}} \int_{A_e} \bar{\mathbf{E}}_{h,\alpha} \cdot \bar{\mathbf{S}}_{h,\alpha}^{\bar{E}} dA \Delta\bar{\boldsymbol{\alpha}} = 0 \end{aligned} \quad (4.146)$$

Several components of equ. (4.146) shall be identified in the sequel:

$$\bar{\mathbf{K}}_{el+u\varphi} = \int_{A_e} \bar{\mathbf{E}}_{h,d}^{u\varphi} \cdot \bar{\mathbf{S}}_{h,d}^{E^{u\varphi}} dA = \int_{A_e} \bar{\mathbf{B}}^T \cdot \bar{\mathbf{D}} \cdot \bar{\mathbf{B}} dA \quad (4.147)$$

represents the system matrix. The last representation in equ. (4.147) assumes a linear material law for the introduction of the matrix $\bar{\mathbf{D}}$. Furthermore,

$$\bar{\mathbf{K}}_{geo} = \int_{A_e} \bar{\mathbf{E}}_{h,dd}^{u\varphi} \cdot \bar{\mathbf{S}}_h^{E^{u\varphi}} dA \quad (4.148)$$

denotes the geometric stiffness matrix. As all enhanced modes are chosen to be linear in $\bar{\alpha}$, no contributions from EAS and EAE modes are delivered to $\bar{\mathbf{K}}_{geo}$. Beyond that, the following abbreviations are introduced:

$$\bar{\mathbf{L}}^T = \int_{A_e} \bar{\mathbf{E}}_{h,d}^{u\varphi} \cdot \bar{\mathbf{S}}_{h,\alpha}^{E^{u\varphi}} dA = \int_{A_e} \bar{\mathbf{B}}^T \cdot \bar{\mathbf{D}} \cdot \bar{\mathbf{M}} dA \quad (4.149)$$

$$\bar{\mathbf{L}} = \int_{A_e} \bar{\mathbf{E}}_{h,\alpha} \cdot \bar{\mathbf{S}}_{h,d}^E dA = \int_{A_e} \bar{\mathbf{M}}^T \cdot \bar{\mathbf{D}} \cdot \bar{\mathbf{B}} dA \quad (4.150)$$

$$\bar{\mathbf{D}} = \int_{A_e} \bar{\mathbf{E}}_{h,\alpha} \cdot \bar{\mathbf{S}}_{h,\alpha}^E dA = \int_{A_e} \bar{\mathbf{M}}^T \cdot \bar{\mathbf{D}} \cdot \bar{\mathbf{M}} dA \quad (4.151)$$

It should be pointed out that all these matrices are related to the generalized representation including both structural and electromechanical measures. Furthermore, the inner forces in equ. (4.151) are abbreviated with:

$$\bar{\mathbf{R}} = \int_{A_e} \bar{\mathbf{E}}_{h,d}^{u\varphi} \cdot \bar{\mathbf{S}}_h^{E^{u\varphi}} dA \quad (4.152)$$

$$\bar{\bar{\mathbf{R}}} = \int_{A_e} \bar{\mathbf{E}}_{h,\alpha} \cdot \bar{\mathbf{S}}_h^E dA \quad (4.153)$$

Now all abbreviations introduced in equ. (4.147) - (4.153) can be inserted in equ. (4.146). Using the fundamental lemma of variational calculus, this leads to the following representation of the linearized incremental element equation system:

$$\begin{bmatrix} \bar{\mathbf{K}}_{el+u\varphi} + \bar{\mathbf{K}}_{geo} & \bar{\mathbf{L}}^T \\ \bar{\mathbf{L}} & \bar{\mathbf{D}} \end{bmatrix} \cdot \begin{bmatrix} \Delta \bar{\mathbf{d}} \\ \Delta \bar{\alpha} \end{bmatrix} = \begin{bmatrix} \bar{\mathbf{P}} - \bar{\mathbf{R}} \\ -\bar{\bar{\mathbf{R}}} \end{bmatrix} \quad (4.154)$$

Now it becomes clear why equ. (4.149) and (4.150) have been related to each other via a transpose operation. Assuming a linear material law, $\bar{\mathbf{D}}$ is a symmetric matrix and thus it holds $(\bar{\mathbf{M}}^T \cdot \bar{\mathbf{D}} \cdot \bar{\mathbf{B}})^T = \bar{\mathbf{B}}^T \cdot \bar{\mathbf{D}} \cdot \bar{\mathbf{M}}$. With $\bar{\bar{\mathbf{D}}}^T = \bar{\bar{\mathbf{D}}}$ it holds that the overall equation system in equ. (4.154) is symmetric.

As explained in chapter 2.9.2, the enhanced strain and electric field modes can be chosen from the Lebesgue space L^2 . Thus the enhanced modes parameter $\bar{\alpha}$ do not need to fulfill compatibility beyond the element boundaries. Consequently, the parameters $\bar{\alpha}$ can be eliminated on the element level via static condensation. The lower line of equation system (4.154) can be reformulated such that:

$$\Delta \bar{\alpha} = \bar{\bar{\mathbf{D}}}^{-1} \left(-\bar{\bar{\mathbf{R}}} - \bar{\mathbf{L}} \Delta \bar{\mathbf{d}} \right) \quad (4.155)$$

Thus in total the incremental element equation system can be stated in the same form as a simple element formulation based on the principle of virtual work:

$$\bar{\mathbf{K}}_{EAS+EAE} \Delta \bar{\mathbf{d}} = \bar{\mathbf{P}} - \bar{\mathbf{R}}_{EAS+EAE} \quad (4.156)$$

with

$$\bar{\mathbf{K}}_{EAS+EAE} = \bar{\mathbf{K}}_{el+u\varphi} + \bar{\mathbf{K}}_{geo} - \bar{\mathbf{L}}^T \bar{\bar{\mathbf{D}}}^{-1} \bar{\mathbf{L}} \quad (4.157)$$

$$\bar{\mathbf{R}}_{EAS+EAE} = \bar{\mathbf{R}} - \bar{\mathbf{L}}^T \bar{\bar{\mathbf{D}}}^{-1} \bar{\bar{\mathbf{R}}} \quad (4.158)$$

The static condensation on the element level has the promising advantage that the assembled system matrix is not increased compared to standard formulations based on the virtual work principle. Modifications take only place on the element level. The subtraction of the term $\bar{\mathbf{L}}^T \bar{\mathbf{D}}^{-1} \bar{\mathbf{L}}$ in equ. (4.157) can be interpreted as well-aimed softening of the element formulation to face and eliminate locking effects.

It is also quite natural that the number of EAS and EAE modes should be chosen with consideration as they directly affect the computational cost. The number of enhanced modes determines the size of the matrices \mathbf{L} and \mathbf{D} , while the latter matrix also has to be inverted for the static condensation step. However, this computational effort for the EAS and EAE method increases only linear with the number of elements which makes this static condensation still a very favorable approach.

In general, the integrals of the system matrices and vectors according to equ. (4.147) - (4.153) are either hardly or impossible to be solved analytically. Thus all these integrals are in general determined by Gaussian quadrature.

4.6.1 Restrictions to Pass the Patch Test

In order to guarantee an a priori passing of the (structural) patch test, the parameters $\bar{\mathbf{a}}$ have to vanish in cases where $\bar{\mathbf{d}}$ represents a rigid body motion or a state of constant strain. The reason is that the original irreducible element is already able to represent constant strain and constant electric field states (compare also chapter 7.1). Thus assuming a linear problem and a field of prescribed primary variables $\bar{\mathbf{d}}_0$ (rigid body motion or constant strain or constant electric field), then the vector $\bar{\mathbf{a}}_0$ can be derived from equ. (4.154) and (4.155) such that:

$$\bar{\mathbf{a}}_0 = -\bar{\mathbf{D}}^{-1} \bar{\mathbf{L}} \bar{\mathbf{d}}_0 \quad (4.159)$$

As $\bar{\mathbf{D}}$ is a positive definite matrix [TBW76], the term $\bar{\mathbf{L}} \bar{\mathbf{d}}_0$ has to vanish in case of $\bar{\mathbf{a}}_0 = \mathbf{0}$:

$$\bar{\mathbf{L}} \bar{\mathbf{d}}_0 = \int_{A_e} \bar{\mathbf{M}}^T \bar{\mathbf{D}} \bar{\mathbf{B}} \bar{\mathbf{d}}_0 dA = 0 \quad (4.160)$$

As the generalized displacement $\bar{\mathbf{d}}_0$ has been chosen to represent a patch test case, the term $\bar{\mathbf{D}} \bar{\mathbf{B}} \bar{\mathbf{d}}_0$ must represent a state of constant stresses or constant electric displacement. Thus the requirement to pass the patch test can be reduced to:

$$\int_{A_e} \bar{\mathbf{M}} dA = 0 \quad (4.161)$$

This condition is in general only true for regular geometries like rectangles [TBW76]. Arbitrary element geometries lead in general to variable metric tensors in the natural element coordinate system. Thus it is not assured that the element can pass the patch test for arbitrary geometries. In order to remedy this deficiency, Simo and Rifai suggested in 1990 to define the strains in a suitable local element coordinate system [SR90]. Furthermore, Pian and Chen defined already in 1982 the covariant base vectors at the element

midpoint to be the basis for the definition of stress modes in the context of hybrid stress elements [PC82]. For the same reason, the enhanced strain and enhanced electric field modes are defined at the element midpoint as described in chapter 4.5.3.

Considering the base transformations according to equ. (4.125) and (4.126) leads to the following simplified requirement to pass the patch test:

$$\int_{-1}^1 \int_{-1}^1 \bar{\mathbf{M}}(\xi, \eta) d\xi d\eta = \mathbf{0} \quad (4.162)$$

This reveals a clear and easy construction rule for the enhanced strains and enhanced electric field strength modes.

4.7 Stress and Electric Displacement Recovery

After the solution of the equation system, the stress and electric displacement recovery can be done via the constitutive equations. To this goal, the EAS- and EAE- improved strains and electric fields are calculated with:

$$\mathbf{E}_h = \mathbf{E}_h^u + \tilde{\mathbf{E}}_h \quad (4.163)$$

$$\vec{\mathbf{E}}_h = \vec{\mathbf{E}}_h^\varphi + \tilde{\vec{\mathbf{E}}}_h \quad (4.164)$$

dependent from the displacements and the electric potential difference field in the nodal result vector \mathbf{d} , as well as the EAS parameters α and the EAE parameters $\vec{\alpha}$.

Using the strains and the electric field according to equ. (4.163) and (4.164), the stresses and the electric displacements can be derived from the coupled constitutive equations.

In the context of structural problems, Simo and Rifai initially casted doubt on the variational consistency of stresses that are derived like that from the material law [SR90]. However, these doubts have been eliminated by the discovery of the correlation between elements derived from the EAS method, and elements derived from the Hellinger-Reissner functional [AR93]. The material law is fulfilled pointwisely exact, both at the Hellinger-Reissner elements and at the equivalent EAS elements [BRB99].

Chapter 5

Closed-Loop Control of Lightweight Structures

As already illustrated in the introduction, structural control can be applied to structures in order to increase functionality, improve usability or to create even more efficient structures [FWB12b, FMWB11, FWB12a, FDM⁺11]. The discussion of the underlying theory shall be focus of this chapter.

5.1 Introduction to control theory

In the sequel, a short overview of basic notions of control theory shall be presented as far as needed in the context of this work. More detailed information about control theory can be found e.g. at [Oga02].

In control engineering, it is a common approach to use *block diagrams* in order to show the functions performed by each component of a control system. A block diagram of a system is a pictorial representation of the functions performed by each component and the relationships between the signals in a system. System variables are linked to each other through functional *blocks* which are symbols for the underlying mathematical operation from the input signal to the output. In general, each block in the block diagram establishes a relationship between signals. Blocks are connected with arrows which are referred to as *signals*. Signal indicate the *input* at the blocks where the arrowhead is pointing to, while in turn signals are the *output* at positions where the arrowhead is leading away from the block. An principle example is given in Figure 5.1.

The *controlled* variable, denoted with y in Figure 5.1, is the quantity or condition that is measured by the *sensor* F and it is usually the output of the system. The *manipulated* variable, denoted by u in the figure, is the quantity or condition that is varied by the *controller* C in order to affect the value of the controlled variable. Control means measuring the value of the controlled variable y and using the manipulated variable u on the system to correct the deviation of the measured value from a desired value. A *plant* P is any physical object to be controlled such as a mechanical or electromechanical structure. In the example of figure 5.1, there is also given a *reference variable* r . A summing point is used

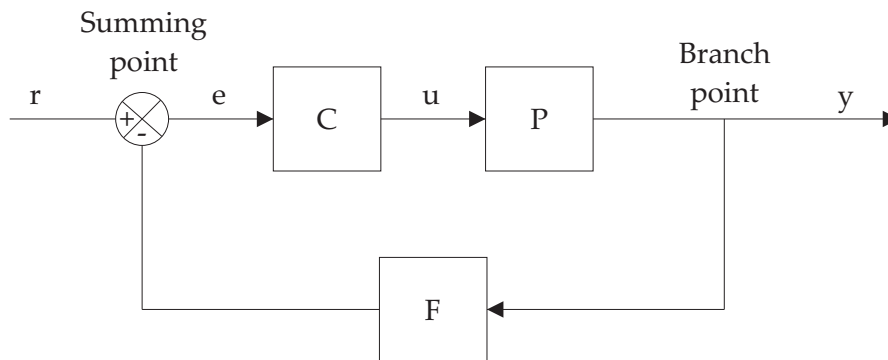


Figure 5.1: Block diagram of a closed-loop control system.

to determine the *error* e . A control system where a sensor monitors the system output and feeds the data to a controller which adjusts the control as necessary to maintain the desired system output is called a *feedback control* or *closed-loop control* system. In contrast to that, systems where the output has no effect on the control system are called *open-loop control* systems. Closed loop control has several advantages like guaranteed performance even with model uncertainties, reduced sensitivity to parameter variations and external disturbances, and improved reference tracking capabilities. However stability issues can occur in closed-loop control which is not the case for open-loop control.

In the context of control, a system is called *linear* if the principle of superposition applies. This means that the response produced by the simultaneous application of two different forcing actions is the sum of the two individual responses. Dynamic systems that are composed of linear time-invariant parameter components can be described by linear time-invariant (constant coefficient) differential equations. Consequently, such systems are called *linear time-invariant (LTI)* systems. However, approaches like the linearization with respect to an operating point have been evolved in order to apply similar approaches also to non-LTI systems. Concerning the mathematical models for control, various types have been developed. Three common representations for LTI systems are:

- Differential equations.
- State space models.
- Transfer functions.

In optimal control problems for example, it is often advantageous to use state-space representations (see also chapter 5.5). For the transient-response or frequency-response of single-input-single-output (SISO) LTI systems, the transfer function representation is more convenient than others.

In the case of LTI systems, the systems as described above can be efficiently analyzed using the Laplace transform on the variables. For the control system according to Figure 5.1, this gives the following relations for system output, system input and the error:

$$Y(s) = P(s)U(s) \quad (5.1)$$

$$U(s) = C(s)E(s) \quad (5.2)$$

$$E(s) = R(s) - F(s)Y(s) \quad (5.3)$$

Solving now for $Y(s)$ in terms of $R(s)$ leads to:

$$Y(s) = \left(\frac{P(s)C(s)}{1 + F(s)P(s)C(s)} \right) R(s) \quad (5.4)$$

In this context, the term *transfer function* has to be introduced. The transfer function of a linear, time-invariant, differential equation system is defined as the ratio of the Laplace transform of the output (*response function*) to the Laplace transform of the input (*driving function*) under the assumption that the initial conditions are zero. Let a LTI system be defined by the following differential equation:

$$a_0 \overset{(n)}{y} + a_1 \overset{(n-1)}{y} + \dots + a_{n-1} \dot{y} + a_n y = b_0 \overset{(m)}{x} + b_1 \overset{(m-1)}{x} + \dots + b_{m-1} \dot{x} + b_m x \quad (5.5)$$

where y is the output of the system and x is the input. Furthermore, it holds $n \geq m$. The transfer function $G(s)$ of this system is then defined with:

$$\begin{aligned} G(s) &= \frac{\mathcal{L}[\text{output}]}{\mathcal{L}[\text{input}]} \Big|_{\text{zero initial conditions}} \\ &= \frac{Y(s)}{X(s)} = \frac{b_0 s^m + b_1 s^{m-1} + \dots + b_{m-1} s + b_m}{a_0 s^n + a_1 s^{n-1} + \dots + a_{n-1} s + a_n} \end{aligned} \quad (5.6)$$

By using the concept of transfer functions, system dynamics can be represented by algebraic equations in s . If the highest power of s in the denominator of $G(s)$ is equal to n , the system is called an n^{th} -order system. The applicability of the transfer function concept is limited to LTI differential equation systems. The transfer function is a property of the system itself and it does not depend on the nature and magnitude of the input. Thus the response of a system for various forms of inputs can be studied once the transfer function is known. Now considering again equ. (5.4), the *closed-loop transfer function* $G(s)$ of the block diagram in Figure 5.1 can be defined:

$$G(s) = \frac{P(s)C(s)}{1 + F(s)P(s)C(s)} \quad (5.7)$$

such that:

$$Y(s) = G(s)R(s) \quad (5.8)$$

Thus it can be observed that the output of the closed-loop system depends on both the closed-loop transfer function as well as the nature of the system input.

5.2 Special Characteristics of Membrane Structures

In general, structural shapes with optimal load carrying behavior prefer a membrane state of stress to transfer loading. This is due to the fact that prestressed membrane structures are optimal in two respects. First of all, they represent structures of optimal material usage: Bending is omitted a priori by the nature of the membrane behavior and thus a constant stress state over the thickness exists. Secondly, membranes reflect surfaces of minimal area or minimal weight in the case of uniform prestress.

For the design of highly efficient structures, it is thus reasonable to aim for the combination of the efficiency of (passive) membrane structures with the advantages of active control.

5.2.1 Equilibrium Formulation of a Surface Stress Field

In general, the underlying mechanical statement for the analysis of prestressed membranes is the demand for equilibrium, which resembles the mathematical equivalence of minimizing the area content in the case of isotropic prestress.

In a nonlinear continuum mechanical description, the unknown shape \mathbf{x} of equilibrium can be identified as actual (deformed) configuration, which has to fulfill the equilibrium condition governed by the principle of virtual work. Using the prescribed Cauchy stress tensor σ and the external loading \mathbf{q} (Figure 5.2), the total virtual work $\delta\Pi$ with its internal and external parts yields:

$$\delta\Pi = \delta\Pi^{int} + \delta\Pi^{ext} = t \int_a \sigma : \delta\mathbf{u}_{,x} da - \int_a \mathbf{q} \cdot \delta\mathbf{u} da \quad (5.9)$$

where $\delta\mathbf{u}_{,x}$ is the derivative of the virtual displacement with respect to the geometry \mathbf{x} of the surface in equilibrium. The integration domain is the area a of the final equilibrium surface. The thickness of the membrane is denoted by t .

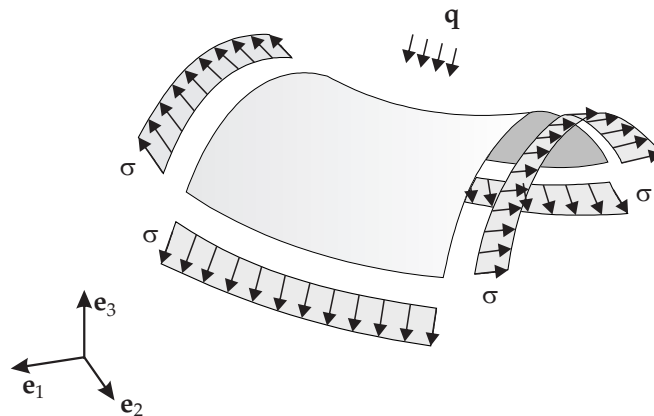


Figure 5.2: Tangential surface stress field of a membrane structure.

Based on the second Piola-Kirchhoff stress tensor \mathbf{S} and the deformation gradient \mathbf{F} , it is now possible to transform the integration domain of the original problem from the yet unknown equilibrium surface to the known reference configuration \mathbf{X} (compare also Figure 2.1). The internal virtual work of equ. (5.9) can thus be rewritten as:

$$\delta\Pi^{int} = t \int_a \boldsymbol{\sigma} : \delta\mathbf{u}_{,x} da = t \int_A \det\mathbf{F} \left(\boldsymbol{\sigma} \cdot \mathbf{F}^{-T} \right) : \delta\mathbf{F} dA = t \int_A (\mathbf{F} \cdot \mathbf{S}) : \delta\mathbf{F} dA \quad (5.10)$$

This transformation (called *pull-back operation*) is especially useful for the algorithmic solution of the form finding problem, as the known reference configuration can serve as a starting point for the solution.

For the numerical solution, equ. (5.10) has to be discretized in order to reduce the number of unknowns to a finite number. Furthermore, as we are dealing with a geometrically nonlinear problem involving large displacements from the starting configuration to the actual equilibrium shape, a linearization of the resulting equation system is necessary, which follows the standard concept of incremental solution schemes [BLM00].

5.2.2 Inverse Problem Formulation and Regularization

Within membrane structures, the material is used optimally due to the constant stress state over the thickness. However, the structure has to be shaped in such a way, that it can achieve equilibrium of forces only by tensile forces, as compressive forces would lead to undesirable wrinkles in the membrane. Due to this coupling of the geometry to the stress state in the structure, special form finding techniques have to be adopted. The equilibrium equations must be solved for the unknown geometry, considering the prescribed prestress and the support conditions as major shaping parameters. However, a straightforward application of the method shown above is not possible due to the inverse nature of the problem: It is searched for the discretized equilibrium surface with a certain topology of the discretization parameters. More precisely in the finite element context, nodes can be moved around on the corresponding equilibrium surface while still maintaining a valid discretization of the desired surface. Consequently, the shape parametrization for the same geometry is not unique.

Numerical methods have to face mathematical singularities, which have to be overcome by specifically tailored algorithms like dynamic relaxation, force density method or the updated reference strategy (URS) [BFLW09]. In this context the similar nature of shape control [HA85] and form finding should be pointed out, as both approaches have to overcome the singularities of an inverse problem by regularization techniques.

The most general method for regularization of the inverse problem of form finding is the URS approach. This method is consistently derived from nonlinear continuum mechanics of elastic bodies and based on an intelligent mixture of configurations. It performs a homotopy mapping between the original, singular problem and a stabilization term

[BR99, WB05]. Starting from equ. (5.10), one can introduce a continuation factor λ and formulate:

$$\delta\Pi = \lambda t \int_A \det\mathbf{F} \left(\boldsymbol{\sigma} \cdot \mathbf{F}^{-T} \right) : \delta\mathbf{F} dA + (1 - \lambda)t \int_A (\mathbf{F} \cdot \mathbf{S}) : \delta\mathbf{F} dA = 0 \quad (5.11)$$

Instead of assuming the Cauchy stress tensor $\boldsymbol{\sigma}$ of the unknown equilibrium surface to be given, the 2nd Piola-Kirchhoff stress tensor \mathbf{S} referring to the arbitrary starting geometry is prescribed. If λ is chosen properly, the second term stabilizes the original expression and allows for the use of a standard finite element discretization and solution. This modification has the convincing property that it disappears at the solution surface. Using equ. (5.11) it is thus possible to calculate a unique equilibrium surface for the given PK2 stress state. The modified and stabilized expression is nonlinear with respect to the final geometry \mathbf{x} and must be solved iteratively applying a Newton-Raphson scheme.

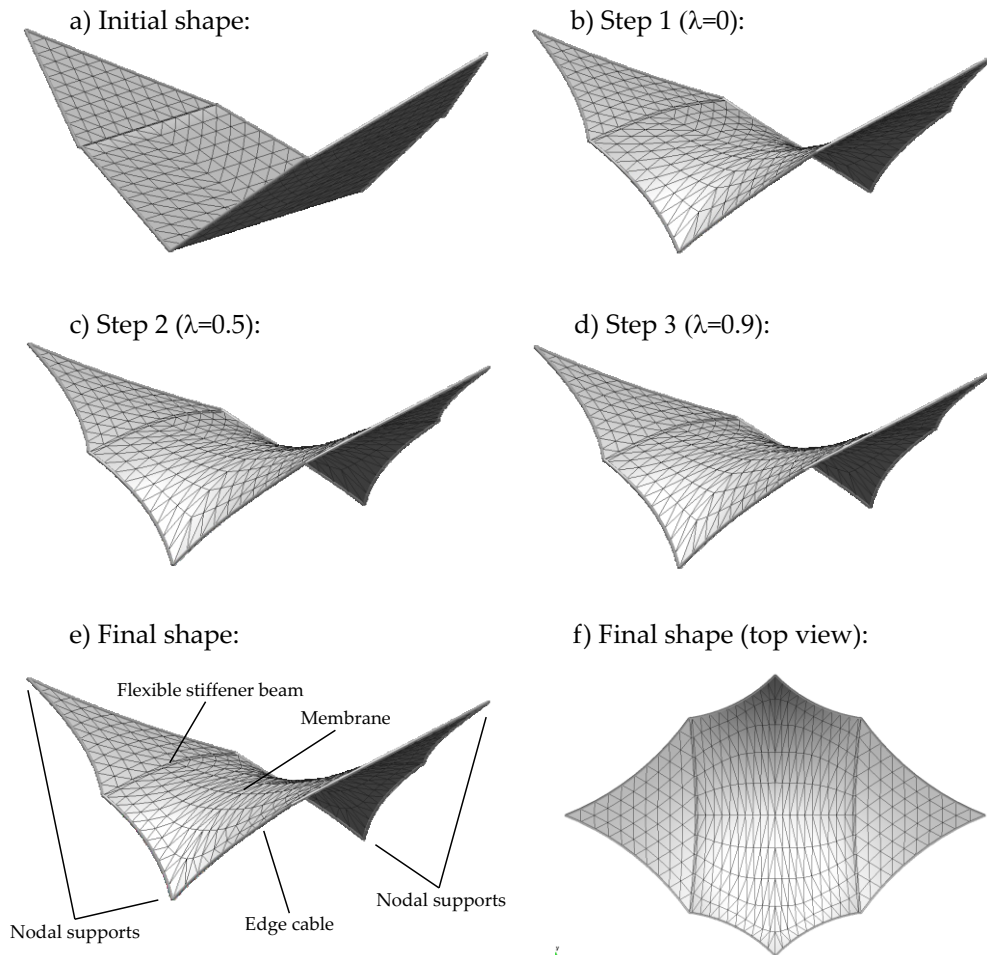


Figure 5.3: "Batwing" structure: application of form finding via the updated reference strategy (URS).

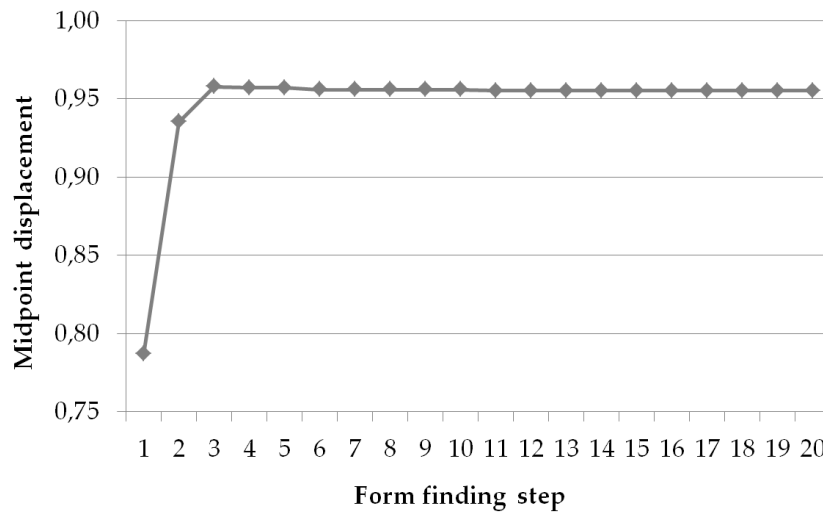


Figure 5.4: "Batwing" structure: Convergence of midpoint displacement over form finding steps.

However, the resulting Cauchy stresses will differ from the targeted stress state depending on the choice for λ . This necessitates a second, outer iteration: The newly obtained actual configuration $\tilde{\mathbf{x}}$ of the modified system in equ. (5.11), which is closer to the final equilibrium shape, can be used to update the reference geometry \mathbf{X} for the next form finding iteration. By repeatedly updating the reference geometry, the difference between the PK2 and Cauchy stresses is consequently reduced and the solution converges safely and robustly to the one of the unmodified problem. It should be noted that the speed of convergence is independent from the number of variables. Furthermore, the approach is capable of handling complex shapes and arbitrary stress states with or without external loading.

Figure 5.3 shows the form finding process for a "batwing" structure [FWB09a]. The only shaping parameters that have to be provided for the form finding method are the prestress and the boundary conditions. Also additional, already materialized structures like the elastic stiffener beams of the "batwing" can be integrated. This additionally enlarges the design space of possible membrane geometries. The fast convergence of this numerical form finding method is demonstrated in Figure 5.4.

In general, when the external loads are known in advance, their effects upon the structural deformation can be taken into account not only in the finite element simulation, but already in the inverse process of form finding. Thus the overall design framework can be easily used for passive control strategies. E.g. with the extension to anisotropic prestress, the different strength in the weft and warp directions of fabrics and the adaptation of the structural load carrying behavior to different load cases (like snow or wind) can be taken into account. However, this contribution will focus in the sequel on active control strategies.

5.2.3 Cutting Pattern Generation

In general, membrane structures exhibit a doubly curved surface in order to establish a good load carrying behavior. This important characteristic of such structures is the main challenge for all methods of cutting pattern generation which have been developed through the past years. From a differential geometry point of view it is important to consider that a doubly curved surface cannot be developed in a plane surface. For all surfaces that exhibit nonzero Gaussian Curvature, stresses occur through the flattening process. However, these stresses can be minimized by the choice of suitable cutting patterns. In the past, a lot of methods for the generation of cutting patterns have been introduced. The most of them are based on geometrical methods (see e.g. [AA97, MT90]). The main drawback of geometrical methods is that it is impossible to consider different material properties or certain prestress states in the membrane. A more general approach is the *inverse engineering method* which is based on the description of the underlying mechanical problem of the cutting pattern generation [LWB08, Lin09]. The three-dimensional surface, which is defined through the form finding process, represents the final structure after manufacturing. For this surface the coordinates in three dimensional space Ω_{3D} and the finally desired prestress state σ_{pre} are known. The aim is to find a surface in a two dimensional space Ω_{2D} which minimizes the difference between the elastic stresses $\sigma_{el,2D \rightarrow 3D}$ arising through the manufacturing process and the final prestress σ_{pre} . Thus the cutting pattern generation leads to an optimization problem, where the positions of the nodes in the two dimensional space Ω_{2D} are the design variables.

Taking the practical manufacturing process into account, it is important to divide the structure into cutting patterns of reasonable size as the width of available textile materials is usually limited. So the questions arises how to divide into patterns and how to define the exact cutting lines. From a manufacturing point of view, the crucial point in defining the cutting lines is also the loss of material due to the cutting. An appropriate way to minimize the loss of material is the usage of geodesic lines for the definition of the cutting lines. Geodesic lines are characterized by connecting two points on a surface with shortest distance. The calculation of geodesic lines on discrete surfaces (like a finite element mesh) is performed in two steps. First of all, an approximation of the geodesic lines along the edges of the elements of the discrete surface is calculated [SK98]. The second step is to perform an optimization of the approximated Geodesic Lines to get the "shortest path" between two given points [Wak99]. With the above described methods all steps which are needed for the cutting pattern generation of membrane structures are developed. It should be mentioned that this method is applicable for different element types and is able to consider different material models and arbitrary prestress states.

In chapter 7.5, the whole process for the generation of cutting patterns will be illustrated at the example of a four point tent.

5.2.4 Challenges for Control in the Context of Membrane Structures

One control objective pursued in this work is to suppress vibrations. This is challenging in the context of membranes for the following reasons: Membranes, especially lightly prestressed ones, exhibit very low mode frequencies in the out-of-plane direction and are thus prone to vibration even for small disturbance loads. Beyond that, attaching many sensors, actuators or dampers directly on the membrane is not recommended, as this disturbs the optimal membrane stress state and results in a heavier system.

As already mentioned in the context of form finding, the consideration of geometrically nonlinear effects is in general indispensable, as large displacements arise already from the starting configuration to the actual equilibrium shape of the prestressed membrane, even if external loads are neglected.

Furthermore, the load carrying behavior via tangential membrane forces leads in general to large deformations. The geometry of the load-bearing structure adapts itself to efficiently gather external loads that act perpendicular to the surface. Thus nonlinear kinematics is vital for the simulation of membrane structures.

The prestress state is a key characteristic of the membrane structure. It is an equilibrium state with residual stresses in the reference configuration. These residual stresses are superposed with elastic deformations due to external loads. Thus the reference state of membrane structures is assumed to be free of strains, but it is not free of stresses. Thus the constitutive law according to equ. (2.99) has to be modified for membrane structures such that:

$$S^{ij} = S_{pre}^{ij} + C^{ijkl} E_{kl} \quad (5.12)$$

The stress in the reference configuration S_{pre}^{ij} is called prestress. The piezoelectric part of the material law can be neglected in the context of passive membrane material.

5.3 Nonlinear Transient Analysis

As already mentioned in section 5.2.4, the consideration of geometrically nonlinear effects at membrane structures is indispensable, as large displacements exist already in the actual equilibrium shape of the prestressed membrane, even if external loads are not yet applied. However, highly lightweight structures are in general prone to distinct deformations, independent from the design decision for membranes or shells or other bearing concepts. This requires in many cases an analysis that considers nonlinear kinematics.

Furthermore, the dynamic contribution due to inertia forces has to be considered in the energy functional in order to analyze the transient behavior of the structure under consideration. Thus keeping the acceleration term in the conservation law of linear momentum according to equ. (2.70), the variation of the energy potential yields:

$$\delta\Pi = \delta\Pi^{int} + \delta\Pi^{dyn} + \Pi_V^{ext} + \Pi_A^{ext} = 0 \quad (5.13)$$

where $\delta\Pi^{dyn}$ represents the contribution of the d'Alembert inertia forces. A finite element discretization leads to:

$$\delta\Pi = \delta\bar{\mathbf{d}}^T \mathbf{M}\ddot{\bar{\mathbf{d}}} + \delta\bar{\mathbf{d}}^T \mathbf{r}_{int}(\bar{\mathbf{d}}) - \delta\bar{\mathbf{d}}^T \mathbf{r}_{ext}(t, \bar{\mathbf{d}}) = 0 \quad (5.14)$$

with the mass matrix \mathbf{M} , the vector of internal forces \mathbf{r}_{int} and the vector of external forces \mathbf{r}_{ext} . The generalized displacement vector $\bar{\mathbf{d}}$ is used here instead of the displacement vector \mathbf{d} in order to demonstrate the general applicability of this equation to both pure structural problems as well as electromechanical problems. However, the mass matrix contains nonzero entries only at structural degrees of freedom.

In order to consider system damping, an additional term proportional to the velocity field is introduced. Then the geometrically nonlinear dynamic equation yields in its semi-discrete form:

$$\mathbf{M}\ddot{\bar{\mathbf{d}}} + \mathbf{C}_d \dot{\bar{\mathbf{d}}} + \mathbf{r}_{int}(\bar{\mathbf{d}}) = \mathbf{r}_{ext}(t, \bar{\mathbf{d}}) \quad (5.15)$$

where the damping is again only related to structural degrees of freedom. The initial conditions of the transient problem of equ. (5.15) can be stated as follows:

$$\ddot{\bar{\mathbf{d}}}(t = t_0) = \ddot{\bar{\mathbf{d}}}_0, \quad \dot{\bar{\mathbf{d}}}(t = t_0) = \dot{\bar{\mathbf{d}}}_0, \quad \bar{\mathbf{d}}(t = t_0) = \bar{\mathbf{d}}_0 \quad (5.16)$$

The damping matrix \mathbf{C}_d can be described in a simplified way as a linear combination of the mass matrix and stiffness matrix (Rayleigh damping):

$$\mathbf{C}_d = \alpha_1 \cdot \mathbf{M} + \alpha_2 \cdot \mathbf{K}_{tan} \quad (5.17)$$

where \mathbf{K}_{tan} denotes the tangent stiffness matrix of the system and thus e.g. also considers prestress effects in the case of membrane structures. Even more realistic damping parameters can be obtained if the structure is analyzed in a coupled multi-field simulation including the surrounding air. Especially in the case of membrane structures, these fluid-structure interaction effects can play a decisive role in the context of damping [Wüc06]. Based on virtual wind tunnel tests, the damping behavior of the structure can be analyzed and taken into account for further simulations.

For the numerical time integration of the semi-discrete form in equ. (5.15), a discretization in time has to be conducted. Thus the system is solved only for discrete points in time $t_n = t_0 + n\Delta t$ assuming equidistant time steps Δt . For time integration, common implicit methods like Newmark- β or Generalized- α are chosen. As the consideration of geometrical nonlinear effects is indispensable, a nonlinear equation system has to be solved in each time step. This is done via complete linearisation and iterative solution by the Newton-Raphson method with predictor-corrector scheme.

5.4 Model Order Reduction

The controller design for a flexible mechanical structure like a membrane represents in general a multiple input - multiple output (MIMO) system. Since advanced controller

design techniques typically produce controllers with orders comparable to the order of the plant, this will inevitably lead to controllers of very high order. Such high-order controllers are not practical for real-time applications. The main issues with large-scale systems are storage, computational speed, accuracy and stability.

Thus the application of nonlinear and large-scale finite element models is not suitable. Reduced order models and related model reduction methods are indispensable for the practical applicability of modern controller design methods for high-order systems. Various reduction techniques have been developed for linear systems, like modal truncation techniques, Padé and Padé type approximations and balanced truncation techniques [AS01, ZE00]. However, this work will focus on modal truncation in the sequel.

As a first step, a linearization of the geometrically nonlinear system of equ. (5.15) is performed for controller design:

$$\mathbf{M}\ddot{\mathbf{d}} + \mathbf{C}\dot{\mathbf{d}} + \mathbf{K}_{tan}\mathbf{d} = \mathbf{E}_f \mathbf{f}(t) \quad (5.18)$$

Here, the generalized stiffness matrix \mathbf{K}_{tan} is of key importance. It should sufficiently describe the stiffness of the controlled system. Thus effects like prestress, geometric stiffness and permanent loading like dead load should be contained in the linearized model. The right hand side of equ. (5.18) contains the load contributions of the external load. The introduced matrix \mathbf{E}_f links the affected degrees of freedom of the load to the related time dependent function $\mathbf{f}(t)$.

Furthermore, an external load part for the actuator-induced load effects is introduced:

$$\mathbf{M}\ddot{\mathbf{d}} + \mathbf{C}\dot{\mathbf{d}} + \mathbf{K}_{tan}\mathbf{d} = \mathbf{E}_f \mathbf{f}(t) + \mathbf{B}_u \mathbf{u}(t) \quad (5.19)$$

where the matrix \mathbf{B}_u links the degrees of freedom of the actuator signal to the time dependent function of the control input $\mathbf{u}(t)$.

Beyond that, also a sensor or output equation has to be defined based on the finite element model. Assuming sensors that measure nodal displacement values, it can be stated:

$$\mathbf{y}(t) = \mathbf{P}_d \mathbf{d} \quad (5.20)$$

where $\mathbf{y}(t)$ is the vector of (time-dependent) sensor values. The matrix \mathbf{P}_d maps the displacement vector to the sensor values. Thus \mathbf{P}_d has in general zero entries except the entries that reflect the measurement positions of the sensors. This formal relation between the sensor values $\mathbf{y}(t)$ and the finite element model data according to equ. (5.20) will be used later for the transformation of the output equation to the modally truncated space.

As explained before, the obtained linearized model of the finite element model would in general yield to very high state-space dimensions. Thus an appropriate model order reduction scheme has to be adopted. Within this work, the modal truncation technique is applied. This method is commonly used in the context of flexible structures due to their low-pass characteristic, which allows for neglecting higher-frequency dynamics.

Starting point of the used modal truncation approach is the solution of the linearized undamped eigenvalue problem of the structure:

$$(\mathbf{K}_{tan} - \lambda_k \mathbf{M}) \boldsymbol{\psi}_k = \mathbf{0} \quad (5.21)$$

Solving equ. (5.21) for r eigenvectors with $r < n$ yields the $(n \times r)$ modal matrix:

$$\boldsymbol{\Psi} = [\boldsymbol{\psi}_1 | \boldsymbol{\psi}_2 | \dots | \boldsymbol{\psi}_r] \quad (5.22)$$

and the $(r \times r)$ spectral matrix:

$$\boldsymbol{\Lambda} = \text{diag}(\lambda_k) \quad (5.23)$$

where $\boldsymbol{\Psi}$ is orthonormalized with $\boldsymbol{\Psi}^T \mathbf{K}_{tan} \boldsymbol{\Psi} = \boldsymbol{\Lambda}$ and $\boldsymbol{\Psi}^T \mathbf{M} \boldsymbol{\Psi} = \mathbf{1}$. Inserting the modal coordinates $\bar{\mathbf{d}} = \boldsymbol{\Psi} \mathbf{z}$ into equ. (5.19) and equ. (5.20), leads to

$$\mathbf{M} \boldsymbol{\Psi} \ddot{\mathbf{z}} + \mathbf{C} \boldsymbol{\Psi} \dot{\mathbf{z}} + \mathbf{K}_{tan} \boldsymbol{\Psi} \mathbf{z} = \mathbf{E}_f \mathbf{f}(t) + \mathbf{B}_u \mathbf{u}(t) \quad (5.24)$$

and:

$$\mathbf{y}(t) = \mathbf{P}_d \boldsymbol{\Psi} \mathbf{z} \quad (5.25)$$

Pre-multiplying equ. (5.24) with $\boldsymbol{\Psi}^T$, the original finite element system with n degrees of freedom can finally be reduced to a decoupled equation system of r modal degrees of freedom:

$$\ddot{\mathbf{z}} + \boldsymbol{\Delta} \dot{\mathbf{z}} + \boldsymbol{\Lambda} \mathbf{z} = \boldsymbol{\Psi}^T \mathbf{E}_f \mathbf{f}(t) + \boldsymbol{\Psi}^T \mathbf{B}_u \mathbf{u}(t) \quad (5.26)$$

with the structural modal damping matrix

$$\boldsymbol{\Delta} = \boldsymbol{\Psi}^T \mathbf{C} \boldsymbol{\Psi} \quad (5.27)$$

A general discussion and estimation of the error introduced by modal truncation can be found at Brenner [Ben06].

5.5 State Space Approach

It is actually not a new trend that engineering systems are heading towards greater complexity and good accuracy. In order to meet increasing demands on the performance of control systems and the system complexity, *modern control theory* has been developed. Modern control theory is based on the description of the *state*. The state of a dynamic system is the smallest set of n variables (*state variables*) such that the knowledge of these variables at time $t = t_0$, together with the knowledge of any input for $t \geq t_0$ completely determines the behavior of the system for any time $t \geq t_0$. The state variables of a dynamic system are collected in the *state vector* \mathbf{x}_c

Based on the modal degrees of freedom of the reduced model, the state vector is defined by:

$$\mathbf{x}_c = \begin{bmatrix} \mathbf{z} \\ \dot{\mathbf{z}} \end{bmatrix} \quad (5.28)$$

with $\mathbf{x}_c \in \mathbb{R}^n$ and n being two times the number of modes considered in the state space model. Assuming a time-invariant system that is linear or linearized at the operating state, the following *state space equation* and *output equation* can be defined:

$$\dot{\mathbf{x}}_c(t) = \mathbf{A}_c \mathbf{x}_c(t) + \mathbf{B}_c \mathbf{u}_c(t) + \mathbf{E}_c \mathbf{f}(t) \quad (5.29)$$

$$\mathbf{y}(t) = \mathbf{C}_c \mathbf{x}_c(t) + \mathbf{D}_c \mathbf{u}_c(t) + \mathbf{F}_c \mathbf{f}_y(t) \quad (5.30)$$

where \mathbf{A}_c is called *system matrix*, \mathbf{B}_c is denoted with *input matrix* and \mathbf{E}_c represents the *external load matrix*. The vector $\mathbf{u}_c \in \mathbb{R}^k$ represents the *control input* of k actuators. Furthermore, $\mathbf{y} \in \mathbb{R}^l$ is the *system output* with l being the number of sensors. In the output equation, \mathbf{C}_c represents the *output matrix* and \mathbf{D}_c is called the *direct transmission matrix*. Last but not least, the matrix \mathbf{F}_c allows for the consideration of disturbances in the output equation.

Using now the state vector \mathbf{x}_c , the reduced model of equ. (5.26) is transformed into the modal form of the state space equation according to equ. (5.29):

$$\dot{\mathbf{x}}_c(t) = \begin{bmatrix} \mathbf{0} & \mathbf{I} \\ -\mathbf{\Lambda} & -\mathbf{\Delta} \end{bmatrix} \mathbf{x}_c(t) + \begin{bmatrix} \mathbf{0} \\ \mathbf{\Psi}^T \mathbf{B}_u \end{bmatrix} \mathbf{u}_c(t) + \begin{bmatrix} \mathbf{0} \\ \mathbf{\Psi}^T \mathbf{E}_f \end{bmatrix} \mathbf{f}(t) \quad (5.31)$$

Besides to the state-space equation, also the output equation can be formulated based on the finite element model data. Using equ. (5.25), it can be derived:

$$\mathbf{y}(t) = \begin{bmatrix} \mathbf{P}_d \mathbf{\Psi} & \mathbf{0} \end{bmatrix} \mathbf{x}_c(t) \quad (5.32)$$

Thus the direct transition matrix is zero in this case. A disturbance signal can also be introduced later in the controller design phase. In contrast to the common notation in the literature, the state vector and all state space matrices are given a subscript c . This is just to avoid name collisions with terms defined in preceding chapters in the context of finite element technology.

Now all required information for the controller design is prepared. It should be pointed out that all matrices \mathbf{A}_c , \mathbf{B}_c , \mathbf{E}_c , \mathbf{C}_c and \mathbf{D}_c are derived from the finite element model and the related modal truncation.

5.6 Placement of Actuators and Sensors

In general, the placement of actuators and sensors plays an important role in the design procedure of smart structures. In the distributed control of continua like e.g. shell or membrane structures, the estimation of an optimal actuator and sensor shape as well as their placement are challenging problems which have not yet been fully solved [GNTK02]. However, the actuator and sensor locations determine to a large extent the effectiveness of the overall smart structure, as they determine the *controllability* and the *observability* properties of a controlled structure.

A LTI system is said to be *controllable* at time t_0 if there exists a control signal $\mathbf{u}_c(t)$ that will transfer an arbitrary initial state $\mathbf{x}_c(t_0)$ to the origin state $\mathbf{x}_c(t_1) = \mathbf{0}$ within a finite time $t_1 - t_0 < \infty$. If this is true for all initial times t_0 and all initial states $\mathbf{x}_c(t_0)$, the system is said to be *completely controllable*. This is equivalent to the following statement:

$$\text{Rank} [\mathbf{Q}_C] = n \quad (5.33)$$

where \mathbf{Q}_C is the $(n \times kn)$ controllability matrix:

$$\mathbf{Q}_C = \left[\mathbf{B}_c \mid \mathbf{A}_c \mathbf{B}_c \mid \mathbf{A}_c^2 \mathbf{B}_c \mid \dots \mid \mathbf{A}_c^{n-1} \mathbf{B}_c \right] \quad (5.34)$$

However, the check of controllability is only an a-posteriori verification and is not suitable for optimal actuator positioning. Thus a controllability index is introduced. Considering the state space model obtained by modal truncation as described in equ. (5.31), the controllability index of the k^{th} eigenmode is defined by:

$$\mu_k = \boldsymbol{\psi}_k^T \mathbf{B}_u \mathbf{B}_u^T \boldsymbol{\psi}_k \quad (5.35)$$

Depending on the type of controller, A system is completely controllable if $\mu_k > 0, \forall k$, where in general μ_k should be as high as possible. The best positions X_p to control the first r eigenmodes are the positions with the highest overall controllability index

$$\mu(\mathbf{X}_p) = \prod_{k=1}^r \mu_k(\mathbf{X}_p) \quad (5.36)$$

Furthermore, a system is said to be *observable* at time t_0 if $\mathbf{x}_c(t_0)$ can be determined from the knowledge of $\mathbf{u}_c(t)$ and $\mathbf{y}(t)$ for $t_0 < t < t_1 < \infty$. If this is true for all t_0 and all $\mathbf{x}_c(t_0)$, the system is said to be *completely observable*. This is equivalent to the following statement:

$$\text{Rank} [\mathbf{Q}_O] = n \quad (5.37)$$

where \mathbf{Q}_O is the $(n \times ln)$ observability matrix:

$$\mathbf{Q}_O = \begin{bmatrix} \mathbf{C}_c \\ \mathbf{C}_c \mathbf{A}_c \\ \mathbf{C}_c \mathbf{A}_c^2 \\ \vdots \\ \mathbf{C}_c \mathbf{A}_c^{n-1} \end{bmatrix} \quad (5.38)$$

Similar to equ. (5.35), an observability index can be defined:

$$v_k = \boldsymbol{\psi}_k^T \mathbf{P}_d^T \mathbf{P}_d \boldsymbol{\psi}_k \quad (5.39)$$

A system is completely observable if $v_k > 0, \forall k$. Just like in the case of the controllability index, it is aimed for maximum values of v_k . The best positions X_p to observe the first r eigenmodes are the positions with the highest overall observability index

$$v(\mathbf{X}_p) = \prod_{k=1}^r v_k(\mathbf{X}_p) \quad (5.40)$$

Using the controllability and observability index, an estimation of the number and positions of the required actuators and sensors can be done. Based on the evaluation of the modal measures of input and output, like modal displacements, strains, or modal electric voltage, a sensor and actuator design can be performed that is driven by original finite element model. The influence of the stiffness and the mass changes due to the active materials and the controller influence are commonly omitted at this stage.

5.7 Controller Design

There exist various methods for designing a controller such as the *root-locus analysis*, the *design by frequency response*, the *pole placement method* or the *quadratic optimal control method* [ZE00, Pre02, Oga02]. In the context of this work the latter method shall be focused.

In the early design phase of the smart structure, it is assumed that the specification of the structure itself, including the objective of the controlled behavior, the external disturbances and frequency range etc. is already known. The linearization and model order reduction at the operating state led to the linearized state and output equations:

$$\dot{\mathbf{x}}_c = \mathbf{A}_c \mathbf{x}_c(t) + \mathbf{B}_c \mathbf{u}_c(t) + \mathbf{E}_c \mathbf{f}(t) \quad (5.41)$$

$$\mathbf{y} = \mathbf{C}_c \mathbf{x}_c(t) + \mathbf{D}_c \mathbf{u}_c(t) + \mathbf{F}_c \mathbf{f}_y(t) \quad (5.42)$$

In this general form of the plant model, \mathbf{f} and \mathbf{f}_y describe in general the disturbance which is assumed to be present in the state and the output equation. For discrete controller design, it is necessary to derive a discrete-time state space model of the plant structure. Performing a discretization of equ. (5.42) with an appropriate sampling time T yields:

$$\mathbf{x}_c[k+1] = \mathbf{G}_c \mathbf{x}_c[k] + \mathbf{H}_c \mathbf{u}_c[k] + \boldsymbol{\epsilon}_c \mathbf{f}[k] \quad (5.43)$$

$$\mathbf{y}[k] = \mathbf{C}_c \mathbf{x}_c[k] + \mathbf{D}_c \mathbf{u}_c[k] + \mathbf{F}_c \mathbf{f}_y[k] \quad (5.44)$$

with

$$\mathbf{G}_c = e^{\mathbf{A}_c T} \quad (5.45)$$

$$\mathbf{H}_c = \int_0^T e^{\mathbf{A}_c t} \mathbf{B}_c dt \quad (5.46)$$

$$\boldsymbol{\epsilon}_c = \int_0^T e^{\mathbf{A}_c t} \mathbf{E}_c dt \quad (5.47)$$

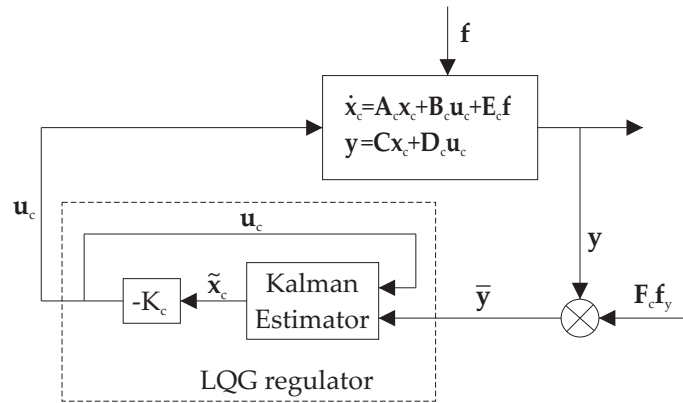


Figure 5.5: Block diagram of closed-loop control with a LQG regulator.

For active control, a linear-quadratic-Gaussian (LQG) regulator according to Figure 5.5 can be chosen (see also example of a smart 4-point tent in section 7.5). The state and output equations reflect the behavior of the plant (compare also Fig. 5.1 and 5.5).

In practice, usually only the sensor signals and not all state variables are available for feedback. Therefore it is necessary to estimate unavailable state variables. Such an estimation is commonly called *observation*. The related device that estimates the state variables is called a *state observer*, *observer* or *estimator*.

The Kalman filter is a very general filtering technique which can be applied to the solution of optimal estimation problems, noise filtering or stochastic optimal control. It can be applied to both stationary and non-stationary processes in contrast to other estimation filters. Thus a Kalman estimator can be used to obtain a state variable estimation \tilde{x}_c of the plant model derived from the information of the sensors (Figure 5.5):

$$\dot{\tilde{x}}_c = \mathbf{A}_c \tilde{x}_c + \mathbf{B}_c \mathbf{u}_c + \mathbf{L}_c (\bar{\mathbf{y}} - \tilde{\mathbf{y}}) \quad (5.48)$$

where

$$\tilde{\mathbf{y}} = \mathbf{C}_c \tilde{x}_c \quad (5.49)$$

is the estimated output. The inputs to the observer are the output $\bar{\mathbf{y}}$ and the control input \mathbf{u}_c . The *observer gain matrix* \mathbf{L}_c is a weighting matrix to the correction term involving the difference between the measured output $\bar{\mathbf{y}}$ and the estimated output $\tilde{\mathbf{y}}$. This term corrects the estimated model output and improves the performance of the observer. Assuming the statistical properties of the system noise $\mathbf{E}_c \mathbf{f}$ and the measurement noise $\mathbf{F}_c \mathbf{f}_y$ to be known, the observer gain matrix \mathbf{L}_c is determined through an algebraic Riccati equation that minimizes the estimation error [Oga02, Oga87].

Based on the estimation of the state, the state feedback gain \mathbf{K}_c is used to generate the actuator signal:

$$\mathbf{u}_c(t) = -\mathbf{K}_c \tilde{x}_c \quad (5.50)$$

Hereby the state feedback gain matrix \mathbf{K}_c is chosen such that the feedback law of equ. (5.47) minimizes the performance index:

$$J_c = \frac{1}{2} \sum_{k=0}^{\infty} \left(\mathbf{y}[k]^T \mathbf{Q}_c \mathbf{y}[k] + \mathbf{u}_c[k]^T \mathbf{R}_c \mathbf{u}_c[k] \right) \quad (5.51)$$

where \mathbf{Q}_c and \mathbf{R}_c are symmetric, positive definite matrices.

5.8 Nonlinear Simulation including Control

In general, the feasibility of the structural behavior including control has to be verified and tested. After controller design, the controller can be directly implemented on a dSPACE system in order to use a *hardware-in-the-loop* configuration for testing and evaluation of the designed controller in real experiments [GNW08].

However, before time-consuming experiments are performed, the overall structural behavior including control can be evaluated on the basis of the original finite element model. To this goal, the designed controller is integrated in the transient analysis according to chapter 5.3. Based on the large-scale and geometrically nonlinear finite element simulation, it can be automatically checked if all components comply with the maximal allowable stresses or if e.g. wrinkling effects appear due to undesired compressive stresses in the membrane [JWB08]. Furthermore it can be evaluated if the efficiency of the controller predicted by the linearized and reduced model is still obtained in the nonlinear finite element model [FWB09a, FWB09b].

This allows for a virtual (re-)design of the smart structure on different levels: the design of the passive structure, the generation of the linearized and reduced model, the assumptions of the state space model, the number and placement of sensors and actuators, as well as the controller design itself can be adapted in the virtual computational model if specific requirements are not met in the nonlinear simulation including control. A related example of the overall design loop is given in chapter 7.5.

Chapter 6

Software Implementation

6.1 Challenges of Modern Finite Element Software

As finite element methods and algorithms evolve, the daily life requires modifications to existing finite element programs. This may be due to the adaptation to latest functional, numerical and physical technologies [FFS90], or just due to the implementation of a new field of research. Thus it is indispensable that a modern finite element software constantly changes to satisfy current and future demands of university research as well as industrial applications.

Beyond that, nowadays the solution of multidisciplinary problems involving several fields (thermal, fluid, structural, electrical), the combination with optimization methods and parallel programming strategies are more and more requested in order to meet modern needs of research and industrial application. Therefore, finite element analysis software must be in general modular and flexible.

6.2 Problems and Pitfalls of Procedural Programming

However, finite element programs are commonly written in programming languages that adhere the procedural programming paradigm like C or Fortran and often consist of several hundred thousand lines of code or even more. The codes contain lots of complex data structures which are directly accessed throughout the program by various components [Arc96]. And of course, the various parts of the program take advantage of this accessibility for the sake of efficiency.

To give only one example: software components for finite elements, nodes and boundary conditions may need to access the matrices and vectors involved in the analysis to obtain and transmit their state information. The components of the software become directly tied to the program's data structures. Access to the data structures occurs throughout the component, and easily becomes inseparable from the component's function. This leads in several ways to a severe inflexibility of the software [Fis10b]:

- *High code complexity*: Modification or extension of a minor portion of code requires not only knowledge of the component at hand, but also a high degree of knowledge of the entire program.
- *Difficulty of code reuse*: Since the layout of the data structures is unique to each program component, the possibility of the reuse of the code in other components is greatly diminished. Also, code from other programs is difficult to adapt for use within the own system.
- *Ripple effects*: Since the data structures are globally accessible, a small change in the data structures can have a ripple effect throughout the program. All code fragments that access the affected data structures must be updated. As a result, the layout of the data structures tend to become fixed regardless of how appropriate they turn out to be as the code evolves.
- *Hidden interdependencies*: The components of the system become dependent on each other via their common access to the data structures. Hardly any control can be placed on the access. As a result, these interdependencies are numerous. More importantly, they are implicit. One component can be completely unaware of another's reliance on the same data structure.
- *Danger for data integrity*: When modification or extension to a component occurs, it is difficult to assure that all affected portions of the code are adjusted accordingly. The integrity of the data structures is not assured.

All in all, conventional procedural finite element codes do in general not provide the optimal basis for an up-to-date multi-disciplinary simulation environment that can successfully face the challenges of the future.

6.3 Chances Offered by the Object-oriented Programming Paradigm

The concept of *object-oriented programming* is a very promising remedy for the problems described above and has been proven to be very beneficial to the development of flexible programs. The reason is very simple: The basis of object-oriented design is abstraction. The object-oriented philosophy abstracts out the essential immutable qualities of the components of the finite element method. This abstraction forms a stable and reliable definition of objects in which the relationships between the objects are explicitly defined. The implicit reliance on another component's data does not occur. Thus, the design can be easily extended with minimal effort. Object-oriented programming provides in general four fundamental concepts [RK93b, CL95]:

- *Objects*. Software is organized into objects that store both its data and operators on the data. This permits developers to abstract out the essential properties of an

object: those that will be used by other objects. This abstraction allows the details of the implementation of the object to be hidden, and thus easily be modified. The necessary scope of the code developer is reduced to only the object of interest and the services other objects provide to the object of interest.

- *Classes*. Objects are instances described by a class definition. Encapsulating the data and operations together isolates the classes and promotes the reuse of code. Changes to a class affect only the class in question, without ripple effects. Interdependencies between the classes are explicitly laid out in the class interfaces. The number of dependencies are minimized and easily determined. Object-oriented programming languages enforce the encapsulation of the classes. Thus the integrity of the data structures is assured by the language.
- *Inheritance*. Classes can be related by inheritance. A subclass inherits behavior through the attributes and operators of the superclass. Thus code reuse is further enhanced by placing attributes common to several subclasses into the superclass, which is implemented once for all.
- *Polymorphism* allows the same operation to behave differently in different classes and thus allows objects of one class to be used in place of those of another related class.

Thus object-oriented programming offers techniques for faster programming, smaller codes and better management of data and procedures compared to equivalent procedural programming [Fis08a]. The object-oriented approach is very attractive for finite element analysis due to the advantages in modularity, maintenance, extensibility and code reuse. However, it should be stated that there is no contradiction between object-oriented and procedural programming. Many tasks can best be solved by a combination of both techniques: While the finite element method can be modeled very elegantly using an object-oriented approach, some inner program parts like equation solvers may still be based on a procedural concept at the same time [FFMB10].

6.4 Object-Oriented Finite Element Programming

The application of object-oriented programming in the structural engineering community has started in the late eighties, leading to first publications in the early nineties. In 1990, Fenves describes the advantages of object-oriented design for the development of engineering software [Fen90]: Based on the data abstraction technique, flexible and modular programs with substantial code reuse can be developed. Also in 1990, Forde, et al. publish one of the first detailed applications of the object-oriented paradigm to finite element analysis [FFS90]. The authors abstract out the essential components of the finite element method to design the main objects.

Other authors increase the general awareness of the advantages of object-oriented programming over traditional Fortran based approaches and demonstrate how to benefit from these advantages in finite element codes. Filho and Devloo apply the object-oriented paradigm to element design [FD91]. Mackie gives another introduction to object-oriented finite element programming by designing a brief hierarchical element [Mac92a]. Furthermore, he presents a more comprehensive finite element program concept providing a data structure for entities and introducing the use of iterators [Mac97]. Pidaparti and Hudli [PH93] present a more detailed object-oriented structure with objects for different algorithms in dynamic analysis of structures. Raphael and Krishnamoorthy [RK93a] also publish an introduction to object-oriented programming and show a sophisticated hierarchy of elements for structural applications. Zahlten, et al. publish one of the most detailed treatments of the material class and thus of the modeling of the constitutive relationships [ZDK95, HZK94].

Also a lot of publications about the development of complete finite element system architectures can be found. In this context, G. R. Miller, et al. [Mil91, Mil94, MR94] present an object-oriented software design for nonlinear dynamic finite element analyses.

T. Zimmermann, et al. present a software architecture for linear dynamic finite element analysis [ZDPB92], with later extensions to account for material nonlinearity [MZ93]. They implemented first a prototype of this structure in Smalltalk [DPZB92] and after that an efficient one in C++ [DPZ93]. They also report about a comparable performance of the latter version compared to a Fortran code. Further object-oriented finite element program designs can be found e.g. at Jun Lu et al. [CSW90, SWC92], J. W. Baugh et al. [BR89, BR92a], H. Adeli et al. [AY95, YA93], Archer et al. [Arc96, AFT99].

In the sequel, also several open source finite element codes and frameworks with object-oriented design have been developed, like the code FELyX from ETH Zurich [KWZE], the multi-disciplinary finite element framework Kratos by P. Dadvand and R. Rossi at CIMNE in Barcelona [Dad07], OFELI (Object Finite Element LIBrary) developed by R. Touzani, FreeFem++ by O. Pironneau et al., OOFem developed by Patzák et al. [PB01], the Object Finite Element Library (OFELI) developed by Touzani [Tou02], the Differential Equations Analysis Library (DEAL) II by Bangerth et al. [BHK], as well as the object-oriented Finite Element Modeling (OOFEM) program by Patzák et al. [PB01].

6.5 Development of Carat++

In order to provide the necessary basis for modern, flexible and sustainable finite element programming, the software Carat++ has been started. [FMFB12c, Fis12, FFMB10, Fis10a, FFB09, FFB10a, FWB11]. In this context, the object-oriented paradigm has been the key design concept. The program is completely written in C++ in order to take advantage of object-oriented programming features. Beyond that, the design objectives have been platform independence, numerical efficiency, as well as suitability for large and complex problems such as industrial applications.

Another design concept has been consistent parallelization of the overall code with MPI [FFB10b, FFMB11a]. Hereby, the method of geometric parallelization has been adopted, i.e. every process executes at the same time the same program but works only on a subset of the model data (domain decomposition). In this context, all software components have been parallelized: simulation, solvers, post-processing, as well as sensitivity analysis and optimization algorithms in the context of optimization problems. Thus the software is capable to perform the overall design process in a consistent parallel computation.

In the context of this work, flexible software modules for form finding, cutting pattern generation, structural analysis, model order reduction, state space calculation, as well as structural optimization have been used [FFMB10, Fis11, Fis13b, FB12, FFB12b, BFF10, BFF11].

For the focused use of Carat++ in the context of simulation and design of composite structures [Fis13a, FMFB12c, FMB12b, FMFB12a, FMFB12b, FMFB11a, FMFB11b, MFFB10] as well as in the context of structural optimization [FFB13, FMB13a, FMB13b, BFF13, BF13, FFB12a, FMB12c, FMB12a, Fis08b, MFFB11, FFMB11b] , the reader is kindly referred to the literature.

Chapter 7

Numerical Application Examples

In the first part of this chapter, several numerical examples are discussed to evaluate the presented composite shell formulation and the related implementation. Different element versions are evaluated in order to verify the need for the single element enhancement techniques, namely ANS (chapter 3.6.2), EAS (chapter 3.6.3) and EAE (chapter 3.6.3). The element formulations are named by acronyms for the reasons of clarity and efficiency:

- S-0: Irreducible form of piezoelectric shell element formulation without enhancements.
- S-Q-EAS: Element with ANS improvement for transverse shear and EAS improvements.
- S-Q-EAS-E: Element with ANS improvement for transverse shear, EAS and EAE enhancements.

Furthermore, several examples provide detailed insight which single EAS or EAE field contributions are actually in detail needed to eliminate the locking phenomenon of the respective example. To this goal, the EAS modes are explicitly specified via the number of modes per strain type according to equ. (4.128). Accordingly, also the EAE modes are explicitly specified via the number of modes per electric field type according to equ. (4.129). To give an example, S-Q-EAS04100-E20 stands for the ANS-improved element with the four bending strain modes and the first thickness strain mode in matrix \mathbf{M} according to equ. (4.128), as well as the two constant electric field modes according to matrix $\tilde{\mathbf{M}}$ in equ. (4.129).

A variety of distinct loadings is investigated in piezoelectric patch tests in chapter 7.1 to evaluate the behavior in a pure states of constant membrane action, bending, shear, etc. It will be shown that the enhanced element formulation is capable to eliminate parasitic strains and parasitic electrical fields that cause locking. Another example focuses on the element quality under high mesh distortions to discover limits of applicability and element quality. Also the widely used bimorph example (chapter 7.2) is tested to evaluate the effects of opposite polarities in different layers. Beyond that, it is shown that the geometrically nonlinear analysis can be indispensable especially in sensor simulation. Furthermore, two examples from the well-known shell obstacle course proposed

by Belytschko et al. [BSL⁺85] are applied in order to test the element's robustness and accuracy in complex strain states of pure structural applications.

The second part of this chapter presents two larger application examples: The virtual design process of a actively controlled smart structure with its components is shown at an example of a civil engineering structure. The final example demonstrates the design of a shape adaptive piezoelectric structure at the example of a variable-camber airfoil wing, including aeroelastic coupling and FE-based structural optimization.

7.1 Piezoelectric Patch Tests

The definition and the background of the patch test has already been introduced in chapter 3.4. In this chapter, the presented piezoelectric finite element is tested in different versions of the patch test. In detail, the patch is subjected to:

- rigid body motion
- tension
- electric field strength (actuator mode)
- bending load
- shear load

in separate tests. This allows for an evaluation of the behavior in distinct states of strains and electric field strength with analytical reference results.

7.1.1 Model Definition

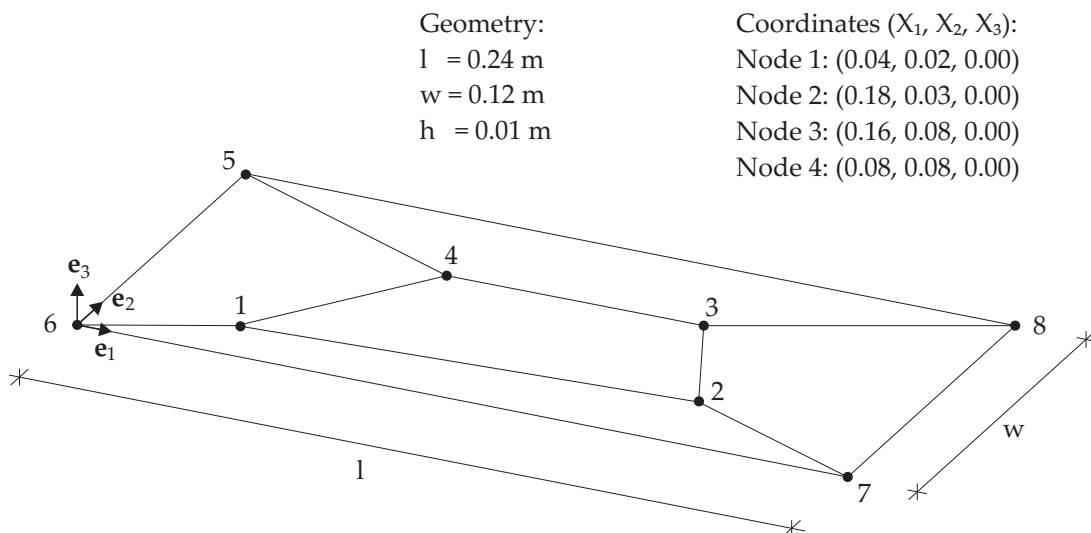


Figure 7.1: Patch test model: Geometry information with position of interior nodes.

The geometry of the model is chosen according to MacNeal and Harder [MH85] (Figure 7.1). For comparison reasons, the material parameters (see table 7.1) are chosen according to Klinkel and Wagner [KW06] who extended this patch test for piezoelectric applications. The piezoelectric coupling parameters are given in the common matrix form as introduced in chapter 2.7.2.2. The polarization is assumed to be in negative \mathbf{e}_3 -direction. For reasons of clarity, the electric potentials at the lower and upper side φ_l and φ_u are specified instead of $\Delta\varphi$. Furthermore, in order to allow for a clear derivation of analytical results, the Poisson's ratio is set to zero. This simplification is admissible here, as the decisive coupling effects under consideration are not dependent on the Poisson's effect.

$E_1 = E_2 = E_3 = 1.23 \cdot 10^{11} \text{ N/m}^2$	$e^{31} = -5.0 \text{ C/m}^2$
$\nu = 0.0$	$e^{32} = 0.0 \text{ C/m}^2$
	$\epsilon^{11} = \epsilon^{33} = 1.25 \cdot 10^{-8} \text{ C}^2/\text{Nm}^2$

Table 7.1: Material parameters for the patch tests. Not listed parameters are zero.

7.1.2 Displacement Patch Test

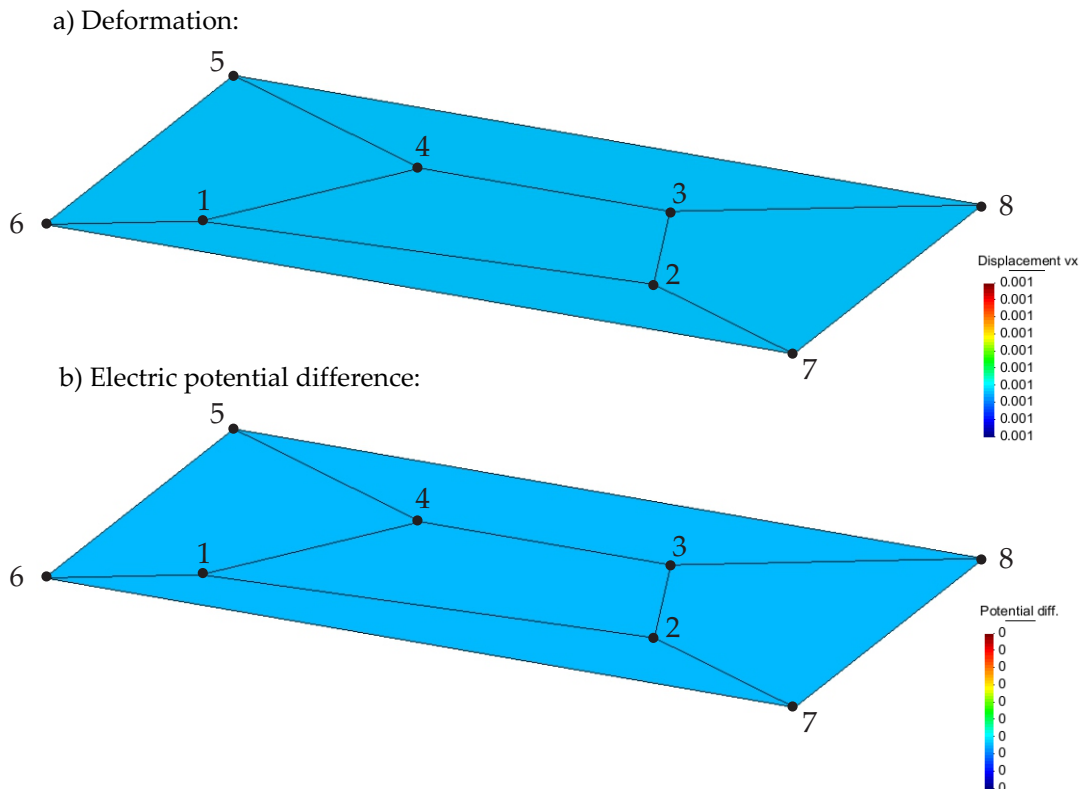


Figure 7.2: Displacement patchtest: Deformation contour plot (a) and electric potential difference contour plot (b) obtained by all tested elements.

In this patch test, the correct reproduction of rigid body motions shall be investigated. The presented model is well suited for that test, as the element in the middle is completely surrounded by other elements. The Dirichlet boundary condition $v_1 = 0.001 m$ is chosen as rigid body motion and thus is applied to the outer nodes 5, 6, 7 and 8.

This patch test is passed by all elements under consideration: S-0, S-QEAS, S-QEAS+E (see introduction to chapter 7). A constant displacement field of $v_1 = 0.001 m$ is obtained for the full model, the nodal potential differences are zero. It should be pointed out that this is not a trivial solution test: While the outer node displacements are prescribed, all other primary variables are obtained by solving the coupled piezoelectric equation system.

7.1.3 Tension Patch Test

The structure according to Figure 7.1 is provided with an statically determinate support: The degrees of freedom v_1 , v_2 , v_3 and w_1 are fixed at node 5, and v_1 and v_3 are fixed at node 6. This statically determinate support is in general important for two reasons: On the one hand side, it eliminates possible restraints which would influence the results, on the other hand side possible zero energy modes (see chapter 3.3) are not stabilized with additional support conditions. For all nodes of the model, the lower side is grounded which means $\varphi_l = 0V$.

As this patch test belongs to the group of force patch tests (sometimes also called stress patch tests), care has to be taken that the applied forces on exterior nodes are set to consistently lumped surface tractions. In order to obtain a constant stress state of $S^{11} = 1 \cdot 10^8 N/m^2$ in this example, forces $F_1 = 6 \cdot 10^4 N$ are assigned to the nodes 7 and 8. All other stress components are zero. Due to the electrical boundary conditions, also all electric displacement components are zero.

Thus using this boundary conditions and material parameters, the coupled electromechanical system is reduced to a 1-D problem that can easily be solved analytically. Two relevant electromechanical equations remain:

$$S^{11} = E \cdot E_{11} - e^{31} \cdot \vec{E}_3 \quad (7.1)$$

$$0 = e^{31} \cdot E_{11} + \epsilon^{33} \cdot \vec{E}_3 \quad (7.2)$$

Solving this equation system with the given material parameters according to table 7.1 leads to a constant strain $E_{11} = 8 \cdot 10^{-4}$ and an electrical field in thickness direction of $\vec{E}_3 = 3.2 \cdot 10^5 V/m$. The analytical result of the electric potential at the overall upper surface of the structure is $\varphi_u = -3.2 \cdot 10^3 V$, the displacement at the free edge is $v_1^{Node 7,8} = 1.92 \cdot 10^{-4} m$. For comparison reasons it shall be mentioned that the displacement of the pure elastic structure without piezoelectric coupling would reveal a tip displacement of $v_{1, mech}^{Node 7,8} = 1.95 \cdot 10^{-4} m$. As shown in Table 7.2, all piezoelectric elements exactly match the analytical result. This means that the tension patch test can also be passed without any ANS-, EAS-, or EAE- enhancements.

The linear ansatz of the electric potential in thickness direction leads to a correct representation of the constant electric field. Eventually offered EAS- and EAE modes are not activated in this load state.

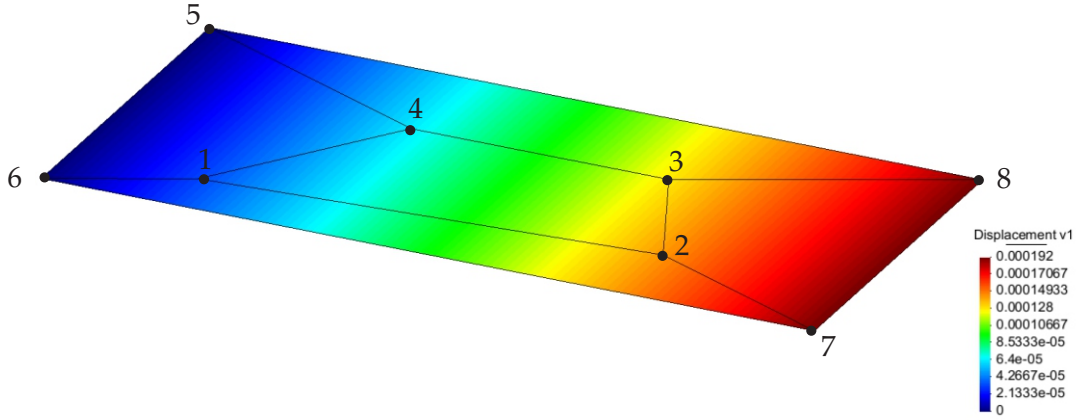


Figure 7.3: Tension patchtest: Deformation contour plot obtained by all tested elements.

	$v_1^{7,8}$ (m)	φ_u (V)	\vec{E}_3 (V/m)	S^{11} (N/m ²)
analytical solution	$1.92 \cdot 10^{-4}$	$-3.20 \cdot 10^3$	$3.20 \cdot 10^5$	$1.00 \cdot 10^8$
S-0	$1.92 \cdot 10^{-4}$	$-3.20 \cdot 10^3$	$3.20 \cdot 10^5$	$1.00 \cdot 10^8$
S-Q-EAS	$1.92 \cdot 10^{-4}$	$-3.20 \cdot 10^3$	$3.20 \cdot 10^5$	$1.00 \cdot 10^8$
S-Q-EAS-E	$1.92 \cdot 10^{-4}$	$-3.20 \cdot 10^3$	$3.20 \cdot 10^5$	$1.00 \cdot 10^8$

Table 7.2: Tension patch test: Comparison of analytical and numerical results.

7.1.4 Electric Field Patch Test

The structure according to Figure 7.1 is used again with an statically determinate support: The degrees of freedom v_1, v_2, v_3, w_1 are fixed at node 5, and v_1, v_3 are fixed at node 6. For all nodes of the model, the lower side is grounded again. Additionally, the voltage at the upper surface is set to $\varphi_u = 1.0 \cdot 10^3 V$. This results in an electrical field $\vec{E}_3 = -\frac{\varphi_u - \varphi_l}{h} = -1.0 \cdot 10^5 V/m$. As no external forces are applied, the stress S^{11} remain zero. Thus the governing equations of this 1d-problem can be stated as:

$$0 = E \cdot E_{11} - \epsilon^{31} \cdot \vec{E}_3 \quad (7.3)$$

$$\vec{D}^3 = \epsilon^{31} \cdot E_{11} + \epsilon^{33} \cdot \vec{E}_3 \quad (7.4)$$

Inserting the material parameters and the given electric field value, one obtains $E_{11} = 4.065 \cdot 10^{-6}$ and $\vec{D}^3 = -1.270 \cdot 10^{-3} C/m^2$. The longitudinal displacement at the free edge is $v_1^{7,8} = 9.756 \cdot 10^{-7} m$.

As it can be seen in Table 7.3, all tested element versions also pass this electric field patch

test. The linear ansatz of the electric potential in thickness direction leads to a correct representation of the constant electric field. Eventually offered EAS- and EAE modes are again not activated in this benchmark.

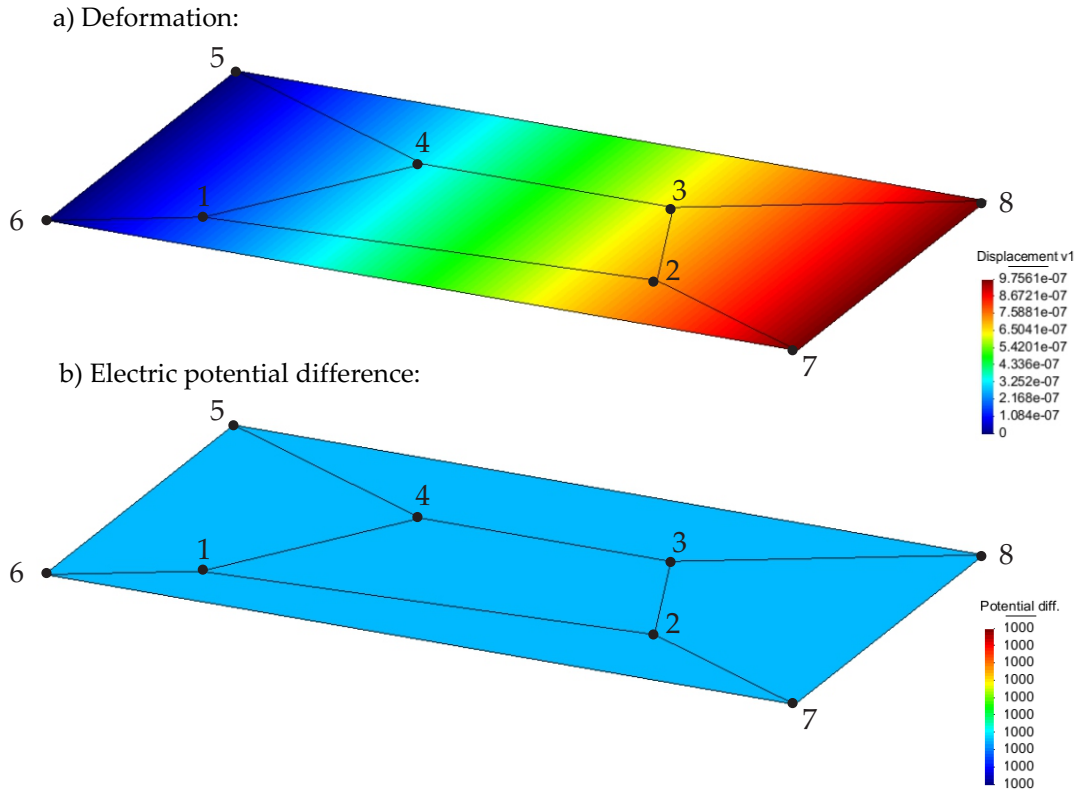


Figure 7.4: Electric field patchtest: Deformation contour plot (a) and electric potential difference contour plot (b) obtained by all tested elements.

	$v_1^{7,8} (m)$	$E_{11} (-)$	$\vec{D}^3 (C/m^2)$
analytical solution	$9.756 \cdot 10^{-7}$	$4.065 \cdot 10^{-6}$	$-1.270 \cdot 10^3$
S-0	$9.756 \cdot 10^{-7}$	$4.065 \cdot 10^{-6}$	$-1.270 \cdot 10^3$
S-Q-EAS	$9.756 \cdot 10^{-7}$	$4.065 \cdot 10^{-6}$	$-1.270 \cdot 10^3$
S-Q-EAS-E	$9.756 \cdot 10^{-7}$	$4.065 \cdot 10^{-6}$	$-1.270 \cdot 10^3$

Table 7.3: Electric field patch test: Comparison of analytical and numerical results.

7.1.5 Bending Patch Test

In this example, the model is subjected to a pure bending state. Two bending moments of value $M = 1000 Nm$ and oriented in e_2 -direction are applied at the nodes 7 and 8. As the rotational degrees of freedom are related to director deformations according to equ. (4.7)

in chapter 4.1, the bending moments are transformed into equivalent loads at the director degrees of freedom in Carat++. For all nodes of the model, the lower side is grounded which means $\varphi_l = 0V$. Just as in the previous patch tests, the structure is provided with an statically determinate support, fixing v_1, v_2, v_3 and w_1 at node 5, and v_1 and v_3 at node 6. This model resembles to a large extent the bending state presented in the context of electromechanical locking in chapter 3.5.4.1. However, not in-plane shear locking but transverse shear locking is critical now.

The normal stress S^{11} in this problem is constant in \mathbf{e}_1 -direction and linear in \mathbf{e}_3 -direction. In accordance to Klinkel and Wagner [KW08], the vertical tip displacement can be calculated analytically with $v_3 = -0.8 \frac{1}{m} \cdot X_1^2 = -0.8 \cdot 0.24^2 m = -0.04608 m$. Beyond that, the analytical result of the voltage is obtained with $\varphi = 0.32 \frac{V}{m^2} \cdot X_3^2 - 8.0 \cdot 10^{-6} V$. For the upper surface voltage at the tip it is obtained $\varphi_u^{7,8} = 0.32 \cdot 0.005^2 - 8.0 \cdot 10^{-6} = 0V$. It should be pointed out again that the analytical distribution of the electric potential over the thickness is a quadratic function. This is due to the fact that the coupled material law generates a linear electric field distribution \vec{E}_3 together with a linear strain distribution E_{11} . Integrating the electric field distribution over the thickness with consideration of the boundary conditions leads to the described quadratic function of the electric potential.

	v_3^7 (m)	v_3^8 (m)	$\varphi_u^{7,8}$ (V)
analytical solution	$-4.60800 \cdot 10^{-2}$	$-4.60800 \cdot 10^{-2}$	0
S-0	$-4.92059 \cdot 10^{-4}$	$-3.96037 \cdot 10^{-2}$	0
S-Q-EAS	$-4.68293 \cdot 10^{-2}$	$-4.68293 \cdot 10^{-2}$	0
S-Q-EAS-E01	$-4.61158 \cdot 10^{-2}$	$-4.61398 \cdot 10^{-2}$	0
S-Q-EAS-E04	$-4.60800 \cdot 10^{-2}$	$-4.60800 \cdot 10^{-2}$	0

Table 7.4: Bending patch test: Comparison of analytical and numerical results.

Table 7.4 lists the results for the different element versions. First of all, it can clearly be seen that the element S-0 without any enhancements produces completely useless results. The described locking effects are dominating the result.

The element S-Q-EAS is able to eliminate the parasitic shear stresses and thus transverse shear locking via the ANS method. EAS modes are actually not needed here. However, the element does not apply any EAE modes to enhance the electric field. Therefore only electric fields can be approximated which are constant through the thickness which is not sufficient here (compare also Figure 3.12 in chapter 3.5.4.1). It is also remarkable that the electromechanical locking leads here to displacement results that are larger than the analytical reference. This is indeed in contrast to the behavior of "classical" structural locking where in general the deformation is reduced and a stiffening effect can be observed. However, this phenomenon can be explained very intuitively: The element offers only a constant approximation of the electrical field which is not activated here. Thus the approximation of \vec{E}_3 collapses to zero. As a consequence, the electromechanical locking eliminates energy that is spent into the electric field and restores it to the strain energy. This leads in this example to an identical behavior as a pure mechanical structure without

piezoelectric coupling.

The S-Q-EAS-E01 element offers a linear interpolation of the electric field in thickness direction. This mode can eliminate the predominant part of the electromechanical locking. However, it misses the exact result due to the mesh distortion of the model and it also loses the symmetry of the results at nodes 7 and 8. Thus also this element does not pass the patch test.

However, the complete structural locking as well as electromechanical locking can be eliminated here by the element S-Q-EAS-E04. Due to the bilinear interpolation of the linear electric field in thickness direction, also the mesh distortion does not deteriorate the element result.

The reader should also be pointed to very similar results by solid shell elements presented by Klinkel and Wagner where all 6 fields of the Hu-Washizu functional are discretized [KW06]. Using element versions with different number of enhanced electric field modes in thickness direction, Klinkel and Wagner obtain almost identical results with their elements in this patch test. The element S-Q-EAS of this work can be compared with the element HSE-0 of Klinkel and Wagner, S-Q-EAS-E01 can be matched with the HSE-1 element and S-Q-EAS-E04 can be compared with the HSE element [KW06]. The reason for the strong similarity of the results is that both element formulations are based on the Hu-Washizu functional and comparable kinematic assumptions. The good match confirms that the shown element formulation based on the modified Hu-Washizu functional can eliminate the stress field and electric displacement field and thus increase numerical efficiency without loss of numerical result quality.

7.1.6 Shear Patch Test

As last benchmark within the series of patch tests, a transverse shear loading shall be examined. This allows for an investigation of the related electromechanical locking phenomenon as described in Figure 3.13 in chapter 3.5.4.2. For the shear patch test, the model shall be used as suggested by Legner [Leg11]. The geometry stays the same as in the preceding patch tests, but the mesh is chosen differently as shown in Figure 7.5.

The material parameters are chosen as shown in section 7.1.1, however $e^{15} = 5.0 \text{ C/m}^2$ is chosen as additional coupling parameter. For convenience, table 7.5 lists again all material parameters of the shear patch test. For all nodes of the model, the lower side is grounded again such that $\varphi_l = 0V$. The structure is supported fixing all 6 displacement degrees of freedom at node 1 and at node 2. The load is defined via two Forces $F_3 = 1000N$ at nodes 3 and 4 in opposite direction of \mathbf{e}_3 (Figure 7.5). The transverse load results in a linear behavior of the strains E_{11} in \mathbf{e}_1 direction. The analytical result assuming a Timoshenko beam kinematics and linear piezoelectricity is derived at Legner [Leg11]. Inserting the parameters of this model, a tip displacement of $v_3^{tip} = -7.38036 \cdot 10^{-3}m$ is obtained. The electric potential at the upper side has an analytical result of $\varphi_u = 0V$ in the case of a geometrically linear analysis.

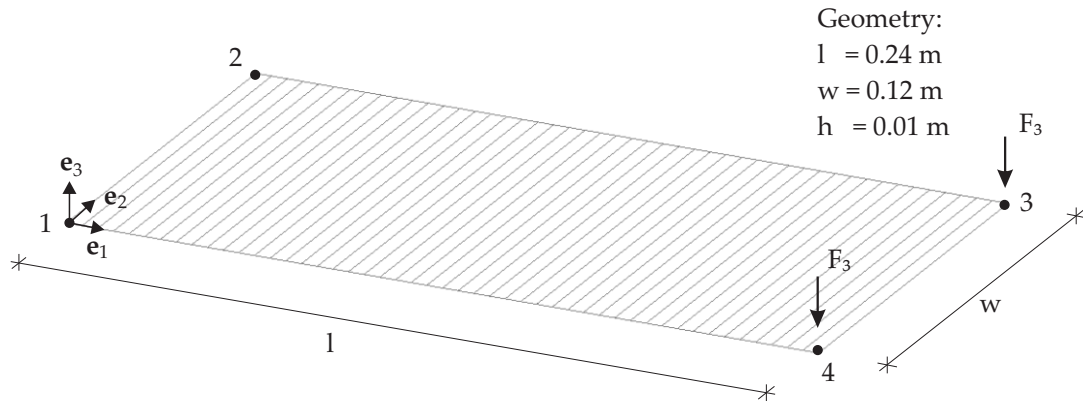


Figure 7.5: Shear patch test model: Geometry information and mesh.

$E_1 = E_2 = E_3 = 1.23 \cdot 10^{11} \text{ N/m}^2$	$e^{31} = -5.0 \text{ C/m}^2$
$\nu = 0.0$	$e^{32} = 0.0 \text{ C/m}^2$
	$e^{15} = 5.0 \text{ C/m}^2$
	$\epsilon^{11} = \epsilon^{33} = 1.25 \cdot 10^{-8} \text{ C}^2/\text{Nm}^2$

Table 7.5: Material parameters for the shear patch test. Not listed parameters are zero.

Now, the numerical results of the element versions shall be examined. Table 7.6 lists the vertical tip displacement at node 4 and the electric potential at the upper side at node 4. The evaluations are made for the mesh with 48 elements as depicted in figure 7.5, as well as a finer mesh with 96 elements in longitudinal direction.

The element S-0 without any enhancements is just listed to show the severity of the locking effects. The element S-Q-EAS leads to an overestimation of the displacement. Again like in the bending patch test before, the element formulation misses here the correct representation of the electric field in thickness direction \vec{E}_3 . With increasing mesh refinement in longitudinal direction, this element formulation would converge to the pure structural deformation result of $v_3^{4,mech} = 7.5005 \cdot 10^{-3} \text{ m}$. Furthermore, it can be observed that the er-

	48 elements		96 elements	
	$v_3^4 \text{ (m)}$	$\varphi_u^4 \text{ (V)}$	$v_3^4 \text{ (m)}$	$\varphi_u^4 \text{ (V)}$
analytical solution	$-7.38036 \cdot 10^{-3}$	0	$-7.38036 \cdot 10^{-3}$	0
S-0	$-6.79288 \cdot 10^{-3}$	-105.042	$-7.31010 \cdot 10^{-3}$	-105.834
S-Q-EAS	$-7.49966 \cdot 10^{-3}$	-105.025	$-7.50027 \cdot 10^{-3}$	-105.830
S-Q-EAS-E01	$-7.37979 \cdot 10^{-3}$	-105.025	$-7.38039 \cdot 10^{-3}$	-105.830
S-Q-EAS-E04	$-7.37979 \cdot 10^{-3}$	-105.025	$-7.38039 \cdot 10^{-3}$	-105.830
S-Q-EAS-E24	$-7.37960 \cdot 10^{-3}$	0	$-7.38020 \cdot 10^{-3}$	0

Table 7.6: Linear shear patch test: Comparison of analytical and numerical results.

ror in the electric potential approximation is even a bit increasing with mesh refinement. The elements S-Q-EAS-E01 and S-Q-EAS-E04 show the same results. The tip displacement result is improved compared to the S-Q-EAS element, as the EAE mode of the linear electric field in thickness direction allows for a correct representation of \vec{E}_3 . As a regular mesh is used here, the additional EAE modes offered by the element S-Q-EAS-E04 are not activated here. However, the elements S-Q-EAS-E01 and S-Q-EAS-E04 are still not able to represent the electric field \vec{E}_1 according to Figure 3.13 in chapter 3.5.4.2. The electric potential at the tip is strongly affected by parasitic electric field effects stemming from the incompatible approximation spaces.

Only element S-Q-EAS-E24 allows for a correct representation of the electric potential field (Figure 7.6 b), as additional constant electric field enhancement modes for \vec{E}_1 and \vec{E}_2 are included. This example shows that all element enhancements are indispensable, especially for sensor applications.

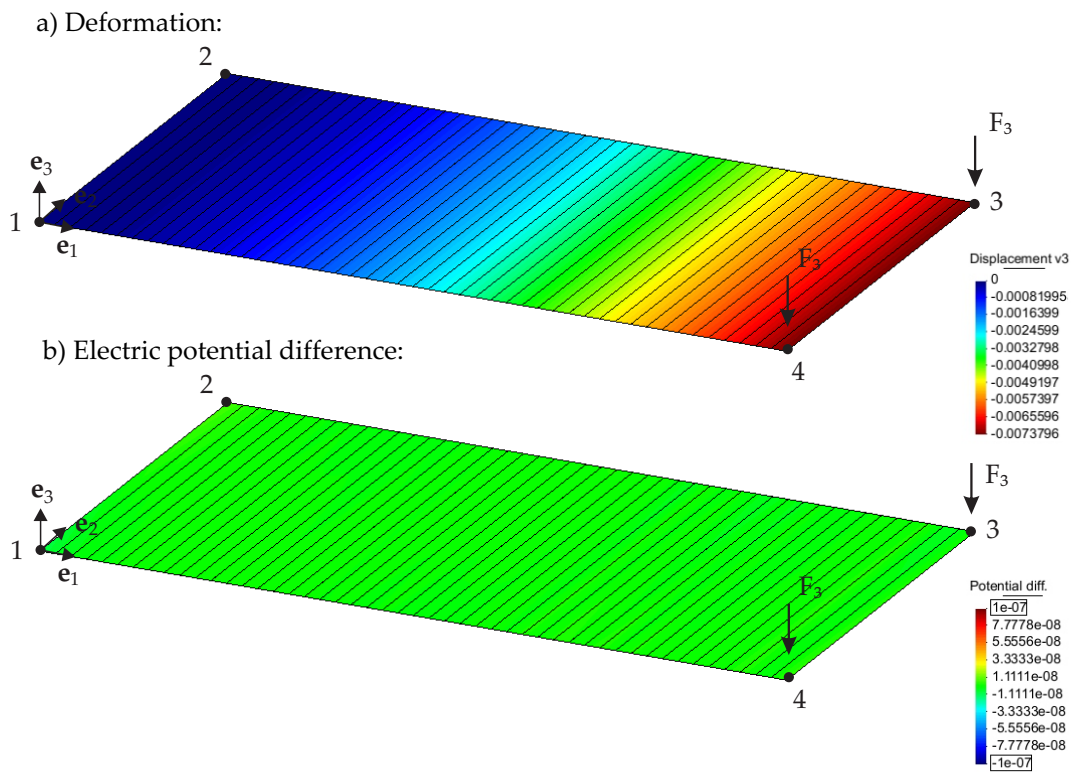


Figure 7.6: Shear patch test model with 48 elements: deformation and electric potential result using the element S-Q-EAS-E24 with ANS-, EAS- and EAE- improvement.

7.2 Bimorph

7.2.1 Sensor Test

The bimorph beam is a commonly used test example in the literature to examine the finite element quality in both sensing and actuation action. It goes back to Tzou and Tseng [TT91] and has also been used e.g. by Hwang and Park [HP93], Sze and Pan [SP99], Chee et al. [CTS99], Mesecke-Rischmann [MR04] and Schulz [Sch10].

The model consists of two identical uniaxial layers of the material polyvinylidene difluoride (PVDF). The layers are attached to each other with opposite polarities (Figure 7.7). The structure has a clamped support at the left edge. In accordance to the literature, the model is discretized with 5 elements. The material parameters are listed in Table 7.7.

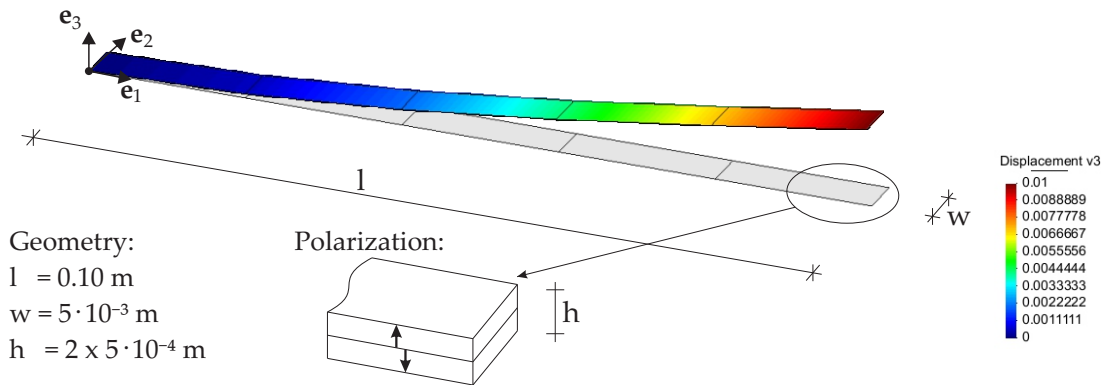


Figure 7.7: Bimorph model: Geometry and polarization of the two layers.

$E_1 = E_2 = E_3 = 2.0 \cdot 10^9 \text{ N/m}^2$	$e^{31} = -4.6 \cdot 10^{-2} \text{ C/m}^2$
$\nu = 0.29$	$\epsilon^{11} = \epsilon^{33} = 1.062 \cdot 10^{-10} \text{ C}^2/\text{Nm}^2$

Table 7.7: Material parameters of the bimorph. Not listed parameters are zero.

For the sensor testing, the bimorph tip is deflected with $v_3^{tip} = 0.01 \text{ m}$ according to Fig. 7.7. The applied deformation results in an electric potential that can be measured along the bimorph. Figure 7.8 shows the results of a linear analysis with the element S-Q-EAS-E and compares it with the results of the mentioned literature. The element S-Q-EAS-E shows very good agreement with the literature results, especially with the element *SM2F Φ 2* of Mesecke-Rischmann [MR04] which also adopts a quadratic interpolation of the electric potential in thickness direction. Schulz and Hwang/Park assume here that 5 pairs of electrodes are used to measure the electric potential. This results in element-wisely constant behavior of the electric potential. Slight deviations from a linear behavior of the electric potential can be identified for element S-Q-EAS-E in Figure 7.8 at the support and the tip of the bimorph beam. This is in accordance with other results in the literature [MR04], while Chee et al. [CTS99] do not show these effects at support and tip.

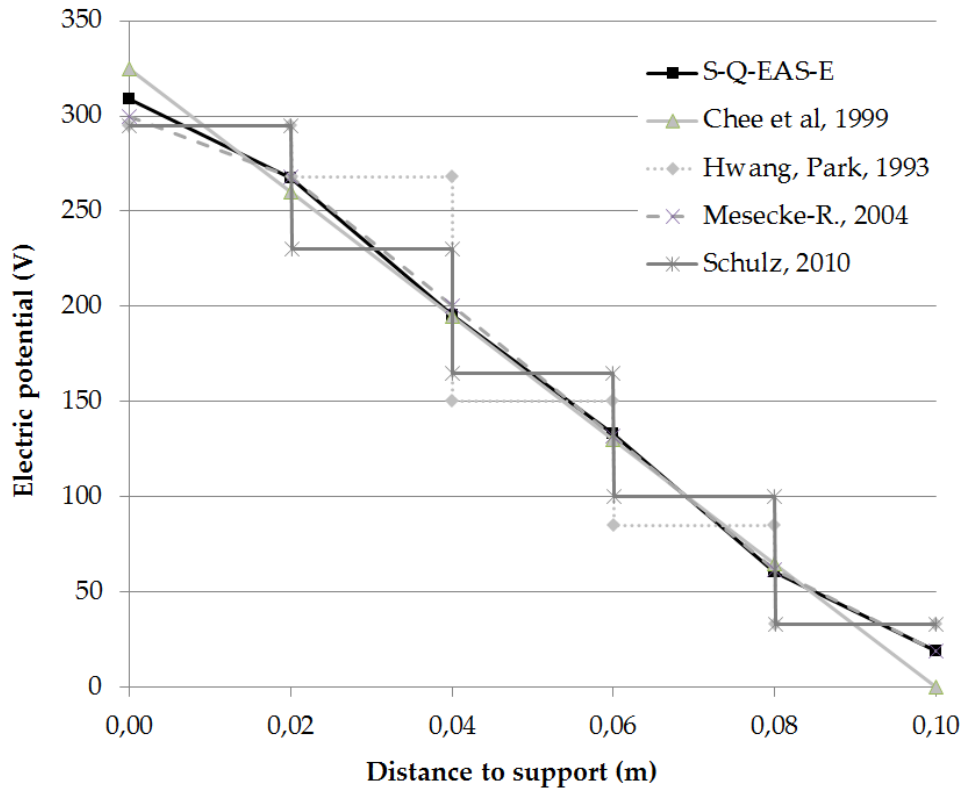


Figure 7.8: Bimorph.

7.2.2 Actor Test

The layers of the bimorph are attached to each other with opposite polarities (Figure 7.7). Thus applying an unidirectional electric field in the transverse direction, one layer is contracting and one layer is expanding, which results in bending of the structure.

To this goal, an electric potential $\Delta\varphi = 1.0V$ is applied across the thickness. This leads to an overall electric field $\vec{E}_3 = -1000V/m$. Thus due to the polarization as depicted in Figure 7.7, the upper layer is contracting while the lower layer is expanding. In total, this results in a lifting deformation of the bimorph tip.

Figure 7.9 demonstrates the perfect agreement of the results with the literature. The tip displacement is $v_3 = 0.345\mu m$ which reflects the analytical solution of a piezoelectric Bernoulli beam [TH93].

7.2.3 Mesh Distortion Test

Finally also mesh distortion effects shall be examined at the bimorph example according to Sze and Pan [SP99]. Geometry and material parameters are chosen as before. However, the baseline mesh is defined with four rectangular elements. The mesh is distorted de-

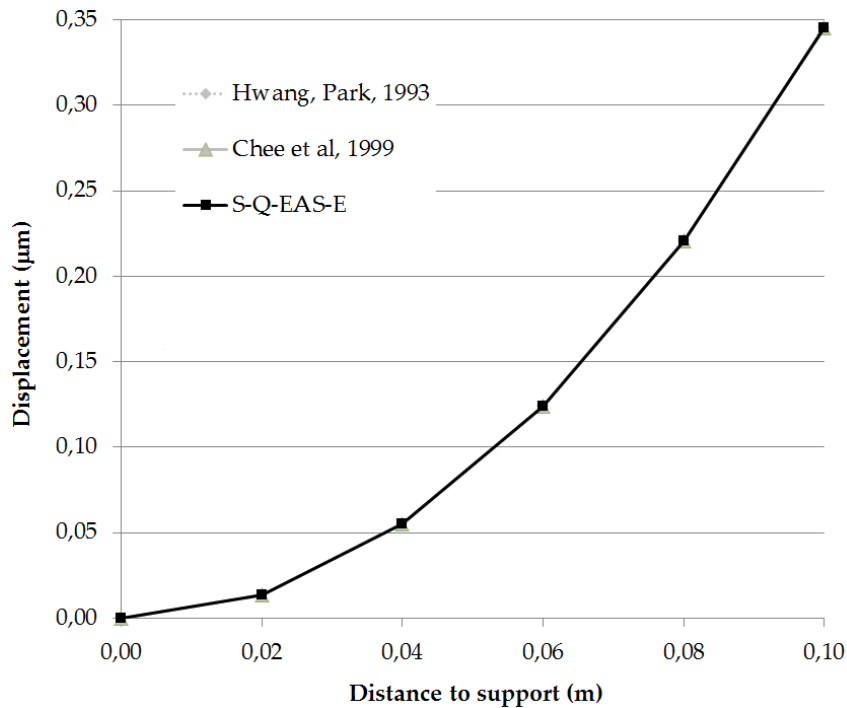


Figure 7.9: Bimorph: Deflection behavior under applied electrical field.

pendent on the parameter s according to Figure 7.10. A statically determinate support is adopted and again an electric field of $\vec{E}_3 = -1000V/m$ is applied to the overall structure.

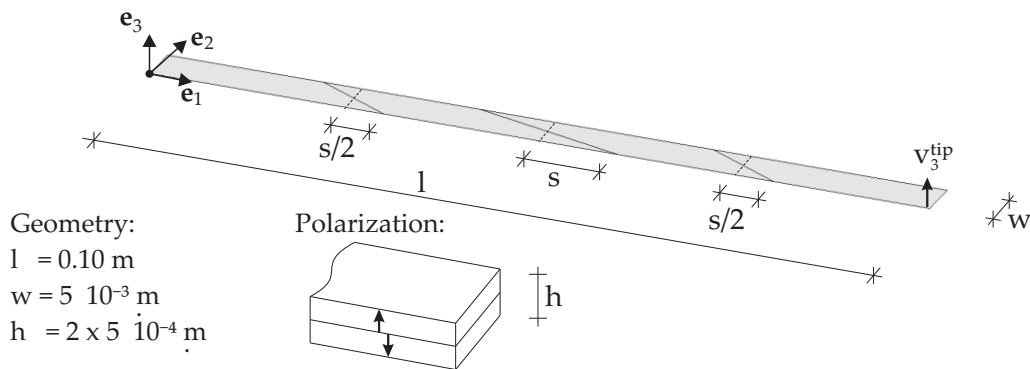


Figure 7.10: Bimorph model with parameterized mesh distortion.

For comparison reasons, also the results of the elements H8D and H8DS of Sze and Pan [SP99], as well as the element H8DS* of Sze and Ghali [SG93] are presented. H8D is a hybrid hexahedral element that adopts enhanced assumed electric displacements besides to the fields of displacements and electric potential. H8DS uses enhanced electric displacements as well as enhanced assumed stresses to improve the element quality.

In Figure 7.11 it can be observed that the elements H8D and H8DS are very sensitive to mesh distortion. The elements have in common that the enhanced fields cannot efficiently eliminate shear locking for distorted meshes. Similar results are obtained by the element S-EAS-E of this work, where the ANS improvement is intentionally omitted for demonstration purposes. The element H8DS* uses a selective scaling technique to alleviate shear locking effects which results in much better results [SG93].

The element S-Q-EAS-E has no stiffening effects in this example and reproduces the analytical result also in the case of high mesh distortion of a coarse mesh.

In general it can be concluded that also mixed elements should be enhanced by further techniques like the ANS method in order to end up in robust formulations that can handle distorted meshes. However, it shall be noted that the error does not increase beyond any limits with growing distortion parameter s . Thus locking effects that depend from a critical parameter have to be considered to be even more malicious in general. The sensitivity of EAS elements goes back to the assumption of a constant metric for the definition of the enhanced strains in equ. (4.125). Thus the passing of the patch test is obtained at the cost of a higher mesh distortion sensitivity. Thus the combination of EAS, EAE and ANS method is favorable.

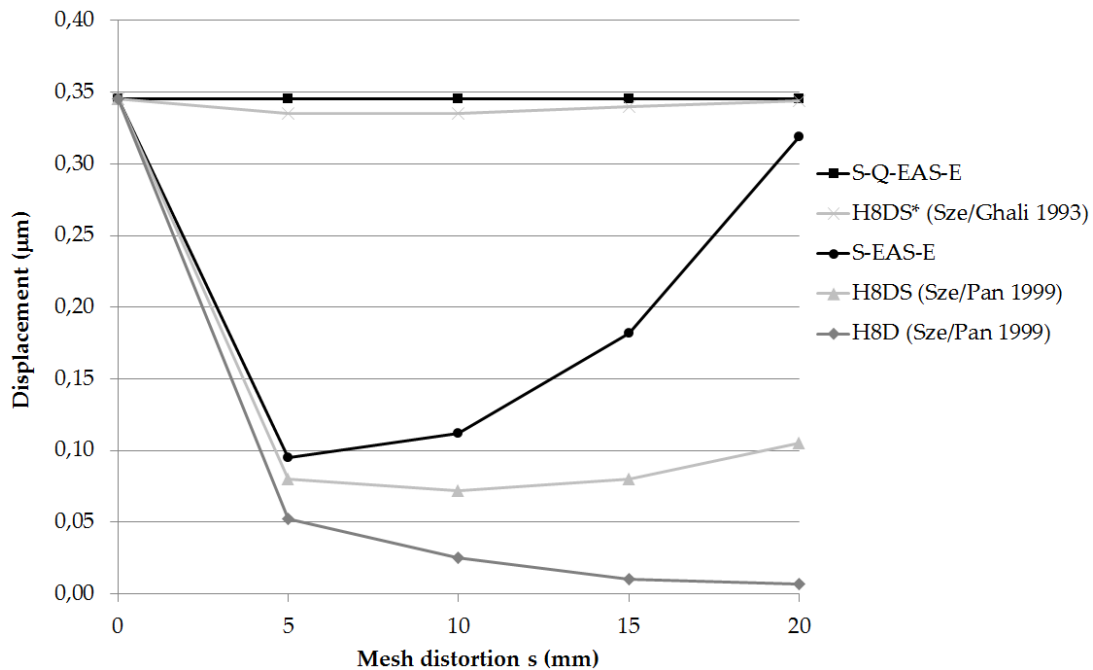


Figure 7.11: Tip displacement of bimorph dependent from mesh distortion.

7.2.4 Geometrically Nonlinear Bimorph Sensor

In many cases of piezoelectric actuation with small deformations, nonlinear kinematics can be neglected and a linear analysis can be performed. However, especially in the case of sensor applications, a geometrically nonlinear formulation is often indispensable. This shall be demonstrated at a bimorph example.

The geometry is chosen as depicted in Figure 7.12. Just as in the bimorph examples before, the model consists of two identical uniaxial layers of PVDF material with opposite polarities (Figure 7.7) and material parameters according to Table 7.7. The structure has a clamped support at the left edge.

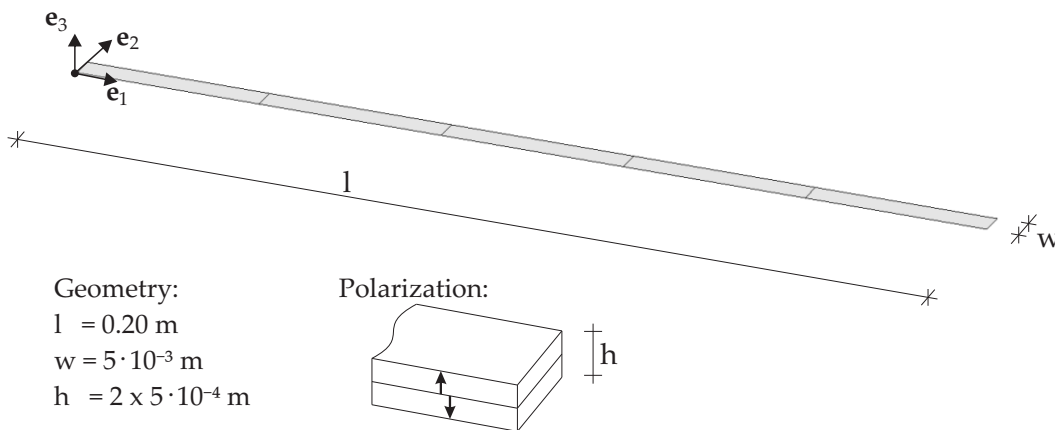


Figure 7.12: Nonlinear bimorph example: geometry and polarization.

The structure is now loaded with single-force loadings at the tip in e_3 -direction. In Figure 7.13, the relations of load-displacement, load-potential and potential displacement are compared for the cases of linear and geometrically nonlinear analysis.

It can be observed that the related displacement for a measured electric potential difference would be strongly overestimated in the linear case. This effect is growing for increasing tip displacement values. Only the geometrically nonlinear simulation is able to represent arising normal stresses in the structure that are growing with increasing load factor. These normal stresses in turn influence the electric potential differences due to the electromechanic coupling.

As shown by Legner [Leg11], this effect is already visible at single layers of piezoelectric material as in the case of the shear patch test in chapter 7.1.6. The normal stresses revealed by the nonlinear kinematics are even needed there to receive any electric potential, as a locking-free linear analysis leads to a vanishing electric potential according to Table 7.5.

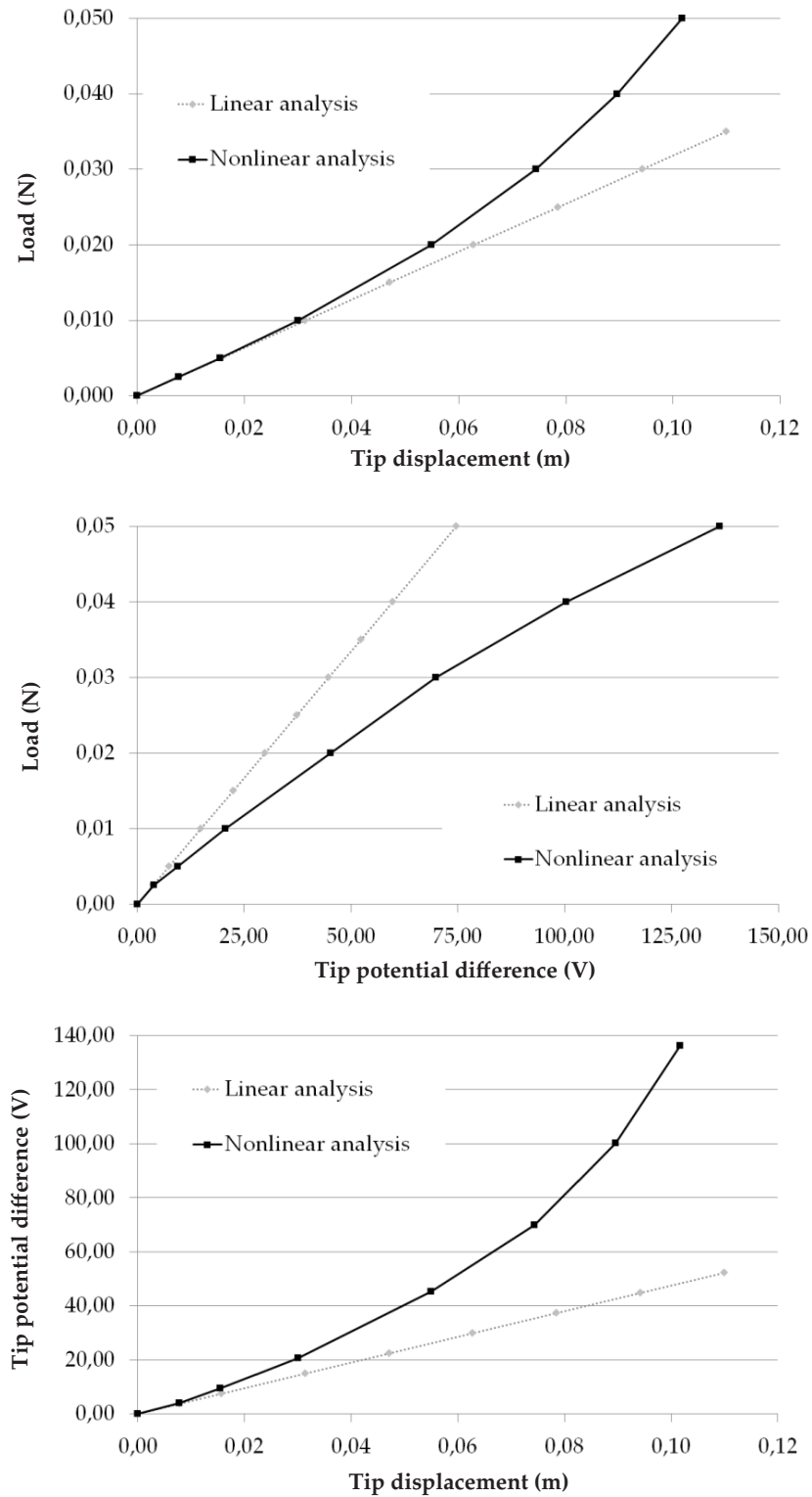


Figure 7.13: Nonlinear bimorph.

7.3 Scordelis-Lo Roof

Piezoelectric elements are commonly used as substructures of larger mechanical structures. The presented finite element formulation allows for a seamless use for both piezoelectric as well as pure mechanical parts of the observed structures. Thus the finite element shall also be benchmarked with regards of pure structural behavior. To this goal, two examples from the well-known shell obstacle course proposed by Belytschko et al. [BSL⁺85] shall be applied in order to test the element's robustness and accuracy in complex strain states. As only small displacements occur, geometrically linear computations are performed here.

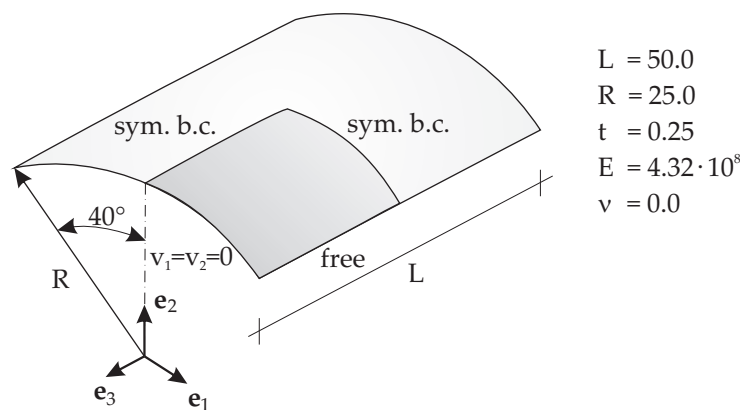


Figure 7.14: Scordelis-Lo roof: Self weight of 90.0 is subjected to the model. The ends are supported by rigid diaphragms.

The benchmark of the Scordelis-Lo roof considers a section of a cylindrical shell. It is supported by rigid diaphragms at its ends, whereas the side edges are free. The roof is subjected to a uniform gravity load. The problem setup and parameters are depicted in Figure 7.14. Due to symmetry, it is sufficient to model only one quarter of the geometry. The vertical displacement at the midpoint of the side edge $v_2 = -0.3024$ is given as the reference solution [BSL⁺85].

A convergence study is performed where different mesh refinements and different element versions are adopted. This allows for a concise investigation of locking phenomena that appear as reduced or highly reduced rate of convergence. The Scordelis-Lo roof is especially useful to test the element ability to accurately solve membrane stress states. As the main part of the strain energy is membrane strain energy, the representation of inextensional modes is not critical here.

Figure 7.15 shows that an element improvement for shear locking is strongly needed. The element S-EAS44404 fails to reach a reasonable result quality even for the finest meshes. Element S-Q-EAS44404 shows already for coarse discretizations with 5 nodes per side a very good performance that is comparable to 9-noded elements of the literature [BSL⁺85]. The element S-Q-EAS44404 converges to $v_2 = -0.3014$. As this example predominantly

activates membrane action, also the element S-Q-EAS04404 without enhanced membrane strain modes is tested. However, as it can be seen, these enhanced modes are only activated for very coarse meshes. It should also be considered that linear elements (3 noded, 4-noded) are known to be almost completely free of membrane locking.

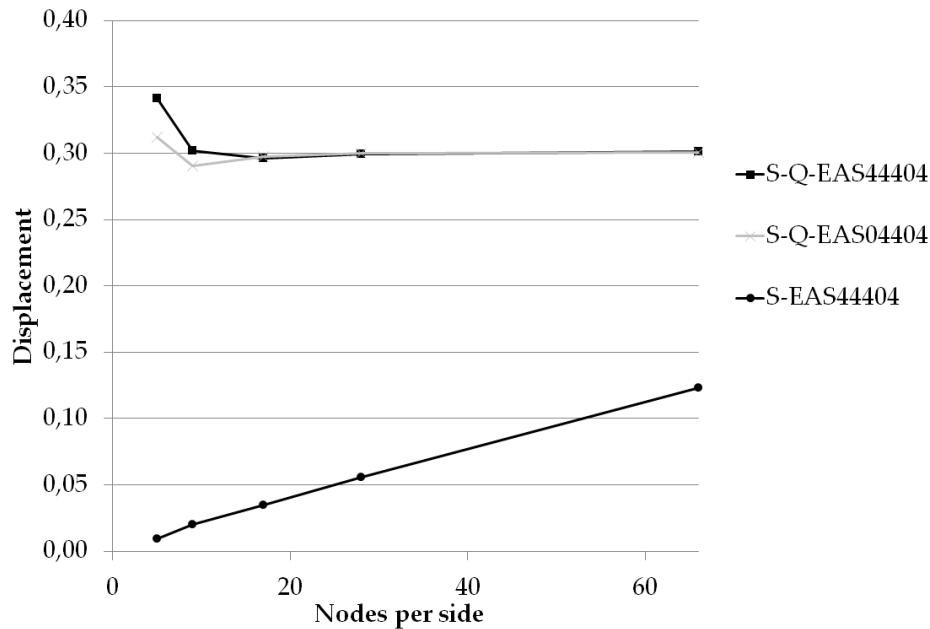


Figure 7.15: Scordelis-Lo roof: Convergence of the absolute value of the vertical displacement at the mid-side of the free edge.

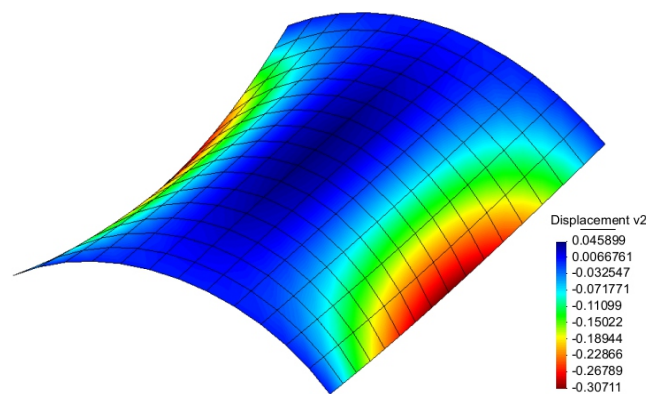


Figure 7.16: Scordelis-Lo roof: Resulting deformation v_2 of the element S-Q-EAS44404 at a mesh with 17 nodes along the side (deformation scaled by factor 10).

The element S-Q-EAS40000 would show practically the same performance as the element S-Q-EAS44404. Thus additional bending strain enhancements, linear shear strains enhancements as well as enhanced normal strains in thickness direction are not needed in this example. This also means that curvature thickness locking is not critical in this ex-

ample. All in all it can be identified that the element is able to efficiently converge in this example, as long as shear locking is eliminated. The latter can be done either by the ANS method or the EAS method, while both approaches result in the same quality of convergence in this example.

7.4 Pinched Cylinder

As second pure structural example, the pinched cylinder from the shell obstacle course proposed by Belytschko et al. [BSL⁺85] is applied. Figure 7.17 shows the model that is supported by rigid diaphragms at the ends and subjected to two opposite point loads in the middle. The pinched cylinder example is a good test for both inextensional bending modes as well as inextensional bending tests. As reference solution, the radial displacement under the point loads is given to be $v_2 = 1.8248 \cdot 10^{-5}$ [BSL⁺85]. Due to symmetry, only one eighth of the geometry is modeled.

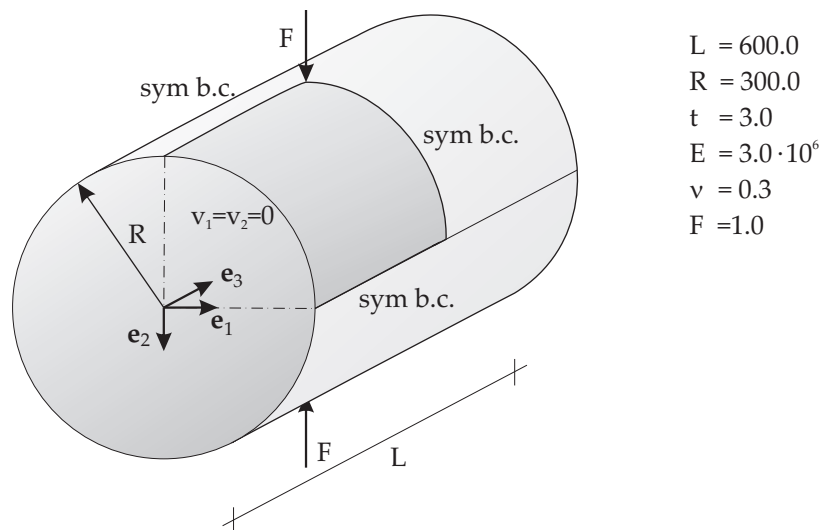


Figure 7.17: Pinched Cylinder, model and problem setup: Equal and opposite single forces are subjected to the model at its midspan. The ends are supported by rigid diaphragms.

Figure 7.18 shows the convergence curves. The enhanced element S-Q-EAS44404 reaches at a mesh density of 30 nodes per side a displacement $v_2 = 1.8153 \cdot 10^{-5}$. The related deformation plot can be seen in Figure 7.19. Again, several element versions with intentionally deactivated element enhancements are tested to evaluate different locking phenomena.

The element S-EAS44404 without transverse shear locking remedy shows again a very low convergence speed. Furthermore, S-Q-EAS44004 reveals the effect of curvature thickness locking. The element reaches only a value of $v_2 = 1.6255 \cdot 10^{-5}$ at the highest mesh density. The reason is the missing EAS enhancements of linear normal strains in thickness direction. Element S-Q-EAS40404 shows nearly the same behavior as the element

S-Q-EAS44404. Thus the enhanced bending strain modes are not needed in this example of a regular mesh. Similarly, also the enhanced assumed membrane modes and linear shear modes are of lower importance in this example.

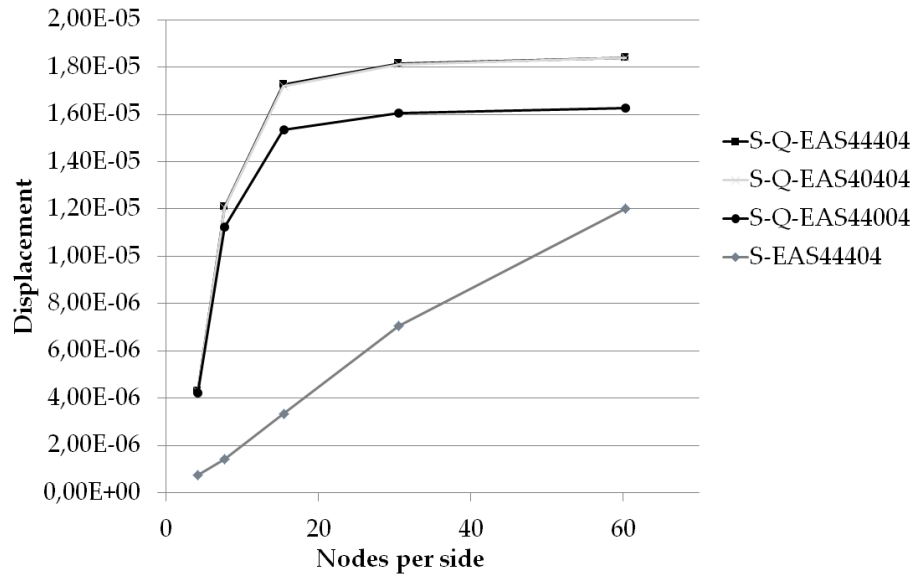


Figure 7.18: Pinched cylinder: Convergence of the radial displacement at the point load position.

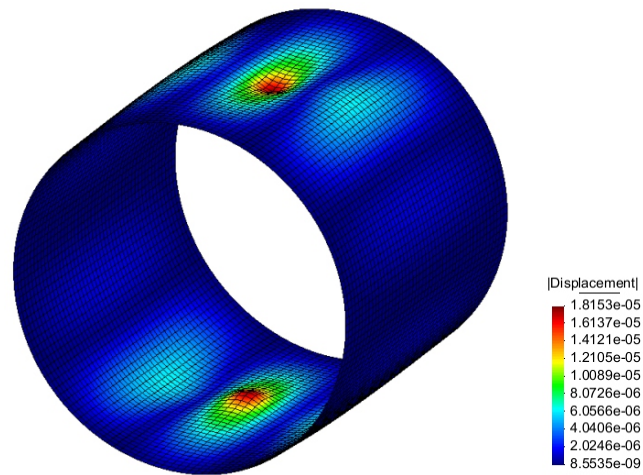


Figure 7.19: Pinched cylinder: Resulting deformation using the element S-Q-EAS44404 (deformation scaled by factor $2 \cdot 10^6$).

7.5 Virtual Design Loop of a Smart Tent

The objective pursued in this example is to design a smart 4-point tent that adopts active control to suppress vibrations in the membrane under external loading [FDI⁺10, FWB10, FB10]. This example presents all steps for the simulation and design of a smart membrane structure and will demonstrate how these steps are combined in one simulation environment. The smart tent example illustrates the methods presented in chapter 5 and verifies the applicability.

7.5.1 Design of the Passive Structure

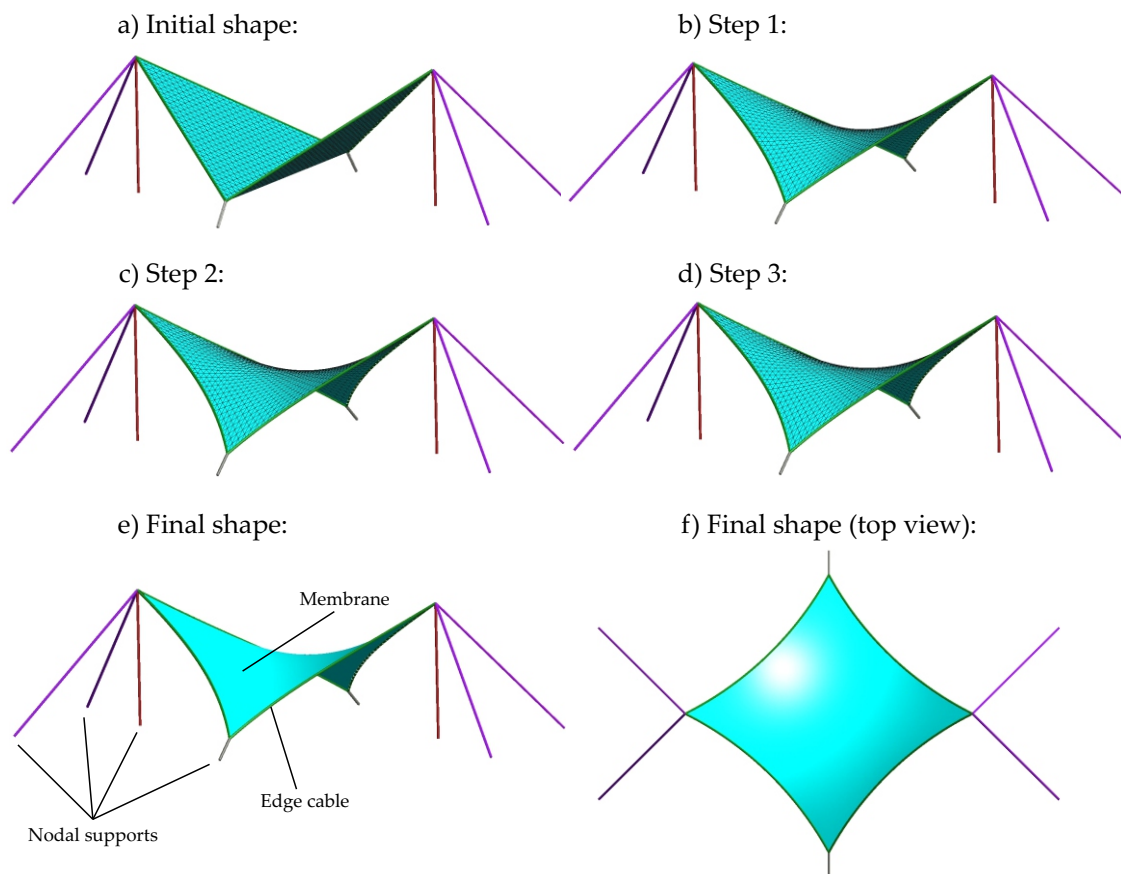


Figure 7.20: Smart 4-point tent: form finding steps and final geometry.

The design process starts with numerical methods of form finding (see also chapter 5.2.2). The guy ropes as well as the pillars are defined as materialized, flexible boundary conditions of the tensile structure. For the form finding process, only the prestress and the boundary conditions have to be provided. Figure 7.20 as well as Figure 7.21 demonstrate the fast convergence to the final shape, despite of the low quality of the initial geometry.

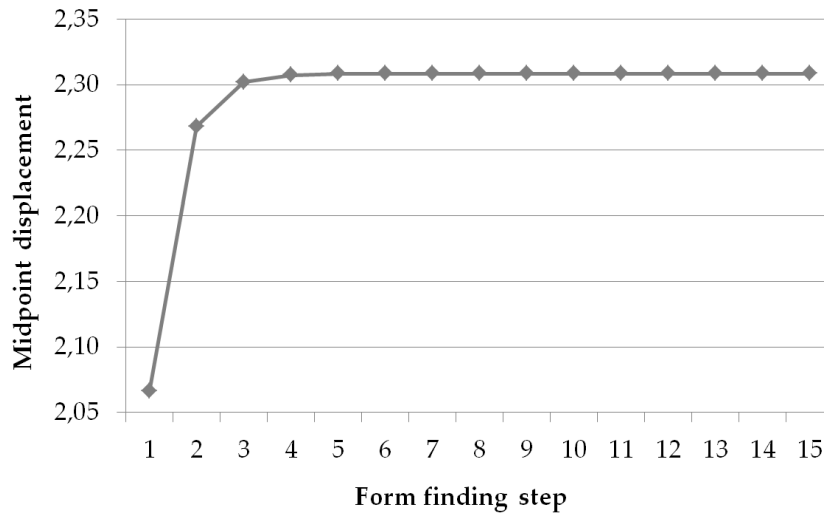


Figure 7.21: Smart 4-point tent: convergence of midpoint over form finding steps.

As the next step, the cutting pattern generation is performed (see also chapter 7.22). Taking the practical manufacturing process into account, the structure is divided into cutting patterns of reasonable size and with small loss of material. Geodesic lines are adopted for the definition of the cutting lines. The flattening process is performed with the inverse engineering method which is based on the description of the underlying mechanical problem of the cutting pattern generation [LWB08, Lin09]. The three-dimensional surface, which is defined through the form finding process, represents the final structure after manufacturing. For this surface the coordinates in three dimensional space and the finally desired prestress state are known. The inverse engineering method determines the surface in a flat two dimensional space which minimizes the difference between the elastic stresses arising through the construction and manufacturing process and the final wanted prestress. Thus the cutting pattern generation leads to an optimization problem, where the positions of the nodes in the two-dimensional space are the design variables.

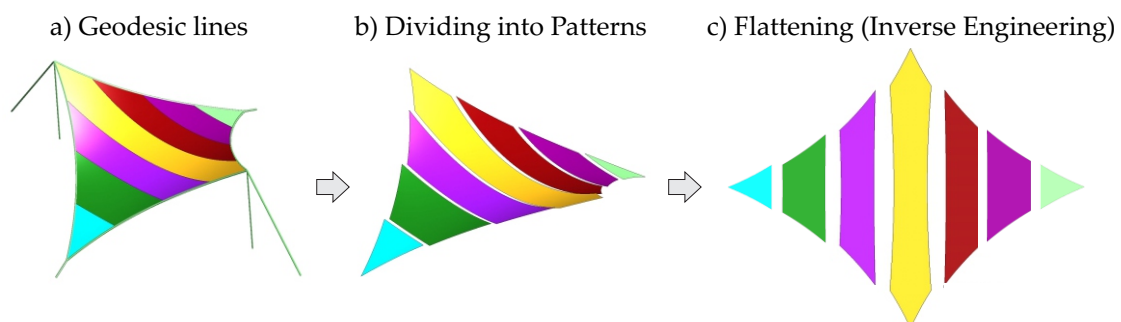


Figure 7.22: Smart 4-point tent: cutting pattern process.

The method is applicable for different element types and is able to consider different material models and arbitrary prestress states. Beyond that, also elastic structural components that are not directly affected by the cutting pattern generation, are integrated in this design phase, as e.g. the supporting trusses of the tent model. This allows for realistic stress and deformation state of the final structure.

7.5.2 Nonlinear Transient Analysis

The next step of the virtual design and simulation process is the geometrically nonlinear transient analysis of the materialized representation of the found membrane shape. The span of the tent is 15.0 m. The material parameters are listed in Table 7.8.

Membrane:	ETFE	$E = 3.00 \cdot 10^8 \text{ N/m}^2$, strength: $4.5 \cdot 10^7 \text{ N/m}^2$ $\sigma_{pre} = 2.5 \cdot 10^5 \text{ N/m}^2$
Edge cables:	Steel	$E = 1.30 \cdot 10^{11} \text{ N/m}^2$ $\sigma_{pre} = 3.3 \cdot 10^7 \text{ N/m}^2$
Guy ropes:	textile material	$E = 1.30 \cdot 10^9 \text{ N/m}^2$ $\sigma_{pre} = 6.0 \cdot 10^7 \text{ N/m}^2$

Table 7.8: Smart 4-point tent: Material parameters.

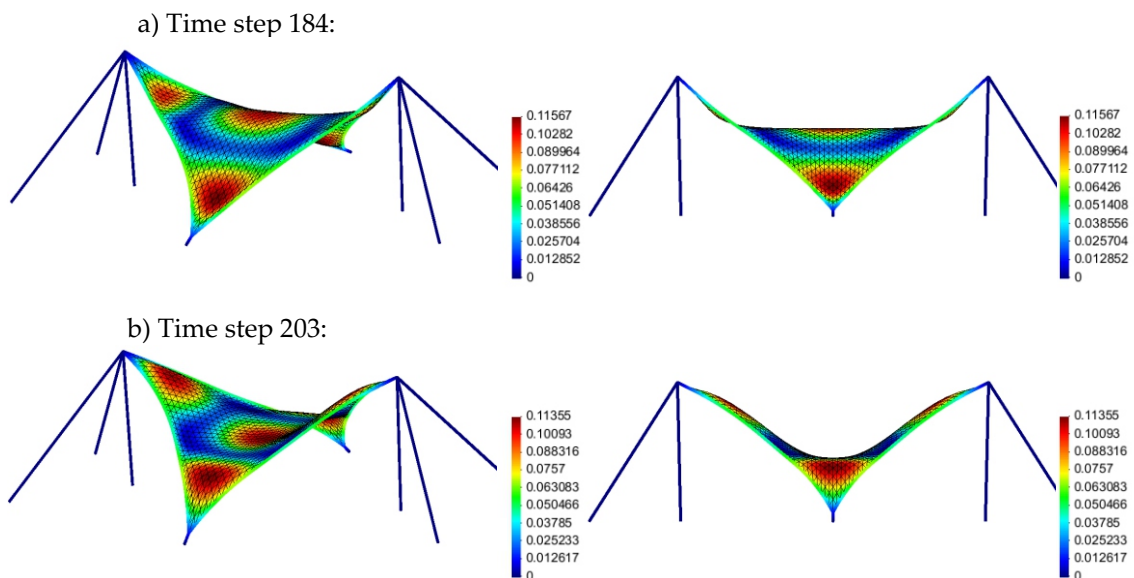


Figure 7.23: Smart 4-point tent: deformations at characteristic time steps of a nonlinear transient analysis of the passive structure under pressure load in 5th eigenfrequency (deformation scaled by factor 5).

A pressure load of $20.0N/m^2$ in 5th eigenfrequency (2.83Hz) is applied to the tent structure. A nonlinear Newmark- β algorithm is used for time integration. The Rayleigh damping parameters according to equ. (5.17) are set to $\alpha_1 = 1.27016$ and $\alpha_2 = 0.0043862$ which reflects 10% damping at the first two natural eigenfrequencies of the structure.

As it can be identified in Figure 7.23, the structure exhibits significant deformations already for small pressure loads. This is also due to the fact that low prestresses have been chosen in this example for demonstration purposes.

7.5.3 Model Order Reduction

In the context of controller design, a flexible membrane structure represents a MIMO system (compare section 5.4), where the application of nonlinear and large-scale finite element models is not suitable. Thus a linearization and model order reduction is performed.

Thus a eigenvalue analysis is performed for the linearized tent model. The six lowest eigenmodes of the structure are presented in Figure 7.24.

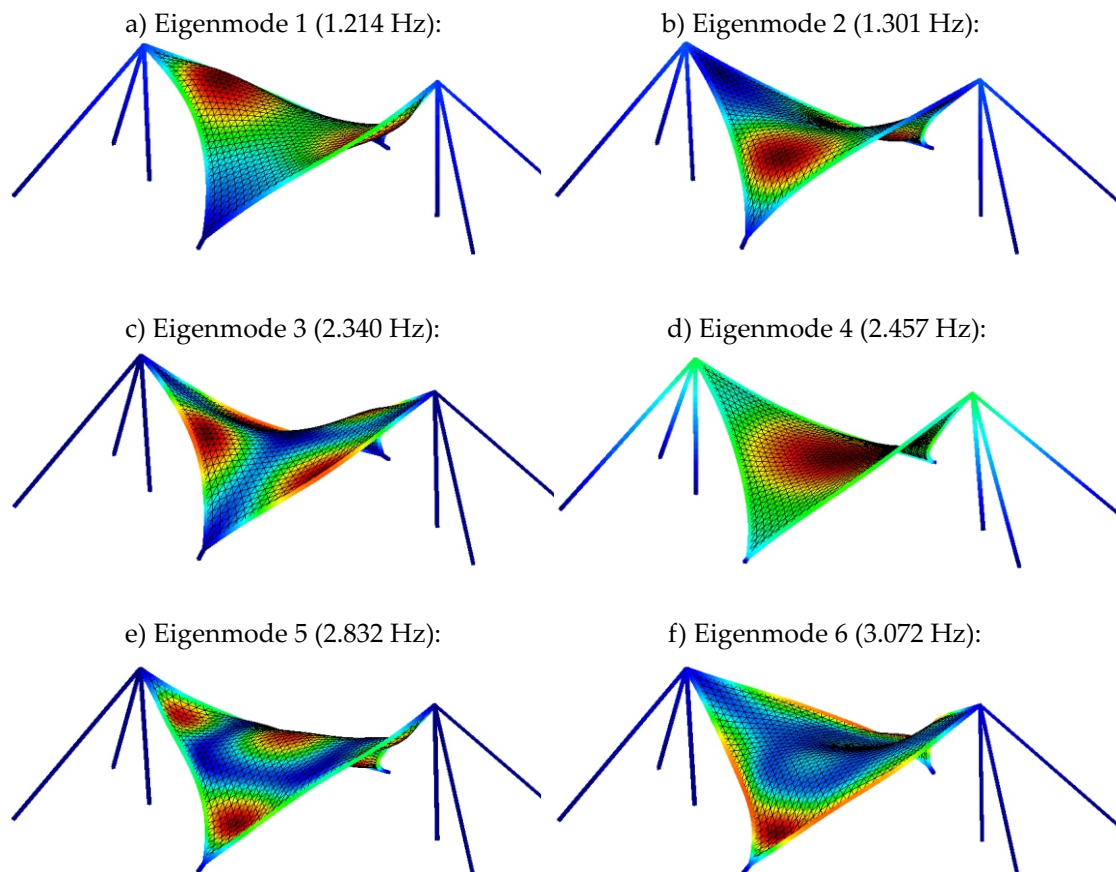


Figure 7.24: Smart 4-point tent: lowest six eigenmodes (scaled deformation and highlighted via contour plot).

It can be observed that the first two eigenmodes are very similar due to the doubly symmetric shape of the structure. However, the related eigenfrequencies do not coincide. This is mainly due to the effect of the different realizations of the lower and upper membrane supports. It can also be identified in eigenmode 4 that the elastic behavior of the guy ropes contributes to the deformational behavior of the overall structure (see contour plot in Figure 7.24 d). Furthermore, an evaluation of all eigenmodes confirms that the vibrations of the membrane predominantly act in the out-of plane direction.

Based on the modal truncation approach as shown in chapter 5.4, the presented 4-point tent model is reduced from 2881 degrees of freedom to 10 modal degrees of freedom. Using the reduced model in a transient analysis allows for a first evaluation of the performed model order reduction and an investigation of induced errors. Figure 7.25 shows exemplarily the displacement plot of the membrane midpoint at a transient analysis of the tent subjected to a half-sin pressure load of $q = 50\text{N}/\text{m}^2$ in the 4th eigenfrequency of the structure. The results of the nonlinear full-order FE model, the linearized full-order FE model and the linearized reduced model are compared. It can be observed that the linearization leads to an overestimation of the deformation, as displacement-dependent stiffness contributions are neglected. Beyond that, it can be seen that the reduced model is not able to exactly reproduce the initial deformation behavior, as the contributions of higher modes are missing. However, in general a good matching of the reduced model can be observed in this test example.

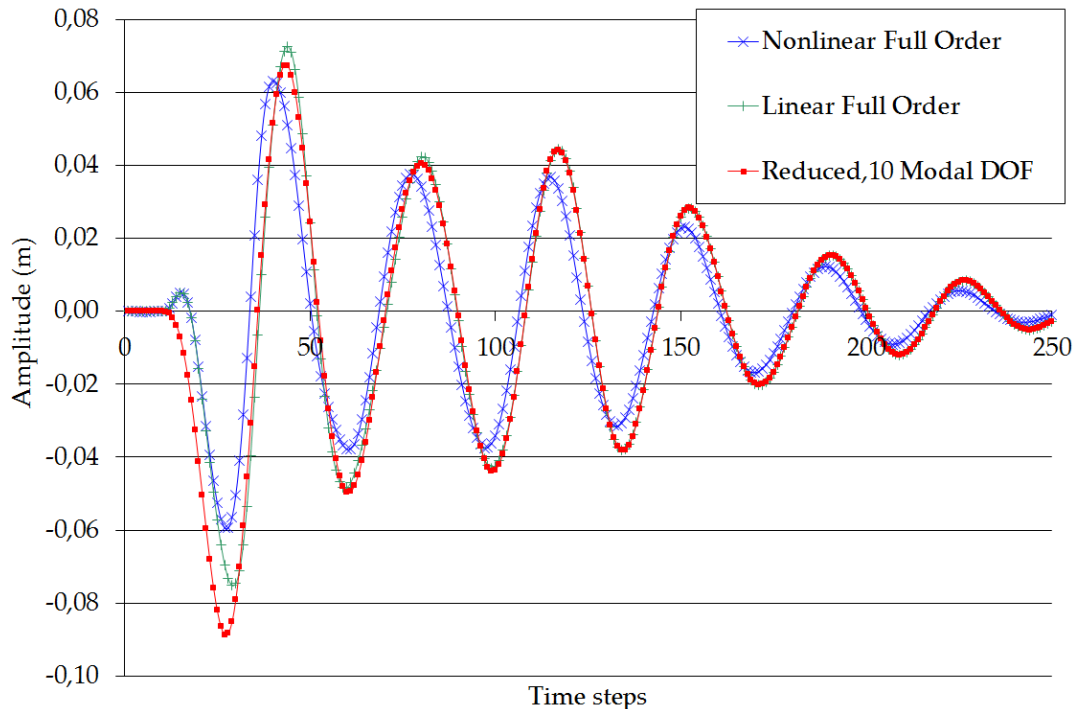


Figure 7.25: Smart 4-point tent: Transient analysis results of the tent midpoint in the case of (a) the full-order nonlinear, (b) the full-order linear, (c) the reduced FE model of the passive structure.

7.5.4 Selection and Placement of Actuators and Sensors

It has been discussed in chapter 5.6 that the selection and placement of sensors and actuators plays a decisive role in the design process of smart structures. This decision highly affects the controllability and observability of the controlled structure and has great influence on the required control effort to satisfy a given design objective and thus on the efficiency of the control system. Beyond that, attaching many sensors, actuators or dampers directly on the membrane is not recommended, as this disturbs the optimal membrane stress state and results in a heavier system. Thus sensor and actuator design has to consider the membrane characteristics.

As already explained in section 5.2 and verified in section 7.5.3, the vibrations of membranes act predominantly in out-of-plane direction, because the membrane's in-plane mode frequencies are much higher than those in the out-of-plane direction. Based on the evaluation of the dominant eigenmodes and the related overall observation index according to equ. (5.40) in chapter 5.6, the positions of 9 laser-based displacement sensors for the 4-point tent are positioned according to Figure 7.26. It should be mentioned that this is already a relatively large number of sensors. Depending on the applied disturbance load, comparable vibration control quality can also be reached with considerably less sensors. For example, in the shown test case in section 7.5.6, similar vibration reduction could be achieved using only the sensors 1-5. However, for evaluation reasons and good observation quality in controller design, the 9 sensors according to Figure 7.26 are used in the sequel of this example.

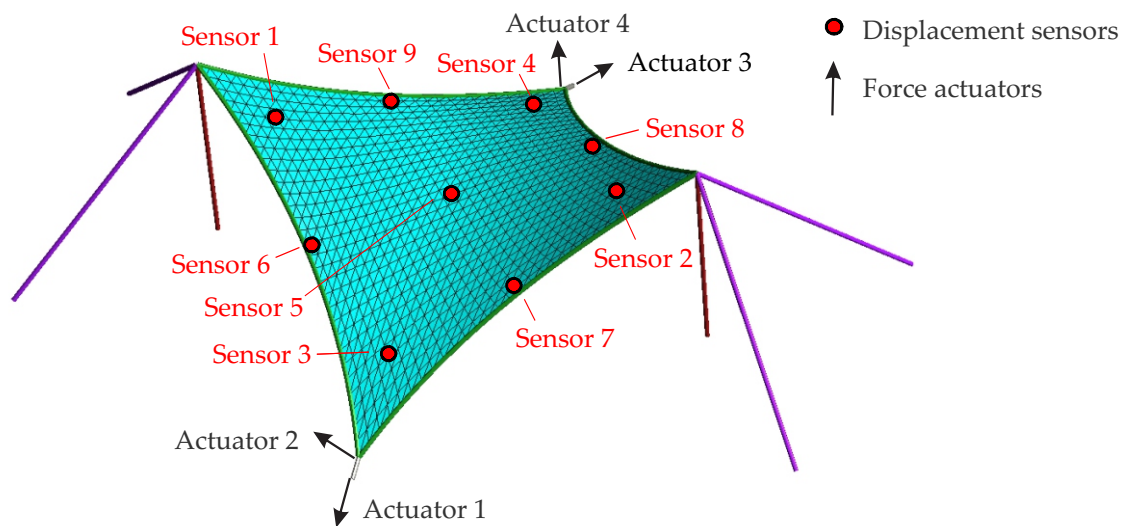


Figure 7.26: Smart 4-point tent: positioning of displacement sensors and force actuators.

The question of type and placement of effective actuators seems to be crucial, because attaching actuators directly on the membrane is in general not recommended due to detraction of the optimal membrane stress state. However, the presented form finding method

itself suggests already reasonable actuator types and places: It has been shown that the form finding algorithm is a very effective alternative for the design of surface structures. The final stresses σ under load and the boundaries Γ of the structure are the major shaping parameters which have to be given and which clearly define the resulting geometry \mathbf{x} as shape of equilibrium [FDI⁺10]. These parameters can be chosen according to the individual preferences, e.g. depending on material, cross section, available design space, geometric restrictions etc. Beyond that, the prestress values and support conditions are as major shaping parameters predestinated to act as shape control parameters. By adaptively modifying the shape of the structure via the mentioned shaping parameters it is possible to maintain optimal behavior with respect to a specified criterion, like vibration reduction, while external effects like loading conditions are changing.

Accordingly, four force actuators at the lower support cables have been chosen for the 4-point tent (Figure 7.26). Actuators 1 and 3 act in-plane to the membrane and actuators 2 and 4 act in out-of-plane direction. From the mechanical point of view, these two actuator groups have in general two different types of effects on the membrane structure: The in-plane actuators manipulate the prestress of the membrane, while the out-of-plane actuators actually change via deformation the Gaussian curvature of the structure.

Summing up, the sensor and actuator positioning driven by form finding characteristics leads in this example to non-collocated sensors and actuators, as the different modal contributions to the displacement field can be best observed within the membrane, while actuator forces should be positioned at the supported corners of the tent.

7.5.5 Controller Design

The linearization at the operating state (prestressed membrane including permanent loads) and the modal truncation have been preparation steps to derive linearized state and output equations suitable for controller design.

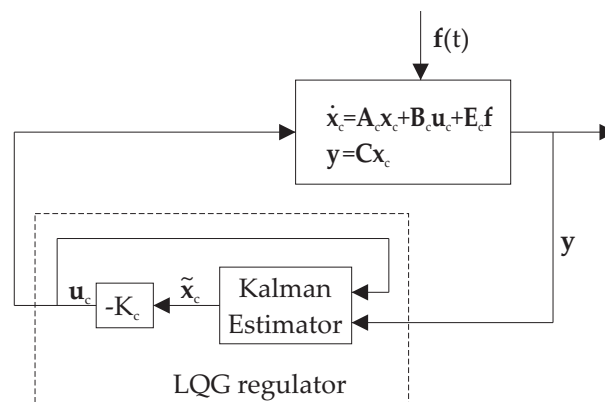


Figure 7.27: Smart 4-point tent: block diagram for closed-loop control with a LQG regulator.

The state space matrices A , B , E and C are derived from the data provided by the finite element model according to equ. (5.31) and equ. (5.31) in chapter 5.7. The matrices D and F are set to be zero.

The actual design of an appropriate regulator is performed in Matlab/Simulink. Thus a data interface between Matlab and Carat++ has been implemented in order to establish an automated simulation and design framework.

A Kalman estimator is used to obtain a state variable estimation \tilde{x}_c of the plant model based on the information of the sensors placed on the membrane. Based on the estimation of the state, the state feedback gain K_c is used to generate the actuator signal (Figure 7.27). The feedback gain matrix is determined according to equ. (5.51) in chapter 5.7.

The sampling interval for discrete-time control is chosen to be $T=0.01$ sec. A pressure load of $q = 20N/m^2$ in the 5th eigenfrequency of the structure is applied as reference disturbing load case. Thus the possibility of resonance is provided. The weighting matrices for the optimal LQG controller design have been chosen like that: $Q = I_{5 \times 5}$ and $R = 0.01 \cdot I_{4 \times 4}$.

The following simulation results were obtained in Matlab/Simulink (Fig. 7.28). The displacement amplitude is reduced by a factor of 2.6 at sensor 1 and 2, by a factor of 2.3 at sensor 3 and 4, and by a factor of 5.2 at sensor 5 (midpoint of the membrane). Error sources like measurement errors induced by the sensing device have been ignored in this example.

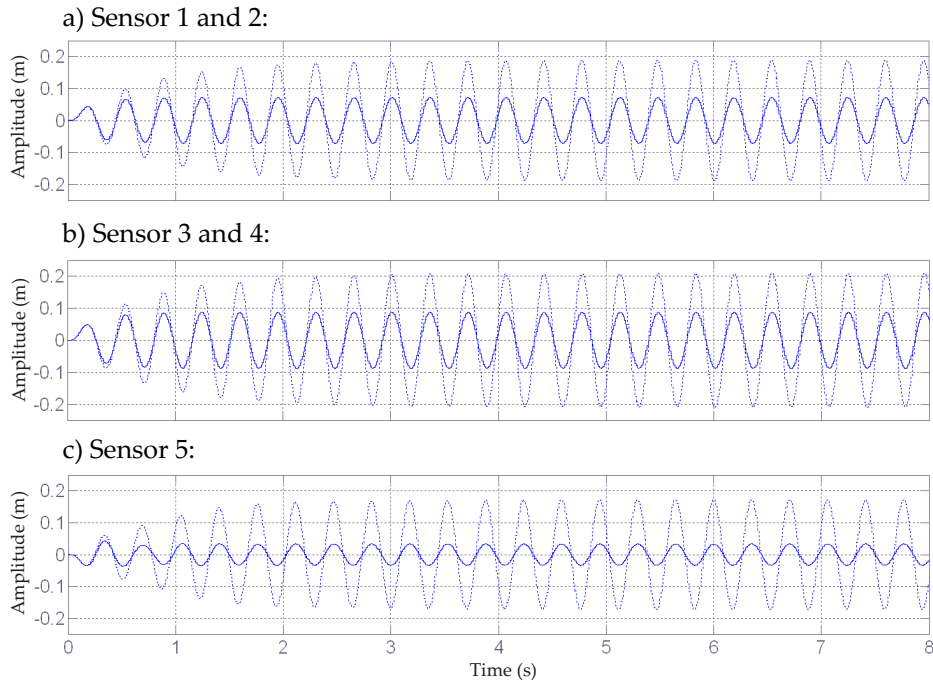


Figure 7.28: Smart 4-point tent: sensor values for uncontrolled (thin line) and controlled (bold-printed line) system simulation in Matlab.

7.5.6 Nonlinear Simulation including Control

The described smart tent model is now simulated including closed-loop control based on the full-order and geometrically nonlinear FE model. For time integration, the implicit Newmark- β method is chosen. Again, a pressure load of $\mathbf{q} = 20\text{N}/\text{m}^2$ in the 5th eigenfrequency of the structure is applied as disturbing load case. Control is activated at time step 200.

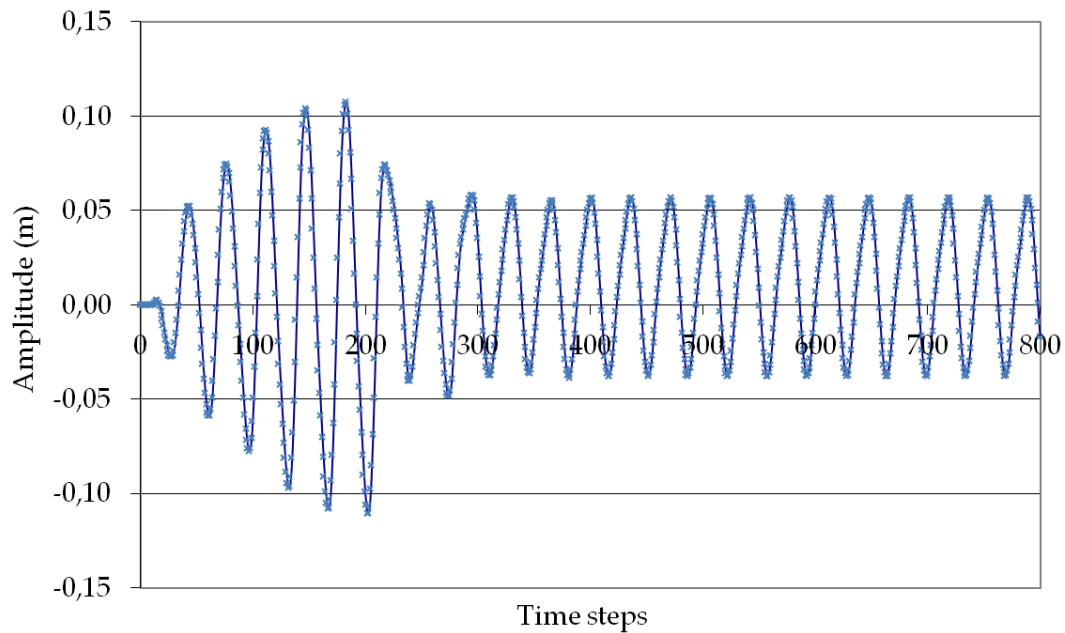


Figure 7.29: Smart 4-point tent: Displacement of the membrane midpoint at a geometrically nonlinear transient analysis including control (control starts at time step 200).

Figure 7.29 shows the resulting displacement of the membrane midpoint. Via control, a reduction of the amplitude of the midpoint displacement by a factor of 2.4 is obtained. Thus the vibration reduction factor is smaller compared to the predicted factor of the reduced model of the controller design, as described in chapter 7.5.5. However, still a successful vibration reduction can be achieved in the nonlinear full-order model simulation.

Beyond that, it can be identified that the vibration of the midpoint is a bit shifted towards positive displacement values due to the control action. This is due to the fact that the actuators are only positioned at the lower tension cables of the 4-point tent (compare Figure 7.26 in chapter 7.5.4).

The vibration reduction of the overall model can be observed in Figure 7.30. Here, the deformation plots for time steps with maximum amplitude for the uncontrolled case and the controlled case are compared. The deformation is additionally highlighted via the contour plot with equal scaling for both pictures.

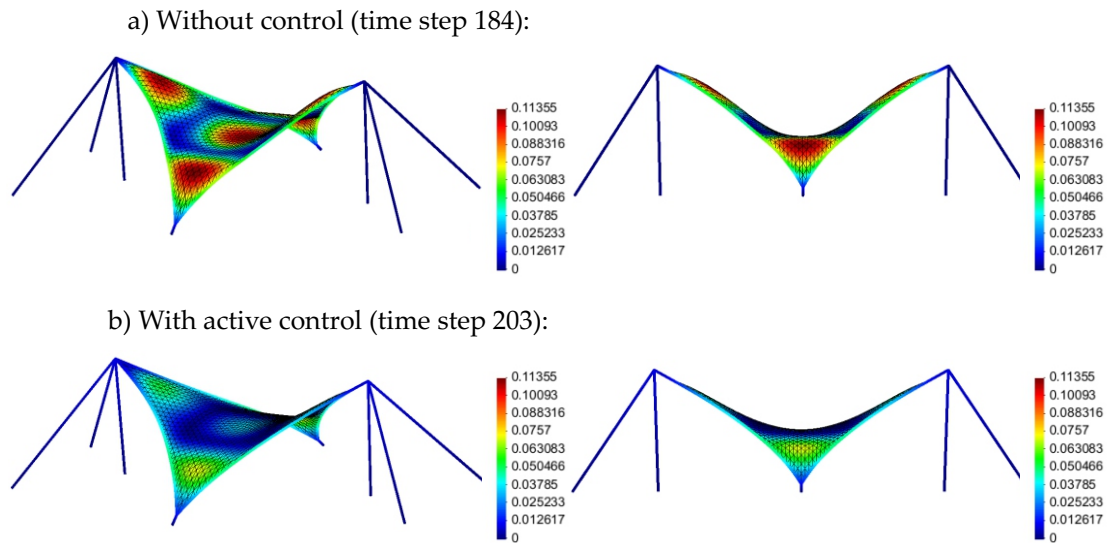


Figure 7.30: Smart 4-point tent: Deformation plot for time steps with maximum amplitude for the uncontrolled case (a) and the controlled case (b).

7.5.7 Overview of the Design Process

Summing up, this example of a four point tent has demonstrated the overall virtual design loop of a smart structure including closed-loop control. An overview of the design process is given in Figure 7.31.

The overall design process is based on the finite element model and starts with the design of the passive structure. Using the numerical methods of form finding and cutting pattern generation, optimal membrane shapes can be designed that include decisive aspects of the manufacturing process.

The simulation of the full-order passive system allows for investigation and design improvement of the uncontrolled model before aspects of the smart structure are focused.

The modal analysis is used in the context of two decisive design steps: First of all, it is the basis for an optimal sensor positioning according to an optimal observability index. Second, it forms the basis for the modal truncation that is needed as preliminary step for controller design.

Based on the reduced state space model, the finite element model-based controller design can be performed. The controller evaluation in the virtual model happens in two stages: First, the controller is directly tested in the environment of the linearized and reduced model of the controller design. Second, the controller is integrated in a nonlinear transient simulation of the full-order model in order to perform controller testing in a more detailed and realistic model setup. Controller design has been conducted in Matlab/Simulink. All other steps of the design and simulation process (Figure 7.31) are performed in the software Carat++.

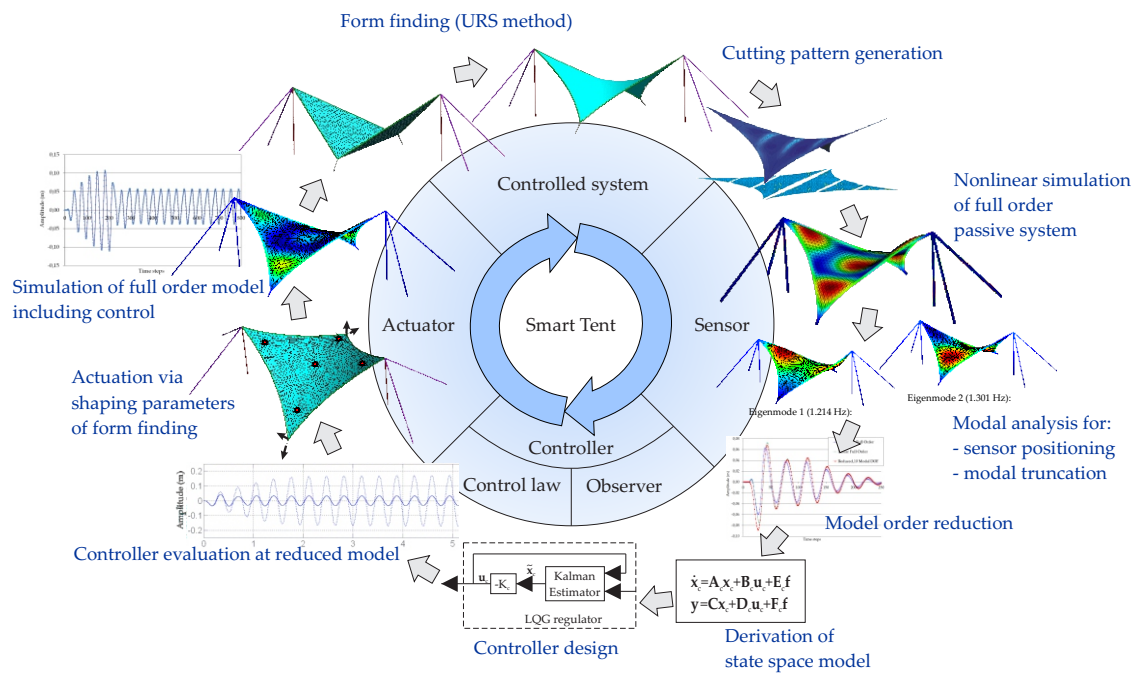


Figure 7.31: Smart 4-point tent: Overview of the overall design process.

The shown controller design approach based on the finite element model as well as the sensor and actuator positioning based on the observability and controllability indices according to chapter 5.6 are also applicable in the same way to structures with bending stiffness and piezoelectric actuation. Examples are provided in the literature e.g. by Gabbert et al. [GTK06, GNW08].

While the smart 4-point tent example mainly addresses questions of the overall design loop of structures with closed-loop control, the next example shall extend the presented design framework to finite element-based structural optimization in the context of static-aeroelastic shape control of a solid-state piezo-actuated variable-camber morphing wing.

7.6 Solid-State Variable-Camber Morphing Wing

In the past decades, smart materials have been widely and successfully tested in the context of controlling smooth and continuous aerodynamic control surfaces [BBA⁺11]. These continuous control surfaces can be superior to conventional discrete trailing-edge control techniques due to higher aerodynamic efficiency, reduced number of parts, reduced complexity, and thus reduced maintenance and fabrication costs. Despite of the proven feasibility of piezoelectric materials in small unmanned aircraft, virtual design and aeroelastic tailoring in a numerical environment is still a major challenge.

In this example, the three-dimensional static-aeroelastic simulation and design of a solid-state piezo-actuated variable-camber morphing wing for low Reynolds number regimes is presented [FMBB13, Fis13b]. The airfoil employs surface-induced forces via smart material actuators. The coupled fluid structure interaction is considered in order to integrate the aerodynamic loads in the airfoil design process. Parameter-free structural optimization is used in order to integrate a flexible, generic and efficient optimization technique in the early stage of design.

7.6.1 Static Aeroelastic Model Setup

7.6.1.1 Structural Simulation

The basis for the development of the simulation model is provided by a real wing model (Figure 7.32) built and tested by Bilgen and Friswell [BSFF11, BF12].

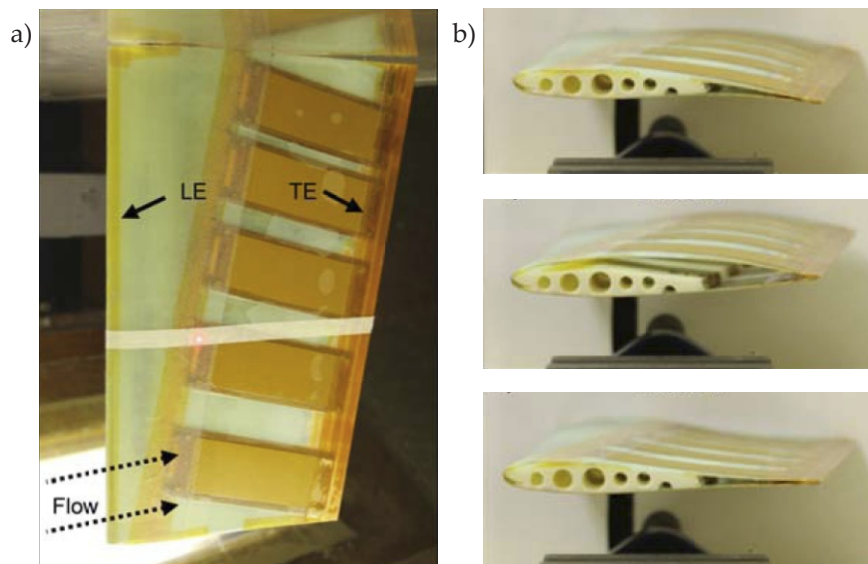


Figure 7.32: Variable-camber tapered wing [BF12]: Installation in the wind tunnel (a) and deformation response for selected choices of piezoelectric excitation (b).

The continuity in the wing surface is achieved by using a single substrate layer that is completely surrounding the shape (Figure 7.33 a). This substrate forms the surface of the airfoil and it serves as the host material for the piezoelectric actuators.

The structure is completely modeled with composite shell elements that cover the layers of both substrate material and piezoceramic material (Figure 7.33 b). The baseline geometry is a tapered wing with a NACA 0012 profile when unactuated and without any external loads. The wing has a span of 248mm, a root chord length of 177mm and a tip chord length of 128mm. The model contains 9877 composite shell elements with a total of 59.724 degrees of freedom. This wing surface structure is pinned to a three-dimensional spar structure that provides line support conditions in spanwise direction at two locations of the cross section.

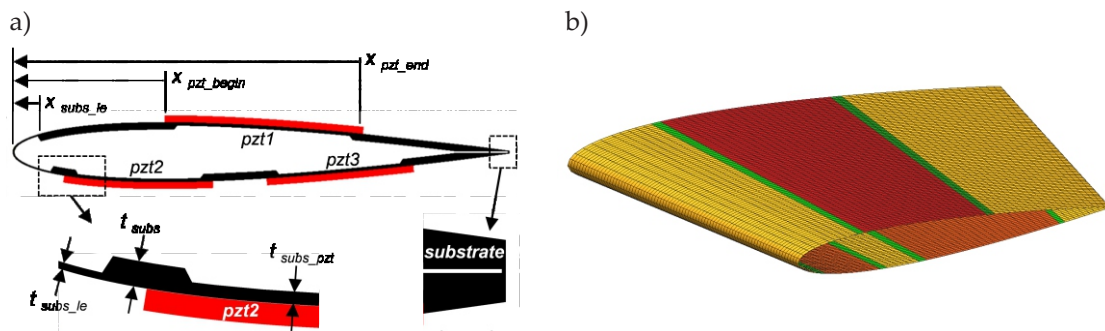


Figure 7.33: Structural airfoil model: Variable thicknesses to allow for optimum thickness ratio (a) and 3D realization of the 2D design (b).

The Macro-Fiber Composite (MFC) actuator is chosen to form the active surfaces. The MFC actuators were originally developed at NASA Langley Research Center and offer structural flexibility and high actuation authority [HW03]. The inplane poling and inplane voltage actuation allows the MFC to utilize the 33 piezoelectric effect, which is higher than the 31 effect used by traditional PZT actuators with through the thickness poling [HKGG93]. The MFC can elongate up to 1800ppm if operated at the maximum voltage rate of -500V to +1500V. The wing has 3 active sections around the cross section (Figure 7.33) with 5 sections each in the spanwise direction (Figure 7.34).

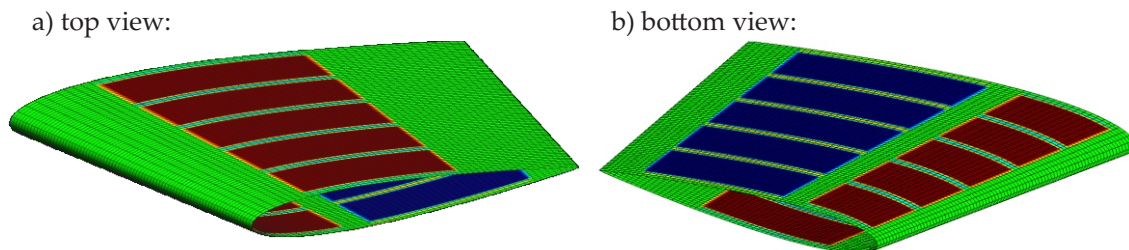


Figure 7.34: Structural airfoil model: 5 active sections at top surface (a) and 10 active sections at bottom surface (b).

The MFCs have a thickness of 0.3mm. The piezoelectric layer is modeled as an orthotropic linear elastic material with a Young's Modulus of 30.336 GPa in chord direction and 15.336 GPa in the other directions. For comparison reasons with earlier work of Bilgen et al., the substrate material is modeled as orthotropic material with a Young's modulus of 290 GPa in chord direction [BSFF11]. A Young's modulus of 145 GPa in the other directions is assumed here. The 33 mode interdigitated MFC actuator is modeled as a 31 PZT ceramic of the same actuation strain at the maximum voltage rate of -500V to +1500V. The applied voltage is modeled with nonzero Dirichlet boundary conditions.

7.6.1.2 Fluid Simulation

The fluid simulation is conducted with the open source software package OpenFOAM 2.1.x, using the SIMPLE algorithm, a steady-state solver for incompressible turbulent flow. Different angles of attack are examined for a flow velocity of 20m/s and a Reynolds number $Re = 2.85 \cdot 10^5$.

The fluid domain is built with an own parameterized generator that creates a readable file for the structured meshing tool blockMesh of OpenFOAM. This mesh generator is derived from an existing 3D C-grid mesh generator [MAC] and allows for independent definitions of root and tip cross sections. The configuration variables controlling the mesh and wing geometry are fully parameterized (see Figure 7.35 a) and can be varied in batch mode. This allows for an automated fluid mesh update in the case of optimization runs.

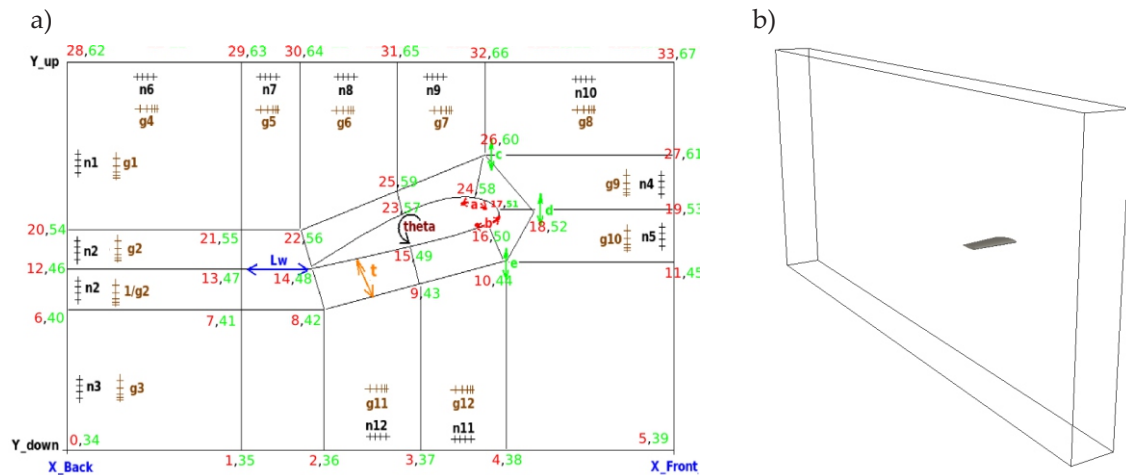


Figure 7.35: 3D CFD simulation: Parameterization for automated meshing (a) and computational fluid domain (b).

The fluid domain (Figure 7.35 b) spans $3.5m \times 1.6m \times 0.248m$ and contains 3.5×10^6 cells. In a first setup, the fluid domain ends at the wing tip. Thus a correction for the wing tip vortices has to be taken in account according to the lifting-line theory. The cells next to the airfoil boundary have a thickness of $3 \cdot 10^{-6}m$ (see also Figure 7.36 b), which leads to a

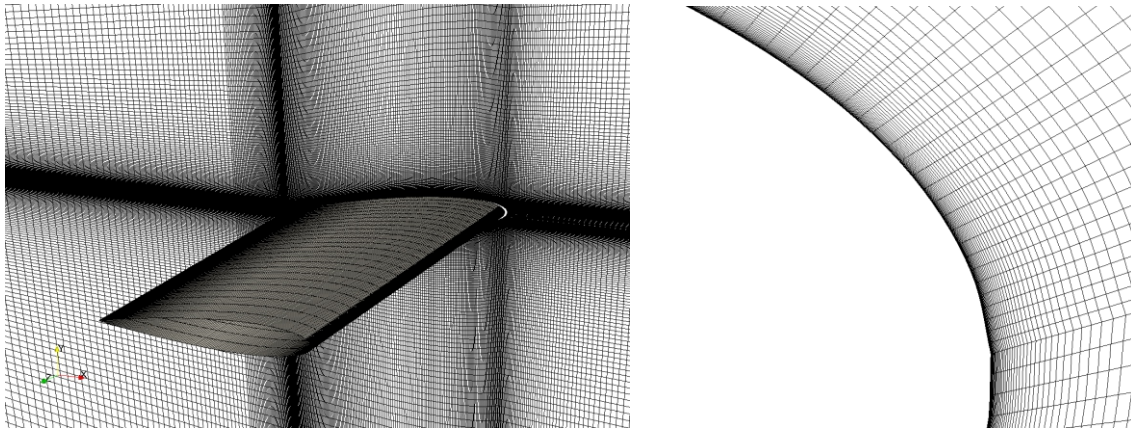


Figure 7.36: 3D C-grid mesh for CFD simulation with OpenFOAM (a) and fluid mesh near the leading edge (b).

maximum non-dimensional wall distance y^+ of 0.6. Consequently, no wall functions are used. For the fluid simulation, a Reynolds Averaged Navier-Stokes (RANS) model with the $k-\omega$ -SST turbulence model is chosen. The turbulence parameters for the free stream ($k = 0.0006 \frac{m}{s^2}$; $\omega = 40 \frac{1}{s^2}$) are derived from the turbulence intensity of 0.1% measured in wind tunnel experiments [BF12, BLF13].

As a preliminary step, the fluid model is evaluated via comparison with experimental data. Figure 7.37 shows the 3D lift coefficient of experiments [BF12, BLF13], numerical analysis and thin airfoil theory for different angles of attack. Simulation results and values from thin airfoil theory are modified with a factor $AR/(AR+2)$ according to lifting-line theory where AR denotes the aspect ratio. As expected, the lift-coefficient for the 3D simulations are smaller than for the 2D case. In general, the 3D simulation results are superior to the thin airfoil theory in matching the experimental results. Accordingly, Figure 7.38 shows the drag coefficients for varying angle of attack. CFD simulation results and thin airfoil theory are calculated with the following approximation according to lifting-line theory [Pra18]:

$$C_d = C_{d0} + \frac{C_l^2}{AR \cdot \pi \cdot e} \quad (7.5)$$

where $e = 0.85$ is assumed. The 3D simulation results with OpenFOAM match the experimental data in a satisfying manner. Slight differences in the setups (e.g. chord lengths, assumed AR) as well as restrictions of the experimental setup and the chosen simulation model have to be considered.

7.6.1.3 Static-Aeroelastic Coupling

In order to solve the 3D fluid structure interaction problem and in order to transfer data between the non-matching meshes of the structure and the fluid, the code EMPIRE can be

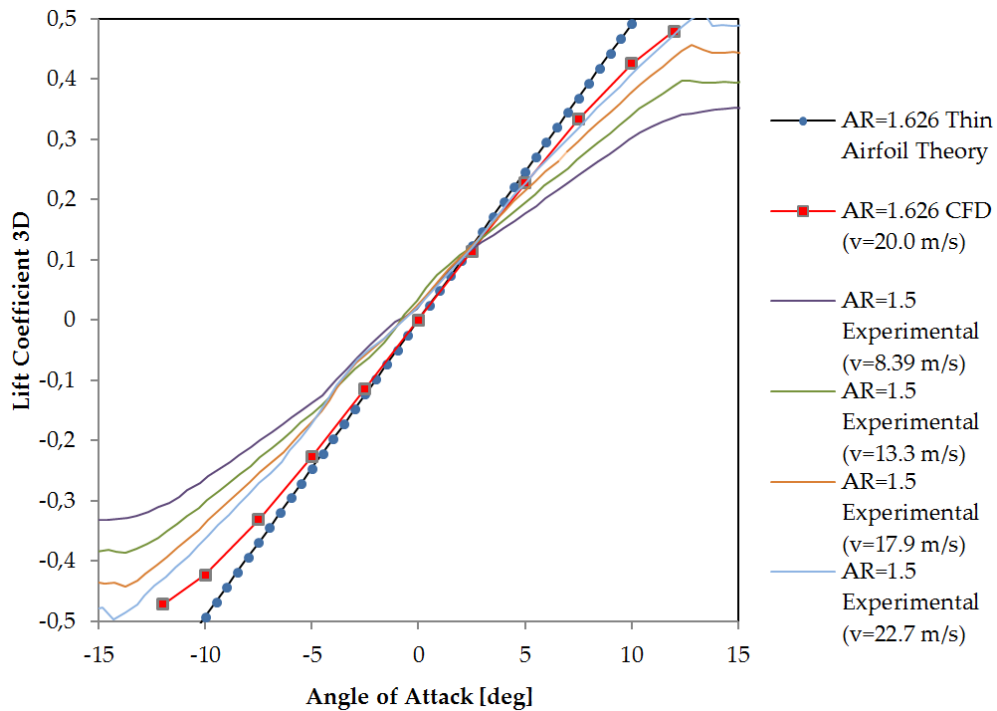


Figure 7.37: Evaluation of lift coefficient: CFD simulation with OpenFOAM at $Re=285000$ compared with thin airfoil theory and experimental data

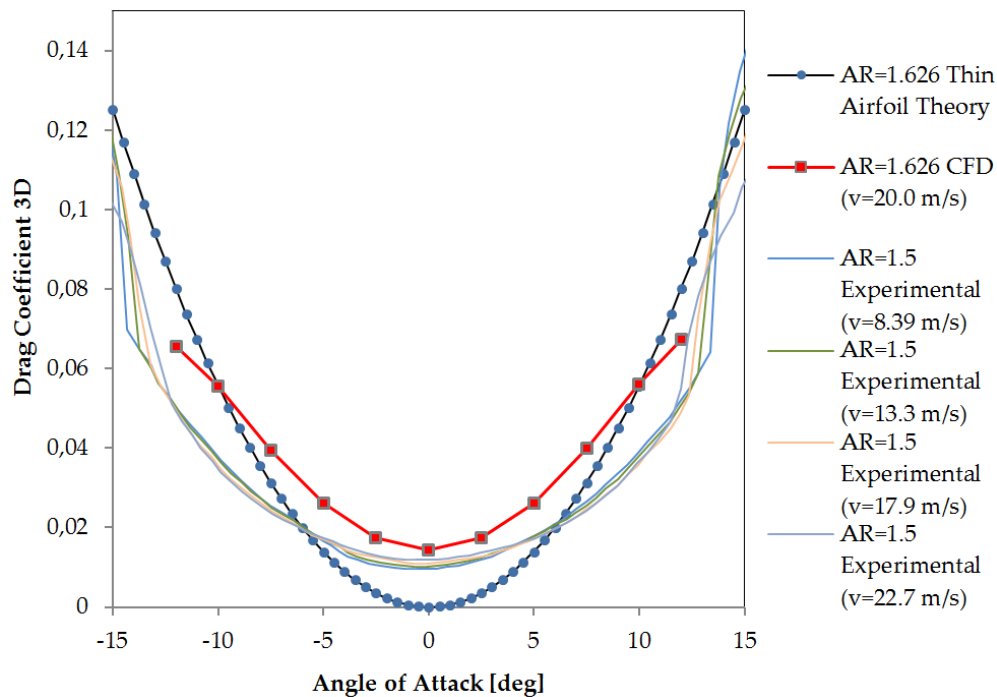


Figure 7.38: Evaluation of drag coefficient: CFD simulation with OpenFOAM at $Re=285000$ compared with thin airfoil theory and experimental data.

used [SWB12]. It provides a MPI-based communication and flexible data mapping in order to transfer updated pressure distributions to the structural code and newly calculated aero-loaded deformed airfoil shapes back to the fluid code.

7.6.2 Parameter-Free Optimization of the Wing

In general, the numerical treatment of shape and sizing optimization requires a suitable parameterization. Typically, optimization variables are the control nodes of an additional CAGD model. However, this results in high modeling effort due to the redesign of CAGD geometries during the optimization steps. In order to integrate gradient-based shape and sizing optimization in an early stage of design, CAGD-free (also called "parameter-free" or "FE-based") optimization methods are adopted. The design variables are directly defined on the finite element model, which eliminates the need for an additional CAGD model [FMB12b]. In general, all parameters of the finite element model can be chosen as design variables: e.g. the finite element nodes can be used for shape optimization, or parameters like finite element thicknesses of fiber orientations for sizing optimization. The CAGD-free optimization is very flexible, easy to be defined, needs no additional model and can be integrated in an early stage of the design process.

First order gradient information is computed by an exact semi-analytical approach [BFD08, BFF10]. Regularization and filtering is performed to overcome arising singularities due to the highly non-convex design spaces [FWB13]. To overcome the problem of an increasing numerical cost due to the large design space, the design sensitivities for objectives and constraints are evaluated via adjoint formulations [BFLW09]. Here the sensitivity of the response functional is obtained directly, with no intermediate computation of derivatives of the state variables.

Focus of the optimization of a wing is usually the maximization of the lift-to-drag-ratio and/or the minimization of weight. However, several constraining effects have to be considered. In the context of variable-camber wings, the structure must be stiff enough to prevent flutter and divergence, but on the other hand it has to be compliant enough to allow for large motions to efficiently operate in a reasonable range of fluid conditions. For the structural optimization of the described wing, the following setup is defined: The geometry according to the preceding section is used as initial geometry of the non-actuated airfoil for the design process. The optimal actuated shape with maximum increase of the cost function F :

$$F = \frac{C_l}{\sqrt{C_d}} \quad (7.6)$$

can be obtained by a preliminary CFD optimization. Here C_l represents the lift coefficient and C_d represents the drag coefficient. In this example, the geometry of the optimal aerodynamic shape is derived from related results of Bilgen et al. [BSFF11] and assumed to be given here.

Then the optimization objective can be stated as minimization of the difference to the given optimal aerodynamic shape under full actuation and aerodynamic loading. A flight speed of 5m/s is assumed. Furthermore, a least squares approach is used to provide a measure for the difference of the actual shape from the optimal shape in a total of 20 discrete points in 5 cross sections of the wing structure. In the case of a higher flight speed, it is reasonable to define in the same manner a constraint condition to maintain the initial shape without actuation under aerodynamic loading. This ensures a reasonable design for both the actuated and the non-actuated airfoil structure.

The element thickness of the substrate is chosen as design variable. In order to provide insight in an optimal material thickness distribution in an early design phase, each finite element substrate thickness is taken as independent design variable which results in 9877 design variables. The thickness optimization is performed with a maximum design update of 0.1mm per optimization step. The conjugate gradient method is applied as optimization algorithm. The filter radius for gradient filtering is chosen to be 4.0cm. As initial choice, a constant substrate thickness of 0.2mm all around the airfoil is assumed. This initial choice is taken to investigate and benchmark the optimization technique without any preliminary engineering decisions like modified substrate thickness at the piezoelectric patches. A minimal thickness of 0.06mm is used as variable bound in the optimization problem. Furthermore, as the material and geometry parameters are chosen according to previous simulations and optimizations of a 2D setup [BSFF11], a comparison of these optimization results is possible.

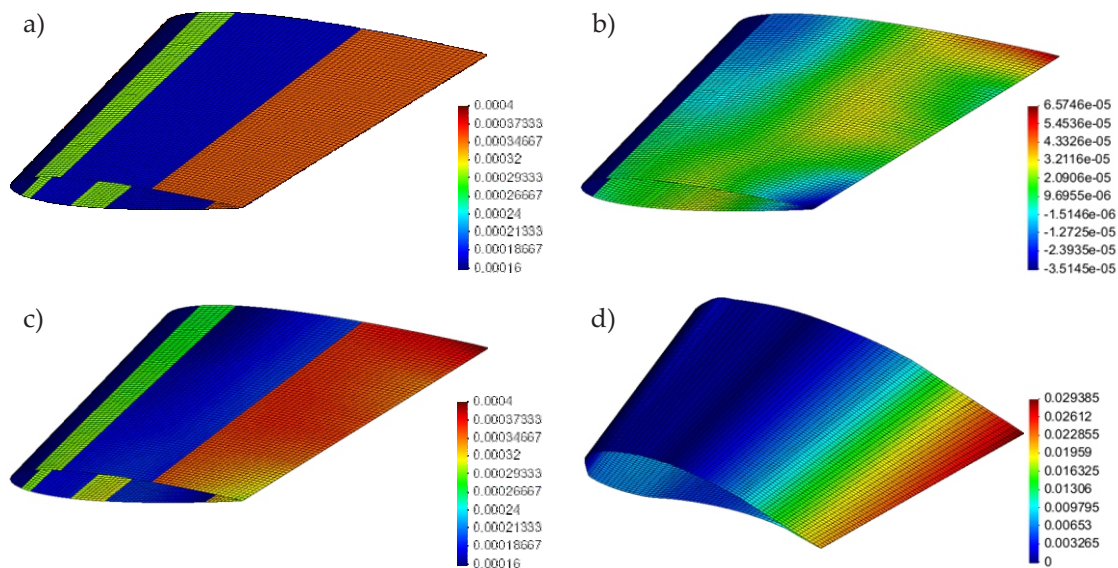


Figure 7.39: Evolution of thickness optimization: Initial geometry (a) with constant thickness and thickness distribution after 4, 7 and 10 optimization steps (figures b, c d).

Figure 7.39 shows the evolution of the thickness distribution during the optimization steps to reach the optimized design. Already after 7 optimization steps the leading edge area converges to the minimal thickness bound of 0.06mm. This coincides with the thin leading edge substrate thickness obtained with Genetic algorithms at the mentioned 2D model setup of Bilgen et al. in earlier work [BSFF11]. The leading edge area with small thickness turns into a compliant hinge to allow for the needed large actuation deformation. The substrate thickness at the areas of the upper piezoelectric patches decreases only slightly to values around 0.18mm during the optimization steps. The trailing edge area results in a thickness that increases from 0.25mm at the root to 0.35mm at the tip. In general, different thickness distributions in spanwise direction are obtained. This is due to the effect of changing pressure loads and piezoelectric actuation with changing cross sections of the tapered wing geometry. The increase in thickness at the tip is related to effects of the free edge: In order to guarantee the optimal shape at the very tip cross section, the optimizer produced a stiffer structure here.

Fig. 7.40 shows the evolution of the deformed shapes under actuation and aeroelastic loading during the thickness optimization. It can be seen that the chosen initial design with constant substrate thickness of 0.2mm would have led to a poor aerodynamic performance (Fig. 7.40 a). Furthermore, the initial design would have required to model contact conditions to prevent self-intrusion. However, the initial self-intrusion is not of importance, as the optimization leads steadily to the optimal aerodynamic shape (Fig. 7.40 d).

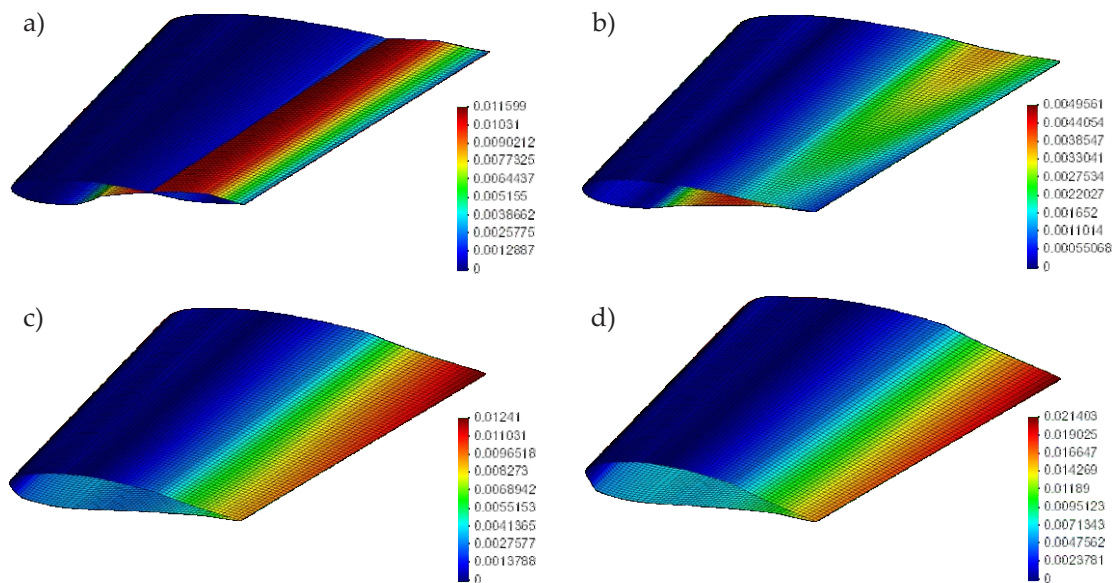


Figure 7.40: Evolution of deformed shape (actuated and aero-loaded) during thickness optimization: Initial (infeasible) deformation shape (a) and deformation shapes after 4, 7 and 10 optimization steps (figures b, c d).

The evolution of the objective value (least-square formulation of difference to optimal aerodynamic shape) during the optimization steps is presented in Figure 7.41. Only 10 optimization steps are needed in order to converge to an optimal substrate thickness distribution.

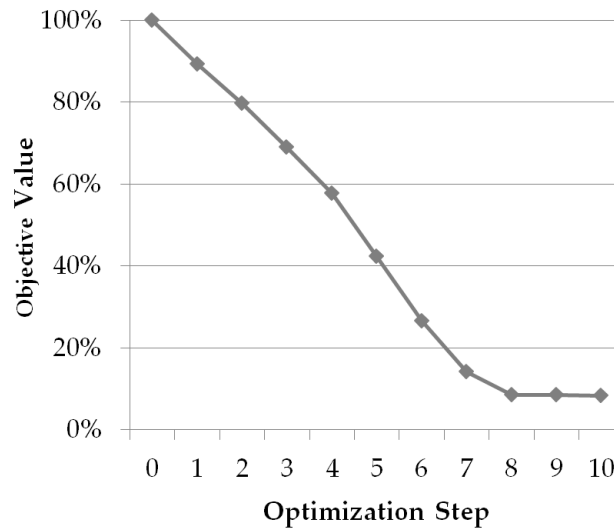


Figure 7.41: Behavior of the objective value (least-square formulation of difference to optimal aerodynamic shape under actuation) during the optimization steps.

Next, the model is prepared for a second optimization run that is meant to integrate further manufacturing aspects and fine-tune the result. The leading edge area is set to a thickness of 0.06mm and is taken out of the design space, as it had already reached the given variable bound. Furthermore, in accordance to Figure 7.33 a, areas of fixed substrate thickness are defined by evaluation of the results of the first optimization run (Figure 7.39 d). The substrate thicknesses are chosen to be 0.18mm at the strips below the patches (blue areas in Figure 7.42 a), 0.35mm at the trailing edge (brown areas) and 0.3mm at the areas between the piezoelectric patches and the leading edge (green areas). The increased thickness areas at the tip are not transferred to this new model, as they are local effects of the chosen objective that tries to exactly maintain a given optimal shape also at the tip edge. This decision is also supportable, as a new increase of thickness in this area is not prevented in the second optimization run.

The resulting model is subjected again to an element-wise optimization of the substrate thickness (Figure 7.42). The substrate areas under the piezoelectric patches converge to thicknesses of about 0.20mm which is considerably thinner than the other substrate areas except the leading edge. This aspect coincides with the results of earlier studies on a 2D model setup [BSFF11].

The trailing edge area results in a thickness that increases from 0.31mm at the tip to 0.42mm at the root. The trailing edge leads to thinner results compared to results at the 2D model where a trailing edge thickness of 0.53mm was obtained. One reason is

the stiffening effect of the slightly doubly curved structure, which can only be addressed in the 3D model. In general it can be identified that the optimization leads to smooth thickness distribution results that are easy to interpret.

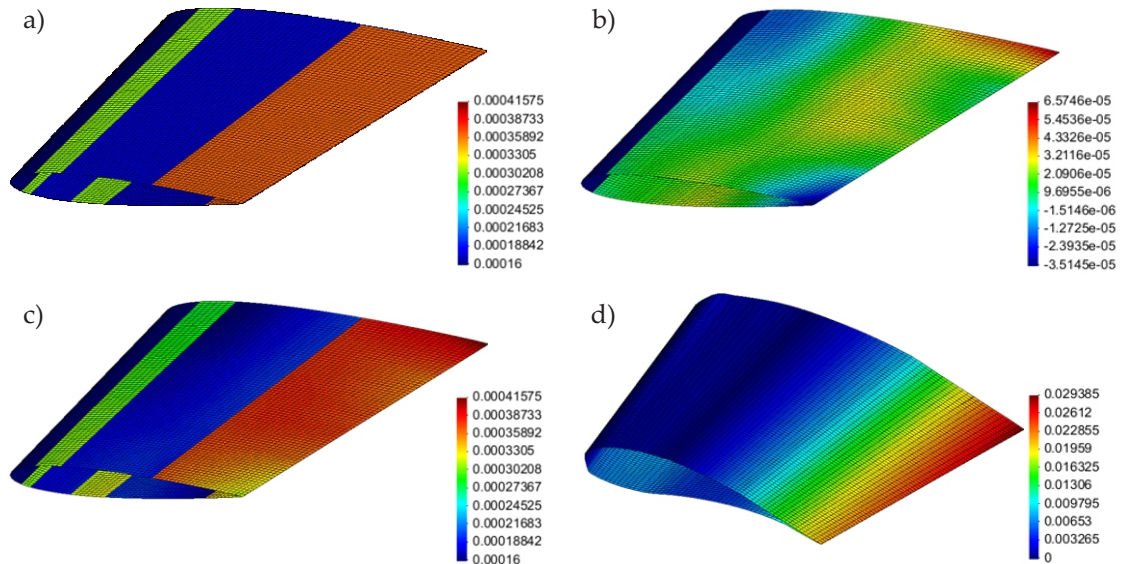


Figure 7.42: Second optimization run that starts from patches with constant thicknesses based on the results of the first optimization run: Initial thickness distribution (a), design update (b), final thickness distribution (c) and deformation under actuation and aerodynamic load (d).

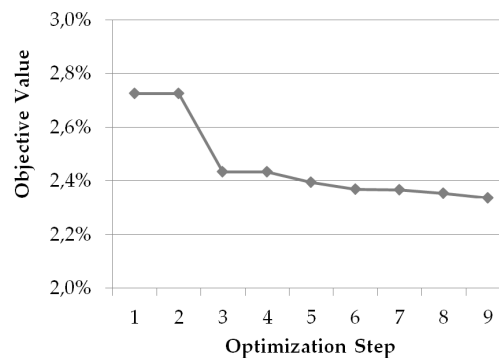


Figure 7.43: Evolution of the objective value (least-square formulation of difference to optimal aerodynamic shape under actuation) during second optimization run starting from areas with fixed substrate thickness.

Comparing Figure 7.41 and Figure 7.43, it can be observed that the predominant part of the improvement of the objective value is already done in the first optimization run, while the second optimization run creates a fine-tuned material distribution especially in spanwise direction with low improvement of the overall objective value. However, the effect of the second optimization run is especially visible at the maximum trailing edge deflection which increases from 2.14cm to 2.94cm (compare Figure 7.40 d and 7.42 d).

In total, both optimization runs lead finally to the given optimal aerodynamic shape under actuation and fluid load (Figure 7.42).

In order to further enhance the presented aeroelastic simulation, the extension of the fluid mesh domain beyond the wing tip is recommended. This leads to a 3D fluid model that directly covers the wing tip vortices and the related losses in lift (Figure 7.44). Then the corrections in section 7.6.1.2 according to the lifting-line theory would be dispensable. However, the general approach of the overall simulation and design process shown in this example would not be affected by this modification.

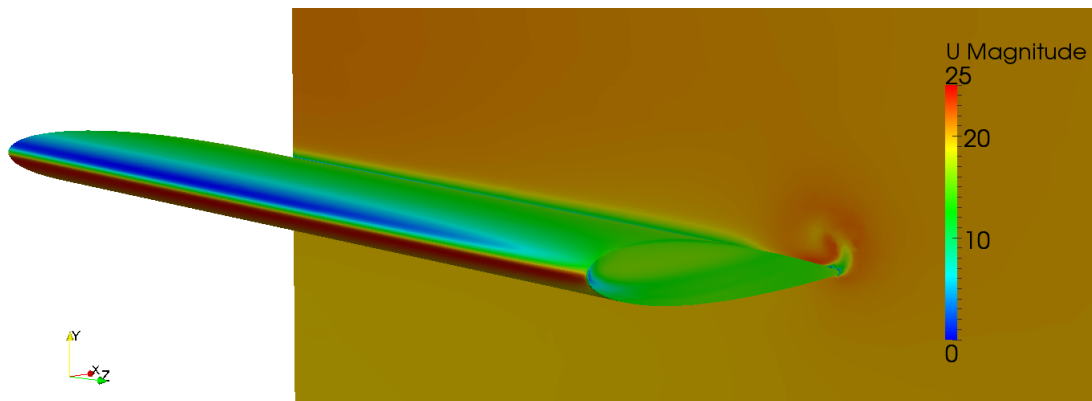


Figure 7.44: Velocity field of the wing: An extension of the fluid domain beyond the wing tip is needed to capture the wing tip vortex and the resulting reduction of pressure.

Chapter 8

Conclusions and Outlook

In this work, a finite element based computational framework and related algorithms for the virtual design and simulation of controlled smart piezoelectric and lightweight structures has been presented.

After an introduction to smart structures in general and in particular to piezoelectric materials, the basic terms and relations of the electromechanical continuum have been defined and deduced. An in-depth presentation of variational methods and related functionals has been presented in order to provide the basis for the derivation of a new piezoelectric finite element formulation. In this context, an extension of the modified Hu-Washizu functional has been presented, which enlarges the idea of an orthogonality condition between enhanced strains and independent stresses to the electromechanical problem. The electromechanical six-field Hu-Washizu functional can thus be reduced to a four-field formulation before the discretization takes place. The numerical cost for the discretization, calculation and static condensation of stresses and electric displacement field can be eliminated.

Furthermore, the different locking phenomena have been defined, interpreted and illustrated in a systematic analysis. The mechanical interpretation has been identified to be the most helpful interpretation method, as the related identification of parasitic strains and incompatible approximation spaces provides clear hints for the construction of enhanced element techniques. However, not only the well-known structural locking effects have been discussed, but also the closely related effects of incompatible approximation spaces of the electric field.

On this basis, a geometrically nonlinear piezoelectric composite shell element has been developed. Using the combination of ANS method, EAS method and EAE method, an efficient and robust concept for the avoidance of locking has been presented. The element formulation is based on nonlinear, three-dimensional continuum theory. Thus it is possible to use arbitrary complete three-dimensional constitutive laws without reduction or manipulation in nonlinear plate and shell analysis. A single-director formulation with Reissner-Mindlin kinematics has been adopted, which integrates deformations in thickness direction.

The efficiency and accuracy of the presented element has been demonstrated in several examples. It has been shown that the element fulfills the two essential aims of finite ele-

ment technology [Kos04]: the avoidance of locking effects and the avoidance of artificial instabilities (ZEMs). The element also passes the diverse electromechanical patch tests. Thus it fulfills the basic idea of a physically motivated patch test: A good element shall solve simple problems exactly, both as a single element and as part of an arbitrary patch of elements [Fel06].

Furthermore, it has been demonstrated that the multi-field elements based on the modified Hu-Washizu functional are rather sensitive to mesh distortions. The passing of the patch test is paid by higher mesh distortion sensitivity. This is in accordance to MacNeal's statement of the limits of finite element perfectibility [Mac92b]. The insensitivity for mesh distortions and the passing of the patch test can be identified as competing requirements. However, it has been shown in this work that the combination of ANS method and EAS method allows for an efficient formulation that both passes the patch test and eliminates the high mesh distortion sensitivity. The static condensation on the element level of the additional degrees of freedom of enhanced assumed strains and enhanced assumed electric field leads to an equation system that is not enlarged compared to the irreducible form.

Beyond that, the overall design process of smart structures including closed-loop control is focus of this work. In the context of control, special focus is put here on prestressed membrane structures and their special issues in the context of controller design. Furthermore, an introduction to the overall simulation and design process of actively controlled elastic structures has been given. Special focus has been put on the special characteristics of prestressed membrane structures in the context of control and controller design. Controller design is based on a state space model that is derived from the finite element model and that preserves the geometrically nonlinear equilibrium state and eventual prestress effects of the structure. Discrete time control with a linear-quadratic-Gaussian (LQG) regulator has been applied. The overall design loop has been completed and evaluated with the nonlinear simulation of the structure including control.

A short introduction to the developed object-oriented software framework *Carat++* has been given that has been the basis to realize the overall simulation and design goal. It turned out that the object-oriented programming paradigm indeed provided a reliable basis for the complex multi-field problems focused in this work.

All in all, this work has presented methods and algorithms for different scales and scopes of smart structures: A detailed discussion of piezoelectric finite element technology has been provided in order to integrate the idea of piezoelectric actuation and sensing in the simulation phase. However, also aspects of a holistic simulation and design loop of lightweight elastic structures including control has been presented. In this context, the overall virtual design process of an actively controlled smart tent structure has been presented, including the aspects of reasonable sensing, actuation and controller design. It has been shown that a smart tent can efficiently reduce vibrations caused by external loads via closed-loop control. In order to demonstrate the usage of piezoelectric actuation in a real structure, the static-aeroelastic simulation and design of a shape adaptive

solid-state piezo-actuated variable-camber morphing wing has been presented. This example also extended the shown design framework to aeroelastic coupling and FE-based structural optimization.

In general, the finite element-based structural optimization approach as shown in the morphing wing example opens the door for further interesting research in this field: Several more design variable types beyond the thickness can be investigated in the context of smart adaptive structures, like optimal fiber orientation in case of composite material, optimal applied voltage to different piezoelectric patches or optimal positioning of the patches. In general, all these design variables can be covered by the parameter free structural optimization approach. In this context, the presented piezoelectric element is one cornerstone to derive semi-analytic sensitivities for the structural responses under consideration. Altogether, a profound design space can be established that helps to approach the goal of a holistic virtual design process.

List of Figures

1.1	The <i>Stuttgart SmartShell</i> : actively controlled shell structure under snow load.	2
1.2	Applications of Piezoelectric materials for smart structures: (a) variable-camber morphing wing [BF12] and (b) active rotor blade with low profile piezoceramic actuators in the blade skin [MW05].	3
2.1	Reference and actual configuration of a differential body element.	19
2.2	Charged particle in an electrical field of two point charges.	25
2.3	Crystal structure of perovskite: Unit cell in cubic phase ($T > T_C$) and tetragonal phase ($T < T_C$).	33
2.4	Phases of barium titanate (see also e.g. at [KLBC93]).	34
2.5	Classification of dielectric materials.	34
2.6	Types of direct piezoelectric effects dependent from mechanical loading with respect to polarization direction.	35
2.7	Tonti diagram of the coupled electromechanical problem.	41
3.1	Convergence requirements for finite element shape functions.	62
3.2	Types of zero energy modes (ZEM).	63
3.3	Patch test meshes.	64
3.4	Overview of the patch test variants (gray: applied variants to test the presented element).	65
3.5	2-noded Timoshenko beam element with its degrees of freedom.	73
3.6	Kinematics of an infinitesimal part of a Timoshenko beam.	73
3.7	Timoshenko beam element: Parasitic shear strain in pure bending state.	74
3.8	Distinction of trapezoidal mesh distortion and trapezoidal locking	76
3.9	Trapezoidal bilinear element subjected to bending.	76
3.10	Curvature thickness locking: Parasitic normal strains.	77
3.11	Volumetric locking of the bilinear plate element.	80
3.12	Pure bending state of a piezoelectric material.	81

3.13	Shear loading on a piezoelectric beam.	81
3.14	ANS method: Illustration at the example of the MITC4 element.	84
3.15	ANS method: Modified shear strain interpolation of the MITC4 element.	85
3.16	EAS and EAE principle at the example of a bilinear 2D element.	89
4.1	Definition of shell geometry with bases of mid-surface and shell body.	91
4.2	Definition of shell deformation.	93
4.3	Piezoelectric Composite: Definition of layer interfaces and layer mid-surfaces.	100
4.4	Piezoelectric Composite: Transformation of layer thickness coordinates into laminate coordinate system (number of Gaussian points depicted with dots).	101
5.1	Block diagram of a closed-loop control system.	116
5.2	Tangential surface stress field of a membrane structure.	118
5.3	"Batwing" structure: application of form finding via the updated reference strategy (URS).	120
5.4	"Batwing" structure: Convergence of midpoint displacement over form finding steps.	121
5.5	Block diagram of closed-loop control with a LQG regulator.	130
7.1	Patch test model: Geometry information with position of interior nodes.	140
7.2	Displacement patchtest: Deformation contour plot (a) and electric potential difference contour plot (b) obtained by all tested elements.	141
7.3	Tension patchtest: Deformation contour plot obtained by all tested elements.	143
7.4	Electric field patchtest: Deformation contour plot (a) and electric potential difference contour plot (b) obtained by all tested elements.	144
7.5	Shear patch test model: Geometry information and mesh.	147
7.6	Shear patch test model with 48 elements: deformation and electric potential result using the element S-Q-EAS-E24 with ANS-, EAS- and EAE- improvement.	148
7.7	Bimorph model: Geometry and polarization of the two layers.	149
7.8	Bimorph.	150
7.9	Bimorph: Deflection behavior under applied electrical field.	151
7.10	Bimorph model with parameterized mesh distortion.	151
7.11	Tip displacement of bimorph dependent from mesh distortion.	152
7.12	Nonlinear bimorph example: geometry and polarization.	153

7.13 Nonlinear bimorph.	154
7.14 Scordelis-Lo roof: Self weight of 90.0 is subjected to the model. The ends are supported by rigid diaphragms.	155
7.15 Scordelis-Lo roof: Convergence of the absolute value of the vertical displacement at the mid-side of the free edge.	156
7.16 Scordelis-Lo roof: Resulting deformation v_2 of the element S-Q-EAS44404 at a mesh with 17 nodes along the side (deformation scaled by factor 10).	156
7.17 Pinched Cylinder, model and problem setup: Equal and opposite single forces are subjected to the model at its midspan. The ends are supported by rigid diaphragms.	157
7.18 Pinched cylinder: Convergence of the radial displacement at the point load position.	158
7.19 Pinched cylinder: Resulting deformation using the element S-Q-EAS44404 (deformation scaled by factor $2 \cdot 10^6$).	158
7.20 Smart 4-point tent: form finding steps and final geometry.	159
7.21 Smart 4-point tent: convergence of midpoint over form finding steps.	160
7.22 Smart 4-point tent: cutting pattern process.	160
7.23 Smart 4-point tent: deformations at characteristic time steps of a nonlinear transient analysis of the passive structure under pressure load in 5th eigenfrequency (deformation scaled by factor 5).	161
7.24 Smart 4-point tent: lowest six eigenmodes (scaled deformation and highlighted via contour plot).	162
7.25 Smart 4-point tent: Transient analysis results of the tent midpoint in the case of (a) the full-order nonlinear, (b) the full-order linear, (c) the reduced FE model of the passive structure.	163
7.26 Smart 4-point tent: positioning of displacement sensors and force actuators.	164
7.27 Smart 4-point tent: block diagram for closed-loop control with a LQG regulator.	165
7.28 Smart 4-point tent: sensor values for uncontrolled (thin line) and controlled (bold-printed line) system simulation in Matlab.	166
7.29 Smart 4-point tent: Displacement of the membrane midpoint at a geometrically nonlinear transient analysis including control (control starts at time step 200).	167
7.30 Smart 4-point tent: Deformation plot for time steps with maximum amplitude for the uncontrolled case (a) and the controlled case (b).	168
7.31 Smart 4-point tent: Overview of the overall design process.	169

7.32	Variable-camber tapered wing [BF12]: Installation in the wind tunnel (a) and deformation response for selected choices of piezoelectric excitation (b).	170
7.33	Structural airfoil model: Variable thicknesses to allow for optimum thickness ratio (a) and 3D realization of the 2D design (b).	171
7.34	Structural airfoil model: 5 active sections at top surface (a) and 10 active sections at bottom surface (b).	171
7.35	3D CFD simulation: Parameterization for automated meshing (a) and computational fluid domain (b).	172
7.36	3D C-grid mesh for CFD simulation with OpenFOAM (a) and fluid mesh near the leading edge (b).	173
7.37	Evaluation of lift coefficient: CFD simulation with OpenFOAM at $Re=285000$ compared with thin airfoil theory and experimental data	174
7.38	Evaluation of drag coefficient: CFD simulation with OpenFOAM at $Re=285000$ compared with thin airfoil theory and experimental data.	174
7.39	Evolution of thickness optimization: Initial geometry (a) with constant thickness and thickness distribution after 4, 7 and 10 optimization steps (figures b, c d).	176
7.40	Evolution of deformed shape (actuated and aero-loaded) during thickness optimization: Initial (infeasible) deformation shape (a) and deformation shapes after 4, 7 and 10 optimization steps (figures b, c d).	177
7.41	Behavior of the objective value (least-square formulation of difference to optimal aerodynamic shape under actuation) during the optimization steps.	178
7.42	Second optimization run that starts from patches with constant thicknesses based on the results of the first optimization run: Initial thickness distribution (a), design update (b), final thickness distribution (c) and deformation under actuation and aerodynamic load (d).	179
7.43	Evolution of the objective value (least-square formulation of difference to optimal aerodynamic shape under actuation) during second optimization run starting from areas with fixed substrate thickness.	179
7.44	Velocity field of the wing: An extension of the fluid domain beyond the wing tip is needed to capture the wing tip vortex and the resulting reduction of pressure.	180
A.1	Lagrange elements: Node numbering and element coordinate positioning.	191

List of Tables

2.1	Relation between piezoelectric tensor entries and common naming in literature with Voigt notation.	40
2.2	Strong form of the coupled electromechanical problem.	40
2.3	Variational principles and their strongly and weakly formulated contributions.	56
3.1	Ratio of node number to element number [Kos04].	68
3.2	Overview: Mechanical locking phenomena and related critical parameters.	70
3.3	Deformation and stress state in case of pure bending.	71
3.4	Overview of the 8 deformation modes of the linear 2D quadrilateral element.	72
3.5	Linear 2D quadrilateral element: compatible deformation modes and EAS modes.	87
7.1	Material parameters for the patch tests. Not listed parameters are zero.	141
7.2	Tension patch test: Comparison of analytical and numerical results.	143
7.3	Electric field patch test: Comparison of analytical and numerical results.	144
7.4	Bending patch test: Comparison of analytical and numerical results.	145
7.5	Material parameters for the shear patch test. Not listed parameters are zero.	147
7.6	Linear shear patch test: Comparison of analytical and numerical results.	147
7.7	Material parameters of the bimorph. Not listed parameters are zero.	149
7.8	Smart 4-point tent: Material parameters.	161
B.1	Nomenclature of used variables.	197

Appendix A

Finite Element Shape Functions

The triangular and quadrilateral finite elements of this work belong to the class of Lagrange elements. The chosen definition of shape functions shall be presented in the sequel. The node numbering and the positioning of the element coordinate system is depicted in Figure A.1.

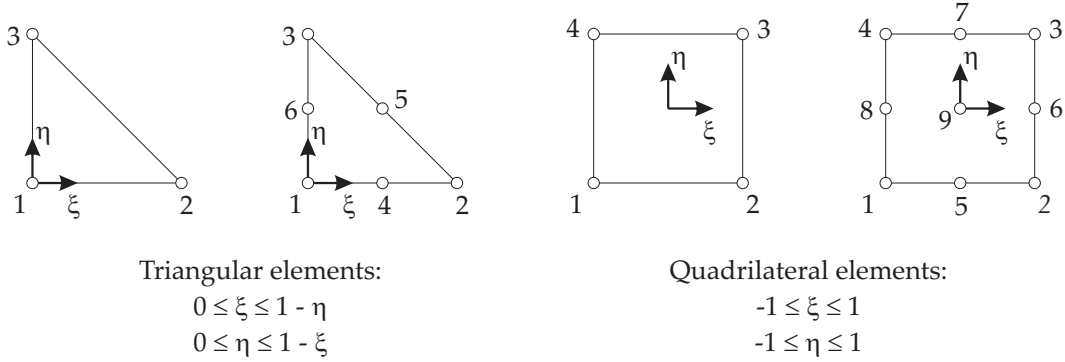


Figure A.1: Lagrange elements: Node numbering and element coordinate positioning.

A.1 Triangular Elements

3-Noded Triangular Element

$$N_1 = 1 - \xi - \eta, \quad N_2 = \xi, \quad N_3 = \eta \quad (\text{A.1})$$

6-Noded Triangular Element

$$N_1 = (1 - 2\xi - 2\eta)(1 - \xi - \eta), \quad N_2 = 2\xi^2 - \xi \quad (\text{A.2})$$

$$N_3 = 2\eta^2 - \eta, \quad N_4 = 4(\xi - \xi^2 - \xi\eta) \quad (\text{A.3})$$

$$N_5 = 4\xi\eta, \quad N_6 = 4(\eta - \eta^2 - \xi\eta) \quad (\text{A.4})$$

A.2 Quadrilateral Elements

4-Noded Quadrilateral Element

$$N_1 = \frac{1}{4} (1 - \xi) (1 - \eta), \quad N_2 = \frac{1}{4} (1 + \xi) (1 - \eta) \quad (\text{A.5})$$

$$N_3 = \frac{1}{4} (1 + \xi) (1 + \eta), \quad N_4 = \frac{1}{4} (1 - \xi) (1 + \eta) \quad (\text{A.6})$$

9-Noded Quadrilateral Element

$$N_1 = \frac{1}{4} \xi \eta (1 - \xi) (1 - \eta), \quad N_2 = -\frac{1}{4} \xi \eta (1 + \xi) (1 - \eta) \quad (\text{A.7})$$

$$N_3 = \frac{1}{4} \xi \eta (1 + \xi) (1 + \eta), \quad N_4 = -\frac{1}{4} \xi \eta (1 - \xi) (1 + \eta) \quad (\text{A.8})$$

$$N_5 = -\frac{1}{2} \eta (1 - \xi^2) (1 - \eta), \quad N_6 = \frac{1}{2} \xi (1 + \xi) (1 - \eta^2) \quad (\text{A.9})$$

$$N_7 = \frac{1}{2} \eta (1 - \xi^2) (1 + \eta), \quad N_8 = -\frac{1}{2} \xi (1 - \xi) (1 - \eta^2) \quad (\text{A.10})$$

$$N_9 = (1 - \xi^2) (1 - \eta^2) \quad (\text{A.11})$$

Appendix B

Nomenclature

As different fields of research, such as shell element technology, piezoelectric materials, as well as control theory a brought together in this work, care has to be taken about a clear and concise nomenclature.

As far as possible, standard notations and definitions of the respective fields have been reused. Differing identifiers have only been used to avoid duplicated meanings. A list of the most important variables used throughout this work is given in table B.1.

Small Latin letters

\mathbf{b}	Body forces in actual configuration (units of an acceleration).
\mathbf{b}_0	Body forces in reference configuration (units of an acceleration).
$\bar{\mathbf{d}}^i$	Generalized vector of degrees of freedom of node i .
$\bar{\mathbf{d}}$	Generalized vector of degrees of freedom of the element.
\vec{d}_0^i	Electric displacement resultant (constant part in θ^3).
\vec{d}_1^i	Electric displacement resultant (linear part in θ^3).
\vec{e}	Electric field in actual configuration.
$\vec{\mathbf{f}}^{el}$	Electromagnetically induced volume forces.
\mathbf{g}	Metric tensor in actual configuration.
$\mathbf{g}_3 = \mathbf{a}_3$	Director.
h	Shell thickness.
h_L	Composite layer thickness.
\mathbf{j}_0^{el}	Electric current density.
m	Body mass.
$\vec{\mathbf{m}}^{el}$	Electrically induced moment per unit volume.
$m^{\alpha\beta}$	Bending moments (static variables).
\mathbf{n}	Unit surface normal in actual configuration.
$n^{\alpha\beta}$	Membrane forces (static variables).
$n^{\alpha 3}$	Shear forces (static variables).
\mathbf{q}	External surface load.
\hat{q}_0	Prescribed electric surface charge (reference configuration).
\mathbf{r}	Position vector (actual geometry).
\mathbf{t}	Cauchy stress vector.

$\hat{\mathbf{t}}$	Vector of prescribed stresses in actual configuration.
$\hat{\mathbf{t}}_0$	Vector of prescribed stresses in reference configuration.
\mathbf{u}	Deformation field vector.
$\mathbf{u}_c(t)$	control input.
$\hat{\mathbf{u}}$	Vector of prescribed displacements (Dirichlet boundary condition).
\mathbf{v}	Displacement components of the nodal degrees of freedom.
\mathbf{w}	Director deformation components of the nodal degrees of freedom.
\mathbf{x}	Position vector of an material point in actual configuration.
\mathbf{x}_c	State vector.
$\tilde{\mathbf{x}}_c$	State variable estimation.
\mathbf{y}	Controlled variable, sensor values.
\mathbf{z}	Modal coordinates.

Large Latin letters

A	Metric tensor of shell midsurface (reference configuration).
\mathbf{A}_c	(state space matrix).
A_i, A^i	Co- and contravariant base vectors of shell midsurface (defined in reference configuration).
$A_3 = G_3$	Director (reference configuration).
A	2-dimensional domain.
A^e	Area of a finite shell element.
dA	Differential area element.
\mathbf{B}_u	Matrix that links the degrees of freedom of the the actuator signal to the time dependent function(s) of the control input.
\mathbf{B}	B-operator.
$\vec{\mathbf{B}}$	Magnetic flux density.
\mathbf{B}_c	(state space matrix).
$\mathbf{B}_{\alpha\beta}$	Curvature tensor.
\mathbf{C}	Material tensor.
\mathbf{C}_c	(state space matrix).
\mathbf{C}_d	Rayleigh damping matrix.
\mathbf{D}	Material tensor, integrated over thickness (shell theory).
$\vec{\mathbf{D}}$	Electric displacement field.
$\bar{\mathbf{D}}$	Generalized strain matrix (EAS and EAE).
\mathbf{D}_c	(state space matrix).
E	Young's Modulus.
\mathbf{E}	Green-Lagrangian strain tensor.
\mathbf{E}_c	(state space matrix).
\mathbf{E}^u	Displacement-dependent Green-Lagrangian strain tensor (compatible strains part in the modified Hu-Washizu functional).
$\tilde{\mathbf{E}}$	Enhanced assumed strain tensor acc. to modified Hu-Washizu functional.
$\tilde{\vec{\mathbf{E}}}$	Enhanced assumed electric field acc. to modified Hu-Washizu functional.

\vec{E}	Electric field tensor.
\vec{E}^φ	Electric potential-dependent electric field tensor (compatible electric field in the modified Hu-Washizu functional).
E_f	Matrix that links the degrees of freedom of the the external load to the time dependent function(s) of the external load.
\bar{E}	Generalized vector of strains E and electrical field \vec{E} .
F	Deformation gradient.
F_c	(state space matrix).
\vec{F}_c	Coulomb force.
G	Shear modulus.
G	Metric tensor in reference configuration.
G_c	Discrete-time system matrix (state space model).
H	Electric enthalpy density.
H_c	Discrete-time input matrix (state space model).
\vec{H}	Magnetic field.
I	Unity tensor.
I	Electric current.
J	Jacobian determinant.
J_c	Performance index for controller design.
K	Stiffness matrix.
K_c	State feedback gain matrix.
L	Angular Momentum.
\bar{L}	Generalized coupling matrix (EAS and EAE method).
M	Mass matrix.
\tilde{M}	Matrix of enhanced assumed strain modes.
\tilde{M}	Matrix of enhanced assumed electric field strength modes.
\bar{M}	Generalized Matrix of enhanced strains and enhanced electrical field strength terms.
N	Unit surface normal in reference configuration.
P	Material point.
P	Piola-Kirchhoff stress tensor of first type.
\bar{P}	Generalized load vector.
\vec{P}	Polarization density.
Q_c	Weighting matrix of performance index.
R_c	Weighting matrix of performance index.
R	Position vector (reference geometry).
\bar{R}	Inner mechanical forces.
\bar{R}	Inner electrical forces.
S	2nd Piola-Kirchhoff stress tensor.
\bar{S}	Generalized vector of resulting static variables.
U	Voltage.
dV	Differential volume element.

W_V^{ext}	Potential of volume loads.
W_A^{ext}	Potential of surface loads.
W^{mech}	Strain energy density in the volume V .
W_H	Electric enthalpy density.
\mathbf{X}	Position vector of an material point in reference configuration.
\mathbf{Z}	Shell shifter tensor.

Small Greek letters

α	Vector of EAS degrees of freedom.
$\bar{\alpha}$	Vector of EAE degrees of freedom.
α_{ij}	Components of Green-Lagrange tensor that are constant in θ^3 .
$\bar{\alpha}_i$	Components of electric field that are constant in θ^3 .
β_{ij}	Components of Green-Lagrange tensor that are linear in θ^3 .
$\bar{\beta}_i$	Components of electric field that are linear in θ^3 .
γ_{ij}	Components of Green-Lagrange tensor that are quadratic in θ^3 .
δ_{ij}	Kronecker symbol.
ϵ_0	Vacuum permittivity.
ϵ_r^{ij}	Relative permittivity tensor.
ϵ^{ij}	Permittivity tensor.
ϵ_c	Discrete-time external load matrix (state space model).
ϵ^{ijk}	Piezoelectric coupling tensor.
λ, μ	Lamé constants.
$\lambda_1, \lambda_2, \mu_1, \mu_2$	Lagrange parameters.
λ_{crit}	Critical parameter.
$\bar{\mu}$	Determinant of shell shifter.
μ_k	Controllability index of mode k .
$\mu(\mathbf{X}_p)$	Overall controllability index of position \mathbf{X}_p .
ν	Poisson ratio.
ν_k	Observability index of mode k .
$\nu(\mathbf{X}_p)$	Overall observability index of position \mathbf{X}_p .
φ	Field of electric potential.
$\Delta\varphi$	Electric potential difference in element thickness direction.
$\hat{\varphi}$	Prescribed field of electric potential.
ρ	Density (actual configuration).
ρ_0	Density (reference configuration).
ρ_0^{el}	Electric charge density.
σ	Cauchy stress tensor.
θ	Coordinate (in co- or contravariant coordinate system).

Large Greek letters

Γ	Domain boundary.
$\Gamma_{\mathbf{s}}$	part of Γ that is subjected to prescribed stresses (loads).
$\Gamma_{\mathbf{u}}$	part of Γ that is subjected to prescribed displacements.

$\Gamma_{\bar{D}}$	part of Γ that is subjected to prescribed electric displacements.
Γ_{φ}	part of Γ that is subjected to prescribed electric potential.
Δ	Structural modal damping matrix.
Λ	Spectral matrix.
Ψ	Electric flux.
Ψ	Modal matrix for model order reduction.
Π^{int}	potential energy.
Ω	Three-dimensional body, domain.

Table B.1: Nomenclature of used variables.

Bibliography

- [AA97] P. AZARIADIS and N. ASPRAGATHOS: *Design of Plane Developments of Doubly Curved Surfaces*. *Computer-Aided Design*, 29:675–685, 1997.
- [Acm11] *Market Report: World Piezoelectric Device Market*. Acmite Market Intelligence, 2011.
- [AF96] D. ARNOLD and R.S. FALK: *Asymptotic Analysis of the Boundary Layer for the Reissner-Mindlin Plate Model*. *SIAM (Society for Industrial and Applied Mathematics) Journal of Mathematical Analysis*, 27:486–514, 1996.
- [AFT99] G. C. ARCHER, G. FENVES and C. THEWALT: *A new object-oriented finite element analysis program architecture*. *Computers & Structures*, 70(1):63–75, 1999.
- [AH70] A. ALLIK and T.J.R. HUGHES: *Finite Element Method for Piezoelectric Vibration*. *International Journal for Numerical Methods in Engineering*, 2:151–157, 1970.
- [AIZ68] S. AHMAD, B.M. IRONS and O.C. ZIENKIEWICZ: *Curved Thick Shell and Membrane Elements with Particular Reference to Axi-Symmetric Problems*. In L. BERKE ET. AL. (editor): *Proc. of the 2nd Conf. on Matrix Methods in Struct. Mech.*, 1968.
- [AR93] U. ANDELFINGER and E. RAMM: *EAS-Elements for Two-Dimensional, Three-Dimensional, Plate and Shell Structures and their Equivalence to HR-Elements*. *International Journal for Numerical Methods in Engineering*, pages 1311–1337, 1993.
- [Arc96] G.C. ARCHER: *Object-Oriented Finite Element Analysis*. PhD thesis, University of California at Berkeley, 1996.
- [Arg65] J.H. ARGYRIS: *Continua and Discontinua*. *Proceedings, Conference on Matrix Methods in Structural Mechanics*, Air Force Institute of Technology, Wright-Patterson, Ohio, USA, pages 111–189, 1965.
- [ARN⁺94] F. AUSTIN, M.J. ROSSI, W. VAN NOSTRAND, G. KNOWLES and A. JAMESON: *Static Shape Control for Adaptive Wings*. *AIAA journal*, 32(9)(9):1895–1901, 1994.

- [AS01] A.C. ANTOULAS and D.C. SORENSEN: *Approximation of Large-Scale Dynamical Systems: An Overview*. Int. J. Appl. Math. Comput. Sci., 11(5):1093–1121, 2001.
- [AY95] H. ADELI and G. YU: *An Integrated Computing Environment for Solution of Complex Engineering Problems Using the Object-Oriented Programming Paradigm and a Blackboard Architecture*. Computers & Structures, 54(2):255–265, 1995.
- [BA72] I. BABUSKA and A.K. AZIS: *Survey Lectures on the Mathematical Foundations of the Finite Element Method*. In *The Mathematical Foundation of the Finite Element Method with Applications to Partial Differential Equations*. Academic Press, 1972.
- [Bal10] H. BALKE: *Einführung in die Technische Mechanik: Festigkeitslehre*. Springer, 2010.
- [Bat02] K.-J. BATHE: *Finite-Element-Methoden*. Springer, Berlin, 2002.
- [BBA⁺11] S. BARBARINO, O. BILGEN, R. M. AJAJ, M. I. FRISWELL and D. J. INMAN: *A Review of Morphing Aircraft*. Journal of Intelligent Material Systems and Structures, 22(9):823 – 877, 2011.
- [BD85] K.-J. BATHE and E.N. DVORKIN: *A Four-Node Plate Bending Element Based on Mindlin/Reissner Theory and a Mixed Interpolation*. International Journal for Numerical Methods in Engineering, 21:367–383, 1985.
- [BD97] S. BRANDT and H.D. DAHMEN: *Elektrodynamik*. Springer Berlin Heidelberg New York, 1997.
- [Ben06] P. BENNER: *Numerical Linear Algebra for Model Reduction in Control and Simulation*. GAMM-Mitt., 29(2):275–296, 2006.
- [Ben07] A. BENJEDDOU: *Shear-Mode Piezoceramic Advanced Materials and Structures: A State of the Art*. Mechanics of Advanced Materials and Structures, 14(4):347–275, 2007.
- [BF91] F. BREZZI and M. FORTIN: *Mixed and Hybrid Finite Element Methods*. Springer New York Berlin Heidelberg, 1991.
- [BF12] O. BILGEN and M.I. FRISWELL: *Piezoceramic Composite Actuators for a Solid-State Variable-Camber Wing*. In *ICAST2012: 23rd International Conference on Adaptive Structures and Technologies*. October 11-13, 2012. Nanjing, China, 2012.
- [BF13] K.-U. BLETZINGER and M. FISCHER: *Entwicklung hocheffizienter frei geformter Bauteile mit Hilfe numerischer Optimierung*. In *Meform 2013: Simulation of Forming Processes*, March 22 - 22, 2013, Altenberg, 2013.

- [BFD08] K.-U. BLETZINGER, M. FIRL and F. DAOUD: *Approximation of Derivatives in Semi-Analytical Structural Optimization*. Computers and Structures, 86(13-14):1404–1416, 2008.
- [BFF10] K.-U. BLETZINGER, M. FIRL and M. FISCHER: *Parameter Free Shape Design of Thin Shells: Efficient and Effective Parallel Solution Techniques for Very Large Design Problems*. In *2nd International Conference on Engineering Optimization*, Lisbon, Portugal, September 6 - 9 2010.
- [BFF11] K.-U. BLETZINGER, M. FIRL and M. FISCHER: *Simulationenmethoden für Optimierung und Kontrolle formadaptiver, leichter Flächentragwerke*. In *Baustatik-Baupraxis 2011*, Innsbruck, Austria, 2011.
- [BFF13] K.-U. BLETZINGER, M. FISCHER and M. FIRL: *Numerische Strukturoptimierung für die Entwicklung hocheffizienter frei geformter Bauteile*. In *Neuere Entwicklungen in der Massivumformung 2013*, Stuttgart, 04.- 05. Juni 2013, 2013.
- [BFLW09] K.-U. BLETZINGER, M. FIRL, J. LINHARD and R. WÜCHNER: *Optimal Shapes of Mechanically Motivated Structures*. Computer Methods in Applied Mechanics and Engineering, 199(5):324–333, 2009.
- [BGKS00] H. BERGER, U. GABBERT, H. KOPPE and F. SEEGER: *Finite Element Analysis and Design of Piezoelectric Controlled Smart Structures*. Journal of Theoretical and Applied Mechanics, 38(3):475–498, 2000.
- [BGS96] P. BETSCH, F. GRUTTMANN and E. STEIN: *A 4-Node Finite Shell Element for the Implementation of General Hyperelastic 3D-Elasticity at Finite Strains*. Computer Methods in Applied Mechanics and Engineering, 130:57–79, 1996.
- [BH76] P.G. BERGAN and L. HANSSEN: *A New Approach for Deriving "Good" Finite Elements*. In J. R. WHITEMAN (editor): *MAFELAP II Conference, Brunel University, 1975*, The Mathematics of Finite Elements and Applications, Volume II, pages 483–497. Academic Press, London, 1976.
- [BH03] M. BERNADOU and C. HAENEL: *Modelization and Numerical Approximation of Piezoelectric Thin Shells, Part 2: Approximation by Finite Element Methods and Numerical Experiments*. Computer Methods in Applied Mechanics and Engineering, 192:4045–4073, 2003.
- [BHK] W. BANGERTH, R. HARTMANN and G. KANSCHAT: *deal.II Differential Equations Analysis Library, Technical Reference*. <http://www.dealii.org>.
- [Bis99] M. BISCHOFF: *Theorie und Numerik einer dreidimensionalen Schalenformulierung*. PhD thesis, Institut für Baustatik, Universität Stuttgart, 1999.
- [Bis05] M. BISCHOFF: *Advanced Finite Element Methods (Vorlesungsskriptum)*. Lehrstuhl für Statik, Prof. Dr.-Ing. K.-U. Bletzinger, Technische Universität München, 2005.

- [BK08] D. BRAESS and M. KALTENBACHER: *Efficient 3D-finite Element Formulation for Thin Mechanical and Piezoelectric Structures*. International Journal for Numerical Methods in Engineering, 73:147–161, 2008.
- [BLF13] O. BILGEN, D. LANDMAN and M. I. FRISWELL: *Low Reynolds Number Behavior of a Solid-State Piezocomposite Variable-Camber Wing*. In *20th AIAA/ASME/AHS Adaptive Structures Conference*, Boston, MA, 2013.
- [BLM00] TED BELYTSCHKO, WING KAM LIU and BRIAN MORAN: *Nonlinear Finite Elements for Continua and Structures*. John Wiley & Sons, 2000.
- [BN01] V. BALAMURUGAN and S. NARAYANAN: *Shell Finite Element for Smart Piezoelectric Composite Plate-Shell Structures and its Application to the Study of Active Vibration Control*. Finite Elements in Analysis and Design, 37(9):713–738, 2001.
- [BR89] J. W. BAUGH and D. R. REHAK: *Computational Abstractions For Finite Element Programming*. Technical Report R-89-182. Technical Report, Department Of Civil Engineering, Carnegie Institute Of Technology, 1989.
- [BR92a] J. W. BAUGH and D. R. REHAK: *Data Abstraction in Engineering Software Development*. Journal of Computing in Civil Engineering, 6(3):282–301, July 1992.
- [BR92b] N. BÜCHTER and E. RAMM: *3d-Extension of Nonlinear Shell Equations Based on the Enhanced Assumed Strain Concept*. Elsevier, 1992.
- [BR92c] N. BÜCHTER and E. RAMM: *Shell Theory versus Degeneration - a Comparison in Large Rotation Finite Element Analysis*. International Journal for Numerical Methods in Engineering, 37:55–62, 1992.
- [BR99] K.-U. BLETZINGER and E. RAMM: *A General Finite Element Approach to the Form Finding of Tensile Structures by the Updated Reference Strategy*. Int. J. Space Struct., 14:131–146, 1999.
- [Bra95] M. BRAUN: *Nichtlineare Analysen von geschichteten, elastischen Flächentragwerken*. PhD thesis, Institut für Baustatik, Universität Stuttgart, 1995.
- [Bra97] D. BRAESS: *Finite Elemente*. Springer, 1997.
- [BRB99] M. BISCHOFF, E. RAMM and D. BRAESS: *A Class of Equivalent Enhanced Assumed Strain and Hybrid Stress Finite Elements*. Computational Mechanics, 22:443–449, 1999.
- [Bre74] F. BREZZI: *On the Existence, Uniqueness and Approximation of Saddle Point Problems Arising from Lagrangian Multipliers*. RAIRO Analysis Numérique, 8:129–151, 1974.

- [BRR94] N. BÜCHTER, E. RAMM and D. ROEHL: *Three-Dimensional Extension of Non-linear Shell Formulation Based on the Enhanced Assumed Strain Concept*. International Journal for Numerical Methods in Engineering, 37:2551–2568, 1994.
- [BS92] I. BABUSKA and M. SURI: *On Locking and Robustness in the Finite Element Method*. SIAM J. Numer. Anal., 29:1261–1293, 1992.
- [BSFF11] O. BILGEN, E.I. SAAVEDRA-FLORES and M.I. FRISWELL: *Optimization of Surface-Actuated Piezocomposite Variable-Camber Morphing Wings*. In *Proceedings of the ASME 2011 Conference in Smart Material, Adaptive Structures and Intelligent Systems SMASIS2011, Sept. 18-21, 2011, Phoenix, Arizona, USA, 2011*.
- [BSL⁺85] T. BELYTSCHKO, H. SOLARSKI, W. K. LIU, N. CARPENTER and J. ONG: *Stress Projections for Membrane and Shear Locking in Shell Finite Elements*. Computer Methods in Applied Mechanics and Engineering, pages 221–258, 1985.
- [BSW96] H.T. BANKS, R.C. SMITH and Y. WANG: *Smart Material Structures, Modeling, Estimation and Control*. Wiley, 1996.
- [Büc92] N. BÜCHTER: *Zusammenführung von Degenerationskonzept und Schalentheorie bei endlichen Rotationen*. Technical Report Report Nr. 14, Institut für Baustatik, Universität Stuttgart, 1992.
- [BWBR04] M. BISCHOFF, W.A. WALL, K.-U. BLETZINGER and E. RAMM: *Encyclopedia of Computational Mechanics*, chapter Models and finite elements for thin-walled structures. Wiley, 2004.
- [Cad64] W.G. CADY: *Piezoelectricity*. Dover, New York, 1964.
- [CC65] E. COSSERAT and F. COSSERAT: *Theorie Des Corps Deformables*. Herman et fils, Paris, 1965.
- [CL95] M. CLINE and G. LOMOW: *C++ FAQs*. Addison-Wesley, New York, 1995.
- [CLM96] P. G. CIARLET, V. LODS and B. MIARA: *Asymptotic Analysis of Linearly Elastic Shells. II. Justification of Flexural Shell Equations*. Archive for rational mechanics and analysis, 136(2):163–190, 1996.
- [Cri81] M.A. CRISFIELD: *A Fast Incremental/Iterative Solution Procedure that Handles SnapThrough*. Computers & Structures, 13:55–62, 1981.
- [Cro86] J. M. CROWLEY: *Fundamentals of Applied Electromechanics*. Wiley & Sons, 1986.
- [CSG98] R.L. CLARK, W.R. SAUNDERS and G.P. GIBBS: *Adaptive Structures. Dynamics and Control*. John Wiley & Sons Inc., New York, 1998.

- [CSW90] W. F. CHEN, E. D. SOTELINO and D. W. WHITE: *High Performance Computing In Civil Engineering Applications*. Ind. School Of Engineering, Purdue University, West Lafayette, 1990.
- [CTS99] C.-Y.-K. CHEE, L. TONG and G.-P. STEVEN: *A Mixed Model for Composite Beams with Piezoelectric Actuators and Sensors*. *Smart Materials and Structures*, 8, 1999.
- [CYL01] S.-H. CHEN, G.F. YAO and H.D. LIAN: *A New Piezoelectric Shell Element and its Application in Static Shape Control*. *Structural Engineering and Mechanics*, 12(5):491–506, 2001.
- [Dad07] POOYAN DADVAND: *A framework for developing finite element codes for multi-disciplinary applications*. PhD thesis, Universitat Politècnica de Catalunya, 2007.
- [DPZ93] YVES DUBOIS-PELERIN and THOMAS ZIMMERMANN: *Object-oriented finite element programming: III. An efficient implementation in C++*. *Computer Methods in Applied Mechanics and Engineering*, 108(1-2):165–183, 1993.
- [DPZB92] YVES DUBOIS-PÈLERIN, THOMAS ZIMMERMANN and PATRICIA BOMME: *Object-oriented finite element programming: II. A prototype program in smalltalk*. *Computer Methods in Applied Mechanics and Engineering*, 98(3):361–397, August 1992.
- [dV65] B. FRAEIJIS DE VEUBEKE: *Displacement and Equilibrium Models in the Finite Element Method*. *Stress Analysis*, 9:145–197, 1965.
- [DWT69] W. P. DOHERTY, E. L. WILSON and R. L. TAYLOR: *Stress Analysis of Axisymmetric Solids Using Higher Order Quadrilateral Finite Elements*. In *Struct. Eng. Lab. Report SESM*, March 1969.
- [EI11] A. ERTURK and D.J. INMAN: *Piezoelectric Energy Harvesting*. Wiley, 2011.
- [Eri62] A.C. ERINGEN: *Nonlinear Theory of Continuous Media*. McGraw-Hill, 1962.
- [FB10] M. FISCHER and K.-U. BLETZINGER: *FEM-Based Simulation, Design and Control of Adaptive Lightweight Structures*. In *Workshop "Robuster Entwurf" der Universitäten Bochum, Weimar und München, 16.07.2010.*, September 14-17 2010.
- [FB12] M. FISCHER and K.-U. BLETZINGER: *Optimalkontrolle elastischer Flächentragwerke*. In *41. Bayerisch-Tirolerisches Mechanik Kolloquium, July 21, München, 2012*.
- [FD91] J. S. R. A. FILHO and P. R. B. DEVLOO: *Object-Oriented Programming in Scientific Computations: The Beginning of a New Era*. *Engineering Computations*, 8:81–87, 1991.

- [FDI⁺10] M. FISCHER, F. DIERINGER, G. IOSIFELIS, R. WÜCHNER and K.-U. BLETZINGER: *FEM-Based Simulation, Design and Control of Adaptive Lightweight Structures*. In B.H.V. TOPPING, J.M. ADAM, F.J. PALLARÉS, R. BRU and M.L. ROMERO (editors): *Proceedings of the Tenth International Conference on Computational Structures Technology*, chapter paper 68. Civil-Comp Press, Stirlingshire, United Kingdom, September 14-17 2010.
- [FDM⁺11] M. FISCHER, F. DIERINGER, H. MASCHING, R. WÜCHNER and K.-U. BLETZINGER: *Smart Adaptive Membrane Structures: Simulation and Design including Control*. In *Membranes 2011*, Barcelona, Spain, October 5 - 7 2011.
- [Fel89] C.A. FELIPPA: *Parametrized Multifield Variational Principles in Elasticity: Part I+II*. *Communications in Applied Numerical Methods*, 5:79–98, 1989.
- [Fel94] C. A. FELIPPA: *A survey of Parametrized Variational Principles and Applications to Computational Mechanics*. *Computer Methods in Applied Mechanics and Engineering*, 113:109–139, 1994.
- [Fel04] C. A. FELIPPA: *Introduction to Finite Element Methods (Lecture Manuscript)*. Department of Aerospace Engineering Sciences and Center for Aerospace Structures, University of Colorado at Boulder, 2004.
- [Fel06] C. A. FELIPPA: *Advanced Finite Element Methods (Lecture Manuscript)*. Department of Aerospace Engineering Sciences and Center for Aerospace Structures, University of Colorado at Boulder, 2006.
- [Fen90] G. L. FENVES: *Object-Oriented Programming For Engineering Software Development*. *Engineering With Computers*, V6 N1:1–15, 1990.
- [FFB09] M. FISCHER, M. FIRL and K.-U. BLETZINGER: *An Object-Oriented Computational Framework for Structural Analysis and Shape Optimal Design*. In *18. Industriearbeitskreis Strukturoptimierung*, Bremen, Germany, March 2009. Industriearbeitskreis Strukturoptimierung.
- [FFB10a] M. FIRL, M. FISCHER and K.-U. BLETZINGER: *Nonlinear Structural Optimization and Simulation based on Object-Oriented and Parallel Programming*. In *euro-LITE, June 06. - 08., Nürnberg*, 2010.
- [FFB10b] M. FISCHER, M. FIRL and K.-U. BLETZINGER: *Nichtlineare Strukturoptimierung und Simulation basierend auf objektorientierter und paralleler Programmierung*. In *Simulation für robuste Produkte und Prozesse*, Bremen, February 9-11 2010.
- [FFB12a] M. FIRL, M. FISCHER and K.-U. BLETZINGER: *Innovative Shape Optimisation in Vehicle Design*. *Automobiltechnische Zeitschrift (ATZ)*, 114:2 – 5, 2012.

- [FFB12b] M. FISCHER, M. FIRL and K.-U. BLETZINGER: *Numerische Formoptimierung für effiziente Leichtbaustrukturen*. *lightweight design*, 1/12:34 – 38, 2012.
- [FFB13] M. FIRL, M. FISCHER and K.-U. BLETZINGER: *Structural lightweight design by innovative optimization strategies*. In *NAFEMS World Congress NWC2013, Salzburg, Austria*, 2013.
- [FFMB10] M. FISCHER, M. FIRL, H. MASCHING and K.-U. BLETZINGER: *Optimization of Nonlinear Structures based on Object-Oriented Parallel Programming*. In B.H.V. TOPPING, J.M. ADAM, F.J. PALLARÉS, R. BRU and M.L. ROMERO (editors): *Proceedings of the Seventh International Conference on Engineering Computational Technology*, chapter paper 67. Civil-Comp Press, Stirlingshire, United Kingdom, Valencia, Spain, September 14-17 2010.
- [FFMB11a] M. FISCHER, M. FIRL, H. MASCHING and K.-U. BLETZINGER: *Efficient Design of Lightweight Structures based on Parameter-free and Parallel Structural Optimization*. In *4th GACM Colloquium, Dresden, Germany, August 31 - September 2 2011*.
- [FFMB11b] M. FISCHER, M. FIRL, H. MASCHING and K.-U. BLETZINGER: *Entwicklung hocheffizienter Leichtbaustrukturen mit Hilfe numerischer Formoptimierung*. In *Landshuter Leichtbau-Colloquium 2011, Landshut, Germany, February 23 -24 2011*.
- [FFS90] B.W.R. FORDE, R.O. FOSCHI and S.F. STIEMER: *Object-Oriented Finite Element Analysis*. *Computers & Structures*, 34(3):355–374, 1990.
- [Fis07] M. FISCHER: *Geometrische und volumetrische Lockingeffekte bei kontinuumsbasierten finiten Elementen und ihre Vermeidung durch die EAS-Methode*. Master's thesis, Lehrstuhl für Statik, Prof. Dr.-Ing. K.-U. Bletzinger, Technische Universität München, 2007.
- [Fis08a] M. FISCHER: *Carat++ Documentation: Object-Oriented Programming*. online documentation, 2008.
- [Fis08b] M. FISCHER: *Eigenfrequency Shape Optimization with CAD-Free Parametrization*. In *FE im Schnee*, February 2008.
- [Fis10a] M. FISCHER: *Carat++: An Object-Oriented and Parallel Finite Element Software*. In *BGCE Research Day*, 21st of January 2010.
- [Fis10b] M. FISCHER: *Carat++ Developers' Wiki*. online documentation, 2010.
- [Fis11] M. FISCHER: *FEM-based Simulation and Design of Smart Adaptive Lightweight Structures*. In *TUM workshop on Multidisciplinary Optimization, April 4-5, Munich*, April 4 - 5 2011.

- [Fis12] M. FISCHER: *Carat++: Some Aspects of Code Management*. In *Invited talk at the Department of Aerospace Engineering Sciences at CU Boulder, USA, Sept. 28st, 2012.*, 2012.
- [Fis13a] M. FISCHER: *Optimale Auslegung von Kompositen durch Strukturoptimierung*. In *CAE-Forum, Hannover Messe 2013*, 2013.
- [Fis13b] M. FISCHER: *Simulation, Design and Control of Smart Membrane and Shell Structures*. In *Invited Talk at ISYS, University of Stuttgart, February 15th 2013.*, 2013.
- [FMB12a] M. FISCHER, H. MASCHING and K.-U. BLETZINGER: *Computergestützte Optimierung von Komposit-Strukturen für den hocheffizienten Leichtbau*. In *Werkstoff-Forum Intelligenter Leichtbau, Hannover Messe, Hannover Messe, 2012*.
- [FMB12b] M. FISCHER, H. MASCHING and K.-U. BLETZINGER: *Efficient Design of Large Lightweight Composite Structures: A Parameter Free Optimization Approach*. In *12th AIAA ATIO/14th AIAA/ISSMO MAO Conferences. 17-19 September 2012.*, Indianapolis, Indiana, USA., 2012.
- [FMB12c] M. FISCHER, H. MASCHING and K.-U. BLETZINGER: *Parameter Free Structural Optimization for the Efficient Design of Large and Lightweight Structures*. In *Invited talk at the Department of Aerospace Engineering Sciences at CU Boulder, USA, Sept. 21st, 2012.*, 2012.
- [FMB13a] M. FISCHER, H. MASCHING and K.-U. BLETZINGER: *FE-basierte Methoden der Strukturoptimierung für den hocheffizienten Leichtbau*. In *ANSYS CONFERENCE & 31. CADFEM USERS' MEETING 2013, 19.-21. Juni 2013, Mannheim, 2013*.
- [FMB13b] M. FISCHER, H. MASCHING and K.-U. BLETZINGER: *FE-basierte Methoden der Strukturoptimierung für den hocheffizienten Leichtbau*. In *6. Landshuter Leichtbau-Colloquium: Systemleichtbau als ganzheitlicher Ansatz, 27.-28. Feb. 2013, Landshut, 2013*.
- [FMBB13] M. FISCHER, H. MASCHING, K.-U. BLETZINGER and O. BILGEN: *Simulation and Parameter-free Optimization of a Piezo-Actuated Solid-State Variable-Camber Wing*. In E. CARRERA, F. MIGLIORETTI and M. PETROLO (editors): *6th ECCOMAS Conference on Smart Structures and Materials, SMART2013, Politecnico di Torino, 24-26 June 2013, 2013*.
- [FMFB11a] M. FISCHER, H. MASCHING, M. FIRL and K.-U. BLETZINGER: *Finite Element Based Parallel Structural Optimization of Lightweight Composite Structures*. In *ICCS 16, Porto, Portugal, June 28.-30. 2011*.
- [FMFB11b] M. FISCHER, H. MASCHING, M. FIRL and K.-U. BLETZINGER: *Parameter Free Structural Optimization of Large Lightweight Composite Structures*. In *ECCOMAS Composites, Sept. 21 -23, 2011, 2011*.

- [FMFB12a] M. FISCHER, H. MASCHING, M. FIRL and K.-U. BLETZINGER: *Design of Lightweight Composite Structures: A Parameter Free Structural Optimization Approach*. In *Material Forming ESAFORM 2012, March 14-16*, volume 504-506 of *Key Engineering Materials*. 2012.
- [FMFB12b] M. FISCHER, H. MASCHING, M. FIRL and K.-U. BLETZINGER: *Design of Lightweight Composite Structures: A Parameter Free Structural Optimization Approach*. In *Key Engineering Materials*, volume 504-506 of *Key Engineering Materials*, pages 1391–1396. 2012.
- [FMFB12c] M. FISCHER, H. MASCHING, M. FIRL and K.-U. BLETZINGER: *Parameter Free Optimization for the Design of Large and Lightweight Composite Structures*. In *3rd Aircraft Structural Design Conference, Delft University, 9-11 October 2012*, 2012.
- [FMWB11] M. FISCHER, H. MASCHING, R. WÜCHNER and K.-U. BLETZINGER: *FEM-Based Simulation, Optimization and Control of Adaptive Lightweight Structures*. In *Smart Structures & Materials 2011*, Saarbrücken, Germany, July 6-8. 2011.
- [FWB09a] M. FISCHER, R. WÜCHNER and K.-U. BLETZINGER: *Computational Framework for Simulation and Design of Adaptive Lightweight Structures*. In *IV ECCOMAS Thematic Conference on Smart Structures and Materials 2009*, Porto, 2009.
- [FWB09b] M. FISCHER, R. WÜCHNER and K.-U. BLETZINGER: *Simulation and Design of Adaptive Lightweight Structures*. In *Forschungskolloquium Baustatik-Baupraxis 2009*, Falkenstein, Germany,, 2009.
- [FWB10] M. FISCHER, R. WÜCHNER and K.-U. BLETZINGER: *FE-Simulation and Optimal Design of Smart Adaptive Lightweight Structures*. In *Fourth European Conference on Computational Mechanics 2010 (ECCM 2010)*, Paris, France, May 16-2 2010.
- [FWB11] M. FISCHER, R. WÜCHNER and K.-U. BLETZINGER: *Simulation, Design and Control of Smart Lightweight Structures based on Object-Oriented and Parallel Programming*. In *Colloquium am Institut für Baustatik und Baudynamik, Universität Stuttgart, 18. April 2011*, 2011.
- [FWB12a] M. FISCHER, R. WÜCHNER and K.-U. BLETZINGER: *FEM-Based Simulation, Optimization and Control of Adaptive Lightweight Structures*. In *Current Trends in Smart Technologies*, Fraunhofer Technical Publication Series. Fraunhofer, 2012.
- [FWB12b] M. FISCHER, R. WÜCHNER and K.-U. BLETZINGER: *Smart Membrane Structures: Efficient Design and Simulation including Control*. In *10th World Congress on Computational Mechanics WCCM 2012, July 8 - 13, Sao Paulo, Brazil.*, 2012.
- [FWB13] M. FIRL, R. WÜCHNER and K.-U. BLETZINGER: *Regularization of Shape Optimization Problems using FE-based parametrization*. *Struct. Multidiscip. Optim.*, 47(4):507–521, 2013.

- [Gab02] U. GABBERT: *Research Activities in Smart Materials and Structures and Expectations to Future Developments*. Journal of Theoretical and Applied Mechanics, 40(3):549–574, 2002.
- [GNTK02] U. GABBERT, T. NESTOROVIC TRAJKOV and H. KÖPPE: *Modelling, Control and Simulation of Piezoelectric Smart Structures using Finite Element Method and Optimal LQ Control*. Mechanics, Automatic Control and Robotics, 3(12):417–430, 2002.
- [GNW65] A.E. GREEN, P.M. NAGHDI and W.L. WAINWRIGHT: *A General Theory of a Cosserat Surface*. Archive for Rational Mechanics and Analysis, 20(4):287–308, 1965.
- [GNW08] U. GABBERT, T. NESTOROVIC and J. WUCHATSCH: *Methods and Possibilities of a Virtual Design for Actively Controlled Smart Systems*. Computers & Structures, 86:240–250, 2008.
- [Goo38] J.N. GOODIER: *On the Problems of the Beam and the Plate in the Theory of Elasticity*. Transactions of the Royal Society Can., Ser. III, 32:65–88, 1938.
- [Gre02] W. GREINER: *Theoretische Physik - Klassische Elektrodynamik*. Verlag Harry Deutsch, 2002.
- [Gri99] D.J. GRIFFITH: *Introduction to Electrodynamics*. Prentice Hall, 1999.
- [GTK06] U. GABBERT, T. NESTOROVIC TRAJKOV and H. KÖPPE: *Finite Element-Based Overall Design of Controlled Smart Structures*. Structural Control and Health Monitoring, 13(6):1052–1067, 2006.
- [HA85] R.T. HAFTKA and H.M. ADELMAN: *An Analytical Investigation of Shape Control of Large Space Structures by Applied Temperatures*. AIAAJ, 23:450–457, 1985.
- [Hel14] E. HELLINGER: *Die allgemeinen Ansätze der Mechanik der Kontinua*, volume 4/4 of *Encyklopädie der Mathematischen Wissenschaften*. 1914.
- [Hen47] H. HENCKY: *Über die Berücksichtigung von Schubverzerrungen in ebenen Platten*. Ingenieurarchiv, 16:72–76, 1947.
- [HKGG93] N. W. HAGOOD, R. KINDEL, K. GHANDI and P. GAUDENZI: *Improving Transverse Actuation using Interdigitated Surface Electrodes*. In *SPIE Paper No. 1917-25, North American Conference on Smart Structures and Materials, Albuquerque, NM*, pages 341–352, 1993.
- [HLW08] W. HEYWANG, K. LUBITZ and W. WERSING: *Piezoelectricity - Evolution and Future Technology*. Springer, Berlin Heidelberg, 2008.
- [Hol04] G.A. HOLZAPFEL: *Nonlinear Solid Mechanics*. John Wiley & Sons, Chichester, 2004.

- [HP93] W.S. HWANG and H.C. PARK: *Finite Element Modeling of Piezoelectric Sensors and Actuators*. AIAA Journal, 31(5):930–937, 1993.
- [HPS96] P. HEYLIGER, K.C. PEI and D. SARAVANOS: *Layerwise Mechanics and FE Model for Laminated Piezoelectric Shells*. AIAA Journal, 34(11):2353–2361, 1996.
- [HT81] T.J.R. HUGHES and T. TEZDUYAR: *Finite Elements Based Upon Mindlin Plate Theory with Particular Reference to the Four-Node Bilinear Isoparametric Element*. Journal of Applied Mechanics, 48:587–596, 1981.
- [HT85] S. HILDEBRANDT and A. TROMBA: *Mathematics and Optimal Form*. Scientific American Library, 1985.
- [Hu55] H.-C. HU: *On Some Variational Principles in the Theory of Elasticity and Plasticity*. Scientia Sinica, 4:33–54, 1955.
- [Hug00] T.J.R. HUGHES: *The Finite Element Method: Linear Static and Dynamic Finite Element Analysis*. Dover Publications, Inc., Mineola, New York, 2000.
- [HW03] J. W. HIGH and W. K. WILKIE: *Method of Fabricating NASA-Standard Macro-Fiber Composite Piezoelectric Actuators*. Technical Report, NASA/TM-2003-212427, ARL-TR-2833, 2003.
- [HZK94] P. HOFFMEISTER, W. ZAHLTEN and W. B. KRATZIG: *Object-Oriented Finite Element Modeling*. In *Second Congress on Computing in Civil Engineering*. ASCE, 1994.
- [Ike90] T. IKEDA: *Fundamentals of Piezoelectricity*. Oxford University Press, New York, 1990.
- [Iro66a] B.M. IRONS: *Engineering Application of Numerical Integraton in Stiffness Methods*. AIAA Journal, 14:2035–2037, 1966.
- [Iro66b] B.M. IRONS: *Numerical Integration Applied to Finite Element Methods*. In *Proc. Conf. on Use of Digital Computers in Structural Engineering*. University of Newcastle, 1966.
- [Irs02] H. IRSCHIK: *A Review on Static and Dynamic Shape Control of Structures by Piezoelectric Actuation*. Engineering Structures, 24:5–11, 2002.
- [Jac99] J.D. JACKSON: *Classical Electrodynamics*. John Wiley & Sons, Inc., 1999.
- [Jaf71] BERNARD JAFFE: *Piezoelectric Ceramics*, volume 3. Academic press, 1971.
- [Joh65] F. JOHN: *Estimates for the Derivatives of the Stresses in a Thin Shell and Interior Shell Equations*. Communications on Pure and Applied Mathematics, 18(1-2):235–267, 1965.
- [Jon02] N. JONASSEN: *Electrostatics*. Springer, 2002.

- [JWB08] A. JARASJARUNGKIAT, R. WÜCHNER and K.-U BLETZINGER: *A Wrinkling Model Based on Material Modification for Isotropic and Orthotropic Membranes*. Computer Methods in Applied Mechanics and Engineering, 197:773–788, 2008.
- [Kam01] M. KAMLAH: *Ferroelectric and Ferroelastic Piezoceramics - Modeling of Electromechanical Hysteresis Phenomena*. Continuum Mechanics and Thermodynamics, 13:219–268, 2001.
- [Kao04] KWAN CHI KAO: *Dielectric Phenomena in Solids*. Kwan Chi Kao, 2004.
- [KB05] M. KÖGL and M.L. BUCALEM: *Analysis of Smart Laminates using Piezoelectric MITC Plate and Shell Elements*. Computers & Structures, 83:1153–1163, 2005.
- [KGF01] P. KALINKE, U. GNAUERT and H. FEHREN: *Einsatz eines aktiven Schwingungsreduktionssystems zur Verbesserung des Schwingungskomforts bei Cabriolets*. In *Adaptronic Congress 2001 in Berlin*, 2001.
- [KGW06] S. KLINKEL, F. GRUTTMANN and W. WAGNER: *A Robust Non-Linear Solid Shell Element Based on a Mixed Variational Formulation*. Computer Methods in Applied Mechanics and Engineering, 195(1-3):179–201, 2006.
- [Kir50] G. KIRCHHOFF: *Über das Gleichgewicht und die Bewegung einer elastischen Scheibe*. Journal für reine angewandte Mathematik, 40:51–58, 1850.
- [KLBC93] G.H. KWEI, A.C. LAWSON, S.J.L. BILLINGE and S.-W. CHEONG: *Structures of the Ferroelectric Phases of Barium Titanate*. J. Phys. Chem., 97:2368–2377, 1993.
- [Kli06] S. KLINKEL: *Nichtlineare Modellierung ferroelektrischer Keramiken und piezoelektrischer Strukturen - Analyse und Finite-Element-Modellierung*. KIT Institut für Baustatik, 2006.
- [Koi60] W.T. KOITER: *The Theory of Thin Elastic Shells*, chapter A: Consistent First Approximation in the General Theory of Thin Elastic Shells, pages 12–33. North-Holland, 1960.
- [Kos04] F. KOSCHNICK: *Geometrische Lockingeffekte bei Finiten Elementen und ein allgemeines Konzept zu ihrer Vermeidung*. PhD thesis, Lehrstuhl für Statik, Prof. Dr.-Ing. K.-U. Bletzinger, Technische Universität München, 2004.
- [KW06] S. KLINKEL and W. WAGNER: *A Geometrically Non-Linear Piezoelectric Solid Shell Element Based on a Mixed Multi-Field Variational Formulation*. International Journal for Numerical Methods in Engineering, 65:349–382, 2006.
- [KW08] S. KLINKEL and W. WAGNER: *A Piezoelectric Solid Shell Element Based on a Mixed Variational Formulation for Geometrically Linear and Nonlinear Applications*. Computers and Structures, 86:38–46, 2008.

- [KWZE] O. KÖNIG, M. WINTERMANTEL, N. ZEHNDER and P. ERMANNI: *FELyX - The Finite Element Library eXperiment*. Technical Report, ETH Zurich, Centre of Structure Technologies.
- [Lam91] R. LAMMERING: *The Application of a Finite Shell Element for Composites Containing Piezoelectric Polymers in Vibration Control*. *Computers & Structures*, 41:1101–1109, 1991.
- [Leg11] D. LEGNER: *Finite-Elemente-Formulierungen mit abgestimmten Approximationsräumen für die Modellierung piezoelektrischer Stab- und Schalenstrukturen*. PhD thesis, Institut für Baustatik, Karlsruher Institut für Technologie, 2011.
- [LGK03] J. LEFÉVRE, U. GABBERT and H. KÖPPE: *Simulation of Piezoelectric Controlled Smart Structures by the Finite Element Method Including Vibroacoustic Effects*. In *Tenth International Congress on Sound and Vibration, Stockholm, Sweden, 2003*.
- [Lin09] J. LINHARD: *Numerisch-mechanische Betrachtung des Entwurfsprozesses von Membrantragwerken*. PhD thesis, Technische Universität München, 2009.
- [LMR03] R. LAMMERING and S. MESECKE-RIESCHMANN: *Multi-Field Variational Formulations and Related Finite Elements for Piezoelectric Shells*. *Smart Materials and Structures*, 12:904–913, 2003.
- [Lov88] A.E.H. LOVE: *On the Small Vibrations and Deformations of Thin Elastic Shells*. *Philosophical Transactions of the Royal Society*, 179:491 ff., 1888.
- [LSV93] M. LYLY, R. STENBERG and T. VIHINEN: *A Stable Bilinear Element for the Reissner-Mindlin Plate Model*. *Computer Methods in Applied Mechanics and Engineering*, 110:343–357, 1993.
- [LT00] T. LEWIŃSKI and J.J. TELEGA: *Plates, Laminates and Shells: Asymptotic Analysis and Homogenization*, volume 52. World Scientific Publishing Company Incorporated, 2000.
- [LW60] P.D LAX and B. WENDROFF: *Systems of Conservation Laws*. *Commun. Pure Appl. Math.*, 13 (2):217–237, 1960.
- [LWB08] J. LINHARD, R. WÜCHNER and K.-U. BLETZINGER: *Textile Composites and Inflatable Structures II*, chapter Introducing cutting patterns in form finding and structural analysis. Springer, 2008.
- [MAC] PROJECT MACS: <https://www.rocq.inria.fr/MACS/spip.php?rubrique69>. Saclay-Ile-de-France Research Center.
- [Mac92a] R. I. MACKIE: *Object oriented programming of the finite element method*. *International Journal for Numerical Methods in Engineering*, 35(2):425–436, August 1992.

- [Mac92b] R.H. MACNEAL: *On the Limits of Finite Element Perfectibility*. International Journal for Numerical Methods in Engineering, 35:1589–1601, 1992.
- [Mac97] R. I. MACKIE: *Using objects to handle complexity in finite element software*. Engineering with Computers, 13(2):99–111, 1997.
- [Mal69] L.E. MALVERN: *Introduction to the Mechanics of a Continuous Medium*. Prentice Hall, Englewood Cliffs, N.J., 1969.
- [Mau88] G.A. MAUGIN: *Continuum Mechanics of Electromagnetic Solids*. World Scientific, Singapore, 1988.
- [MFFB10] H. MASCHING, M. FISCHER, M. FIRL and K.-U. BLETZINGER: *Parameter Free Optimization of Large Scale Lightweight Composite Structures*. In *EUROMECH 522, Erlangen, 10th – 12th October, 2010*, 2010.
- [MFFB11] H. MASCHING, M. FISCHER, M. FIRL and K.-U. BLETZINGER: *Finite Element Based Structural Optimization in Object-Oriented Parallel Programming*. In *PARENG 2011, 12.-15. April, 2011, Corsica, Italy*, 2011.
- [MH78] D.S. MALKUS and T.J.R. HUGHES: *Mixed Finite Element Methods - Reduced and Selective Integration Techniques: A Unification of Concepts*. Computer Methods in Applied Mechanics and Engineering, 15:63–81, 1978.
- [MH83] J.E. MARSDEN and T.J.R. HUGHES: *The Mathematical Foundation of Elasticity*. Prentice-Hall, Englewood Cliffs, New Jersey, 1983.
- [MH85] R. MACNEAL and L. HARDER: *A Proposed Standard Set of Problems to Test Finite Element Accuracy*. Finite Elements in Analysis and Design, 1:3–20, 1985.
- [MH00] H. MANG and G. HOFSTETTER: *Festigkeitslehre*. Springer, 2000.
- [Mil91] G.R. MILLER: *An object-oriented approach to structural analysis and design*. Computers and Structures, 40:75–82, 1991.
- [Mil94] G. R. MILLER: *Coordinate-free isoparametric elements*. Computers & Structures, 49(6):1027–1035, 1994.
- [Min51] R.D. MINDLIN: *Influence of Rotatory Inertia and Shear on Flexural Motions of Isotropic Elastic Plates*. Journal of Applied Mechanics, 18:31–38, 1951.
- [Mül06] G. MÜLLER: *Continuum Mechanics and Tensor Analysis (Vorlesungsskriptum)*. Lehrstuhl für Baumechanik, Prof. Dr.-Ing. G. Müller, Technische Universität München, 2006.
- [Mor59] D. MORGENSTERN: *Herleitung der Plattentheorie aus der dreidimensionalen Elastizitätstheorie*. Archive of Rational Mechanics and Analysis, 4:145–152, 1959.

- [MR94] G. R. MILLER and M. D. RUCKI: *A Program Architecture for Interactive Non-Linear Dynamic Analysis of Structures*. In *Second Congress on Computing in Civil Engineering*. ASCE, 1994.
- [MR04] S. MESECKE-RISCHMANN: *Modellierung von flachen piezoelektrischen Schalen mit zuverlässigen finiten Elementen*. PhD thesis, Helmut-Schmidt-Universität, Hamburg, 2004.
- [MS00] A.K. MAJI and M.A. STARNES: *Shape Measurement and Control of Deployable Membrane Structures*. *Experimental mechanics*, 40(2):154–159, 2000.
- [MT90] E. MONCRIEFF and B.H.V. TOPPING: *Computer Methods for the Generation of Membrane Cutting Patterns*. *Computers and Structures*, 37:441–450, 1990.
- [MU03] S. DE MIRANDA and F. UBERTINI: *Consistency and Recovery in Electroelasticity Part I: Standard Finite Elements*. *Computer Methods in Applied Mechanics and Engineering*, 192:831–850, 2003.
- [MU04] S. DE MIRANDA and F. UBERTINI: *Consistency and Recovery in Electroelasticity Part II: Equilibrium and Mixed Finite Elements*. *Computer Methods in Applied Mechanics and Engineering*, 193:2155–2168, 2004.
- [MW05] H.P. MONNER and P. WIERACH: *Overview of Smart-Structures Technology at the German Aerospace Center*. Technical Report, German Aerospace Center (DLR), Institute of Composite Structures and Adaptive Systems, 2005.
- [MZ93] P. MENÉTREY and T. ZIMMERMANN: *Object-oriented non-linear finite element analysis: Application to J2 plasticity*. *Computers & Structures*, 49(5):767–777, December 1993.
- [Nag72] P.M. NAGHDI: *The Theory of Shells and Plates*. In S. FLÜGGE (editor): *Handbuch der Physik*, volume V1/2, page 425–640. Springer, Berlin, 1972.
- [Oga87] K. OGATA: *Discrete-Time Control Systems*. Prentice Hall, 1987.
- [Oga02] K. OGATA: *Modern Control Engineering*. Prentice Hall, 2002.
- [OR76] J. T. ODEN and J. N. REDDY: *Variational Methods in Theoretical Mechanics*. Springer, 1976.
- [Par95] H. PARISCH: *A Continuum Based Shell Theory for Nonlinear Applications*. *International Journal for Numerical Methods in Engineering*, 38:1855–1883, 1995.
- [Par03] H. PARISCH: *Festkörper-Kontinuumsmechanik*. Teubner, 2003.
- [PB01] BOREK PATZÁK and ZDENEK BITTNAR: *Design of object oriented finite element code*. *Advances in Engineering Software*, 32:759–767, 2001.

- [PC82] T. H. H. PIAN and D. P. CHEN: *Alternative Ways for Formulation of Hybrid Stress Elements*. International Journal for Numerical Methods in Engineering, 18:1679–1684, 1982.
- [PH93] R. M. V. PIDAPARTI and A. V. HUDLI: *Dynamic analysis of structures using object-oriented techniques*. Computers & Structures, 49:149–156, 1993.
- [PHN06] F. PENG, Y.-R. HU and A. NG: *Testing of Membrane Space Structure Shape Control Using Genetic Algorithm*. Journal of spacecraft and rockets, 43(4):788–793, 2006.
- [PN79] S.C. PANDA and R. NATARAJAN: *Finite Element Analysis of Laminated Composite Plates*. International Journal for Numerical Methods in Engineering, 14:69–79, 1979.
- [Pra18] L. PRANDTL: *Tragflügeltheorie*. Abhandlungen der Königlichen Gesellschaft der Wissenschaften zu Göttingen. 1918.
- [Pre35] F. PREISACH: *Über die magnetische Nachwirkung*. Zeitschrift für Physik, 94:277–302, 1935.
- [Pre02] A. PREUMONT: *Vibration Control of Active Structures, An Introduction*. Solid Mechanics and its Applications. Kluwer Academic Publishers, 2002.
- [PS84] T. H. H. PIAN and K. SUMIHARA: *Rational Approach for Assumed Stress Finite Elements*. International Journal for Numerical Methods in Engineering, 20:1685–1695, 1984.
- [Ram81] E. RAMM: *Nonlinear Finite Element Analysis in Structural Mechanics*, chapter Strategies for Tracing the Nonlinear Response near Limit Points, pages 63–89. Springer, 1981.
- [RBB94] E. RAMM, M. BISCHOFF and M. BRAUN: *Higher Order Nonlinear Shell Formulation - a Step back into three dimensions*. In K. BELL (editor): *From Finite Elements to the Troll Platform*, pages 65–88. Department of Structural Engineering, The Norwegian Institute of Technology, Trondheim, 1994.
- [Rei44] E. REISSNER: *On the Theory of Bending of Elastic Plates*. Journal of Mathematics and Physics, 23:184–191, 1944.
- [Rei45] E. REISSNER: *The Effect of Transverse Shear Deformation on the Bending of Elastic Plates*. Journal of Applied Mechanics, 12:69–76, 1945.
- [Rei50] E. REISSNER: *On a Variational Theorem in Elasticity*. Journal of Mathematics and Physics, 29:90–95, 1950.

- [RK93a] B. RAPHAEL and C. S. KRISHNAMOORTHY: *Automating Finite Element Development Using Object-Oriented Techniques*. Engineering Computations, 10:267 – 278, 1993.
- [RK93b] B. RAPHAEL and C.S. KRISHNAMOORTHY: *Automating Finite Element Development Using Object-Oriented Techniques*. Engineering Computations, 10:267–278, 1993.
- [RRS93] M. C. RAY, K. M. RAO and B. SAMANTHA: *Exact Solution for Static Analysis of an Intelligent Structure under Cylindrical Bending*. Computers and Structures, 47:1031 –1042, 1993.
- [SB93] E. STEIN and F.J. BARTHOLD: *Der Ingenieurbau - Werkstoffe, Elastizitätstheorie. Kapitel Elastizitätstheorie*. Ernst & Sohn, 1993.
- [SC74] C.T. SUN and N.C. CHENG: *Piezoelectric Waves on a Layered Cylinder*. Journal of Applied Physics, 45:4288–4294, 1974.
- [Sch10] K. SCHULZ: *Theorie und Finite-Elemente-Modellierung geometrisch und materiell nichtlinearer piezoelektrischer Schalenstrukturen*. PhD thesis, Karlsruher Institut für Technologie, Institut für Baustatik, 2010.
- [SF73] G. STRANG and G. FIX: *An Analysis of the Finite Element Method*. Prentice-Hall, 1973.
- [SFR89a] J.C. SIMO, D.D. FOX and M.S. RIFAI: *On a Stress Resultant Geometrically Exact Shell Model. Part I: Formulation and Optimal Parametrization*. Computer Methods in Applied Mechanics and Engineering, 72(1):267–304, 1989.
- [SFR89b] J.C. SIMO, D.D. FOX and M.S. RIFAI: *On a Stress Resultant Geometrically Exact Shell Model. Part II: the linear theory; computational aspects*. Computer Methods in Applied Mechanics and Engineering, 73(1):53–92, 1989.
- [SG93] K.Y. SZE and A. GHALI: *Hybrid Hexahedral Element for Solids, Plates and Beams by Selective Scaling*. International Journal for Numerical Methods in Engineering, 36:1519–1540, 1993.
- [SH86] J.C. SIMO and T.J.R. HUGHES: *On the Variational Formulation of Assumed Strain Methods*. Journal of Applied Mechanics, 53:51–54, 1986.
- [SH98] J.C. SIMO and T.J.R. HUGHES: *Computational Inelasticity*. Springer Verlag, New York, 1998.
- [SH99] D.A. SARAVANOS and P.R. HEYLIGER: *Mechanics and Computational Models for Laminated Piezoelectric Beams, Plates and Shells*. Applied Mechanics Review, 52:305–320, 1999.

- [SK98] J.A. SETHIAN and R. KIMMEL: *Computing Geodesic Paths on Manifolds*. Proceedings of the National Academy of Sciences, 95(15):8431–8435, 1998.
- [SM01] A.V. SRINIVASAN and D.M. MCFARLAND: *Smart Structures - Analysis and Design*. Cambridge University Press, Cambridge, UK, 2001.
- [SmS12] *Stuttgart SmartShell*. <http://smartshell-stuttgart.de/>, 2012.
- [SP99] K. Y. SZE and Y. S. PAN: *Hybrid Finite Element Models for Piezoelectric Materials*. Journal of Sound and Vibration, 226 (3):519 – 547, 1999.
- [SPM06] H. SAKAMOTO, K.C. PARK and Y. MIYAZAKI: *Distributed and Localized Active Vibration Isolation in Membrane Structures*. Journal of Space Craft and Rockets, 43(5):1107–1116, 2006.
- [SR90] J.C. SIMO and S. RIFAI: *A Class of Mixed Assumed Strain Methods and the Method of Incompatible Modes*. International Journal for Numerical Methods in Engineering, 29:1595–1638, 1990.
- [Ste64] E. STEIN: *Beiträge zu den direkten Variationsverfahren in der Elastostatik der Balken und Flächentragwerke*. PhD thesis, Institut für Baustatik, Universität Stuttgart, 1964.
- [SWB12] S. SICKLINGER, R. WÜCHNER and K.-U. BLETZINGER: *EMPIRE: A N-Code Coupling Tool for Multiphysic Co-Simulations with OpenFOAM*. In *7th OpenFOAM Workshop, Technische Universität at Darmstadt, Germany*, 2012.
- [SWC92] E. D. SOTELINO, D. W. WHITE and W. F. CHEN: *Domain-Specific Object-Oriented Environment For Parallel Computing*. Report: Ce-Str-92-41, School Of Civil Engineering, Purdue Univ., West Lafayette, Indiana, (Presented At The 2nd International Conference On Discrete Element Methods, Mar. 18, 1993.) edition, 1992.
- [SY00] K.Y. SZE and L.Q. YAO: *A Hybrid Stress ANS Solid-Shell Element and its Generalization for Smart Structure Modelling. Part I - Solid-Shell Element Formulation*. International Journal for Numerical Methods in Engineering, 48:545–564, 2000.
- [SYY00] K.Y. SZE, L.Q. YAO and S. YI: *A Hybrid Stress ANS Solid-Shell Element and its Generalization for Smart Structure Modelling. Part II - Smart Structure Modelling*. International Journal for Numerical Methods in Engineering, 48:565–582, 2000.
- [SYY04] K.Y. SZE, X.-M. YANG and L.-Q. YAO: *Stabilized Plane and Axisymmetric Piezoelectric Finite Element Models*. Finite elements in analysis and design, 40(9):1105–1122, 2004.

- [TB97] H.S. TZOU and Y. BAO: *Nonlinear Piezothermelasticity and Multi-Field Actuations: Part 1: Nonlinear Anisotropic Piezothermoelastic Shell Elements*. Journal of Vibration and Accoustics, 119:374–381, 1997.
- [TBW76] R.L. TAYLOR, P.J. BERESFORD and E.L. WILSON: *A Non-Conforming Element for Stress Analysis*. International Journal for Numerical Methods in Engineering, 10:1211–1220, 1976.
- [TG89] H.S. TZOU and M. GRANDE: *Theoretical Analysis of a Multi-Layered Thin Shell Coupled with Piezoelectric Shell Actuators for Distributed Vibration Control*. Journal of Sound and Virbation, 132(3):433–450, 1989.
- [TH93] H. S. TZOU and S. HORN: *Piezoelectric Shells: Distributed Sensing and Control of Continua*. Solid mechanics and its applications. Kluwer Academic, Dordrecht, Boston, 1993.
- [Tie69] H.F. TIERSTEN: *Linear Piezoelectric Plate Vibrations*. Plenum Press, New York, 1969.
- [TKG06] T. NESTOROVIC TRAJKOV, H. KÖPPE and U. GABBERT: *Vibration Control of a Funnel-Shaped Shell Structure with Distributed Piezoelectric Actuators and Sensors*. Smart Materials and Structures, 15:1119–1132, 2006.
- [TN60] C. TRUESDELL and W. NOLL: *The Nonlinear Field Theories of Mechanics*. Springer, Berlin, 1960.
- [Ton72] E. TONTI: *On the mathematical structure of a large class of physical theories*. Accademia Nazionale dei Lincei, estratto dai Rendiconti della Classe di Scienze fisiche, matematiche e naturali, Serie VIII, Vol. LII, fasc. 1, 1972.
- [Ton03] E. TONTI: *A Classification Diagram for Physical Variables (Preliminary Draft)*. Technical Report, 2003.
- [Tou02] R. TOUZANI: *An object oriented finite element toolkit*. In *Proceedings of the Fifth World Congress on Computational Mechanics (WCCM V)*, 2002.
- [TT91] H.S. TZOU and C.I. TSENG: *Distributed Vibration Control and Identification of Coupled Elastic/Piezoelectric Systems: Finite Element Formulation and Application*. Mechanical Systems and Signal Processing, 5 (3):215–231, 1991.
- [TVQ05] X. TAN and L. VU-QUOK: *Optimal Solid Shell Element for Large Deformable Composite Structures with Piezoelectric Layers and Active Vibration*. International Journal for Numerical Methods in Engineering, 64:1981–2013, 2005.
- [TY96] H.S. TZOU and R. YE: *Analysis of Piezoelectric Structures with Laminated Piezoelectric Triangle Shell Elements*. AIAA Journal, 1:110–115, 1996.

- [TZ93] H.S. TZOU and J.P. ZHONG: *Electromechanics and Vibrations of Piezoelectric Shell Distributed Systems*. Journal of Dynamic Systems Measurement and Control, 115(3):506–517, 1993.
- [TZSC86] R.L. TAYLOR, O.C. ZIENKIEWICZ, J.C. SIMO and A.H.C. CHAN: *The Patch Test - a Condition for Assessing FEM Convergence*. International Journal for Numerical Methods in Engineering, 22:39–62, 1986.
- [Voi28] W. VOIGT: *Lehrbuch der Kristallphysik*. B. G. Teubner, Leipzig, Berlin, 1910 and 1928.
- [VS06] D. VARELIS and D.A. SARAVANOS: *Coupled Mechanics and Finite Element for Non-Linear Laminated Piezoelectric Shallow Shells Undergoing Large Displacements and Rotations*. International Journal for Numerical Methods in Engineering, 66:1211–1233, 2006.
- [Wak99] D.S. WAKEFIELD: *Engineering Analysis of Tension Structures: Theory and Practice*. Engineering Structures, 21:680–690, 1999.
- [WB05] R. WÜCHNER and K.U. BLETZINGER: *Stress-Adapted Numerical Form Finding of Prestressed Surfaces by the Updated Reference Strategy*. International Journal for Numerical Methods in Engineering, 64:143–166, 2005.
- [Whi04] E.T. WHITTAKER: *A Treatise on the Analytical Dynamics of Particles and Rigid Bodies*. Cambridge University Press, 1904.
- [WTDG73] E.L. WILSON, R.L. TAYLOR, W. P. DOHERTY and J. GHABOUSSI: *Incompatible Displacement Models*. Numerical and Computer Methods in Structural Mechanics, pages 43–57, 1973.
- [Wüc06] R. WÜCHNER: *Mechanik und Numerik der Formfindung und Fluid-Struktur-Interaktion von Membrantragwerken*. PhD thesis, Technische Universität München, 2006.
- [WW02] X. WANG and Y. WANG: *On Nonlinear Behaviour of Spherical Shallow Shells Bonded with Piezoelectric Actuators by the Differential Quadrature Element Method*. International Journal for Numerical Methods in Engineering, 53:1477–1490, 2002.
- [YA93] G. YU and H. ADELI: *Object-Oriented Finite Element Analysis Using EER Model*. Journal Of Structural Engineering, 119(9):2763–2781, 1993.
- [Yan05] J. YANG: *An Introduction to the Theory of Piezoelectricity*, volume 9 of *Advances in Mechanics and Mathematics*. Springer, 2005.
- [YBL94] J. S. YANG, R. C. BATRA and X. Q. LIANG: *The Cylindrical Bending Vibration of a Laminated Elastic Plastic due to Piezoelectric Actuators*. Smart Materials and Structures, 3:485 – 493, 1994.

- [ZDK95] W. ZAHLTEN, P. DEMMERT and W. B. KRATZIG: *An Object-Oriented Approach to Physically Nonlinear Problems in Computational Mechanics*. Computing in Civil and Building Engineering, 1995.
- [ZDPB92] THOMAS ZIMMERMANN, YVES DUBOIS-PÈLERIN and PATRICIA BOMME: *Object-oriented finite element programming: I. Governing principles*. Computer Methods in Applied Mechanics and Engineering, 98(2):291–303, July 1992.
- [ZE00] M. W. ZEHN and M. ENZMANN: *Simulation of Structure Control and Controller Design Within a Finite Element Code*. Journal of Vibration and Control, 6:223–242, 2000.
- [Zie05] F. ZIEGLER: *Computational Aspects of Structural Shape Control*. Computers & Structures, 83:1191–1204, 2005.
- [ZT05] O.C. ZIENKIEWICZ and R.L. TAYLOR: *The Finite Element Method: Solid and Structural Mechanics*. Butterworth-Heinemann, 2005.
- [ZTZ05] O.C. ZIENKIEWICZ, R.L. TAYLOR and J.Z. ZHU: *The Finite Element Method: Its Basis & Fundamentals*. Butterworth-Heinemann, 2005.
- [ZWC04] S. ZHENG, X. WANG and W. CHEN: *The Formulation of a Refined Hybrid Enhanced Assumed Strain Solid Shell Element and its Application to Model Smart Structures Containing Distributed Piezoelectric Sensors/Actuators*. Smart Materials and Structures, 13:43–50, 2004.
- [ZZF03] J. ZHANG, B. ZHANG and J. FAN: *A Coupled Electromechanical Analysis of a Piezoelectric Layer Bonded to an Elastic Substrate: Part I, Development of Governing Equations*. International journal of solids and structures, 40(24):6781–6797, 2003.